Reconstructing last glacial changes in Atlantic meridional overturning rate using marine sediment (231Pa/230Th)

Pierre Burckel

THESE

Présentée pour l'obtention du grade de

Docteur de l'Université de Versailles Saint-Quentin en Yvelines

Spécialité : Paléoclimatologie et Paléocéanographie

par

Pierre Burckel

Thèse intitulée

Utilisation du rapport ($^{231}Pa/^{230}Th$) des sédiments marins pour caractériser les changements de circulation océanique lors des variations climatiques de la dernière période glaciaire

---

Dont la soutenance aura lieu le 28 novembre 2014, devant le jury composé de :

- Mme. Claire Waelbroeck	Directrice de thèse
- Mme Jeanne Gherardi	Codirectrice de thèse
- M. Sylvain Pichat	Codirecteur de thèse
- M. Alex Thomas	Rapporteur
- Mme Mary Elliot	Rapporteur
- M. Joerg Lippold	Examinateur
-M. Philippe Bousquet	Professeur à l'UVSQ

LSCE/IPSL, Laboratoire des Sciences du Climat et de l'Environnement
(CEA-CNRS-UVSQ)
Domaine du CNRS – Avenue de la Terrasse – 91190 - Gif-sur-Yvette - France

A ma famille et aux copains

Remerciements

Je tiens à démarrer ce manuscrit (ou à le finir, question de point de vue) en remerciant toutes les personnes qui m'ont aidé ou soutenu pendant cette thèse. Et en trois ans de thèse, trois ans d'aventure professionnelle mais également personnelle, ces personnes sont nombreuses. Je vais donc tâcher de n'oublier personne. Mais si, vous qui me lisez, ne voyez pas apparaître votre nom ci-dessous et que vous vous en sentez lésé, c'est certainement que je vous dois beaucoup, et je vous en remercie.

Je souhaite remercier en premier lieu Claire Waelbroeck, ma directrice de thèse. En effet, un doctorat commence par un sujet de thèse, et le sujet que Claire a élaboré était passionnant. Il m'a permis d'utiliser un matériel et des méthodes géochimiques de pointe, afin d'étudier une zone clef pour la compréhension du climat et de l'océan de la dernière période glaciaire. Claire, ta rigueur et ta franchise m'ont permis de développer ma réflexion scientifique et d'adopter une méthode de travail qui m'a été précieuse notamment lors de ma collaboration avec d'autres laboratoires. Dans les hauts et les bas de cette thèse, tu m'as toujours fondamentalement fait confiance et, pour tout cela, un grand merci à toi.

Un grand merci également à mes co-directeurs de thèse, Jeanne Gherardi et Sylvain Pichat, qui assuraient, entre autres, la partie expérimentale de mon encadrement, partie à laquelle, vous le savez, je porte un immense intérêt. C'est notamment grâce à vous que j'ai pu mettre le pied dans la communauté du Pa/Th, où j'ai rencontré des personnes passionnées. Jeanne, merci de m'avoir fait découvrir l'enseignement et de m'avoir prodigué tes conseils et idées sur l'après thèse.

Au cours de cette thèse, j'ai eu la chance de travailler avec deux équipes : Paléocean et Geotrac. Un grand merci aux membres de ces deux équipes. Je pense tout d'abord à Matthieu Roy Barman, auprès de qui j'ai pu bénéficier de nombreux conseils concernant la mesure du rapport Pa/Th au laboratoire. Merci pour ces longues discussions et le temps que tu y consacrais, ainsi que pour le covoiturage vers Chevry qui m'a bien économisé les pieds ! Merci à Edwige Pons-Branchu pour ses conseils et sa gentillesse. Et encore désolé d'être entré en salle blanche avec des sédiments ! Un grand merci à Dominique Blamart, qui a toujours su trouver les mots pour me motiver. Toujours un plaisir d'entrer dans le bureau de « Dominique et Hervé » ! Merci également à Eric Douville pour son calme et ses conseils, en particulier dans l'utilisation des spectromètres. Un grand merci à Frank Bassinot, pour sa bonne humeur communicative et maintes fois communiquée, et pour m'avoir permis de participer à la mission océanographique MONOPOL qui a été une des expériences les plus marquantes de ma thèse. Merci à Elisabeth Michel et à Jean Jouzel pour leur gentillesse et leurs conseils sur mon premier article, et à Jean-Claude Duplessy pour ses critiques qui m'ont aidé à

améliorer mes articles et mon manuscrit de thèse. Un grand merci à Gulay pour son soutien moral inconditionnel et évidemment pour son aide dans la reconnaissance de ces petites bestioles que sont les foraminifères. Merci à Fabien pour sa bonne humeur et ses nombreux conseils, que ce soit au niveau des mesures ou sur mon futur professionnel et personnel. Un immense merci à François qui m'a appris à dompter le Neptune (enfin quand il se laissait faire). François, ton calme et ta bonne humeur ont probablement renforcé mon intérêt pour la spectrométrie, quoique ta blague « y a pas de signal dans tes échantillons » m'ait fait perdre beaucoup de cheveux. Un grand merci, Natalia, pour tes conseils et ta gentillesse, et pour m'avoir évité de perdre le reste de mes cheveux lorsqu'au moment fatidique, mon ordinateur refusait d'afficher correctement les power-points. Un immense merci à Hélène également, avec qui c'était toujours un plaisir de prendre le thé ou simplement de discuter. Merci, Aline, pour ta réactivité et tes explications claires, Louise pour tout le travail que tu accomplis (presque) toujours dans la bonne humeur, Lorna, toi qui es toujours prompte à aider les autres. Merci à Evelyn Böhm avec qui ce fut un plaisir de travailler pendant ce dernier mois au LSCE.

Merci aussi à Virginie, Jean-Pascal, Jean-Louis Reyss, Hélène Valladas, Evelyne Kaltnecker.

Je tiens également à remercier les gens d'en haut, les gens de l'Orme : Masa Kageyama et Didier Roche, Gilles Ramstein et Jean Claude Dutay. Merci à Christophe Colin d'IDES avec qui j'ai pu troquer du matériel de labo grâce à certains recoupements inattendus entre la mesure des isotopes du néodyme et celle du rapport Pa/Th.

Un grand merci aux membres de mon comité de thèse Luke Skinner et Joerg Lippold. Votre venue était toujours une bouffée d'air frais sur mon travail, et j'ai pris énormément de plaisir à travailler très régulièrement avec Joerg. Egalement merci aux membres de mon jury de thèse, Mary Elliot, Alex Thomas Philippe Bousquet et (encore) Joerg Lippold.

Ce travail de thèse n'aurait pas été possible sans une bonne ambiance au laboratoire, sans des épaules auxquelles se tenir, sans les copains. Hugo le goal ultra volant, Cindy et ses séances de yoga, Jens qui me rappelle le pays, Naoufel qui se cache dans les buissons pour « prendre des photos d'oiseaux », Marion qui est née du mauvais côté des Vosges, Elian le sauveur de violon. Et bien sûr un grand merci à mon collègue de bureau, Romain. J'espère que les successeurs du bureau 307 apprécieront nos moments de décontraction placardés sur les murs et sur la porte ☺. Merci également aux thésards partis plus tôt : Cécile, Flora, Romain, Thomas, Sandra, David, Qiong, Véronique. A ceux qu'on voit moins souvent ou qui sont là depuis peu : Quentin, Alison, Lucie, Wiem.

Enfin, un grand merci à ma famille et aux copains d'enfance, de fac, d'Erasmus. Votre confiance, vos conseils et vos encouragements sont les fondations de ce travail.

Table of contents

Thesis abstract **1**

Résumé de la these **3**

Résumé détaillé en français **5**

Introduction **15**

Chapter 1: Thesis objectives and study area **19**

1.1 Thesis objectives **19**

1.1.1 Oceanic circulation variability during the past 60 ka 19

1.1.2 Origin of the Dansgaard Oeschger variability 21

1.1.3 Dansgaard Oeschger variability outside the high latitude North Atlantic 23

1.2 Sedimentary Pa/Th **25**

1.2.1 Behavior of protactinium and thorium in the ocean. 25

1.2.2 Pa/Th as a tracer of deep-water renewal rate 26

1.2.3 Effect of particle type and flux 27

1.2.3 a) Use of the sedimentary Pa/Th ratio as a proxy of particle type and flux 27

1.2.3 b) Acquisition of the sedimentary Pa/Th signal 28

1.3 Stratigraphy of the cores **28**

1.3.1 Influence of the Amazon 29

1.3.2. Study area and stratigraphy of the cores 31

Chapter 2: Methodology **41**

2.1 Opal measurements **42**

2.1.1 Method 42

2.1.2 Calculation 43

2.1.3 Uncertainties 45

2.2 ^{233}Pa, ^{236}U and ^{229}Th spikes **46**

2.2.1 ^{233}Pa spike milking from ^{237}Np 46

2.2.2 ^{233}Pa calibration 46

2.2.3 ^{236}U and ^{229}Th calibration 47

2.3 Measurement by mass-spectrometry and Pa/Th calculation **48**

2.3.1 Measurements by mass-spectrometry 48

2.3.2 Pa/Th calculation 52

2.4 Pa/Th sediment results and inter-comparison **53**

2.4.1 Methodological recommendations for the analysis of sedimentary Pa/Th. 53

2.4.2 Supporting Information 76

Chapter 3 : Timing of Oceanic circulation changes in the Atlantic during the last glacial **93**

3.1 Introduction **93**

3.2 Atlantic Ocean circulation changes preceded millennial tropical South America rainfall events during the last glacial **94**

3.3 Supporting Information **115**

3.4 Additional elements of discussion **135**

Chapter 4: Changes in the geometry and strength of the AMOC during the last glacial **137**

4.1 Introduction **137**

4.2 Changes in the geometry and strength of the AMOC during the last glacial **139**

4.3 Supporting Information **164**

Chapter 5: Conclusion and perspectives **175**

5.1 Conclusion **175**
5.1.1 Dansgaard-Oeschger interstadials 175
5.1.2 Heinrich Stadials 176
5.1.3 Dansgaard Oeschger Stadials 177
5.1.4 Mechanisms of climate variability 177
5.1.4 a) Difference between Dansgaard Oeschger and Heinrich Stadials 177
5.1.4 b) Effect of the AMOC on Greenland temperatures 178
5.2 Perspectives **178**
LIST OF FIGURES AND TABLES **181**
REFERENCES **189**

Thesis abstract

The upper circulation cell of the Atlantic Meridional Overturning Circulation (AMOC) plays an important role in the climate system as it transports heat from the tropical Atlantic to the North Atlantic high latitudes. Understanding the precise relation between AMOC and climate requires long-term data extracted from natural climate archives (e.g., marine sediment records, ice cores, stalagmites, …), as instrumental time series are too short and impaired by the difficulty of distinguishing natural variability from anthropogenic change.

My thesis objective has been to reconstruct the vertical layout and strength of the water masses constituting the AMOC during fast climate changes of the last glacial using sedimentary Pa/Th, a proxy of water mass flow rate.

My study area is situated on the Brazilian margin, an area that is the locus of the western boundary currents and therefore ideal to monitor changes in the AMOC. The sediment cores I studied also recorded the precipitation increases associated with the southward shifts of the Inter Tropical Convergence Zone (ITCZ) occurring during stadials of the last glacial. Because both precipitation proxies and water mass flow rate proxies are recorded in the same core, I was able to reliably assess the timing of the AMOC upper circulation cell slowdown with respect to the southward shifts of the ITCZ. I find that the AMOC upper circulation cell started to slowdown 1420 ± 250 (1σ) and 690 ± 180 (1σ) years before the southward ITCZ shifts associated with Heinrich Stadial 2 and Heinrich Stadial 4, respectively. Hence, my results confirm that a slowdown of the AMOC could be the origin of the ITCZ shifts associated with Heinrich Stadials and provide the first precise estimate of the phasing between these two climate variables. Based on these results I propose a mechanism explaining the difference between Heinrich and Dansgaard-Oeschger stadials.

Using modeling results, I show that the Atlantic Ocean circulation during periods of higher Greenland temperatures (interstadials) was markedly different from that of the Holocene. Two overturning cells were likely active in the Atlantic Ocean: an upper overturning circulation cell initiated by northern-sourced deep water flowing southward above ~2500 m depth at the equator, and a lower overturning circulation cell initiated by southern sourced deep water flowing northward below ~4000 m depth at the equator. The overturning rate of the upper overturning cell was likely lower than that of present-day North Atlantic Deep Water. At the onset of Heinrich Stadials, the structure of the AMOC significantly changed, and southern-sourced deep-waters likely dominated the equatorial Atlantic Ocean below 1300 m depth.

Résumé de la these

La cellule supérieure de la circulation méridienne de retournement de l'Atlantique (AMOC) transporte de la chaleur depuis l'Atlantique tropical vers les hautes latitudes de l'océan Atlantique Nord, jouant ainsi un rôle clé dans le système climatique. Comprendre précisément les relations entre l'AMOC et le climat requiert l'analyse d'enregistrements climatiques longs, issus d'archives naturelles (telles que les carottes sédimentaires marines, carottes de glaces, stalagmites…) car les séries de données instrumentales sont trop courtes et ne permettent pas de distinguer les variations climatiques naturelles de l'influence anthropique.

L'objectif de ma thèse a été de reconstituer la structure verticale et la dynamique des masses d'eaux constituant l'AMOC au cours des variations climatiques rapides de la dernière période glaciaire à partir du rapport Pa/Th sédimentaire, un traceur de la vitesse d'écoulement des masses d'eaux.

Ma zone d'étude est située sur la marge nord-est du Brésil, une zone affectée par les courants de bord ouest et donc idéale pour reconstituer la variabilité de l'AMOC. Les carottes sédimentaires que j'ai analysées ont également enregistré les augmentations de précipitations associées aux migrations vers le sud de la zone de convergence intertropicale (ITCZ) survenant durant les stadiaires de la dernière période glaciaire. Comme les variations de précipitation et de circulation océanique sont enregistrées dans la même carotte, j'ai pu précisément estimer le délai entre le ralentissement de l'AMOC et le déplacement vers le sud de l'ITCZ. Je trouve ainsi que le ralentissement de la cellule supérieure de l'AMOC commence 1420 ± 250 (1σ) années avant le déplacement vers le sud de l'ITCZ associé au « Heinrich Stadial » 2 et 690 ± 180 (1σ) années avant celui associé au « Heinrich Stadial » 4. Mes résultats confirment donc qu'un ralentissement de l'AMOC pourrait être à l'origine des migrations de l'ITCZ associées aux « Heinrich Stadials » et fournissent une première estimation précise du décalage temporel entre ces deux variables climatiques. Sur la base de ces résultats, je propose un mécanisme expliquant les différences entre les « Heinrich Stadials » et les « Dansgaard-Oeschger Stadials ».

A partir de résultats de modélisation, je montre que la circulation océanique pendant les périodes chaudes au Groenland (« interstadials ») était très différente de celle de l'Holocène. Deux cellules de circulation étaient probablement actives dans l'océan Atlantique : une cellule supérieure initiée par l'écoulement au-dessus de 2500 m à l'équateur d'une masse d'eau en provenance du nord et se dirigeant vers le sud, et une cellule inférieure initiée par l'écoulement au-dessous de 4000 m à l'équateur d'une masse d'eau en provenance du sud et se dirigeant vers le nord. Le taux de renouvellement de la masse d'eau profonde de la cellule supérieure était probablement

plus faible que celle de la masse d'eau actuellement formée dans les hautes latitudes de l'océan Atlantique Nord. Au début des « Heinrich Stadials », la structure de l'AMOC a significativement changé et des eaux en provenance du sud ont probablement dominé l'océan Atlantique équatorial en-dessous de 1300 m de profondeur.

Résumé détaillé en français

Au cours de la dernière période glaciaire, les températures de l'air au-dessus du Groenland ont oscillé à l'échelle du millénaire entre périodes chaudes (interstadiaires) et périodes froides (stadiaires) (Johnsen et al., 1992). Chaque stadiaire est terminé par une augmentation des températures de l'air de l'ordre d'une dizaine de degrés, atteinte en quelques décennies seulement, et marquant l'entrée dans des conditions interstadiaires (Kindler et al., 2014). Durant chaque interstadiaire, les températures de l'air diminuent vers de nouvelles conditions stadiaires (températures minimales) maintenues pendant plusieurs centaines d'années. Ces réchauffements abrupts enregistrés dans la glace du Groenland sont appelés « évènements de Dansgaard-Oeschger » (Dansgaard et al., 1993).

Pendant certains stadiaires, des fragments lithogènes grossiers ont été déposés dans les sédiments de l'Atlantique Nord. Ces débris ne pouvant être amenés dans l'océan ouvert que par des icebergs, ils sont appelés « Ice Rafted Detritus » (IRD). Les épaisses couches d'IRD déposées dans l'Atlantique Nord sont appelées « Heinrich Events » (HE) (Heinrich, 1988), et les stadiaires au cours desquels elles sont déposées sont appelés « Heinrich Stadials » (HS). Au cours des derniers 60 milles ans (ka), cinq Heinrich Stadials sont observés dans les sédiments de l'Atlantique Nord (HS1-HS5). Les stadiaires non associés à des évènements d'Heinrich sont appelés DO-stadials et les interstadiaires de la dernière période glaciaire sont appelés DO-interstadials.

La variabilité millénaire décrite ci-dessus est associée à d'importantes variations de la circulation méridienne de retournement de l'Atlantique (Atlantic Meridional Overturning Circulation, AMOC). En effet, pendant les Heinrich Stadials, des réductions de l'intensité de circulation des masses d'eau profonde constituant l'AMOC sont observées (Gherardi et al., 2005; McManus et al., 2004). De plus, la formation d'eau profonde dans l'Atlantique Nord semble diminuer (Elliot et al., 2002; Vidal et al., 1997), ce qui pourrait être lié à la diminution de la salinité des eaux de surface de l'Atlantique Nord observée pendant ces périodes (Bard et al., 2000; Cortijo et al., 1997; Maslin et al., 1995).

Etant donné que l'AMOC redistribue la chaleur des tropiques vers l'Atlantique Nord, les variations climatiques rapides observées au cours de la dernière période glaciaire pourraient être engendrées par des variations de l'AMOC (Broecker et al., 1985). Or, le dernier rapport de l'IPCC (2013) conclut que l'intensité de l'AMOC a de très fortes chances de diminuer dans le futur, suite au réchauffement climatique induit par les émissions anthropiques de gaz à effet de serre. Il est donc important de comprendre la

dynamique de l'AMOC lors des variations climatiques rapides de la dernière période glaciaire pour mieux prévoir l'évolution future du climat.

Mon premier objectif de thèse consiste à reconstituer la dynamique des masses d'eau formant l'AMOC au cours des variations climatiques rapides de la dernière période glaciaire. Pour ce faire, j'utilise le rapport $(^{231}Pa/^{230}Th)_{xs,0}$ (rapport d'activité du protactinium et du thorium non supportés par l'uranium lithogène et authigène, et corrigés de la décroissance radioactive) des sédiments marins qui est un proxy assez récent de l'intensité de circulation des masses d'eau (Francois, 2007; Yu et al., 1996). Mon second objectif consiste à comprendre la relation entre les variations de l'AMOC et les changements climatiques rapides de la dernière période glaciaire. Pour ce faire, je crée un modèle d'âge (i.e. correspondance entre profondeurs dans la carotte et âge calendaire) pour mes carottes sédimentaires qui est entièrement radiométrique et indépendant de l'échelle d'âge des carottes Groenlandaise (Greenland Ice Core Chronology, GICC05). Je compare ensuite les enregistrements Pa/Th de mes carottes aux variations de température du Groenland et aux variations de précipitations dans les tropiques.

Ma zone d'étude est la marge nord-est du Brésil. Cette région est idéale pour étudier la variabilité de l'AMOC. En effet, elle est affectée par les courants de bord ouest, et les masses d'eaux constituant l'AMOC y circulent donc de manière intense (Schott, 2003). De plus, le talus continental permet d'étudier des carottes sédimentaires à différentes profondeurs et donc d'étudier différentes masses d'eau. Les carottes sédimentaires que j'ai étudiées au cours de ma thèse (MD09-3257, 04°14.69'S, 36°21.18'W, 2344m de profondeur; MD09-3256Q, 03°32.81'S, 35°23.11'W, 3537m de profondeur) ont été prélevées par le NR Marion Dufresne, au cours de la mission océanographique MD173/RETRO3.

Afin de pouvoir comparer le signal de circulation enregistré dans mes carottes avec d'autres enregistrements climatiques, j'ai tout d'abord établi la chronologie la plus précise possible pour les deux carottes de ma zone d'étude. Les fortes pluies issues de la migration vers le sud de la zone de convergence intertropicale (Intertropical Convergence Zone, ITCZ) au cours des stadiaires ont occasionné une augmentation de l'apport d'éléments terrigènes à la marge brésilienne par rapport à la sédimentation carbonatée (Jaeschke et al., 2007). Ces migrations sont donc visibles grâce aux augmentations du rapport Ti/Ca mesuré par XRF (X ray fluorescence) dans les carottes sédimentaires de la zone d'étude (Arz et al., 1998; Jaeschke et al., 2007). Les pics du rapport Ti/Ca sont très utiles pour corréler entre elles les carottes sédimentaires de la

marge. Ainsi, le modèle d'âge de la carotte MD09-3257 (~2300 m de profondeur) est basé sur la corrélation de ses pics de Ti/Ca avec ceux d'une carotte voisine (GeoB3910, 04°14.7'S, 36°20.7'W, 2362 m de profondeur) bien datée par ^{14}C. Afin de vérifier cette corrélation, plusieurs dates ^{14}C ont été mesurées directement sur la carotte MD09-3257. Pour obtenir le modèle d'âge le plus précis possible, la partie de la carotte au-delà de 38 ka a été datée par corrélation de ses pics de Ti/Ca avec les excursions négatives de $\delta^{18}O$ de spéléothèmes des grottes de Botuvera et de Diamante (Andes tropicales) (Cheng et al., 2013). En effet, une diminution du $\delta^{18}O$ des spéléothèmes indique, comme une augmentation du Ti/Ca, une intensification des précipitations au-dessus de la zone d'étude. J'ai corrélé la partie de la carotte au-delà de 38 ka aux spéléothèmes, car, après 35-40 ka, les datations ^{14}C sont très peu fiables (Reimer et al., 2013). Or les spéléothèmes sont datés par U-Th et permettent donc d'augmenter la justesse et la précision du modèle d'âge sur la partie inférieure de la carotte. J'ai vérifié la validité de la corrélation entre carottes marines et spéléothèmes sur les intervalles de temps où la datation de la carotte sédimentaire par ^{14}C est précise.
J'ai établi le modèle d'âge de la carotte MD09-3256Q (~3500 m de profondeur) par datation ^{14}C jusqu'à 27 ka. Après cette date, j'ai corrélé les pics de Ti/Ca associés à HS3, HS4 et HS5 dans la carotte aux pics de Ti/Ca de la carotte GeoB3910.

Pour estimer l'intensité de circulation des masses d'eau, j'utilise le rapport Pa/Th sédimentaire. Le protactinium et le thorium sont produits à taux constant par l'uranium dissous dans l'eau de mer avec un rapport de production de 0.093 (Henderson and Anderson, 2003). Ces deux éléments sont très réactifs vis-à-vis des particules, et leur temps de résidence dans l'océan est donc très faible. Toutefois, le temps de résidence du thorium dans l'océan (30-40 ans) est plus faible que celui du protactinium (~200 ans) (Francois, 2007)). Ainsi, alors que le thorium est très rapidement adsorbé sur les particules, le protactinium a tendance à rester en phase dissoute. Dans l'océan Atlantique où le temps de résidence des masses d'eau est faible (100-275 ans, (Yu et al., 1996)), le protactinium peut donc être exporté latéralement par advection. Plus le débit d'une masse d'eau est grand, moins le protactinium sera adsorbé sur les particules qui sédimentent, et le rapport Pa/Th du sédiment sous-jacent sera inférieur au rapport de production de 0.093. A l'inverse, au sein d'une masse circulant très lentement, le protactinium ne sera pas exporté latéralement et finira adsorbé sur les particules. Le rapport Pa/Th sédimentaire se rapprochera donc du rapport de production. Etant donné que le rapport Pa/Th sédimentaire est à l'équilibre avec le rapport Pa/Th dissous dans les 1000 m de la masse d'eau au-dessus du sédiment (Thomas et al., 2006), il peut être utilisé pour estimer l'intensité de circulation des masses d'eau dans l'océan Atlantique. En effet, en étudiant le Pa/Th sédimentaire de carottes verticalement

distantes de ~1000 m, on peut reconstruire le taux de renouvellement de plusieurs masses d'eau.

Le rapport Pa/Th sédimentaire en tant que proxy du taux de renouvellement des masses d'eau a néanmoins des limites. En effet, le protactinium a une forte affinité pour l'opale. Ainsi, dans les zones à forte production d'opale ou à forts flux particulaires, le protactinium peut être rapidement soustrait à la colonne d'eau par adsorption sur les particules. Ces zones sont souvent des marges influencées par des upwellings côtiers, comme la marge Africaine. La faible concentration en protactinium dissous résultant de la forte productivité sur les marges entraîne la diffusion du protactinium depuis les zones de forte concentration de l'océan ouvert vers les zones de faible concentration de la marge. Cet apport de protactinium augmente le rapport Pa/Th sédimentaire sans variation de circulation océanique. L'influence de la variation du type et des flux de particules sur le rapport Pa/Th sédimentaire doit donc être évaluée avant d'interpréter le Pa/Th comme un proxy du taux de renouvellement des masses d'eau.

J'ai également mesuré le $\delta^{13}C$ des foraminifères benthiques *C. wuellerstorfi* afin de reconstituer la ventilation des masses d'eau profondes (Duplessy et al., 1988). Ces mesures sont complémentaires des mesures Pa/Th qui reflètent le débit des masses d'eau.

J'ai concentré mes mesures Pa/Th autour de HS2 et de HS4. J'ai choisi ces périodes car elles sont caractérisées par des calottes de glace de volumes différents (Lambeck and Chappell, 2001). En effet, les calottes de glace de l'hémisphère nord sont plus étendues pendant HS2 que pendant HS4. Il est donc intéressant de voir si ces configurations différentes peuvent avoir un impact sur l'AMOC. Mes mesures Pa/Th sont les premières effectuées à haute résolution autour de HS4, et les premières à être effectuées autour de HS2 à ~2300 m de profondeur. J'ai mesuré le $\delta^{13}C$ de *C. wuellerstorfi* sur la carotte MD09-3256Q (~3500 m de profondeur). Le $\delta^{13}C$ de la carotte GeoB3910 située à proximité de la carotte MD09-3257 (~2300 m) a été mesuré par un autre laboratoire lors d'une étude précédente et mis à ma disposition dans le cadre du projet ESF RETRO.

Les mesures Pa/Th que j'ai effectuées sur la carotte MD09-3257 montrent l'importante variabilité du débit de la cellule supérieure de l'AMOC au cours de la dernière période glaciaire. Les stadiaires sont associés à de fortes valeurs du Pa/Th, indiquant une réduction de l'intensité de la circulation entre ~1300 et 2300 m de profondeur. Malheureusement, la portion de carotte correspondant au milieu de HS2 est affectée par une turbidite, et je n'ai pu mesurer le Pa/Th que pendant le début de l'événement. De plus, les fortes valeurs de Pa/Th observées pendant HS4 pourraient n'être pas uniquement liées à des variations de circulation et je n'ai donc pas interprété ces valeurs. En effet, les fortes valeurs Pa/Th pendant HS4 semblent corréler avec les forts

flux terrigènes. Il se pourrait donc que l'augmentation du flux particulaire ait entraîné une forte diminution de la concentration en protactinium dissous sur notre zone d'étude, ce qui aurait pu provoquer une arrivée de protactinium depuis l'océan ouvert. Cela aurait pu masquer les variations du Pa/Th liées à des variations de circulation. Les variations du Pa/Th précédant et suivant HS2 et HS4 peuvent toutefois être interprétées, ainsi que les variations du Pa/Th observées lors des DO-stadials et DO-interstadials.
Les mesures Pa/Th que j'ai effectuées dans la carotte MD09-3256Q présentent une moins grande variabilité que celles de la carotte MD09-3257. La principale variation se situe au sein d'HS4 qui voit le Pa/Th augmenter de ~0.06 à ~0.08. Toutefois, étant donné que ces fortes valeurs Pa/Th sont associées à de forts flux terrigènes, les mesures dans HS4 pourraient n'être pas uniquement liées à des variations de circulation et je ne les ai donc pas interprétées.

Les mesures du rapport Pa/Th sur la carotte MD09-3257 (~2300 m de profondeur) montrent un ralentissement de la masse d'eau circulant au-dessus du site avant les pics de Ti/Ca associés à HS2 et à HS4. Etant donné que les mesures de circulation océanique et de précipitations sont effectuées dans la même carotte, je peux précisément déterminer la distance entre le début de l'augmentation du rapport Pa/Th sédimentaire et le pic du Ti/Ca. Je trouve ainsi que le Pa/Th commence à augmenter 9 cm avant le pic de Ti/Ca associé à HS2 et 5 cm avant celui associé à HS4. J'ai converti ces intervalles de profondeur en intervalles de temps à l'aide du modèle d'âge que j'ai développé. Je trouve ainsi que le débit de la cellule de circulation supérieure de l'AMOC diminue 1420 ± 250 (1σ) années avant la migration de l'ITCZ associée à HS2, et 690 ± 180 (1σ) années avant celle associée à HS4. Mes résultats confirment qu'un ralentissement de l'AMOC et une diminution du transport de chaleur vers l'Atlantique Nord pourraient être à l'origine de la migration de l'ITCZ vers le sud.
Ces résultats contrastent avec les résultats des modèles climatiques. En effet, bien que ces derniers soient capables de reproduire une migration de l'ITCZ vers le sud suite à un ralentissement de l'AMOC, ce déplacement se produit rapidement après le début du ralentissement de la circulation (Kageyama et al., 2009). Cela pourrait être dû au fait que l'AMOC atteint son intensité minimale rapidement après le début du ralentissement de la circulation en réponse à un apport d'eau douce dans les zones de formation d'eau profonde de l'Atlantique Nord. Une réponse plus lente de l'AMOC occasionnerait probablement une migration plus tardive de l'ITCZ vers le sud.

Les variations de circulation océanique au cours des DO-stadials sont bien visibles sur la carotte de profondeur intermédiaire de la marge brésilienne. L'intensité du

ralentissement de la cellule de circulation supérieure de l'AMOC associée à ces stadiaires semble moins importante que celle associée aux Heinrich Stadials. Le rapport Ti/Ca montre également que les DO-stadials sont associés à une plus faible augmentation des précipitations tropicales. La baisse du débit de la branche supérieure de l'AMOC et la diminution des températures au Groenland semblent survenir en phase avec les variations de précipitations. L'absence de délai significatif entre diminution des températures au Groenland et migration de l'ITCZ pourrait impliquer que des processus atmosphériques contrôlent la position de l'ITCZ pendant les DO-stadials. Toutefois, les DO-stadials sont également associés à un ralentissement de la cellule supérieure de l'AMOC. Ainsi, je ne peux pas déterminer quel mécanisme est à l'origine de la variabilité de l'ITCZ au cours des DO-stadials.

Le délai entre la baisse d'intensité de l'AMOC et la migration de l'ITCZ est très différent pour les Heinrich Stadials et les DO-stadials, ce qui m'a amené à proposer le mécanisme suivant. Pendant les Heinrich Stadials, une diminution initiale du débit de la cellule de circulation supérieure de l'AMOC a pu engendrer un réchauffement des eaux de subsurface dans les hautes latitudes de l'Atlantique Nord (Alvarez-Solas et al., 2013; Mignot et al., 2007). Ce réchauffement aurait ensuite déstabilisé les plateformes de glace en bordure des calottes de glace continentales, entraînant ainsi le vêlage de la calotte Laurentide (Alvarez-Solas et al., 2013). L'apport d'eau douce lié aux icebergs issus de la Laurentide aurait alors entraîné la diminution du débit de la cellule supérieure de l'AMOC, entraînant ainsi une accentuation du réchauffement des eaux de subsurface. Cette boucle de rétroaction positive aurait ainsi pu se poursuivre, entraînant le déplacement de l'ITCZ de plus en plus loin vers le sud. En revanche, je propose que cette boucle n'ait pas été activée au cours des DO-stadials, rendant ainsi la variation du débit de la cellule supérieure de l'AMOC et la migration de l'ITCZ vers le sud limitées. Les Heinrich Stadials seraient donc caractérisés par des débâcles d'icebergs très importantes en raison de la boucle de rétroaction positive, alors que les décharges d'icebergs auraient pu être davantage limitées au cours des DO-stadials. Le mécanisme proposé est par ailleurs en accord avec la différence de quantité d'IRD observée dans l'Atlantique Nord entre les Heinrich Stadials, caractérisés par de grandes quantités d'IRD (les évènements d'Heinrich), et les DO-stadials, caractérisés par des quantités d'IRD limitées.

Afin de comprendre les variations de l'agencement vertical et du débit des masses d'eau constituant l'AMOC au cours des variations climatiques rapides de la dernière période glaciaire, j'ai comparé mes données Pa/Th à des valeurs Pa/Th simulées par un simple modèle 2D en boîtes forcé par différentes fonctions de courant. Ces fonctions de

courants ont été générées par le modèle iLOVECLIM (Roche et al., 2014, in press) sous différentes conditions climatiques. Ainsi, avec l'aide du $\delta^{13}C$ benthique, la comparaison des valeurs Pa/Th de mes carottes sédimentaires et de deux autres carottes de l'Atlantique avec les résultats du modèle m'a permis de proposer une configuration de l'AMOC en accord avec les données pendant les DO-interstadials et les Heinrich Stadials (HS2) de la dernière période glaciaire.

Mes résultats montrent que la configuration de l'AMOC durant les DO-interstadials de la dernière période glaciaire était différente de la configuration actuelle. Les eaux profondes en provenance de l'Atlantique Nord circulaient au-dessus de 2500 m de profondeur au niveau de l'équateur, alors qu'actuellement, les eaux profondes en provenance du nord (NADW) s'étendent de 1200 à 4000 m de profondeur (Schott, 2003). De même, j'ai pu estimer que le débit de cette masse d'eau au niveau de l'équateur était de 2 à 10 Sv, ce qui est inférieur à l'intensité de circulation actuelle de NADW, qui est de 23 ± 3 Sv (Ganachaud and Wunsch, 2000). La masse d'eau profonde en provenance des hautes latitudes sud circulait vers le nord au-dessous de ~4000 m de profondeur, et vers le sud en tant que courant de retour entre ~2500 et 4000 m de profondeur. J'ai estimé que le débit de cette masse d'eau était de 2 à 10 Sv. Cette estimation est trop peu précise pour en déduire un éventuel changement par rapport à l'intensité de circulation actuelle de l'eau abyssale antarctique (AABW, 6 ± 1.3 Sv (Ganachaud and Wunsch, 2000)).

Mes résultats montrent que la configuration de l'AMOC au cours des Heinrich Stadials est très différente de la configuration au cours des DO-interstadials. En effet, lors des Heinrich Stadials, la production d'eau profonde dans l'Atlantique Nord semble avoir suffisamment diminué pour que cette masse d'eau ne soit plus clairement visible à ~2300 m de profondeur au niveau de l'équateur. Une masse d'eau en provenance du sud pourrait donc dominer la colonne d'eau en-dessous de 1300 m de profondeur. La circulation entre 1300 et 2300 m de profondeur semble être très fortement ralentie, voire stoppée. La masse d'eau en provenance du sud semble directement affecter la carotte sédimentaire profonde, et pourrait occuper la partie inférieure de la colonne d'eau des abysses jusque vers 3500 à 2500 m de profondeur. Les données disponibles montrent qu'à 4500 m cette masse d'eau s'étendait au moins jusqu'à 35°N. Je n'ai toutefois pas pu estimer son débit car la fonction de courant associée à un arrêt complet de la production d'eau profonde dans l'Atlantique Nord ne reproduit pas exactement mes données Pa/Th.

Mes données ne montrent pas de différence majeure entre HS2 et HS4, malgré le fait que ces deux stadiaires soient caractérisés par des calottes de glace de volumes différents. Dans les deux cas, la diminution de la circulation océanique précède la migration de l'ITCZ. Bien que mes résultats aient permis de mieux comprendre la structure de l'Atlantique équatorial au cours de HS2, les doutes émis sur la capacité du Pa/Th à représenter la circulation océanique au cours de HS4 m'ont empêché de comparer la géométrie et la force de l'AMOC au cours de ces deux périodes de temps. La seule différence manifeste entre les deux stadiaires est le plus faible $\delta^{13}C$ des DO-interstadials entourant HS2 par rapport à ceux entourant HS4. Toutefois, cette différence pourrait être due à l'évolution de la biosphère continentale accompagnant le développement progressif des calottes de glace depuis l'entrée en glaciation jusqu'au dernier maximum glaciaire (~21 ka) (Duplessy et al., 1988; Lambeck and Chappell, 2001). Rien ne nous permet donc de dire que la circulation océanique dans l'Atlantique et son lien avec le climat étaient significativement différents entre HS4 et HS2.

Finalement, la comparaison de mes résultats avec l'enregistrement de la température au Groenland montre que les températures du Groenland sont restées inchangées alors que la cellule de circulation supérieure de l'AMOC était ralentie durant HS2. Cela implique que l'impact de l'apport de chaleur océanique sur les températures du Groenland est modulé par d'autres processus. D'une part, des études de modélisation montrent que la glace de mer pourrait être un agent important de la variabilité des températures au Groenland, et pourrait agir comme un isolant sur ce dernier, empêchant ainsi une diminution de l'apport de chaleur océanique de réduire davantage les températures groenlandaises (Kaspi et al., 2004; Li et al., 2010).
D'autre part, les études de modélisation montrent qu'une diminution de l'apport de chaleur par les océans pourrait être compensée par une augmentation du transport de chaleur par l'atmosphère (Kageyama et al., 2009; Shaffrey and Sutton, 2006).

En conclusion, je montre au cours de cette thèse que le débit et la distribution des différentes masses d'eau constituant l'AMOC ont significativement varié au cours des variations climatiques rapides de la dernière période glaciaire. Pendant les DO-interstadials, deux cellules de circulation étaient actives au-dessus et au-dessous de 2500 m, avec un débit de la cellule supérieure inférieur au débit actuel de NADW. La diminution du débit de la masse d'eau supérieure associée aux Heinrich-Stadials intervient 500 à 1700 ans avant la migration vers le sud de l'ITCZ. Ainsi, un ralentissement de la cellule supérieure de l'AMOC pourrait avoir causé le déplacement de la zone de convergence intertropicale. Enfin, au cours des Heinrich Stadials, la convection d'eau profonde dans l'Atlantique Nord était probablement limitée, et l'océan

Atlantique était dominé par une masse d'eau en provenance du sud au moins en-dessous de 1300 m de profondeur.

Introduction

Deep ice core drilling revealed millennial scale Greenland air temperature variability over the course of the last glacial, referred to as Dansgaard-Oeschger variability (Fig. 1) (Dansgaard et al., 1993; Kindler et al., 2014). DO events are characterized by rapid transitions from cold (stadial) to warm (interstadial) conditions. In marine sediment cores from the mid-high latitude North Atlantic, sea surface temperatures estimates display a similar variability, with cold sea surface temperatures (SST) occurring during DO stadials (Bard et al., 2000; Bond et al., 1993; Elliot et al., 2002; Sachs and Lehman, 1999). During some of these stadials, layers of coarse lithic fragments occur in mid-high latitude North Atlantic marine sediment cores (Bond et al., 1992). The coarse grains found within these layers were transported by icebergs before being deposited in oceanic sediments and are termed Ice Rafted Detritus (IRD). Anomalously thick layers of IRD are called Heinrich Events and the stadials during which they occur are called Heinrich Stadials (Heinrich, 1988). Evidences for climatic variability associated with Heinrich and Dansgaard-Oeschger events are not limited to the high latitude North Atlantic and can be found worldwide (Voelker, 2002).

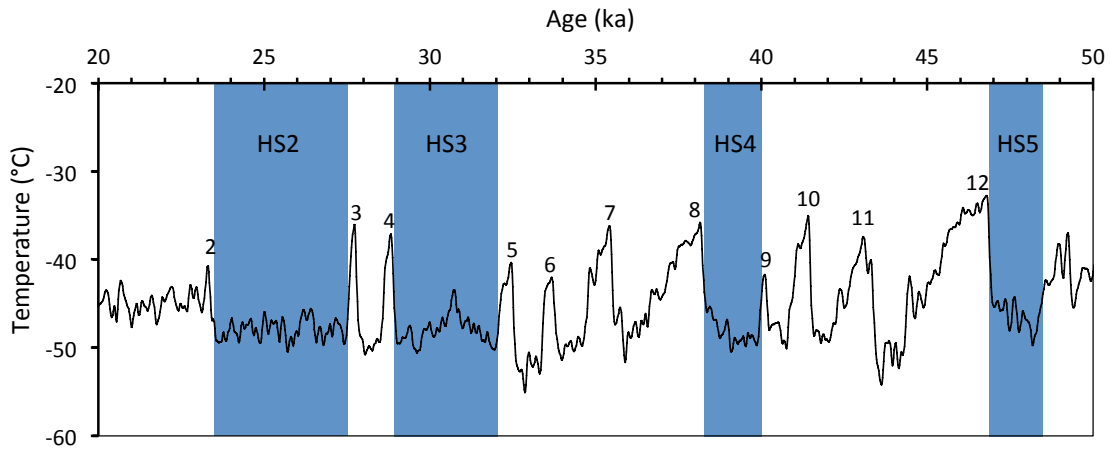

Figure **1** : Greenland air temperatures of the last 20-50 ka (Kindler et al., 2014). Numbers indicate Dansgaard-Oeschger interstadials and HS indicates Heinrich Stadials.

Heinrich stadials are accompanied by decreased flow rate of the deep water masses contributing to the Atlantic Meridonal Overturning Circulation (AMOC) (Gherardi et al., 2005; McManus et al., 2004) and by reduced deep water formation in the high latitude North Atlantic (Elliot et al., 2002; Vidal et al., 1997). The AMOC is the meridional component of the Atlantic circulation (Fig. 2). (Kuhlbrodt et al., 2007). It

consists of two overturning cells: the upper cell is initiated by deep convection in the Nordic seas and the lower cell is initiated by deep convection in the Southern Ocean. The surface circulation of the upper circulation cell is responsible for the transport of heat and salt from the tropical Atlantic towards the high latitude North Atlantic. Hence, it has been hypothesized that decreased inter-hemispheric heat transport related to a reduction of the AMOC strength could be at the origin of the climate variability observed in Greenland ice cores (Broecker et al., 1985).

The last IPCC report (AR5) concluded that a slowdown of the AMOC is very likely in the future, as a consequence of the warming induced by greenhouse gas emissions due to human activities. Although modern climate could respond differently to an AMOC slowdown than that of the last glacial, studying the AMOC of the last glacial and its links with abrupt climate shifts could help improving current climate models and hence predicting future climate change.

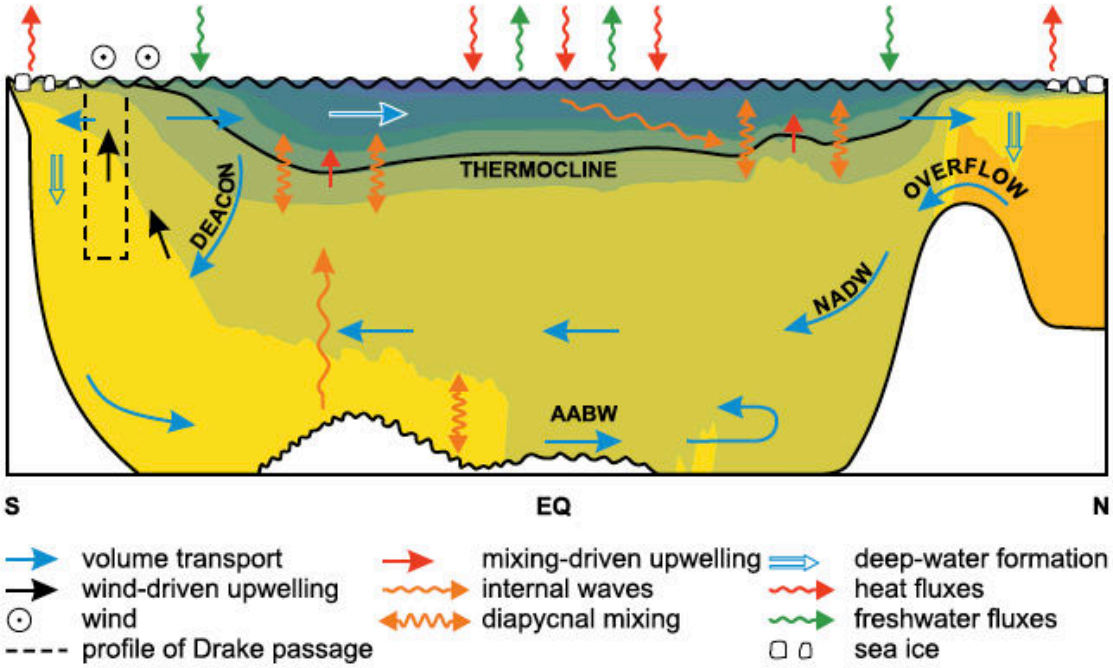

Figure **2** : Sketch of the Atlantic Meridional Overturning Circulation (AMOC) from (Kuhlbrodt et al., 2007). Blue arrows indicate the approximate flow direction of NADW (North Atlantic Deep Water) and AABW (Antarctic Bottom Water), the northern and southern sourced deep water masses initiating the upper and lower overturning cells of the AMOC respectively.

In this thesis, I reconstruct the dynamic of the AMOC during warm and cold periods associated with the DO variability. In order to do that, I use the sedimentary Pa/Th ratio, a relatively recent proxy that can record water masses renewal rates (Francois, 2007; Yu et al., 1996). I also study the relationship between AMOC and fast climate changes of the last glacial. My study area is situated on the Brazilian margin, a region affected by strong western boundary currents and therefore by the main water

masses constituting the AMOC (Schott, 2003). The sedimentary Pa/Th ratio in this region was shown to reflect present day oceanic circulation (Lippold et al., 2011).

In Chapter 1, I present the current knowledge on the strength and layout of the water masses constituting the AMOC, and their links with climate of the past 60 cal ky BP (ka hereafter). I also present the objectives of this thesis, which aim at understanding some actively discussed aspects concerning the configuration of the water masses constituting the AMOC and their relationship with climate of the last glacial. I also present the current knowledge of the sedimentary Pa/Th ratio in the Atlantic. Finally, I detail my study area and the stratigraphy of my sediment cores, which has been crucial in my choice of the fast climatic events to study.

Chapter 2 provides details about the methods I implemented at LSCE. The core of this chapter is one of my three research papers, intended for submission in Analytical Chemistry. This article is an intercomparison of sedimentary Pa/Th methods, and provides advices for Pa/Th measurements and ^{233}Pa spike calibration. Within the frame of this thesis, it provides an assessment of the quality of the data that I produced.

In chapter 3, I assess the timing of AMOC change with respect to shifts of the Inter Tropical Convergence Zone. In order to that, I build an age model for the sediment cores that is entirely radiogenic. Hence, as this age model is independent from the ice core GICC05 age scale, I compare AMOC changes to temperature changes in Greenland. This study is the subject of an article that was submitted to Nature Geoscience and Proceedings of the National Academy of Sciences, but that was not accepted with 1/3 and 1/2 positive reviews. It is now intended for submission in Geophysical Research Letters.

In chapter 4, I compare the Pa/Th data in the sediment cores of this study and in other Atlantic cores to Pa/Th values simulated using a 2D box model forced by various streamfunctions. It allows me to infer possible states of the AMOC during different climate periods of the last glacial. This article, currently in preparation, is intended for submission to Climate of the Past.

The last chapter summarizes all the results that arise from this thesis. It also provides perspectives for future work aiming at testing the hypotheses I emitted, and at providing further insights into our understanding of the AMOC and its relation with last glacial climate.

Chapter 1: Thesis objectives and study area

1.1 Thesis objectives

In this section, I present the current knowledge on the structure of the AMOC during the past 60 cal ky BP (ka hereafter) and its relationship with climate. I separate my presentation into different topics, and detail my thesis objectives related to these topics at the end of each associated subsection (1.1.1-1.1.3).

1.1.1 Oceanic circulation variability during the past 60 ka

During the last 60 ka, the Atlantic Meridional Overturning Circulation (AMOC) shifted between different states (Alley and Clark, 1999; Rahmstorf, 2002). At present, deep convection in the high latitude North Atlantic mainly occurs in the Greenland, Norwegian, Island and Labrador seas (Dickson and Brown, 1994; Reid, 1994) by brine rejection from sea ice formation, heat loss to the atmosphere and cyclonic wind induced vertical mixing (Kuhlbrodt et al., 2007). The deep water formed is called North Atlantic Deep Water (NADW), and overflows the Greenland-Scotland ridge into the Atlantic before flowing southwards towards the Southern Ocean. NADW salinity is high (34.8-35 ‰) (Emery, 2001) and its nutrient content is low, as reflected by the high $\delta^{13}C$ (0.9-1.1 ‰) of its dissolved inorganic carbon (DIC) (Kroopnick, 1985). NADW flows in the Atlantic Ocean between 1.2 and 4-5 km depth (Schott, 2003). The Antarctic Bottom Water (AABW) is a cold water mass of low salinity (-0.9-1.7°C, 34.64-34.72 ‰) (Emery, 2001) mainly formed during austral winter by deep convection in the Weddell Sea (Dickson and Brown, 1994). It enters the North Atlantic below 4000 m depth, through the equatorial path (Schott, 2003), and its influence can be seen as far north as 50°N. The Antarctic Intermediate Water (AAIW) is formed in the vicinity of the Antarctic polar front (Lynch-Stieglitz et al., 1994) and flows northwards between 550 and 1200 m depth along the South American margin, at least up to 16°N where it is disturbed by the occurrence of the Mediterranean overflow waters (Lankhorst et al., 2009; Reid, 1994; Viana et al., 1998). As for AABW, AAIW is rich in nutrients (Reid, 1994) and its salinity is low (33.8-34.8 ‰) (Emery, 2001).

During the Last Glacial Maximum (LGM), deep convection appears to have been still active but shifted south of Iceland, on the Rockall plateau (Vidal et al., 1997). At that time, the deep water mass formed in the high latitude North Atlantic could have been active above 2000 m depth, down to 10°S, and is therefore named Glacial North Atlantic

Intermediate Water (GNAIW) (Alley and Clark, 1999; Boyle and Keigwin, 1987; Curry and Oppo, 2005; Duplessy et al., 1988; Gherardi et al., 2009; Oppo and Lehman, 1993). At greater depth, poorly ventilated northward flowing waters originating from the Southern Ocean probably dominated the Atlantic Ocean up to 50°N (Alley and Clark, 1999; Boyle and Keigwin, 1987; Curry and Oppo, 2005; Duplessy et al., 1988; Oppo and Lehman, 1993). AAIW became colder and less saline, as it received more contribution from the Indian Ocean (Lynch-Stieglitz et al., 1994) and its influence spread at least up to the Demerara rise (Huang et al., 2014), but not as far north as the Caribbean Sea (Straub et al., 2013).

During Heinrich Stadials 1 to 5, the low δ^{13C} values in the northern North Atlantic Ocean could indicate that deep convection was weakened, if not stopped (Elliot et al., 2002; Vidal et al., 1997). A deep convection zone was however potentially still active south of Iceland during HS4, within the present day polar and subtropical modal water formation zone (Vidal et al., 1997). The apparent decreased deep convection during Heinrich Stadials 1 to 5 could be related to the release of icebergs in the Atlantic Ocean from the Nordic ice sheets (Hemming, 2004), which is accompanied by decreased salinity (Bond et al., 1993; Labeyrie et al., 1995; Maslin et al., 1995) and temperatures (McManus et al., 1999; Vautravers et al., 2004) in high latitude North Atlantic surface waters (see section 1.1.2).

During Heinrich Stadials, the influence of the AMOC upper circulation cell decreased, which is visible through the increased influence of southern sourced water masses in the northern North Atlantic, deduced from paleo-nutrient proxies (Elliot et al., 2002; Oppo and Lehman, 1995), but also from the reduced overflow of Nordic seas into the Atlantic Ocean inferred from the presence of Atlantic benthic species at the Faeroe margin (Rasmussen et al., 1996).

Moreover, several studies using the sedimentary Pa/Th ratio show that the AMOC strength decreased below 2000 m depth in the northern North Atlantic, but these studies are restricted to Heinrich Stadial 1 and the Younger Dryas (Gherardi et al., 2005; Gherardi et al., 2009; McManus et al., 2004). However, a few studies show that a shallow circulation cell could have been still active above 2000 m depth during Heinrich Stadials 1-3 (Gherardi et al., 2009; Lynch-Stieglitz et al., 2014), meaning that Heinrich Stadials may not be associated with a complete shutdown of the AMOC upper circulation cell. Hence, further progress needs to be made regarding the configuration and intensity of the water masses constituting the AMOC during Heinrich Stadials of the last glacial.

The extent of AAIW during Heinrich Stadials is still under discussion. Some studies claim that it increased during these periods in the Atlantic (Mangini et al., 2010; Pahnke et al., 2008) and in the Pacific (Pena et al., 2013), while others argue the opposite (Huang et al., 2014).

Most of our knowledge about the AMOC during Heinrich Stadials is based on paleo-nutrient proxies. Moreover, the few reconstructions of the AMOC strength are focused on HS1 and the Younger Dryas. **My first thesis objective** is therefore to reconstruct the dynamic of the AMOC over some rapid climate variations of the last glacial, using the sedimentary Pa/Th ratio (Chapter 3 and 4, (Burckel et al., 2014 a, in prep.; Burckel et al., 2014 b, in prep.)).

1.1.2 Origin of the Dansgaard Oeschger variability

Different mechanisms have been proposed to explain the abrupt Greenland air temperature changes that occurred during the last glacial. Changes in the intensity of the Atlantic Meridional Overturning Circulation (AMOC), which exports heat and salt from the equator towards the high latitude North Atlantic (Talley et al., 2003), were suggested to drive Greenland temperature oscillations (Broecker et al., 1990; Broecker et al., 1985). A decreased AMOC intensity could be at the origin of Dansgaard Oeschger (DO) and Heinrich stadials, while DO interstadials could be related to increased meridional heat export to the northern hemisphere by the resumption of an active oceanic circulation in the Atlantic (Broecker et al., 1985). A decreased intensity of the AMOC and an increased influence of Southern Ocean waters has been shown to occur during Heinrich (Elliot et al., 2002; Gherardi et al., 2005; McManus et al., 2004; Vidal et al., 1997) and DO stadials (Charles et al., 1996; Kissel et al., 1999) in agreement with the hypothesis of an AMOC influence on Greenland temperatures. A slowdown of the AMOC could result from the decreased sea surface salinity (SSS), which is recorded in the North Atlantic down to the sub-tropics (~38°N) during Heinrich Events (Bard et al., 2000; Cortijo et al., 1997; Maslin et al., 1995). Indeed, increased freshwater input into the high latitude North Atlantic Ocean could increase the buoyancy of surface waters and prevent deep convection and formation of deep northern sourced waters, therefore decreasing the AMOC strength. Using fully coupled climate models, a freshwater forcing in agreement with northern North Atlantic salinity proxies during HE4 indeed induces a shutdown of the AMOC (Roche et al., 2004), which results in a drop of northern North Atlantic temperatures (Kageyama et al., 2009). A freshwater input in the northern North Atlantic could therefore trigger an AMOC slowdown that would in turn lead to a decrease in air temperatures above Greenland.

Melting of icebergs released into the North Atlantic during Heinrich Events could have been at the origin of the freshwater input required to disrupt the AMOC. Different hypotheses exist to explain Heinrich Events. They could be the consequence of jökulhlaups (major flood) from a Hudson Bay lake, of ice sheets collapse because of basal melting by geothermal heat (binge purge mechanism), or of ice shelf build-up/collapse (see (Hemming, 2004) for a review). However, some recent studies suggest that, rather than causing the AMOC slowdown, Heinrich Events could be a consequence of the reduced overturning circulation (Alvarez-Solas et al., 2013). Indeed, a warming of subsurface waters is observed in the high latitude North Atlantic during Heinrich Events, which could be due to a cessation of deep convection and increased stratification (Marcott et al., 2011). Modelling experiments show that a subsurface warming could have destabilized the ice shelves, leading to the iceberg release observed during Heinrich Events, so that a decrease of the AMOC could have induced the Heinrich Events (Alvarez-Solas et al., 2013). Such an idea is comforted by a study from the apparent lead of water mass proxies, indicating increased Southern Ocean water influence, with respect to Heinrich Events (Gutjahr and Lippold, 2011). Moreover, increased buoyancy of subsurface waters could lead to a disruption of oceanic stratification and to the emergence of warm waters in the high latitude North Atlantic (Rasmussen and Thomsen, 2004). The amounts of heat released to the atmosphere could in turn lead to the fast temperature rise associated with DO interstadials. Hence, it is yet unclear whether AMOC slowdowns observed during the last glacial are the cause or the consequence of Heinrich Events.

Also, based on spectral analysis of the GISP2 $\delta^{18}O$ signal, DO events have been suggested to occur with a 1470 year periodicity (Schulz, 2002). Although no orbital or solar forcing presents such a periodicity, it was shown that a combination of centennial scale solar cycles and its effects on the AMOC could result in 1470 years cyclical temperature oscillations in Greenland (Braun et al., 2005). However, such a periodicity is for now rejected from spectral analysis on Greenland data in the most recent GICC05 NGRIP age scale (Ditlevsen et al., 2007).

Some recent studies based on shallow North Atlantic sediment cores suggest that the AMOC did not slow down during HE1-3 (Gherardi et al., 2009; Lynch-Stieglitz et al., 2014). Instead, there could have been an active overturning cell operating at mid water depths (>2000 m) at that time. These results challenge the classical idea that variations in Greenland temperatures are related to variations in the intensity of the AMOC, and alternative hypotheses may therefore be necessary to explain the DO variability.

Sea ice through its effect on albedo and insulation could have triggered DO like events with only a weak AMOC variability (Kaspi et al., 2004). Indeed, a slight reduction of the AMOC triggered for instance by ice sheet discharge into the high latitude North

Atlantic Ocean would allow sea ice expansion. Because of the positive feedback caused by increased surface albedo, ocean and atmosphere temperature would cool, leading to rapid sea ice expansion. The expansion of sea ice would be limited by its insulation effect on the ocean. The heat and salt stored in the tropics would then start diffusing towards the high latitude North Atlantic, causing sea ice to melt rapidly because of the positive feedback resulting from decreased albedo and insulation. This effect would rapidly warm the atmosphere and could lead to the DO variability observed in Greenland temperatures with a minor change of the AMOC.

Moreover, sea ice could have acted as a positive feedback through its effect on the position of the polar jet (Li et al., 2010). Indeed, during cold periods above Greenland, the Inter Tropical Convergence Zone shifted southwards (see section 1.1.3) which could have led to a southward shift of the polar jet, resulting in a decreased transport of heat by the atmosphere into the North Atlantic region and to enhanced sea ice formation.

My second thesis objective is to increase our understanding of the relationship between AMOC and climate variations of the last glacial, and the mechanisms through which they interact. In order to do that, I deploy **two strategies** (see also section 1.1.3). **My first strategy** is to compare changes in AMOC intensity to Greenland temperatures to assess the effect of reduced or intensified oceanic circulation on Greenland climate. I therefore build an age model independent from the GICC05 time scale to compare the timing and extent of the Atlantic circulation changes with respect to fast Greenland temperature variations of the last glacial (Chapter 3, (Burckel et al., 2014 a, in prep.)).

1.1.3 Dansgaard Oeschger variability outside the high latitude North Atlantic

During the last glacial, temperature oscillations are also observed in Antarctic ice cores $\delta^{18}O$ and δD records. Temperatures signals from the northern and southern hemisphere ice cores are out of phase (Blunier and Brook, 2001; EPICA, 2006). This observation led to the formulation of the bipolar seesaw concept (Stocker, 1998). In this concept, southern and northern hemispheres have a temperature response to an AMOC variation of opposite sign. Active oceanic circulation results in the transport of heat towards the high latitude North Atlantic. This leads to Greenland warming and Antarctic cooling. During AMOC slowdowns, heat is retained south of the equator, and leads to a warming of the southern tropical Atlantic and to a cooling of the North Atlantic. Such a concept is reproduced by climate models (Kageyama et al., 2009) and is able to produce the abrupt warming and slow cooling characteristic of DO events in Greenland (Stocker and Johnsen, 2003). Indeed, when the AMOC resumes, the heat stored at low latitudes is abruptly transferred to the high latitude northern Atlantic, thereby producing an abrupt

warming. A slow AMOC decrease is then able to progressively lower the heat supply and decrease Greenland temperatures.

Last glacial climate variability was also shown to impact tropical precipitation. During cold stadials such as Heinrich stadials and, to a lesser extent, during DO stadials, the reflectance and Ti/Ca signals recorded in northern tropics sediment cores (Cariaco basin and Arabian sea (Deplazes et al., 2013; Lea et al., 2003)) increased and decreased respectively, indicating lower terrigenous input to the cores' sites. At the same time, the $\delta^{18}O$ signal of speleothems from the Hulu cave in China increased (Wang et al., 2001). Both these variations are interpreted as a decrease in northern tropics precipitation, related to a southward shift of the Inter Tropical Convergence Zone (ITCZ). Indeed, at the same time, the southern tropics experienced increased precipitation, which are seen in marine sediment cores from the Brazilian margin (Jaeschke et al., 2007) as well as in South American speleothems (Cheng et al., 2013). Climate models are able to reproduce these ITCZ shifts by simulating a cold SST anomaly in the northern tropics. Indeed, the ITCZ lies above warm waters, where air convection and intense precipitation occurs (Hastenrath, 2011) so that a cold anomaly in the northern tropics induces a shift of the tropical rain-belt towards the warmer southern tropics. Modelling experiments can produce a cold SST anomaly in the northern tropics by two different mechanisms. In the first mechanism (Chiang and Bitz, 2005), extended sea ice or ice sheet cover in the northern high latitudes cools and dries the atmosphere. This cooling and drying propagates to the entire northern high and mid latitude by atmospheric transport and mixing. In the tropics, northeastern trade winds are intensified because of the cool mid-latitude ocean, which leads to further evaporation and cooling and pushes the SST anomaly southwards leading to a southward shift of the ITCZ. In the second mechanism (Kageyama et al., 2010), an AMOC slowdown causes the northern tropical ocean to cool and southern tropical ocean to warm, as predicted by the bipolar seesaw concept. The ITCZ therefore shifts towards the warmer southern tropics.

My second strategy to understand the relationship between AMOC and climate variability of the last glacial is to analyse the phasing of AMOC circulation changes and ITCZ shifts. Because the sediment cores I use in this study are situated on the Brazilian margin, precipitation and circulation proxies are recorded in the same core, which allows me to reliably assess the time interval between the beginning of the AMOC slowdown and the ITCZ shift (Chapter 3, (Burckel et al., 2014 a, in prep.)).

1.2 Sedimentary Pa/Th

1.2.1 Behavior of protactinium and thorium in the ocean.

^{231}Pa and ^{230}Th production in the ocean results from the decay of dissolved ^{235}U and ^{234}U, respectively. Under oxic conditions, uranium is very soluble (Dunk et al., 2002; Weyer et al., 2008). Its residence time in the Ocean is therefore very large (~500 ky) (Weyer et al., 2008). The mixing time of the ocean is comparatively very short (from 1-1,6 ky) (Broecker and Peng, 1982) so that uranium concentration in the ocean is uniform and proportional to salinity (Dunk et al., 2002). The isotopic composition of uranium is also uniform, with a measured ^{234}U/^{238}U activity ratio of 1,1466 (Robinson et al., 2004b) and a ^{235}U/^{238}U activity ratio of 0,04604 (Francois, 2007). Hence, we can calculate that the protactinium and thorium are produced at a constant activity ratio of 0.093 in the ocean:

$$\frac{P_{Pa}}{P_{Th}} = \frac{\lambda_{231} \times \frac{A_{235}}{A_{238}}}{\lambda_{230} \times \frac{A_{234}}{A_{238}}} = \frac{2{,}12 \times 10^{-5} \times 0{,}04604}{9{,}20 \times 10^{-6} \times 1{,}1466} \cong 0{,}093$$

where λ_{231} and λ_{230} are the decay constant of ^{231}Pa and ^{230}Th respectively (Audi et al., 2003).

Protactinium and thorium have a different behavior in the ocean. Both elements are very particle reactive and are quickly adsorbed on particles. They can consequently be removed from the water column by settling to the seafloor. Adsorption of Pa and Th on particles and subsequent removal to the seafloor is termed scavenging (Henderson and Anderson, 2003) and is particularly active for Pa and Th, as reflected by their low mean residence time in the ocean (~200 years for Pa and 30 years for Th) (Yu et al., 1996).

Dissolved and particulate Th concentrations have been shown to broadly increase with depth at several locations (Fig. 1) (Henderson and Anderson, 2003). A linear increase of dissolved concentrations implies the existence of reversible scavenging, i.e. the Th adsorbed on the particulate fraction continuously exchanges with the dissolved pool (Francois, 2007). The protactinium also shows such a trend in some water profiles, but this is very rare because of its longer residence time with respect to scavenging, which allows protactinium to be transported horizontally (Fig. 1) (Choi et al., 2001). Indeed, with increasing depth and therefore increasing residence time, dissolved and particulate protactinium depth-profiles tend to deviate from linearity because of the increased protactinium export caused by advection in the Atlantic Ocean (Fig. 1).

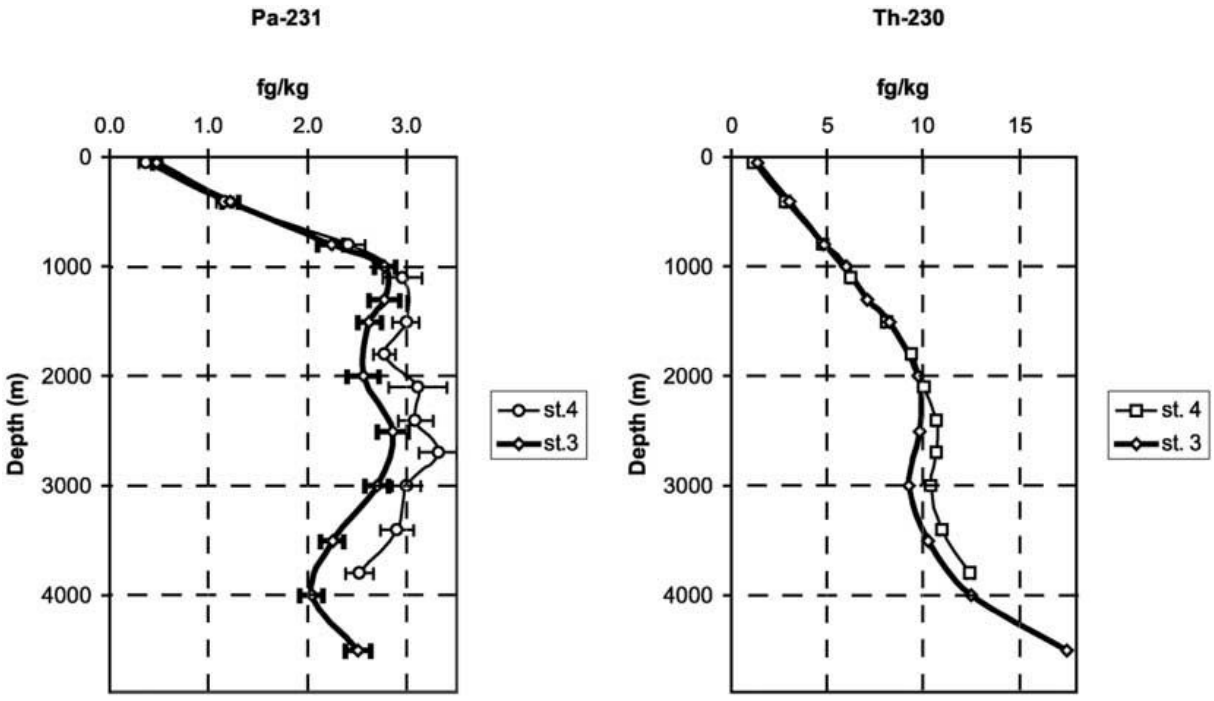

Figure 1.**1** : Dissolved ^{231}Pa and ^{230}Th profiles in the equatorial Atlantic (st.3 and st.4) from (Choi et al., 2001). Note that the ^{230}Th profile increases linearly with depth as predicted by reversible scavenging, while protactinium is exported at depth, resulting in an almost constant concentration with depth below 1000 m.

1.2.2 Pa/Th as a tracer of deep-water renewal rate

In the Atlantic Ocean, the mean residence time of Pa is similar to the residence time of NADW (100-275 yr) (Yu et al., 1996). A significant amount of protactinium can therefore be advected out of the basin, resulting in a sedimentary Pa/Th ratio below the production ratio of 0.093 in the open ocean. At present, the ^{231}Pa export out of the North Atlantic is estimated to be 33-68 % of the production while only 6-11 % of the ^{230}Th produced is exported (Deng et al., 2014; Moran et al., 2002; Yu et al., 1996). The sedimentary Pa/Th ratio can therefore be used as a proxy of deep water mass renewal rate in the Atlantic Ocean, with low Pa/Th ratio indicative of a strong Pa export and circulation intensity (Gherardi et al., 2005; Gherardi et al., 2009; Lippold et al., 2011; Lippold et al., 2012a; McManus et al., 2004; Negre et al., 2010; Yu et al., 1996).

Pa/Th data in the modern Atlantic Ocean are well simulated by 3D (Chase et al., 2002; Siddall et al., 2005) and 2D models (Lippold et al., 2011; Luo et al., 2010), offering new prospects for studies of paleo-circulation based on data-model comparison. Modeling studies show that the sedimentary Pa/Th ratio does not answer linearly to flow rate variations (Luo et al., 2010). Hence, comparing the Pa/Th ratio of sediment cores recovered from different depths and latitudes to Pa/Th values simulated with a Pa/Th model appears as the most robust way of interpreting the Pa/Th ratio in terms of circulation intensity. Indeed, a simple 2D box model (Luo et al., 2010) has already been

used to estimate the AMOC intensity during the LGM based on sediment cores recovered from various latitudes and depths in the Atlantic Ocean (Lippold et al., 2012a).
The method of sedimentary Pa/Th analysis that I implemented at the LSCE produces accurate and precise results, allowing me to identify flow rate variations with high confidence and to compare my Pa/Th values to other sediment cores in the Atlantic Ocean. I detail the method in Chapter 2 and in a Pa/Th intercomparison study (Burckel et al., 2014 c, in prep.).

1.2.3 Effect of particle type and flux

1.2.3 a) Use of the sedimentary Pa/Th ratio as a proxy of particle type and flux

Although both isotopes are particle reactive, ^{231}Pa and ^{230}Th have different affinities with respect to different types of particles. This is reflected by their fractionation factor F(Th/Pa), expressed as the ratio of the partition coefficient of Th and Pa between sediment and seawater: Kd(Th)/Kd(Pa). Partition coefficients are expressed as the activity of excess ^{231}Pa or ^{230}Th per gram of sediment divided by the activity of dissolved ^{231}Pa or ^{230}Th per gram of seawater (Chase et al., 2002). Thorium is usually an order of magnitude more reactive than protactinium (Henderson and Anderson, 2003; Yu et al., 1996), and has a strong affinity for carbonates, as reflected by the high $F(Th/Pa)_{carbonate}$ of 10-40 estimated from sediment trap and core top measurements (Chase et al., 2002; Luo and Ku, 2004). Protactinium on the other hand has a high affinity for biogenic opal, as reflected by the low $F(Th/Pa)_{opal}$ of 0.2-0.3 (Chase et al., 2002; Luo and Ku, 2004). A similar range of affinities is observed from laboratory experiments (Geibert and Usbeck, 2004). As a consequence, sedimentary Pa/Th depends both on the dissolved Pa/Th, which mainly depends on the lateral transport of Pa, and on the fractionation factor, reflecting particle type and fluxes.
The sedimentary Pa/Th ratio is shown to be particularly sensitive to variations in the opal fluxes in high productivity regions. In the opal belt, high opal concentrations result in a sedimentary Pa/Th ratio above the production ratio of 0.093, as part of the protactinium exported from the Atlantic Ocean is scavenged there (Chase et al., 2003). In this region, variations of the sedimentary Pa/Th is not interpreted in terms of changes in the intensity of the AMOC, but rather in terms of sediment composition (Chase et al., 2003) and opal fluxes variations (Anderson et al., 2009; Bradtmiller et al., 2009; Kretschmer et al., 2011).
Depletion of dissolved Pa and Th near some ocean margins is termed boundary scavenging. It results in lateral transport of protactinium by diffusion from the open ocean to the margin, because of the greater residence time of Pa compared to Th, resulting in high sedimentary Pa/Th ratio (>0.093) (Anderson et al., 1990; Scholten et al., 2005). Hence, past Pa/Th variations on the western African coast have been

attributed to varying boundary scavenging intensity, related to changes in opal production (Bradtmiller et al., 2007). The relation between Pa/Th ratio and opal fluxes could also induce a depth dependent variation of the Pa/Th ratio, following opal remineralization at depth (Scholten et al., 2008). Hence, the strong dependency of Pa and Th on particle types and fluxes can overprint the effect of Pa advection by oceanic circulation, and therefore limit the use of the Pa/Th ratio as a water mass renewal rate proxy in some regions.

1.2.3 b) Acquisition of the sedimentary Pa/Th signal

Sedimentary ^{230}Th and ^{231}Pa were shown to equilibrate with waters occupying a ~1000 m thick layer above the seafloor (Thomas et al., 2006). Sedimentary Pa/Th may thus be used to record the renewal rate of different was masses on a depth transect (Lippold et al., 2011). More work is required to understand the exact relationship between dissolved and particulate Pa/Th, as a recent study showed that the dissolved Pa/Th ratio on a meridional section of the south Atlantic Ocean does not clearly depicts the distribution of the Atlantic water masses (Deng et al., 2014). However, a study of the Pa/Th ratio of core tops at different depths on the Brazilian margin reveals that sedimentary Pa/Th can be interpreted as a proxy of circulation intensity in the modern Atlantic Ocean (Lippold et al., 2011).

As explained above (1.2.3 a), boundary scavenging can in some regions overprint the effect of Pa export by water mass advection. At present, boundary scavenging in the Atlantic Ocean seems restricted to the eastern margin, such as the western African coast. During periods of reduced AMOC, model results show that the influence of particulate fluxes on the Pa/Th ratio in the Atlantic could have increased, as the residence time of the water masses in the basin increased (Siddall et al., 2007). However, a study on the Namibian margin shows that the western African coast does not seem to have acted as a major inner Atlantic sink of ^{231}Pa during periods of weak AMOC of the last glacial, therefore still allowing the use of sedimentary Pa/Th as a water mass renewal rate proxy (Lippold et al., 2012b).

Because opal could influence the Pa/Th ratio, I implemented at the LSCE a method for determining the opal weight percent of sediment samples. I detail the method in Chapter 2.

1.3 Stratigraphy of the cores

I focused my study on the Brazilian margin, a region that recorded both the oceanic and atmospheric reorganization concurrent with fast climate changes of the last glacial. The Brazilian margin is ideal for the study of sedimentary Pa/Th, as deep

western boundary currents affect the region (Schott, 2003), so that sediments from the margin have recorded the flow rate of the main water masses constituting the AMOC. Hence, I can reconstruct the flow rate of the AMOC water masses by analysing the sedimentary Pa/Th ratio of cores located at different depths on the margin. A recent study performed on core tops of the Brazilian margin has shown that the strength of the present day NADW can indeed be reconstructed in this area by comparison of Pa/Th measurements to Pa/Th values simulated with a simple 2D box model (Lippold et al., 2011; Luo et al., 2010).

Before delving into the stratigraphy of our sediment cores, I assess the influence of freshwater and sediment originating from the Amazon River on surface waters of our study area and on the Ti/Ca and Pa/Th signals recorded in our sediment cores.

1.3.1 Influence of the Amazon

The eastern Brazilian margin is affected by the South Equatorial Current (SEC), which flows westwards along the equator (Fig. 2). As the SEC reaches the Brazilian continental margin at about 8°S, it bifurcates into a southward flowing current, the Brazilian Current (BC), and a northwestward flowing current, the North Brazilian Current (NBC).

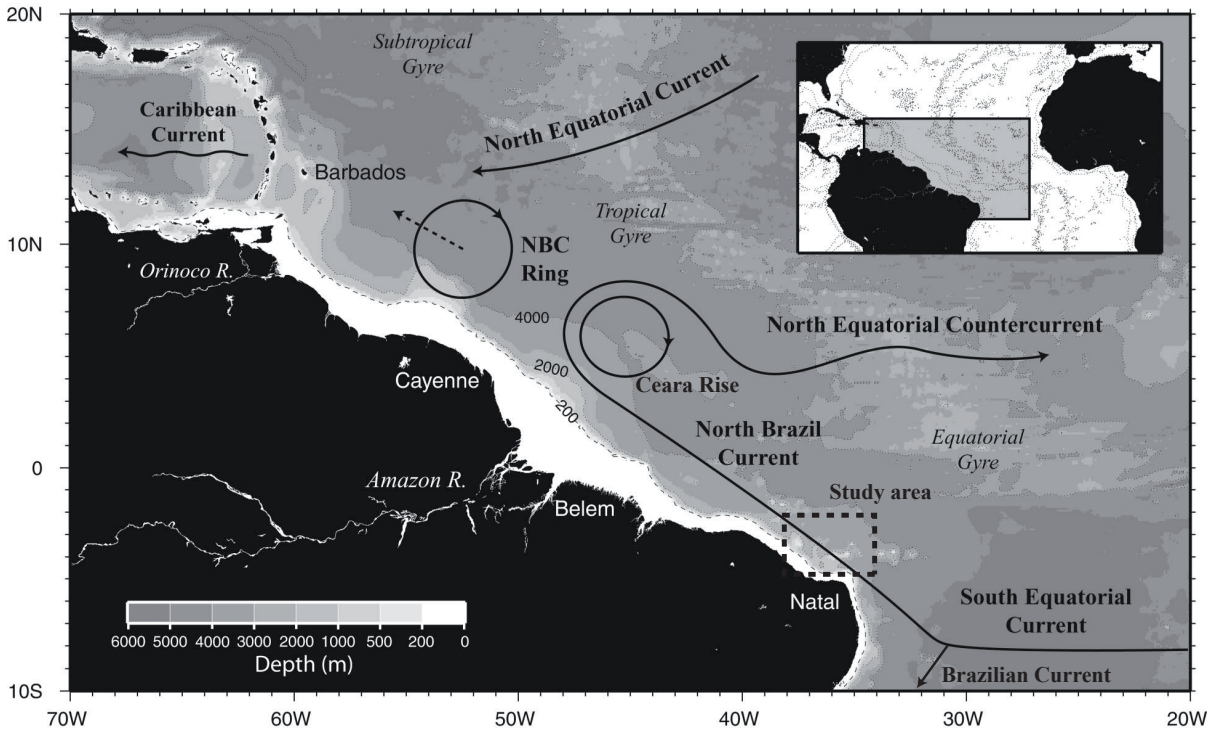

Figure 1.**2** : Study area and position of the main surface currents (modified from (Fratantoni and Glickson, 2002))

The intensity of the SEC and NBC is directly related to the strength of the southeastern trade winds, with maximum transport occurring during maximum intensity of the trades, i.e. during boreal fall. Because of the East-West pressure gradient generated by the westward flow of the SEC and because of the inter-annual variability of the SEC, the NBC is seasonally retroflected at about 6-8°N into the North Equatorial Countercurrent (NECC) (Fig. 2) (Fratantoni and Glickson, 2002). Hence, between the beginning of boreal summer and the end of boreal fall, the NECC reaches its maximum intensity. During boreal spring, its intensity is minimal and the NECC can even flow westwards (Johns et al., 1998).

During periods of weak NECC, Amazon waters are deviated northward by the NBC (Fratantoni and Glickson, 2002). During periods of maximum NBC retroflexion and NECC intensity, up to 70% of the freshwater brought by the Amazon River is deviated by the NECC (Ruhlemann et al., 2001), and only part is deviated northward by current rings separated from the retroflexion (Fratantoni and Glickson, 2002). However, the southward influence of the NECC does not reach the equator (Carton and Katz, 1990), as observed from surface drifter data (Fig. 3)(Lumpkin and Garzoli, 2005).

Because our study area is situated south of 3°S, it is not presently influenced by freshwater release from the Amazon.

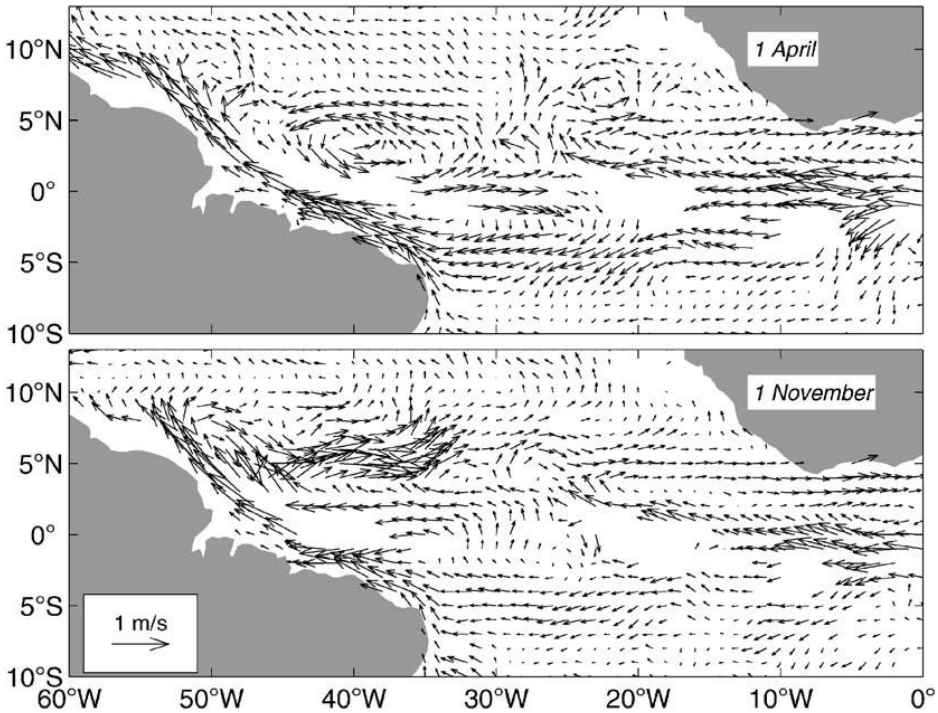

Figure 1.**3** : Surface currents during april (top) and november (bottom). During times of minimum NECC intensity (April), Amazon waters are deviated northwards. During times of maximum NECC (November), Amazon waters are deviated eastwards but do not reach our study area (Lumpkin and Garzoli, 2005).

During the last glacial, the average intensity and position of the NECC appears to have been analogous to present day boreal summer. This is probably related to the increased

thermal gradient between high and low latitudes that induced intensified trade winds, and enhanced retroflexion of the NBC (Ruhlemann et al., 2001; Wilson et al., 2011). We conclude that, during both Holocene and the last glacial, freshwater delivered by the Amazon did not affect the study area, so that the $\delta^{18}O$, ^{14}C and dissolved Pa/Th of surface waters were undisturbed.

Sediment delivered from the Amazon River and transported to our study area could also lead to misinterpretation of the Ti/Ca and sedimentary Pa/Th ratio of our sediment cores. At present, sediment from the Amazon are trapped on the continental margin and deflected northward by the NBC (Wilson et al., 2011). During glacial times, sea level fell below the shelf break and most of the sediment delivered by the Amazon River was deposited on the Amazon fan, i.e. north of the equator (Flood et al., 1995), whereas some sediment was transported by surface waters along the NECC, affecting for instance the Ceara rise (Ruhlemann et al., 2001).

We conclude that the sediments reaching our study area are not brought by the Amazon River but rather by local rivers and in situ carbonate production. Proxies recorded in the sediment core from my study area can therefore be interpreted without further complication.

1.3.2. Study area and stratigraphy of the cores

I studied sediment cores that were recovered from the Brazilian margin during R/V Marion Dufresne cruise MD 173/RETRO3: cores MD09-3251/52, MD09-3256Q and MD09-3257 (in red in Fig. 4, Table 1). These sediment cores are located at various depths (~700, ~2300 and ~3500 m) and can therefore record the vertical structure of the water masses constituting the AMOC. At present, the shallowest core is influenced by AAIW, the intermediate and deep cores by upper and lower NADW respectively (Fig. 5). A few marine sediment cores recovered from the North Eastern Brazilian margin during the R/V Meteor cruise M34/4 and Victor Hensen cruise JOPSII-6 have been previously studied (Arz et al., 1999; Jaeschke et al., 2007), some of which are close to RETRO3 cores (in green in Fig. 4, Table 1).

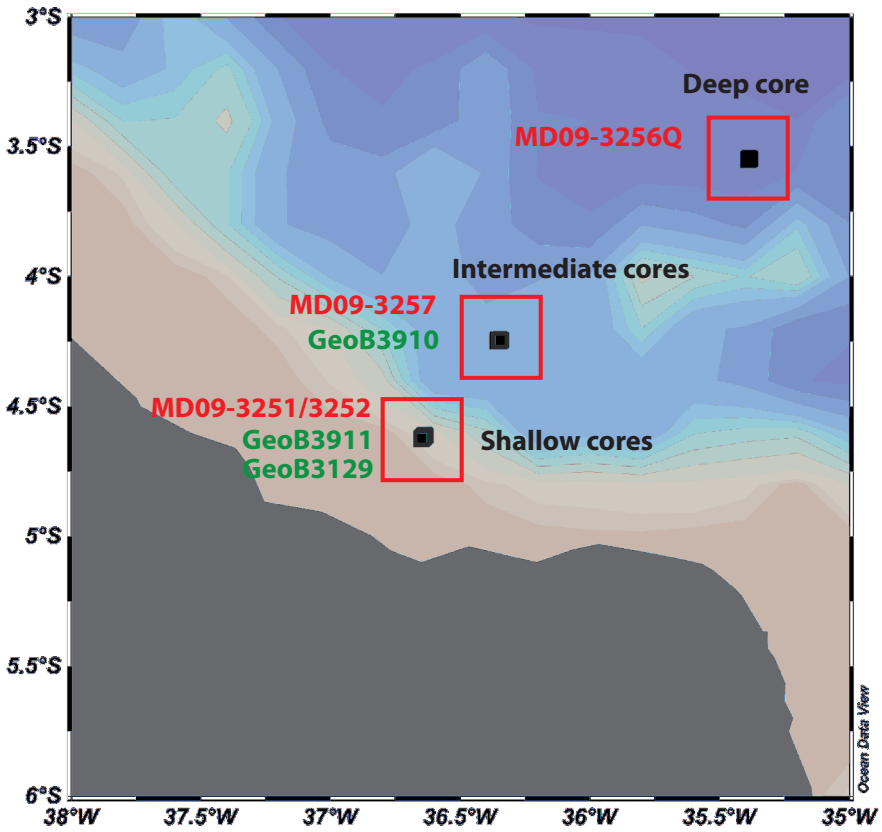

Figure 1.**4** : Map of the North Eastern Brazilian margin. Names of RETRO3 cores are written in red and names of M34/4 cores in green.

Table 1.**1** : Name, position and depth of the cores displayed in Figure 1 and discussed in the text. Gravity cores are indicated in RETRO3 cores by the letter "Q". RETRO3 cores are otherwise piston cores.

Cruise	Name	Coordinates	Depth (m)
RETRO3	MDO9-3251Q/3252	04°37.29'S 36°38.69'W	725
RETRO3	MDO9-3257	04°14.69'S 36°21.18'W	2344
RETRO3	MDO9-3256Q	03°32.81'S 35°23.11'W	3537
M34/4	GeoB3911	04°36.8'S 36°38.2'W	828
M34/4	GeoB3910	04°14.7'S 36°20.7'W	2362
JOPSII-6	GeoB3129	04°36.8'S 36°38.2'W	830

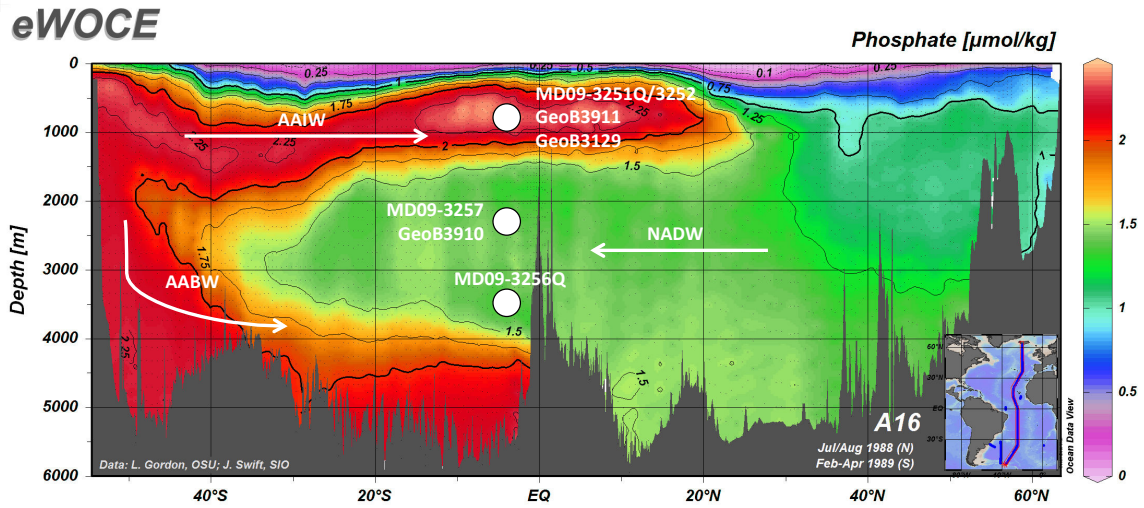

Figure 1.**5** : Phosphate section of the Atlantic Ocean showing the sites of the cores listed in Table 1. White arrows indicate the approximate flow directions of the Antarctic Intermediate Water (AAIW), Antarctic Bottom Water (AABW) and North Atlantic Deep Water (NADW).

In this section, I present the stratigraphy work that I have done on the marine sediment cores in order to choose intervals of interest for the study of last glacial fast climate variability. X-Ray fluorescence data on RETRO3 sediment cores were measured at the Bjerknes Centre for Climate Research (Bergen) and Marum (Bremen). For the RETRO3 cores, I picked and prepared all planktic foraminifera *G. ruber* white and analyzed most of their $\delta^{18}O$ on Finnigan Δ+ mass spectrometer. Samples I did not analyze were measured on an Elementar Isoprime mass spectrometer. I also picked foraminifera *G. ruber* white for ^{14}C analyses. Note that ^{14}C dates are not used to build the age models in this section, but to identify potential turbidites. Precise chronology of the cores is discussed in chapters 3 and 4.

The Ti/Ca record of sediment cores recovered from the Brazilian margin displays several peaks during the last 50 ka (Arz et al., 1999, 1998; Jaeschke et al., 2007). These peaks are associated with periods of increased precipitation on the Brazilian hinterland that caused increased terrigenous input to the margin and therefore increased proportion of titanium bearing material with respect to carbonates in marine sediment cores.

Core GeoB3910 has been extensively studied and its age model is based on 20 ^{14}C dates. Its Ti/Ca record exhibits marked Ti/Ca peaks associated with Heinrich Stadials 1-5 (Fig. 6) (Jaeschke et al., 2007). As terrigenous peaks are observed in sediment cores of the entire area, sediment cores from this region can be correlated to the well-dated GeoB3910 core.

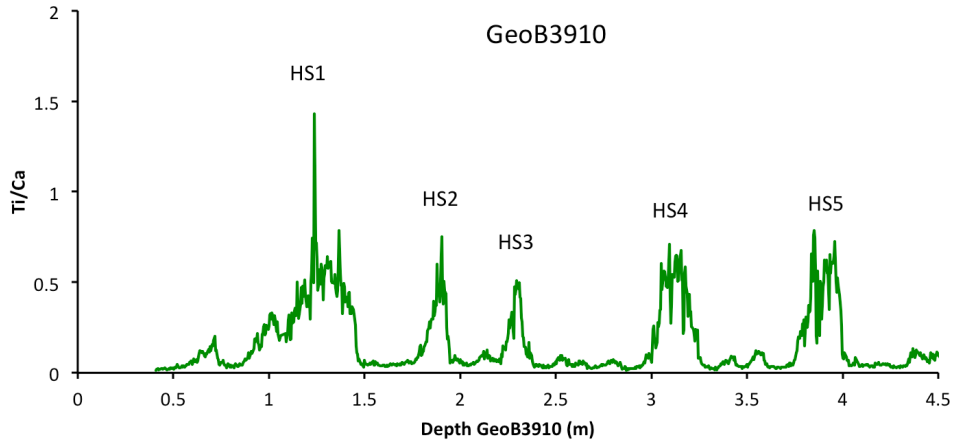

Figure 1.**6** : Ti/Ca record of core GeoB3910. Each Ti/Ca peak is associated with one Heinrich Stadial (HS1-5).

Because core MD09-3257 was recovered from the same depth and position as core GeoB3910, Ti/Ca peaks of both cores are quasi identical. When plotted on the GeoB3910 depth scale, both Ti/Ca records overlap almost perfectly (Fig. 7). $\delta^{18}O$ measurements confirm the good correspondence between the cores, but also highlight two major differences revealed by $\delta^{18}O$ peaks in core MD09-3257 (Fig. 7). During HS2, these $\delta^{18}O$ peaks are associated with sharp drops in Ti/Ca, but with no significant change in the Ti/Ca record after HS2. Sand layers occur at the depths of the $\delta^{18}O$ peaks and ^{14}C dating reveals an age inversion within HS2 (Fig. 8). We conclude that $\delta^{18}O$ peaks are associated to turbidite layers, one of which occurs during HS2, therefore preventing any measurement within this time interval at intermediate depth.

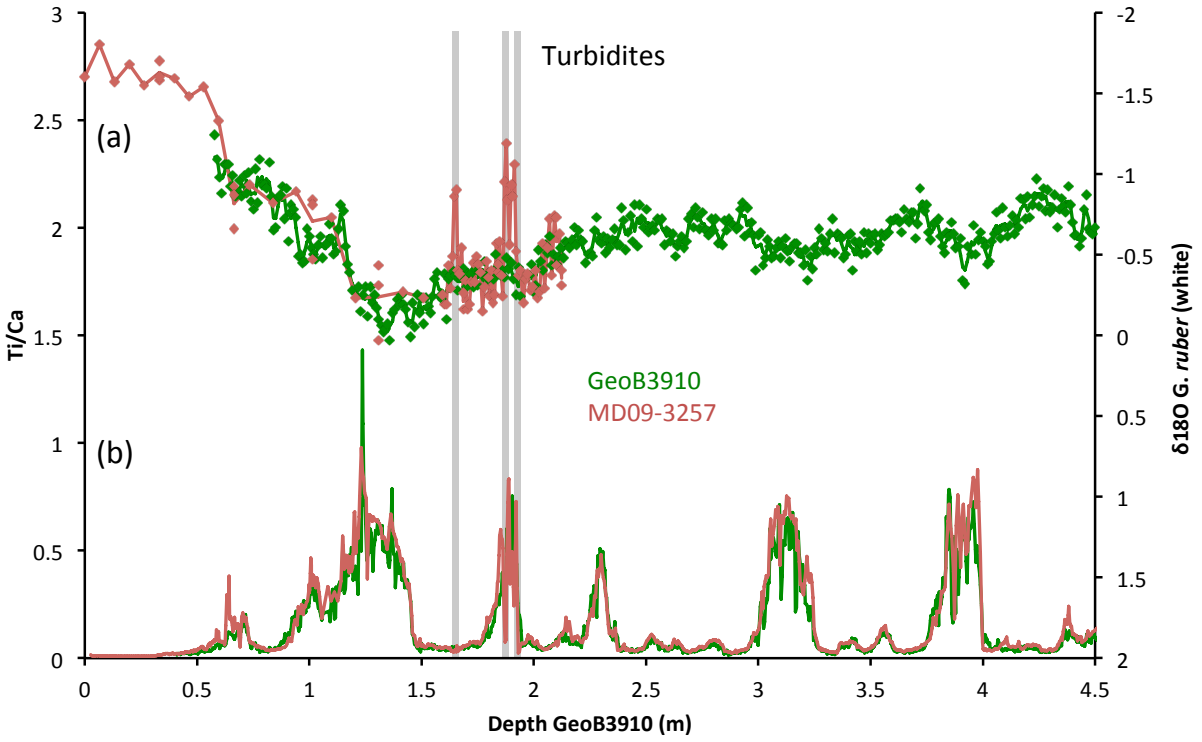

Figure 1.7 : (a) $\delta^{18}O$ and (b) Ti/Ca signals of intermediate depth cores on the GeoB3910 depth scale.

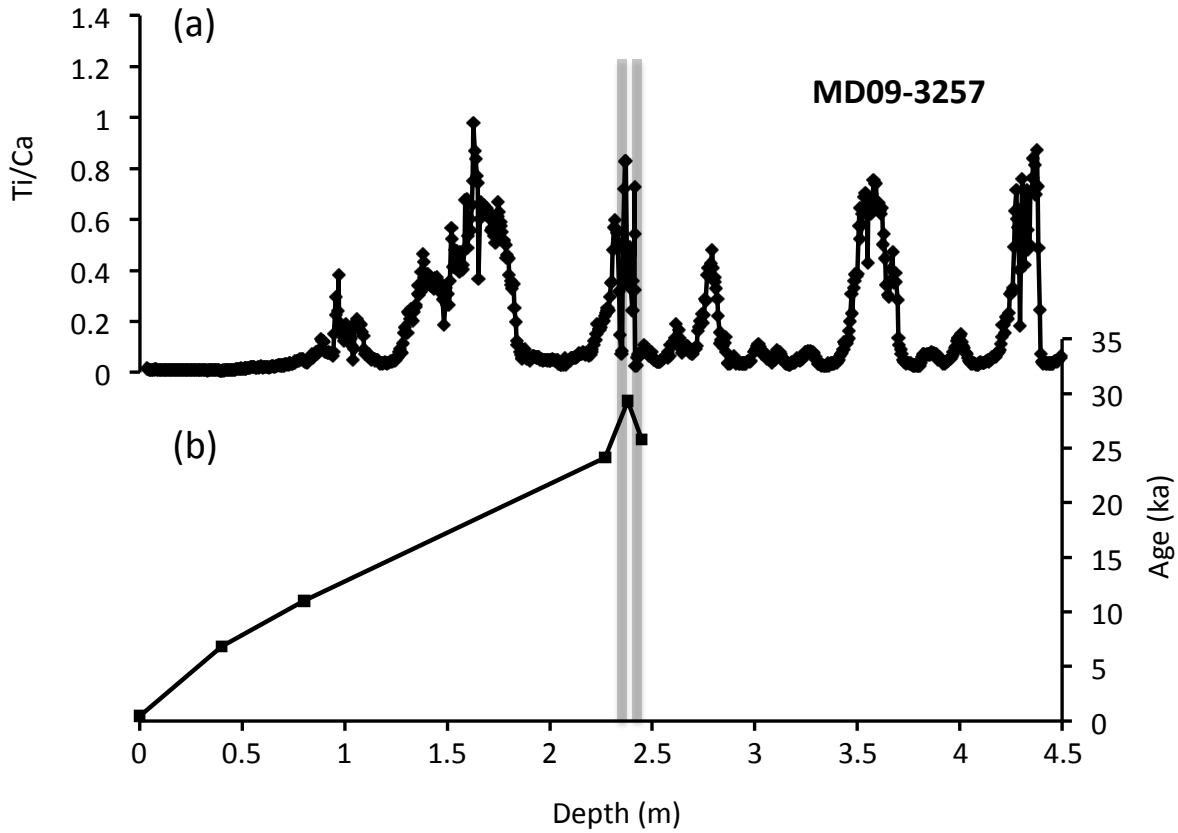

Figure 1.8 : (a) Ti/Ca and (b) ^{14}C dates (Marine13, (Reimer et al., 2013)) in core MD09-3257

The large distance of core MD09-3256Q from the coast lowers considerably the terrigenous input to the site, therefore smoothing the Ti/Ca signal in the core. Ti/Ca peaks are therefore less sharp in core MD09-3256Q than in intermediate depth cores, hence complicating the recognition of fast climatic events. An approximate correlation of core MD09-3256Q to core GeoB3910 is shown in Fig. 9. A few differences in $\delta^{18}O$ are observed between the two cores. The large deviation of ~0.5 ‰ at the beginning of core GeoB3910 $\delta^{18}O$ record is likely related to the absence of tie points between cores GeoB3910 and MD09-3256Q below the depth of HS1. Other small deviations can be observed and could be explained by the difference in temperature and salinity between the cores sites (0.2°C and 0.15 psu at present at 30 m depth, Fig. 10), which directly affects the $\delta^{18}O$ of planktic foraminifera. The $\delta^{18}O$ peak and Ti/Ca through occurring at 1.64 m (GeoB3910 depth scale) in core MD09-3256Q is likely related to a large turbidite. As no sand layers occurs in the core therefore preventing us from visually delimitating the extent of the turbidite, we used ^{14}C dates instead. As seen in Fig. 11, an age inversion occurs in the ^{14}C dates measured between 0.66 and 0.88 m (limits not included). We conclude that the core section delimited by these depths is affected by a turbidite. The Ti/Ca peak first attributed to HS2 lies within this interval. However, ^{14}C dates indicate that HS2 is actually situated deeper in the core, and that it is not affected by any turbidite (Fig. 11). Hence, all fast climatic events of the period between 20-50 ka are recorded in core MD09-3256Q.

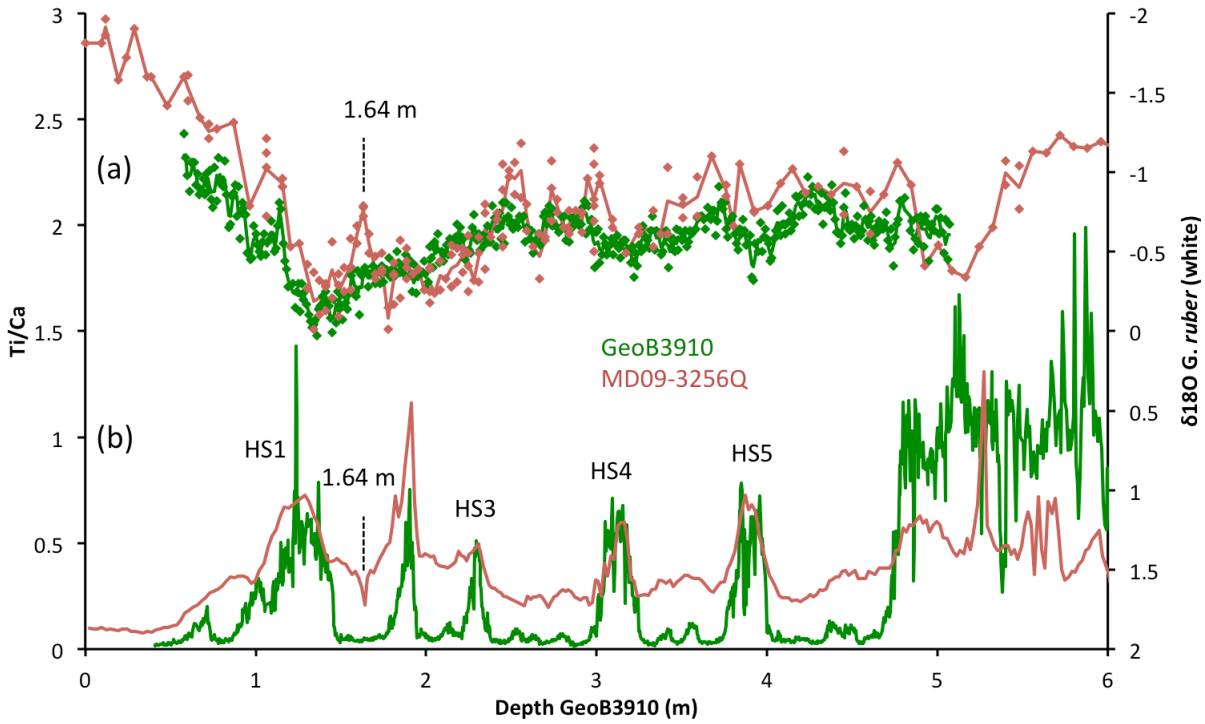

Figure 1.**9** : (a) $\delta^{18}O$ and (b) Ti/Ca signals of intermediate (GeoB3910) and deep (MD09-3256Q) cores on the GeoB3910 depth scale. Note that correlation of HS2 between core MD09-3256Q and core GeoB3910 revealed to be incorrect, as inferred from ^{14}C dating.

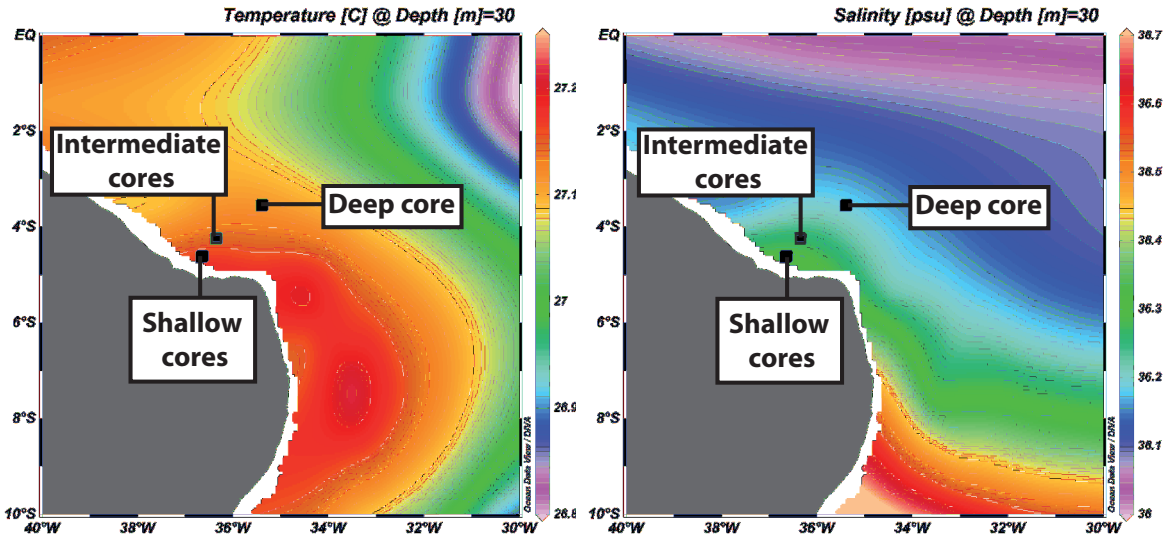

Figure 1.**10** : Present day temperature and salinity at 30 m depth on the Brazilian margin (WOA09).

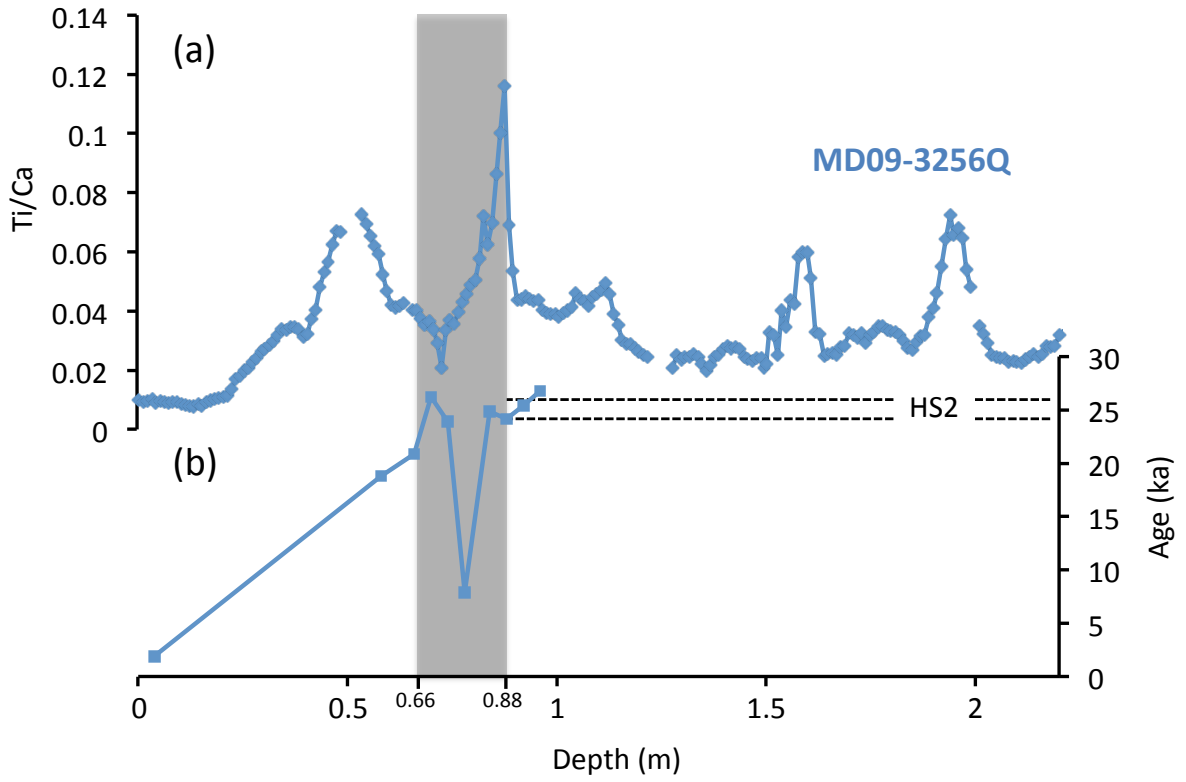

Figure 1.**11** : (a) Ti/Ca and (b) ^{14}C dates (Marine13, (Reimer et al., 2013)) in core MD09-3256Q

Core GeoB3911 and neighboring core GeoB3129 are ^{14}C dated by 16 ^{14}C dates and show no apparent hiatus (Arz et al., 1999). They were therefore used for comparison with RETRO3 shallow sediment cores, which were recovered from their vicinity. Core MD09-3251Q is 8.72 m long and is extended by core MD09-3252 (25.55 m long) (Fig. 12). Comparison of cores GeoB3911 and MD09-3251Q/3252 reveals a good correlation from the core top to the Ti/Ca peak associated with HS1, where the record of core GeoB3911 ends. In core MD09-3252, the Ti/Ca peak attributed to HS2 exhibits a discontinuity. At the same depth, the $\delta^{18}O$ of G. *ruber* white jumps towards much lighter values. In other sediment cores of the region, these light $\delta^{18}O$ values are only achieved during MIS5. MIS3 and MIS4 are thus likely not recorded in core MD09-3252 and were probably lost because of a turbidite, as evidenced by the occurrence of a sand layer at the depth of the abrupt $\delta^{18}O$ and Ti/Ca decreases.

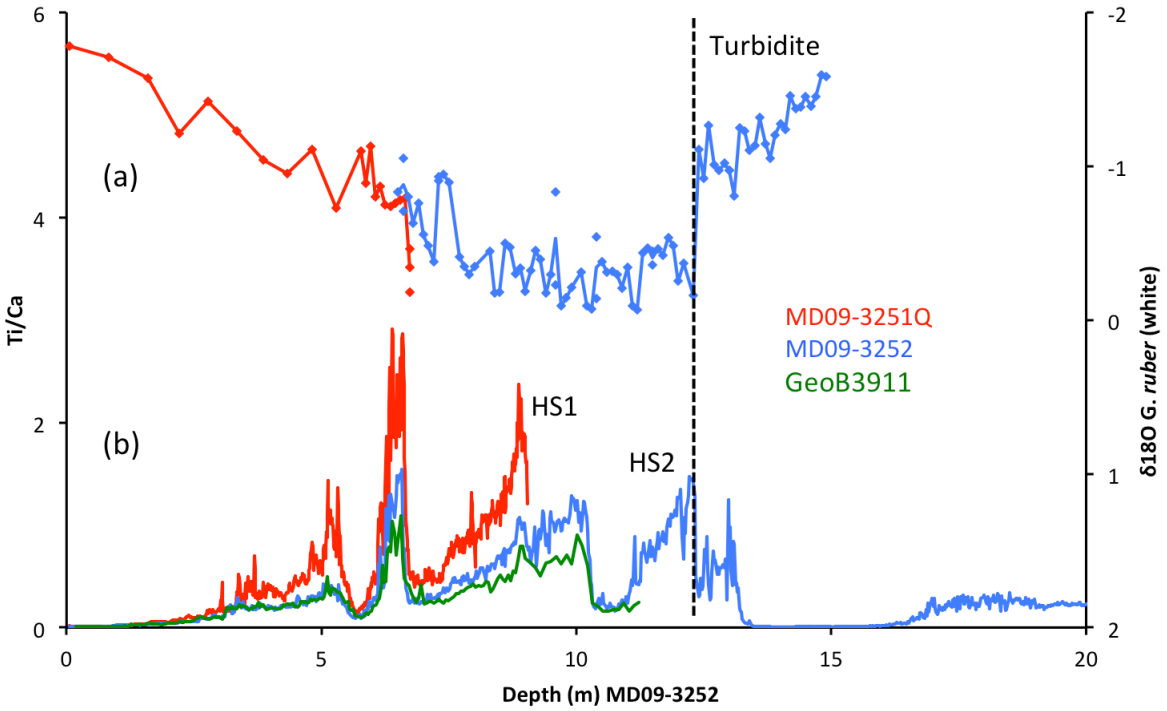

Figure 1.**12** : (a) $\delta^{18}O$ and (b) Ti/Ca signals in shallow sediment cores.

We conclude that fast climatic events of the past 20-50 ka are recorded in the intermediate and deep sediment cores, but not in the shallow sediment core. I therefore modified my initial objectives and decided to study HS2 and HS4 on the intermediate and deep cores. I chose HS2 and HS4 as different northern hemisphere ice sheet volumes characterize these stadials (Lambeck and Chappell, 2001). It is indeed interesting to assess the effect of different ice sheet volumes on the configuration and flow rate of the water masses constituting the AMOC. Even though HS2 is affected by a turbidite on the intermediate core, it can still be studied at the onset and end of the event.

Chapter 2: Methodology

In my thesis, I dedicated a considerable amount of time implementing and optimizing the method for the analysis of sedimentary Pa/Th (Yu et al., 1996) at the LSCE. The focus of this chapter is to detail this method. I measured the protactinium, thorium and uranium isotopic concentrations necessary for the calculation of the Pa/Th ratio by isotope-dilution on a multi-collector inductively-coupled plasma mass-spectrometer (MC-ICP-MS). The principle of isotopic dilution (Vogl and Pritzkow, 2010) is to add a known quantity of spike (non-natural isotope in our case) to a sediment sample of unknown isotopic concentration, and to measure the ratio of both isotopes by mass-spectrometry to determine the isotopic concentration of the sediment. Isotopes in the spike and in the sediment must be of the same element. Measuring protactinium by isotope-dilution is complicated by the absence of non-natural long-lived protactinium isotopes. ^{233}Pa is the only non-natural isotope with a half-life long enough (26.967 days, (Audi et al., 2003)) to be used for analysis of ^{231}Pa concentration. However, this half-life is short and it is therefore necessary to produce the ^{233}Pa spike a short time before starting the procedure required for ^{231}Pa concentration measurements. Producing a ^{233}Pa spike can be done either by neutron activation of thorium (Anderson and Fleer, 1982) or by milking of a ^{237}Np solution (Regelous et al., 2004). ^{237}Np indeed decays into ^{233}Pa with a half-life of 2.14 My (Audi et al., 2003), and secular equilibrium (Np/Pa activity ratio of 1, maximum concentration of ^{233}Pa) is reached after ~6 months (~6 ^{233}Pa half-lives). Hence, every 6 months, a quantity of ^{233}Pa with the activity of the ^{237}Np solution can be separated from the ^{237}Np solution and used to spike sediment samples. This method therefore offers the advantage of providing an unlimited source of ^{233}Pa.

Because the affinity of protactinium for opal is very high (Chase et al., 2002) (see Chapter 1), I measured the weight percentage of opal (%Opal) in some sediment samples to investigate whether opal could be a cause of Pa/Th variability in the sediment cores I studied. Hence, in the first section of this chapter and before discussing the Pa/Th method, I present the method that I implemented at the LSCE for the determination of biogenic silica.

In a second section, I present the procedure I used to produce a ^{233}Pa spike by milking of a ^{237}Np solution. I describe how I calibrated the spikes, i.e. how I measured the ^{233}Pa, ^{236}U and ^{229}Th concentrations, used for the measurement of the Pa/Th ratio,

In a third section, I focus on how I analyzed and corrected the isotopic ratios of interest by mass-spectrometry. I also present the equations I used to calculate the sedimentary Pa/Th ratio.

The fourth and final section is the core of this chapter. It is an intercomparison study (Burckel et al., 2014 c, in prep.) that presents the protocol for sedimentary Pa/Th analysis that I used and results on various sample types. This study provides an assessment of the accuracy of the Pa/Th measurements done during my thesis, as well as an idea of the Pa/Th variability than can be expected when comparing sediment samples measured in different laboratories.

2.1 Opal measurements

I implemented at the LSCE a method to estimate %Opal in marine sediments by wet alkaline sequential extraction (Demaster, 2013; Mortlock and Froelich, 1989). Silicate concentrations are estimated by spectrophotometry, using the heteropoly blue method. Silica is dissolved and mixed with ammonium molybdate, which forms molybdosilicates under acidic conditions (Galhardo and Masini, 2000). Consequent reduction of Mo(VI) to Mo(V) results in the formation of molybdenum blue compounds. The concentration of these compounds depends on the amount of silicate initially available in the solution, and results in a more or less pronounced blue colorization of the solution. Silicon concentration is therefore determined by spectrophotometry, by comparing absorption intensities of samples to an array of standards of known Si concentration.

2.1.1 Method

Sediment samples were dried and crushed to powder using an agate mortar and pestle. Sediment was crushed lightly in order to avoid incorporating silica from the mortar and pestle. ~0.1 g of sediment powder was weighed and transferred to 50 ml centrifuge tubes. A pretreatment of the sediment is done by addition of 5 ml 10 % H_2O_2 and 5 ml 1N HCl in order to remove organic matter and carbonates. Tubes were then sonified for a few minutes and left for 30 minutes. 20 ml MilliQ water was then added to each tube that were centrifuged, the supernatant decanted to waste. Centrifuge tubes were then opened and left to dry at 50°C in an oven.

Exactly 40 ml of Na_2CO_3 (2M) was then added to each tube in order to dissolve biogenic silica. Sediment was suspended by agitation and centrifuge tubes were placed in a shaking bath at 85°C. After 2, 3 and 5 hours (Demaster, 2013), centrifuge tubes were taken out of the bath, centrifuged for a few minutes and cooled in water at ambient temperature for 5 minutes. 125 µl of each sample are pipetted and transferred to new centrifuge tubes containing 17.5 ml of molybdate solution (Mortlock and Froelich, 1989), and the centrifuge tubes containing the sediment are closed and put back in the shaking bath. As this procedure is done at three different times, each sediment sample is

associated to three molybdate solutions reacting with the Si extracted after 2, 3 and 5 hours. Centrifuge tubes containing the molybdate solution and the sample aliquot are mixed by swirling to allow Si to react and complex as molybdosilicates. After exactly 20 minutes, 7.5 ml of reducing solution (Mortlock and Froelich, 1989) is added to each tube containing the molybdate solution, which is mixed by swirling. Solutions are ready to be measured the day after, when all molybdosilicates are reduced to molybdenum blue compounds.

2.1.2 Calculation

Absorptions are measured for each molybdate solution on a spectrophotometer peaked at 816 nm. Absorptions are then compared to the absorbance-weight(Si) relationship of different standards of known Si concentration, to deduce the mass of Si in each molybdate solution (Fig. 1, Table 1). Si masses are divided by the sediment mass to calculate %Si in the sediment. Note that his is done for the three molybdate solutions measured after 2, 3 and 5 hours. The Silicon standard used for calibration of the absorbance-weight(Si) relationship is a Silicon AAS standard solution Specpure 500ml (1000 $mg.l^{-1}$).

For each sediment samples, three solutions are measured and their silicon concentrations inform us about the evolution of Si leaching through time (at 2, 3 and 5 hours). This method is termed “sequential extraction” (Demaster, 2013) and aims at differentiating the Si extracted by biogenic silica dissolution from alumino-silicate leaching. Indeed, while biogenic silica is quickly dissolved (Demaster, 2013), alumino-silicates are assumed to continuously leach Si at the same rate through time. Hence, by measuring the silicate concentration of the extracting solution at different times, we can estimate the Si concentration resulting from biogenic silica and from alumino-silicates (Fig. 2). %Si are multiplied by a factor of 2.139 to calculate %Opal in the sediment (molar mass $SiO_2/Si = 2.139$ (Muller and Schneider, 1993)).

I compared my results with measurements made at the Institute for Environmental Physics at the University of Heidelberg (IUP), which routinely analyzes the opal content of sediment samples using sequential extraction (Muller and Schneider, 1993) (Fig. 3). Even though I used a different base (Na_2CO_3 2M) for the dissolution of biogenic silica than the IUP (NaOH 1 M), our results are coherent. The good efficiency of Na_2CO_3 could be related to the relatively young age of our sediment samples (20-50 ka), as the resistance of biogenic silica is dependent on the geological period of opal production (Lyle et al., 2002).

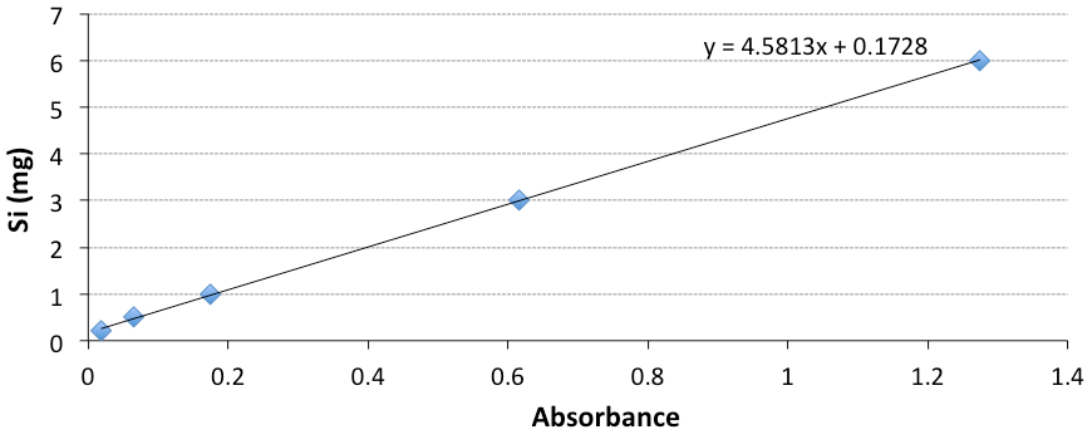

Figure 2.1 : Si (mg) as a function of absorbance. Si content of a sample solution is estimated based on its measured absorbance and on the relation absorbance-weight(Si) of the standards.

Table 2.**1** : Si mass and related absorbance for standards used to form the linear regression in Fig. 1. Si calculated is the estimate of the concentration in the standards based on the linear regression.

Standard Name	Absorbance	Si (mg)	Si (mg) Calculated
Std 0,2mg	0.019	0.2	0.2598447
Std 0,5mg	0.065	0.5	0.4705845
Std 1mg	0.174	1	0.9699462
Std 3mg	0.615	3	2.9902995
Std 6mg	1.274	6	6.0093762

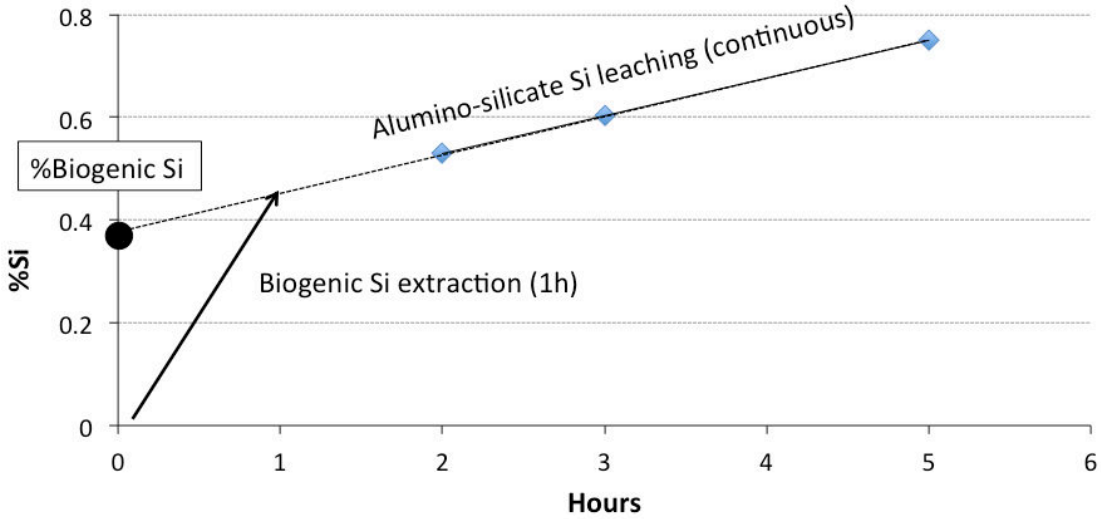

Figure 2.**2** : Extraction of Si as a function of time in a sediment sample containing biogenic silica and alumino-silicate. After 1-2h, all biogenic silica is dissolved (Demaster, 2013). Si leaching continues at a constant rate, which allows finding the initial %Si biogenic in the sample from the intercept.

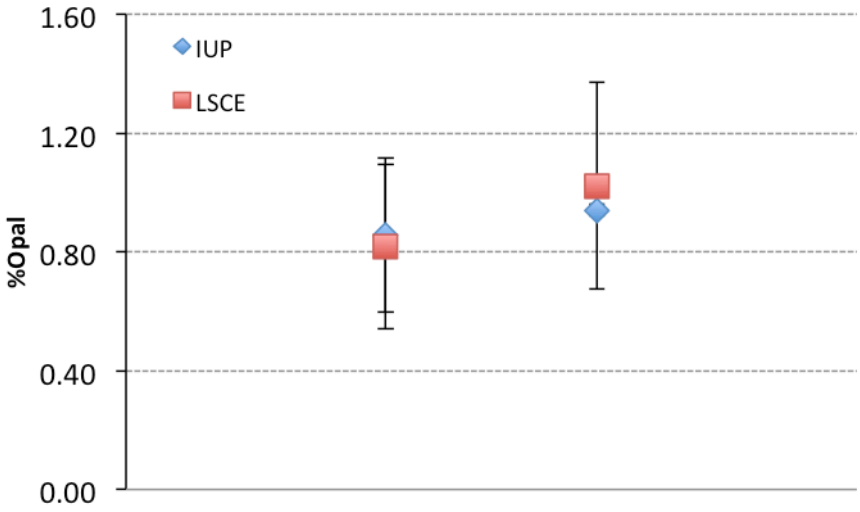

Figure 2.**3** : %Opal in two samples measured both at the IUP (blue diamonds) and LSCE (red squares).

2.1.3 Uncertainties

The main uncertainty on the silica concentration of sediment samples is probably related to the difficulty of disaggregating sediment during alkaline extraction. Sediment samples from the studied sediment cores are indeed mainly consisted of clays. After the drying step following the pre-treatment with H_2O_2 and HCl, sediment already formed aggregates although heating was stopped before complete evaporation. Centrifuging sediment samples also probably caused sediment aggregation, but this step appears necessary to avoid pipetting silica that would both cause a material loss in the sample being opal digested, and a high silica gain in the aliquot being analyzed with the molybdate blue. A pair of full chemistry replicates was measured: one sediment sample formed a thin cloud when mixed by swirling, and the other formed sediment aggregates difficult to dissociate. I therefore used the difference of concentration between the two replicates (0.99 and 0.49 %SiO_2) to assess uncertainty on measurements, which are of 34% at 1 SE. Although this uncertainty is large, it is sufficient to estimate the order of opal concentration of sediment samples.

One procedural blank was also measured. After 5 hours, the weight of Si in the blank was of 0.017 mg, less than 3 % of the least concentrated sample. Considering the uncertainty resulting from sediment aggregation, I considered this negligible.

2.2 ^{233}Pa, ^{236}U and ^{229}Th spikes

2.2.1 ^{233}Pa spike milking from ^{237}Np

The ^{233}Pa spike was produced by milking of a ^{237}Np solution following the protocol of Guihou et al., 2010 (Guihou et al., 2010b). The method takes advantage of the affinity of protactinium for hydrated silica in the absence of fluorides (Regelous et al., 2004). I used two neptunium solutions during this thesis, one of 20 kBq and the other of 12 kBq. Milking of one neptunium solution resulted in ~10-20 pg of ^{233}Pa, depending on the activity of the neptunium solution used. These quantities of ^{233}Pa allow the measurement of 30-40 sediment samples. After each milking, the neptunium solution was left to regenerate for 6 months. Here I briefly describe the method of ^{237}Np-^{233}Pa separation I used for the production of ^{233}Pa spikes.

A disposable column is filled with 5 ml of hydrated silica gel (63-200 µm). The gel is rinsed several times with 8N HNO_3 and H_2O, and conditioned with 5 ml 8N HNO_3. The neptunium mother solution is evaporated several times to a drop with 8N HNO_3 in order to ensure the absence of hydrofluoric acid in the solution, which could cause Pa losses. The mother solution is then added to the column in 2 ml 8N HNO_3. 23 ml of 8N HNO_3 is then added to the column, by 0.5 ml step for the first 3 ml then by 5 ml steps. Decreasing the volumes of acids added at each step results in better separation efficiencies as neptunium immediately enters the gel and is not suspended on the column walls. Once the neptunium fraction is eluted, the protactinium fraction is extracted with 40-50 ml 8N HNO_3 + 0.13N HF. ^{233}Pa emits gamma rays and its extraction can be monitored using a COMO170 mobile contamination monitor. We consider that no significant amount of Pa is left on the column when the gamma counts monitored on the column fall close to the background level, and when addition of 8N HNO_3 + 0.13N HF has no more effect on the gamma counting, i.e. when no more Pa is eluted. The column is then discarded to a special radioactive waste container. The ^{237}Np-^{233}Pa separation is repeated twice to avoid Np loss in the ^{233}Pa spike which could result in production of ^{233}Pa after the Pa-Np separation step. The quality of the ^{237}Np-^{233}Pa separation was monitored for each spike by mass-spectrometry and the ^{237}Np/(^{233}U + ^{233}Pa) ratio always fell below 1.

2.2.2 ^{233}Pa calibration

^{231}Pa concentrations were measured by isotopic dilution, but the ^{233}Pa spike was not directly calibrated. Instead, measurement of a ^{233}Pa-spiked ^{231}Pa standard was directly used to estimate the ^{231}Pa concentration of sediment samples (see section 2.4.1). Estimating the ^{233}Pa concentration of the spike is indeed problematic, as ^{233}Pa decays into ^{233}U, and as uranium and protactinium can have different ionization efficiencies (Regelous et al., 2004). In a regular calibration, a known quantity of ^{231}Pa would be

added to the ^{233}Pa spike to estimate its concentration by mass-spectrometry. However, because ^{233}U and ^{233}Pa may have different ionization efficiencies, the ^{231}Pa addition and ^{231}Pa/^{233}Pa measurement must be done before a significant amount of ^{233}Pa decayed into ^{233}U. Measuring a ^{231}Pa solution of known concentration, spiked with the ^{233}Pa spike and U-Pa separated at the same time as sediment samples can circumvent this problem.

The ^{231}Pa/^{233}(Pa + U) ratio of sediment samples (R(Smp)) and of the ^{233}Pa spiked ^{231}Pa standard (R(Std)) are measured during the same mass-spectrometer session. ^{231}Pa concentrations of sediment samples can be calculated by the following equation (1):

$$[^{231}Pa]_{sed} = \left(\frac{R(Smp) * \mathrm{M_{Spike}(Smp)} * N_{231}i(Std)}{R(Std) * \mathrm{M_{Spike}(Std)}} \right) \Big/ M_{sed} \quad (1)$$

where $[^{231}Pa]_{sed}$ is the ^{231}Pa concentration of the sediment, M_{spike}(Smp) and M_{spike}(Std) the mass of ^{233}Pa spike in the sediment sample and ^{231}Pa standard respectively, Msed the sediment mass and N_{231}i(Std) the quantity of ^{231}Pa initially in the the standard.

Usually, the problem of ^{233}Pa decay to ^{233}U is solved by measuring the sediment samples (^{231}Pa/^{233}Pa ratio) immediately after U-Pa separation, so that all mass 233 consists of ^{233}Pa. A calibration solution is measured either at the same time, using ^{231}Pa to estimate the ^{233}Pa concentration of the spike (Auro et al., 2012), or 6 months later (Negre et al., 2009), when all mass 233 consists of ^{233}U, so that the initial ^{233}Pa concentration of the spike can be estimated by addition of known amounts of natural uranium. The advantage of using equation (1) for the estimation of ^{231}Pa concentrations is that the sediment samples can be measured at any time after U-Pa separation, providing more flexibility with respect to the analysis on mass-spectrometer.
In this study, the ^{231}Pa standard is a HU1 solution of known ^{238}U concentration (see section 2.2.3 for the estimation of the concentration of HU1). Considering a ^{235}U/^{238}U activity ratio of 0.04604 (Francois, 2007) and that ^{235}U is at secular equilibrium with ^{231}Pa, we know the ^{231}Pa concentration of the solution.

2.2.3 ^{236}U and ^{229}Th calibration

A mixed ^{236}U-^{229}Th spike was used to estimate uranium and thorium isotopic concentrations of sediment samples. In this study, using a mix of two spikes is only useful to avoid weighing each spike separately. The ^{236}U spike was calibrated by spiking and measuring the ^{236}U/^{238}U ratio of a solution of certified Uranium concentration (SCP SCIENCE, PlasmaCAL, 1000µg/ml Uranium) by mass-spectrometry on MC-ICP-MS Neptune. The ^{238}U concentration of the PlasmaCAL solution was calculated by correcting the total uranium from the ^{235}U contribution, which was done by analysis of the

$^{238}U/^{235}U$ ratio by mass-spectrometry (note that the $^{238}U/^{235}U$ ratio in the PlasmaCAL solution is different from the natural $^{238}U/^{235}U$ atomic ratio of 137.88 (Condon et al., 2010)). The calibrated ^{236}U spike was then used to estimate the ^{238}U concentration of a HU1 solution. As HU1 is considered to be at secular equilibrium, its ^{238}U concentration was used to find its ^{230}Th concentration. The ^{229}Th concentration of the spike was consequently calibrated by spiking the HU1 solution and measuring the $^{229}Th/^{230}Th$ ratio by mass-spectrometry.

2.3 Measurement by mass-spectrometry and Pa/Th calculation

2.3.1 Measurements by mass-spectrometry

Protactinium, thorium and uranium isotopic concentrations were measured by isotope dilution on a MC-ICP-MS (Neptune, Thermo Finnigan). I developed the protocol of analysis at the LSCE together with François Thil. The cup configurations used for mass-spectrometry analysis are presented in Table 2 and 3 for Pa-U and Th respectively. Different cup configurations were used because of the different spacing of the cups required for Pa-U and Th isotopic measurements. One ion counter was dedicated to ^{233}Pa measurements, as the dark noise on the counter strongly increases during Pa sample analysis. Dark noise increased typically from 10-20 counts per minutes (cpm) at the beginning of the analysis to 100-160 cpm at the end. The increasing dark noise during the run is corrected by machine blanks that are measured between each sample. The dark noise increase is related to the short half-life of ^{233}Pa, which sticks to the ion counters, activating them upon decay. After a few months, the dark noise of the ion counter used for ^{233}Pa measurements decreased back to its initial value, as ^{233}Pa decays to ^{233}U.

Multiple corrections are applied on the raw spectrometer ratios. Here I describe how each correction is measured (Table 2, 3). Equations applied to the isotopic ratios or signals for the various corrections are given in Table 4. I also briefly comment each correction.

Table 2.**2** : MC-ICP-MS cup configuration for the analysis of U and Pa isotopic ratios. “Solution” column: the type of solution analyzed, “IC4”-“H3” columns: ion counters and faraday cups used for isotopic analyses, “Ratio” column: the ratios of interest, “Use” column: how are the isotopic ratios used, “For” column: elements for which the measured isotopic ratios are useful. AS stands for Abundance sensitivity. Shaded cells in column C(C)/IC1 indicate which detector was used (ion counter versus faraday cup). Shaded=C(C), not shaded = IC1. Cup distances in atomic mass units (u) are shown on top. Lx, Hx and C(C) are faraday cups, ICx are ion counters.

	2u	2u	1u		1u	1u	1u	2u			
Solution	IC4	IC5	IC6	L4	L1	C(C)/IC1	H1	H2	H3	Ratio	Use	For
U sample						234U			238U	234U/238U 236U/238U	U concentration	**U**
						236U		238U				
Pa sample		231Pa								231Pa/233Pa	Pa concentration	**Pa**
	231Pa	233Pa										
				232Th								
Natural uranium							235U		238U	238U/235U	Mass bias correction	**U, Pa**
Natural uranium						238U				239/238U 235.5/238U 236.5/238U	**239/238U**: Hydride correction **236/238U calculated by exponential interpolation:** AS correction	**U**
						239						
						235.5						
						236.5						
238U + 236U solution						236U		238U		$\frac{236U(IC1)/238U}{236U(C(C))/238U}$	Yield between IC1 and C(C) correction	**U**
						236U		238U				
232Th solution					232Th	233				233/232Th	Hydride correction	**Pa**
Natural uranium			237	238U						237/238U	AS correction	**Pa**
231Pa + 233U solution		231Pa								$\frac{231Pa(IC4)}{231Pa(IC5)}$	Yield between IC5 and IC4 correction	**Pa**
	231Pa	233U										

Table 2.**3** : MC-ICP-MS cup configuration for the analysis Th isotopic ratios. “Solution” column: the type of solution analyzed, “IC4”-“H3” columns: ion counters and faraday cups used for isotopic analyses, “Ratio” column: the ratios of interest, “Use” column: how are the isotopic ratios used, “For” column: elements for which the measured isotopic ratios are useful. AS stands for Abundance sensitivity. Shaded cells in column C(C)/IC1 indicate which detector was used (ion counter versus faraday cup). Shaded=C(C), not shaded = IC1. Cup distances in atomic mass units (u) are shown on top. Lx, Hx and C(C) are faraday cups, ICx are ion counters.

		1u	2u	1u		3u				
Solution	L1	C(C)/IC1	H1	H2	H3	H4	Ratio	Use	For
Th sample		229Th		232Th			232Th/229Th 232Th/230Th 229.5/232Th 230.5/232Th	**232Th/229Th and 232Th/230Th:** Th concentration **230/232Th calculated by exponential interpolation:** AS correction	**Th**
		229.5							
		230Th	232Th						
		230.5							
Natural uranium		235U		238U			$\frac{235U(IC1)/238U}{235U(C(C))/238U}$	Yield between IC1 and C(C) correction	**Th**
		235U		238U					
Natural uranium					235U	238U	238U/235U	Mass bias correction	**Th**
232Th solution	232Th	233					233/232Th	Hydride correction	**Th**

Table 2.**4** : Calculation and application of corrections to isotopic signals and ratios. “Correction” column: type of correction, “Calculation” column: calculation of the correction, “Application” column: application of the correction on isotopic ratios or signals, “Note” column: notes for clarification of the equations. X and Y are elements. X can be the same element as Y. Cor. stands for corrected. “u” stands for atomic mass unit.

Correction	Calculation	Application	Note
Mass bias	$\mathrm{mb} = \left(\frac{238U/235U}{137.88} - 1\right)/3$	$\left(\frac{^{a}X}{^{b}X}\right)_{\mathrm{bm\ cor.}} = \frac{^{a}X}{^{b}X}(* \text{ or } /)(1 + \lvert a - b \rvert * \mathrm{mb})$	"*" if a < b and "/" if a > b
Yield IC1-C(C)	$y = \frac{236U(IC1)/238U}{236U(C(C))/238U} \text{or} \frac{235U(IC1)/238U}{235U(C(C))/238U}$	$\left(\frac{^{a}X(IC1)}{^{b}X(C(C))}\right)_{\mathrm{y\ cor.}} = \frac{^{a}X(IC1)}{^{b}X(C(C))}/y$	Calculation configuration dependent (cup spacement)
Yield IC4-IC5	$y = \frac{231Pa(IC4)}{231Pa(IC5)}$	$\left(\frac{^{231}Pa(IC4)}{^{233}Pa(IC5)}\right)_{\mathrm{y\ cor.}} = \frac{^{231}Pa(IC4)}{^{233}Pa(IC5)}/y$	Specific to 231Pa/233Pa
Abundance sensitivity	$AS(1u) = \frac{237}{238U}, AS(2u) = \frac{236}{238U} \text{ or} \frac{230}{232Th}$	$(^{a}X)_{\mathrm{AS\ cor.}} = {}^{a}X - {}^{a+(1 \text{ or } 2)}Y * AS(1 \text{ or } 2\ u)$	Correction not element dependent
Hydride	$H(238U) = \frac{239}{238U}, H(232Th) = \frac{233}{232Th}$	$(^{a}X)_{\mathrm{H\ cor.}} = {}^{a}X - {}^{a-1}Y * H(238U \text{ or } 232Th)$	Correction element dependent

Mass bias: mass bias is calculated using an internal uranium standard with a natural $^{238}U/^{235}U$ atomic ratio of 137.88 (Condon et al., 2010) (Table 2, 3, 4). Isotopic ratios of all elements (uranium, thorium and protactinium) are mass bias corrected using the uranium standard.

Yield IC1-C(C): The yield is the ratio between the signal measured on the central ion counter (in cps) and the signal measured on faraday cups (in V, converted to cps using a factor of 62500000) for a same isotope and solution (Table 2, 3). For my measurements, this ratio was between 0.9 and 1 and I therefore had to correct the ratio of isotopes measured simultaneously on IC1 and on faraday cups (Table 4).

Yield IC4-IC5: Ion counters have different yields. This difference is corrected by measuring the same isotope (^{231}Pa) twice, but switching the ion counter in between. Only the $^{231}Pa/^{233}Pa$ ratio requires this correction (Table 2, 4).

Abundance sensitivity: Abundance sensitivity (AS) (Murray et al., 2013) can significantly affect isotopic signals on masses close to abundant isotopes. The AS depends on the resolving power of the mass-spectrometer. This means that the AS effect of ^{232}Th on ^{231}Pa can be calculated by the effect of ^{238}U on mass 237. Because no isotope is present at mass 237 in the solution, AS can be directly measured with the $M237/^{238}U$ ratio (Table 2). The estimation of the AS 2 masses apart is more problematic as there could be ^{236}U in the analyzed solution, thus, the measured $M236/^{238}U$ ratio is not a direct representation of the AS. The AS two masses appart is therefore estimated by exponential interpolation of the AS signal on masses 235.5 and 236.5 (Table 2). A retardation lens (RPQ) on IC1 allows to decrease the effect of AS. Because ^{231}Pa is not measured on IC1 (no RPQ), AS is not measured on IC1 for correcting the contribution of ^{232}Th on the ^{231}Pa signal (Table 2).

Hydrides: Hydrides ($X\text{-}H^+$ where X is an isotope) (Murray et al., 2013) can significantly affect isotopic signals that are one mass above abundant isotopes. Hydrides formation is element dependent and more important for thorium than for uranium (by a factor of ~2). Uranium hydrides are corrected by measuring the $239/^{238}U$ ratio, while thorium hydrides are corrected with the $233/^{232}Th$ ratio in a ^{233}U free solution.

Natural isotopes in the spike: Signals are corrected from the presence of ^{230}Th in the ^{229}Th spike. ^{232}Th in the ^{229}Th spike is negligible, as are ^{234}U, ^{235}U and ^{238}U in the ^{236}U spike. ^{231}Pa in the ^{233}Pa spike is not negligible but is corrected with chemistry blanks.

Chemistry blanks: Chemistry blanks are estimated by measuring a mixture of ^{236}U, ^{233}Pa and ^{229}Th spikes that was processed as a sediment sample. One blank is measured for each batch of 9 samples. The blank's natural isotopes on tracer ratios are then removed from sediment samples ratios.

2.3.2 Pa/Th calculation

The Pa/Th ratio is the ratio of excess protactinium and thorium activities, corrected from decay to the time of sediment deposition. Excess protactinium (thorium) is calculated by subtracting from the total protactinium (thorium) the protactinium (thorium) resulting from authigenic uranium decay and protactinium (thorium) supported by uranium present in the sediment mineral lattices (lithogenic). We can write:

$$(X)_{measured} = (X)_{lithogenic} + (X)_{authigenic} + (X)_{excess} \quad (2)$$

where X is ^{231}Pa or ^{230}Th and $(X)_{measured}$ is the total ^{231}Pa or ^{230}Th, which is measured by mass spectrometry.

^{232}Th is mainly of lithogenic origin and lithogenic uranium can therefore be calculated from the lithogenic $^{238}U/^{232}Th$ ratio (R), assumed to be equal to 0.5 ± 0.1 (Guihou et al., 2010b). As a consequence, lithogenic protactinium (thorium) can be calculated as it is assumed to be at secular equilibrium with lithogenic ^{238}U (^{235}U). As ^{238}U consists of lithogenic and authigenic uranium, knowing lithogenic ^{238}U and total ^{238}U allows the calculation of authigenic ^{238}U. Assuming a $^{234}U/^{238}U$ activity ratio of 1.1466 (Robinson et al., 2004a) in the ocean and a natural $^{235}U/^{238}U$ activity ratio of 0.04604 (Francois, 2007), we can estimate the protactinium and thorium produced by authigenic ^{235}U and ^{234}U respectively since the time of sediment deposition.

Equations (3, 4) detail the calculation of excess thorium and protactinium, for more information refer to (Henderson and Anderson, 2003):

$$(^{230}Th)_{excess} = (^{230}Th)_{measured} - \left[(^{232}Th)_{measured} * \left(\frac{^{238}U}{^{232}Th}\right)_{lithogenic}\right] - \left[\left(\frac{^{234}U}{^{238}U}\right)_{ocean} * \left\{(^{238}U)_{measured} - (^{232}Th)_{measured} * \left(\frac{^{238}U}{^{232}Th}\right)_{lithogenic}\right\} * \left\{1 - e^{-\lambda_{230} * t}\right\}\right] \quad (3)$$

$$(^{231}Pa)_{excess} = (^{231}Pa)_{measured} - \left[\left(\frac{^{235}U}{^{238}U}\right)_{natural} * (^{232}Th)_{measured} * \left(\frac{^{238}U}{^{232}Th}\right)_{lithogenic}\right] - \left[\left(\frac{^{235}U}{^{238}U}\right)_{natural} * \left\{(^{238}U)_{measured} - (^{232}Th)_{measured} * \left(\frac{^{238}U}{^{232}Th}\right)_{lithogenic}\right\} * \left\{1 - e^{-\lambda_{231} * t}\right\}\right] \quad (4)$$

where t is the time since sediment deposition and λ are the decay constants of ^{231}Pa or ^{230}Th.

Excess protactinium and thorium are then corrected from decay since the time of sediment deposition by the following equation:

$$(X)_{excess,0} = (X)_{excess} * e^{-\lambda_x * t} \quad (5)$$

where X is ^{231}Pa or ^{230}Th.

Calculation of measurement uncertainties is based on the work of Guihou et al., 2010. Analytical and systematic errors are propagated through the Pa/Th equations assuming that all variables are independent and have a Gaussian distribution (Guihou et al., 2010a).

2.4 Pa/Th sediment results and inter-comparison

2.4.1 Methodological recommendations for the analysis of sedimentary Pa/Th.

This article has already been reviewed by all co-authors, and corrections have been implemented. Information concerning the method of uncertainties calculation and ^{231}Pa standard calibration will be added before submission to Analytical Chemistry. The masses of ^{233}Pa, ^{236}U and ^{229}Th used by the LDEO to spike sediment samples are still missing in Table 1 but will not change the content of the article.

Methodological recommendations for the analysis of sedimentary Pa/Th.

P. Burckel[1], G. Henry[2], H-C Ng[3], J. Lippold[4], S. Pichat[5], M. Roy Barman[1], F. Thil[1], J. Gherardi[1], C. Waelbroeck[1], J.F. McManus[2], L.F. Robinson[3], B. Antz[4]

[1]LSCE/IPSL, Laboratoire CNRS-CEA-UVSQ, Bât.12, avenue de la Terrasse, F-91198 Gif sur Yvette, France
[2]Lamont-Doherty Earth Observatory of Columbia University, P.O. Box 1000, Palisades, NY 10964 USA
School of Earth Sciences, University of Bristol, Wills Memorial Building, Queen's Road, Clifton BS8 1RJ
[4]Oeschger Centre for Climate Change Research, Institute of Geological Sciences, University of Bern, Zähringerstrasse 25, CH-3012, Bern, Switzerland
[5]Laboratoire de Géologie de Lyon (LGL-TPE), Ecole Normale Supérieure de Lyon, 46 allée d'Italie, 69007 Lyon, France

Abstract:
We present recommendations for the measurement of sedimentary U, Th and Pa isotopes using isotope dilution method. Our study is based on an inter-laboratory comparison of different protocols and mass-spectrometers. We provide a detailed comparison of the methods in terms of efficacy, rapidity, and acid volumes used, which serves as reference for emerging Pa/Th laboratories to develop their protocols based on available equipment and facility. Concentration results highlight the necessity of complete homogenization of distributed sediment samples prior to any intercalibration study, for instance by using a coning and quartering method. This study also provides and validates a new method of measurement of ^{231}Pa concentrations, which allows Pa mass-spectrometer measurements to be done at any time after U-Pa separation. Finally, we provide an estimate of the current inter-laboratory Pa/Th variability based on results of the four participating laboratories.

Introduction

U-series decay products, such as ^{230}Th, ^{231}Pa, ^{232}Th, ^{234}U, and ^{238}U, can be used for a wide array of applications in geosciences. For example, deviation of their isotopic

ratios from secular equilibrium (activity ratio of 1) allows age determination of geological events [1,2], quantification of weathering rates [3] and riverine sediments transfer time [4]. In paleoceanography, sedimentary ^{230}Th concentrations can be used to examine post-deposition sediment redistribution (focusing and winnowing) [5,6] or variations in vertical particle flux [7,8], and the sedimentary $(^{231}Pa/^{230}Th)_{xs,0}$ activity ratio (Pa/Th hereafter) is used as a proxy for vertical particle flux [9], changes in productivity [10], and variations in ocean circulation intensity [11-15].

Sedimentary Pa/Th is usually measured by isotope dilution. The chemical methods used to purify the radionuclide isotopes of interest in the bulk sediment mostly follows the early work of Anderson et al [16]. These methods usually comprise the following steps: 1) sediment spiking and digestion, 2) separation of actinides from the sediment matrix, notably alkali and alkaline earth metals which is often done by oxyhydroxide precipitation, 3) Pa, Th, and U purification, and 4) measurements by Inductively-Coupled Plasma Mass-Spectrometry (ICP-MS) [17-19], that has replaced alpha and beta counting [11,16] over the years. ^{233}Pa spike decays into ^{233}U ($T_{1/2}$= 26.967d [20]) that may have different ionization efficiency [17]. Spike calibration is therefore done either when all mass 233 consists of protactinium, i.e. typically within 24h after U-Pa separation [17,21], or when all ^{233}Pa is decayed into ^{233}U, i.e. more than 6 months after U-Pa separation [22].

The present study provides, in details, some of the main methods available for the analysis of sedimentary Pa/Th by different mass-spectrometers. We apply these methods to various samples and discuss the results. The methods are assessed in terms of optimal sediment digestion, U-Th-Pa separation and purification, and procedural yields. We also assess the quickest methods, as well as those requiring the least acid volumes. Based on the results, we provide recommendations for homogenized distribution of sediment sample prior to inter-laboratory analysis, and the pros and cons of each of the methods and mass-spectrometers. We also present a new method to measure sedimentary ^{231}Pa concentrations, circumventing the problem of the ^{233}Pa decay and allowing protactinium samples to be measured at any time after separation of uranium from the protactinium fraction. Finally, we compare Pa/Th results of the different laboratories and examine potential inter-laboratory Pa/Th variability. Four Pa/Th laboratories participated in this study for the measurements: the Laboratoire des Sciences du Climat et de l'Environnement (LSCE), the University of Bristol (UB), the Lamont Doherty Earth Observatory (LDEO) and the Institute for Environmental Physics at the University of Heidelberg (IUP).

Experimental section

Isotopic reference material. Thorium isotopic reference material IRMM-035 and uranium isotopic reference material NBS-SRM-960 (also called CRM 112-A) were analyzed for $^{230}Th/^{232}Th$ and $^{234}U/^{238}U$, respectively, to assess both precision and accuracy of the isotope-dilution ICP-MS measurements.

Solid Samples. Three solid samples were analyzed for their Pa, Th, and U isotopic concentrations. Geotraces_Sed is a near-surface siliceous ooze sediment (71% biogenic silica, 7% $CaCO_3$) recovered during a cruise of the RVIB Nathaniel B. Palmer (NBP9604 Station 3, 61.95°S/170.05°W, 3404 m water depth) [23]. This sample was previously measured as part of the GEOTRACES intercalibration study [23], which makes it valuable to assess data quality of this study. Margin_Sed is an early Marine Isotope Stage 2 sediment sample, recovered during a cruise of the R/V Marion Dufresne (MD 173/RETRO3, 03.55°S/35.39°W, 3537 m water depth) from the Brazilian margin, which mainly consists of calcium carbonate and terrigenous material. Sediment ages are given in Supporting Information. UREM11 is a uranium ore reference material, certified for its uranium concentration and supplied by the Council for Mineral Technology, South Africa [24]. The three samples have very different isotopic composition and span most of the Atlantic sediment ^{231}Pa and ^{230}Th concentration range (0.2-1 and 1-12 dpm.g-1 respectively [25]) and the lower part of the Pacific range (0.1-6.5 and 1-190 dpm.g-1 respectively [26]). Therefore they allow a thorough assessment of the presented Pa/Th methods.

Sample homogeneity. The problem with sediment heterogeneity when measuring ^{230}Th was raised by the GEOTRACES program and might lead to inter-laboratory variability [23]. The sediment sample from the GEOTRACES intercalibration (Geotraces_Sed) was therefore split using the coning and quartering method (Fig. S1) in order to assess the effect of this procedure on sediment heterogeneity. Sediment was then sent to the laboratories participating in this study. Margin_Sed was hand powdered with an agate mortar and pestle. The resulting powder was distributed stepwise and alternatively among the different shipment containers until all containers were full. The sediment was then sent to the participating laboratories. Sediment distribution was systematically done with a spatula. Sediment was not poured but deposited in the containers. These cautions aimed at minimizing the risk of grain size sorting during distribution. No particular care was taken with respect to sample homogeneity for the distribution of the UREM11 reference material, as this sample is a solid standard of small grain size (<75μm) therefore expected to be homogeneous.

Safety considerations. All methods require adequate protection equipment for the various reagents used, such as lab coats, nitrile gloves and safety glasses. Handling hydrofluoric acid usually requires additional precautions (refer to local regulations). Acids must be handled and evaporated under a chemical fume hood. Solution containing perchloric acid must be evaporated in hoods certified for such use. Radioactive tracers have to be used following the local regulation.

Sample weighing, spiking and digestion. Sediment sample powders and spike are weighed and mixed, except for UB that adds spikes after sediment digestion. The approach used by UB necessitates the prevention of any material loss before spike addition, and in microwave digestion this is achieved by the use of microwavable closed pressurized vessels.

Sediment mass and spike quantities used by each lab are given in Table 1. They do not differ significantly except for the much lower amount of ^{236}U spike used by the LSCE (see Discussion).

Sample digestion methods are detailed in Table 1. They mainly differ by the use of microwave or hotplate.

Oxy-hydroxide precipitation. After the digestion step, samples are evaporated to semi-solid gel, which is consequently dissolved in HCl (UB, LDEO) or HNO_3 (LSCE, IUP) and heated to clear solutions at 150-180°C (LSCE, UB). At this point, sample-spike equilibration should have been reached [27], thus any subsequent material loss would not impact the final concentration results. However, the methods used for purification and separation of radionuclides influence the yield and purity of each element, which ultimately impact the precision and accuracy of the mass-spectrometer measurements as well as the magnitude of the applied corrections.

Three laboratories (LSCE, UB, LDEO) use the classical step of separation of the radionuclides from the alkali and alkaline earth metals by oxyhydroxide precipitation [16]. Briefly, digested sample solutions are transferred to centrifuge tubes and NH_4OH is added until the formation of Fe-Al precipitates at around pH = 8. The samples are then centrifuged, and the supernatant decanted to waste. Precipitates are washed several times. The number and type of washes is the main difference between the three laboratories. After the first co-precipitation, precipitates are washed with 18.2 MΩ water and a few drops of ammonia (LSCE, UB: 20ml H_2O LDEO: 5ml). The washing step is achieved by agitation of the centrifuge tube to re-suspend the precipitate. Tubes are then centrifuged and the supernatant decanted to waste. The LDEO and UB group then dissolve the precipitate in 2 ml and 20 ml HCl 9N, respectively, for column separation.

The LSCE group dissolves the precipitate in 20 ml HNO_3 2N, before oxyhydroxide co-precipitation with ammonia. Tubes are then centrifuged and the supernatant decanted to waste. The precipitate water washing/acid dissolving process is repeated once. Precipitate is then washed one last time with MilliQ water and a few drops of ammonia, before samples are centrifuged and the supernatant decanted to waste. The precipitate is then dissolved in 2 ml HNO_3 8N for column separation.

The large number of water washing/acid dissolving steps achieved by the LSCE is meant to better separate U, Pa, and Th from alkali and alkali earth metals. However, the separation efficiency was not verified, and it could be that these time-consuming steps reduce the chemistry yield without major improvement of the separation.

IUP skips the oxyhydroxide precipitation step as this process is time consuming. This could however lead to poorer elemental separation and purification by anion-exchange chromatography because of a higher matrix load, which could both diminish the ionization efficiency and increase the interferences during mass-spectrometry measurements. These side effects thus need to be monitored and corrected for.

Pa, Th, and U separation and purification. The four labs use slightly different anion-exchange chromatography separation and purification step (Fig. 1). The method used by the LSCE is derived from Guihou et al [28]. Whole chemistry yields and elemental separation efficiencies are given in Table 2.

Analysis by mass-spectrometry. Precision and accuracy of the analyses by mass-spectrometry depend on many variables, some inherent to the type of mass-spectrometer and introduction system (Table 3) and some due to the previous chemistry steps (Table 2). We compared three types of ICP-MS in this study: multi-collector (MC) (LSCE and UB; Thermo-Fisher Finnigan Neptune), sector-field single-collector (SF) (LDEO; Finnigan Element XR), quadrupole single-collector (Q) (IUP; Thermo Scientific iCAP Qs).

^{231}Pa concentration measurements. As ^{233}Pa decays rapidly to ^{233}U ($T_{1/2}$= 26.967d), which possibly has a different ionization efficiency [17], the ^{231}Pa/^{233}Pa ratio is usually measured within 24h [17] after U-Pa separation. Different methods to estimate sediment ^{231}Pa concentrations were used by the laboratories participating in this study. UB and LDEO measure the ^{231}Pa/^{233}Pa ratio 1 and 3 days after Pa-U separation respectively, i.e. before the decay of a significant fraction of the ^{233}Pa spike. Moreover, the LDEO group considers that the ionization difference between Pa and U is negligible on their SF-ICP-

MS, based on the results obtained by Choi et al [19] on the same type of instrument. This allows them to estimate the concentration of the ^{233}Pa spike, which in turn is used to estimate the ^{231}Pa concentration of sediment samples. However, these methods require mass-spectrometer measurements to be done immediately after column chromatography.

Here we present the new method of measurement of ^{231}Pa concentrations developed by the LSCE and IUP. It presents the advantage of removing the time constraints on mass-spectrometer measurements linked to the short ^{233}Pa half-life.

^{233}Pa spike is added both to sediment samples and to a ^{231}Pa solution of known concentration. After sediment digestion, the Pa fractions of the sediment samples and of the spiked ^{231}Pa standard are separated from U at the same time by column chromatography. The ^{231}Pa/^{233}(Pa + U) fractions can be measured at any time after separation, as long as the samples and spiked ^{231}Pa standard are measured during the same mass-spectrometer run (within ~24h [17]). Here we briefly present the mathematical validity of this method of measurement of ^{231}Pa concentrations, for more details refer to SI.

Consider a ^{231}Pa standard of known concentration spiked with a ^{233}Pa solution of unknown concentration, and a digested sediment sample spiked with the same ^{233}Pa solution. The Pa fraction of both solutions was purified from U at the same time by column chromatography. When measured on mass-spectrometer, the spiked ^{231}Pa standard contains N_{231}(Std) and N_{233}(Std) atoms of ^{231}Pa and ^{233}(Pa + U) respectively. The sediment sample contains N_{231}(Smp) and N_{233}(Smp) atoms of ^{231}Pa and ^{233}(Pa + U) respectively. The ^{231}Pa/^{233}(Pa + U) ratio R measured on mass-spectrometer for any of the solutions depends on α, the U/Pa ionization efficiency ratio, and on t2, the time since column elution, which dictates the proportion of Pa and U in the solution:

$$R = \frac{N_{231}}{N_{233} * A(t2, \alpha)} = \frac{N_{231}i}{N_{233}i * B(t1, t2, \alpha)} = \frac{N_{231}i}{M_{Spike} * [^{233}Pa]_i * B(t1, t2, \alpha)} \quad (1)$$

N_{231}i and N_{233}i are the number of atoms of ^{231}Pa and ^{233}Pa respectively present before digestion for sediment samples and before column chromatography for spiked ^{231}Pa standards (i.e. initial concentrations). A depends on t2 and α, B depends on t1, the time between spike creation and column elution as well as on t2 and α, $[^{233}\mathrm{Pa}]_i$ is the unknown initial concentration of the ^{233}Pa spike, M_{Spike} is the known mass of spike added to the sample. α equals 1 if there is no ionization difference.

For a spiked ^{231}Pa standard (Std) we can write:

$$[^{233}Pa]_i * \mathrm{B(t1, t2, \alpha)} = \frac{N_{231}i(Std)}{\mathrm{M_{Spike}(Std)} * R(Std)} \quad (2)$$

Equation (2) can be inserted in equation (1) for a sediment sample (Smp) in order to get rid of the unknown initial spike concentration and of B(t1,t2,α), as this term is the same for sediment samples and spiked ^{231}Pa standards which are U-Pa separated and measured on mass-spectrometer at the same time.

We obtain:

$$[^{231}Pa]_{sed} = \left(\frac{R(Smp) * \mathrm{M_{Spike}(Smp)} * N_{231}i(Std)}{R(Std) * \mathrm{M_{Spike}(Std)}} \right) \Big/ M_{sed} \quad (3)$$

where $[^{231}\mathrm{Pa}]_{sed}$ is the concentration of the sediment sample and M_{sed} is the sample mass. R(Smp) and R(Std) are measured by mass-spectrometry, N_{231}i(Std), M_{sed}, M_{spike}(Smp) and M_{spike}(Std) are known or weighed.

Results and discussion

Isotopic ratio accuracy and precision. As a first step, thorium IRMM-035 and uranium NBS-SRM-960 isotopic reference materials were measured to evaluate mass-spectrometer accuracy and precision. Results for each laboratory are shown in Fig. 2, along with certified ratios.

MC-ICP-MS (LSCE, UB) give accurate measurements (see Table S1), within uncertainties for both isotopic ratios and their precision are better (ca. 8 times better) than other ICP-MS types (Fig. 2). Single collector ICP-MS (LDEO, IUP) display an offset from thorium and uranium certified isotopic ratios of up to several percent and can have variable results. This offset may be due to the low concentration of the standard solutions (0.01-0.02 dpm.g^{-1}) as shown by the results in the next section. Note also that the series of measurements made by the IUP group in this study is one of the first made by their Q-ICP mass-spectrometer. Accordingly, performance may not be comparable to a mass-spectrometer routinely used for several months.

Pa, Th and U isotopic concentrations on solid samples. Protactinium, thorium and uranium isotopes concentrations of solid samples (sediments and uranium ore UREM11) measured by isotope-dilution in this study are shown in Table S2 and Figures S2-S6. Figure 3 and 4 summarize these results by showing deviations (in %) of the isotopic concentrations of each laboratory from the inter-laboratory mean.

Protactinium, thorium and uranium isotopes concentrations of sediments and uranium ore UREM11 measured by the 4 laboratories generally agree within 2 sigma uncertainties (Fig. 3, 4, see also Table S2 and Fig. S2-S6). The only outliers are the ^{230}Th and the ^{234}U concentrations measured on Margin_Sed by the LDEO. Moreover, no laboratory displays a systematic positive or negative deviation from the inter-laboratory mean on U-Th measurements. Systematic biases such as different spike calibrations and digestion efficiencies are therefore not the main factors leading to inter-laboratory concentration differences for U and Th. A systematic Pa concentration bias could be the reason for the differences between LSCE and UB results. It is unlikely that this difference results from incomplete organic matter degradation [22], as both labs use perchloric acid. Systematic concentration differences could be related to issues in the estimation of the concentration of the ^{231}Pa standard used for spike calibration or to an effect of the two methods of measurement of ^{231}Pa concentrations used by the LSCE and UB groups. The validity of the new ^{231}Pa concentration measurement method used by the LSCE and IUP groups is assessed later in this study. The UREM11 sample displays the most consistent inter-laboratory concentration results (Fig. 3, 4). This is probably due to its high concentration and homogeneity. This result tends to confirm that isotopic ratio offset and variability measured on single collector ICP-MS was due to the low concentrations of the standards. Our results on Geotraces_Sed are also consistent with the GEOTRACES intercalibration, confirming the validity of the presented methods (Table 4).

Small quantities of ^{236}U spike are used for measurement on the LSCE MC-ICP-MS (Table 1). The mass-spectrometer is also used for U-Th dating, for which precision of uranium measurement is critical. The LSCE group therefore had to find a trade-off to allow multiple utilization of the instrument. Using low concentrations of ^{236}U for Pa/Th measurements reduces machine blank levels and carry-over, which increase the precision for dating of low concentration uranium samples. As a consequence, the ^{236}U had to be measured on an ion counter for Pa/Th, which could decrease the precision compared to measurements of higher spike quantities on faraday cup. However, precision on uranium concentration measurements is quite similar between the MC-ICP-MS users (LSCE and UB), despite the different mass of ^{236}U used. Low ^{236}U spike quantities can therefore be used to precisely measure the uranium concentration of sediment samples.

Comparison of the digestion methods: microwave-assisted versus hotplate. Both microwave and hotplate digestion were used by the UB group in order to compare digestion efficiencies. Results are shown in Fig. 5. Almost all pairs of measurements (hotplate-microwave) are similar within error bars. Moreover, none of the two digestion methods yields systematically lower or higher isotopic concentrations. Hence we

conclude that microwave and hotplate digestion have similar efficiencies. Microwave digestion is therefore not necessarily the most efficacious digestion method, unlike stated in earlier studies [30].

Heterogeneity effects. In the GEOTRACES intercalibration, concentration measurements on Geotraces_Sed showed that the inter-laboratory variability of ^{230}Th measurements was similar to the intra-laboratory variability of some laboratories (range of 5-6 dpm.g^{-1}) [23]. For this reason, the authors concluded that the sediment that was distributed to the participating laboratories was heterogeneous. Prior to distributing the Geotraces_Sed sample for this study, we homogenized the sediment using the coning and quartering method. The inter-laboratory ^{230}Th concentrations we obtain on Geotraces_Sed shows much less variability than in the GEOTRACES intercalibration (2.3%, 2 sigma, range of 5-5.6 dpm.g^{-1}). This result indicates that the original GEOTRACES intercalibration indeed measured heterogeneous material. Grinding and mixing of sediment before a thorium inter-calibration study therefore appears insufficient, and a more intense sediment homogenization method needs to be used for inter-comparisons.

Evaluation of the new method of measurement of ^{231}Pa concentrations. The good consistency of the Pa measurements indicates that the 2 methods used by the four laboratories to measure ^{231}Pa concentrations (i.e., Pa measurement immediately after column separation for the UB and LDEO group and possibly a few weeks after for the LSCE and IUP groups) have a minor impact on the results. However, in this study, Pa solutions were analyzed quite quickly after column separation even for the LSCE and IUP groups (4 and 7 days after column separation respectively). Moreover, there is an offset between UB and LSCE Pa concentration results, which could be attributed to the different methods of measurements of ^{231}Pa concentrations or to the estimation of the concentration of the ^{231}Pa calibration solution.

Hence, to demonstrate the validity of the ^{231}Pa measurement method described in this paper, protactinium concentrations of pairs of full sediment replicates were analyzed by the LSCE group at different times between U-Pa separation and measurement on ICP-MS, i.e. with different ^{233}U/^{233}Pa ratios. All first replicates are measured 6 days after U-Pa separation, except one which is measured after 10 days (square on Fig. 6, more details hereafter). Second replicates are measured 13 to 52 days after U-Pa separation. If our method of ^{231}Pa measurement is robust, the additional time left for ^{233}Pa to decay between the measurement of the first and second replicates should not impact concentration results. We therefore present our results as deviations

(%) of the concentration of one replicate from the other, and as a function of the additional time left for the ^{233}Pa to decay in the second replicate (Fig. 6, Table S3). One of the presented pair of replicates is not composed of two full sediment replicates but of a single sample whose Pa fraction was measured at two different times (10 and 52 days, square on Fig. 6). Although its ^{233}(Pa + U)/^{231}Pa ratio varies by more than 20% (0.629 to 0.494) reflecting the higher ionization efficiency of Pa compared to U, the ^{231}Pa concentration varies only slightly (1.6%, 0.197 to 0.194 dpm.g^{-1}), almost within the statistical uncertainty of the measurements (Table S3). Moreover, we see that full sediment replicates measured at different times do not display a systematic increase or decrease of their Pa concentration with time (Fig. 6). This confirms that the method of measurement of ^{231}Pa concentration presented in this paper can be used even if uranium and protactinium have different ionization efficiencies. The major advantage of this method is that it is not time dependent as other methods that necessitate the spike calibration to be done either immediately after U-Pa separation [17,21] or more than 6 months later [22]. Note however that the spiked ^{231}Pa standard solution and protactinium blanks need to be measured at the same time as the samples (within 24h, [17]) and it is therefore necessary to produce enough blank and standard solution. Blanks are also needed because the ^{231}Pa/^{233}(Pa + U) ratio in the blank changes through time and therefore needs to be measured at the same time as the samples.

Given the consistency of this new ^{231}Pa measurement method, it is more likely that the Pa concentration differences between the LCSE and UB groups (Fig. 3) result from issues on the estimation of the concentration of the ^{231}Pa solution used for the calculation of sedimentary ^{231}Pa concentrations.

Sedimentary Pa/Th calculation and variability. Inter-laboratory comparison of particulate and dissolved Pa/Th measurements is one of the ultimate targets of the GEOTRACES program. In order to have an idea of the current inter-laboratory Pa/Th differences, we calculated the Pa/Th values associated to both sediment samples measured in this study.

The inter-laboratory mean Pa/Th of the Margin_Sed sample is 0.065 ± 0.008 (13.1% 2 sigma) and the mean of the Geotraces_Sed sample is 0.222 ± 0.016 (7.3% 2 sigma) (Fig. S7, Table S4). The Pa/Th result from the LDEO is excluded from the calculation of the mean Pa/Th on the Margin_Sed sample because of its anomalously low ^{230}Th concentration (Fig. 4). Maximum Pa/Th differences between two labs are 12.2% for the Margin_Sed sample and 9.1% for the Geotraces_Sed sample. Such differences are significant and highlight the necessity to continue and intensify intercalibration efforts.

Pa/Th differences are however lower between the laboratories using multi collector mass-spectrometers, with 5.6% difference on both samples. By intercalibrating spikes and ^{231}Pa standards, it could be possible to increase the consistency of the measurements.

Advantages of the presented methods. Table 5 lists the best chemistry methods based on three main categories: efficacy, rapidity, as well as on the lowest acid volumes used. The most efficacious digestion is the most complete, and the most efficacious U-Th-Pa separation achieves the highest separation and yield.

All methods are equally efficacious concerning sediment digestion. Given the separation efficiency and yield in Table 2, the UB group method achieves the most efficacious U-Th-Pa separation. High yields allow more precise measurement of Pa, Th and U concentrations. The high separation efficiency of the elution by column chromatography minimizes the corrections applied to the ratios measured on mass-spectrometer and therefore maximizes precision.

Using microwave digestion is the quickest method (a few hours, Table 1), as hotplate requires samples to be heated overnight. Both the UB and IUP methods can therefore be used. The most rapid column chemistry is achieved by the IUP group by not having a Th purification step (Fig. 1). However, the higher matrix load resulting from the absence of separation could result in matrix effects on some mass-spectrometer, particularly given that the IUP group skips the oxy-hydroxide separation [31].

Pa/Th analyses are expensive and require large waste treatment due to the large amounts of acid used that therefore need to be minimized. The LDEO achieves digestion with the lowest volume of acids (6 ml/sample) (Table S5). The LSCE method uses the smallest volume of acids during the column chemistry step (98 ml/sample).

Mass-spectrometer recommendations. The sensitivity of the Q-ICP-MS is lower (6-40 times) than the LSCE MC-ICP-MS, which has a similar introduction system (Table 3). Moreover, the poor abundance sensitivity of the Q-ICP-MS makes precise ^{231}Pa measurements difficult if ^{232}Th is not separated well enough. Given the method used by the IUP group, ^{231}Pa abundance sensitivity correction on the sample with the highest ^{232}Th/^{231}Pa ratio (Margin_Sed, ^{232}Th/^{231}Pa = 4.3×10^{6}) is 58% of the total ^{231}Pa signal. This correction is calculated based on the separation efficiency of Th from the Pa fraction in Table 2, on abundance sensitivity correction in Table 3 and on the sedimentary ^{232}Th/^{231}Pa atomic ratio. We therefore recommend to use this mass-spectrometer with the most efficacious Pa-Th separation method (UB) only (Table 2), and to avoid its use for Pa/Th measurements of samples with high ^{232}Th/^{231}Pa atomic ratios.

The UB and LDEO groups use an Aridus desolvating nebulizer system. This greatly reduces hydrides and increases sensitivity. Tests with the Aridus II performed by the LSCE group show a 10-fold decrease in hydrides and 3-fold increase in sensitivity. Side effect is the large sample gas (Ar) consumption increased by 10 times. It is known that such systems impact sensitivity and hydrides, but the Aridus is better than a simple desolvating membrane plugged after the Apex HF (2-fold sensitivity increase, 4-fold hydrides decrease). The LSCE group did not use the Aridus but an Apex HF system (no desolvating membrane) for measurements presented in this study.

Conclusions

Many Pa/Th analysis methods exist, each with their own specificities. The four methods used in this study achieve coherent results. However, progress can be made to improve inter-laboratory variability of Pa/Th measurements, which is in this study of 5.6 % at best. The first step to achieve is to distribute homogeneous sediment samples prior to intercalibration studies. A coning and quartering method is proven to be adequate for this purpose. Results could also be made more consistent through the intercalibration of spikes and calibration solutions. Finally, our new method of measurement of ^{231}Pa concentrations should facilitate the measurement of sedimentary Pa/Th, by giving more flexibility with respect to the analysis on mass-spectrometer that can be done long after the separation of U from the Pa fraction by column chromatography.

Acknowledgments

Measurements performed at LSCE were funded by the CNRS/INSU LEFE project ACCENT. This work is a contribution to the RETRO project, a joint European Science Foundation (ESF)/EUROMARC, funded by Research Council of Norway (RCN), France (CNRS/INSU), Germany, and the Netherlands. Part of the sedimentary analyzed was collected on board R/V Marion Dufresne during RETRO Cruise III, supported by ESF EUROMARC project RETRO, IPEV and ANR project ANR-09-BLAN-0347. We thank the IPEV team, crew members of R/V Marion Dufresne and all scientists who participated in RETRO Cruise III. This is LSCE contribution xxxx.

References

(1) Knight, A. W.; Eitrheim, E. S.; Nelson, A. W.; Nelson, S.; Schultz, M. K. *Journal of environmental radioactivity* **2014**, *134*, 66-74.
(2) Martinez-Aguirre, A.; Alcaraz-Pelegrina, J. M. *Journal of Radioanalytical and Nuclear Chemistry* **2013**, *298*, 1005-1016.
(3) Chabaux, F.; Blaes, E.; Stille, P.; Roupert, R. d. C.; Pelt, E.; Dosseto, A.; Ma, L.; Buss, H. L.; Brantley, S. L. *Geochimica Et Cosmochimica Acta* **2013**, *100*, 73-95.

(4) Granet, M.; Chabaux, F.; Stille, P.; Dosseto, A.; France-Lanord, C.; Blaes, E. *Geochimica Et Cosmochimica Acta* **2010**, *74*, 2851-2865.
(5) Francois, R.; Frank, M.; van der Loeff, M. M. R.; Bacon, M. P. *Paleoceanography* **2004**, *19*.
(6) Kienast, S. S.; Kienast, M.; Mix, A. C.; Calvert, S. E.; Francois, R. *Paleoceanography* **2007**, *22*.
(7) Francois, R.; Bacon, M. P.; Suman, D. O. *Paleoceanography* **1990**, *5*, 761-787.
(8) Richaud, M.; Loubere, P.; Pichat, S.; Francois, R. *Deep-Sea Research Part Ii-Topical Studies in Oceanography* **2007**, *54*, 762-771.
(9) Christl, M.; Lippold, J.; Hofmann, A.; Wacker, L.; Lahaye, Y.; Synal, H.-A. *Nuclear Instruments & Methods in Physics Research Section B-Beam Interactions with Materials and Atoms* **2010**, *268*, 1159-1162.
(10) Pichat, S.; Sims, K. W. W.; Francois, R.; McManus, J. F.; Leger, S. B.; Albarede, F. *Paleoceanography* **2004**, *19*.
(11) Yu, E.-F.; Francois, R.; Bacon, M. *Nature* **1996**, *379*, 689-694.
(12) McManus, J. F.; Francois, R.; Gherardi, J.-M.; Keigwin, L. D.; Brown-Leger, S. *Nature* **2004**, *428*, 834-837.
(13) Gherardi, J.-M.; Labeyrie, L.; Nave, S.; Francois, R.; McManus, J. F.; Cortijo, E. *Paleoceanography* **2009**, *24*, doi:10.1029/2008PA001696.
(14) Lippold, J.; Gherardi, J.-M.; Luo, Y. *Geophys. Res. Lett.* **2011**, *38*, doi:10.1029/2011GL049282.
(15) Guihou, A.; Pichat, S.; Govin, A.; Nave, S.; Michel, E.; Duplessy, J.-C. *Quat. Sci. Rev.* **2011**, *30*, 1576-1582.
(16) Anderson, R. F.; Fleer, A. P. *Analytical Chemistry* **1982**, *54*, 1142-1147.
(17) Regelous, M.; Turner, S. P.; Elliot, T. R.; Rostami, K.; Hawkesworth, C. J. *Anal. Chem.* **2004**, *76*, 3584-3589.
(18) Edwards, R. L.; Cheng, H.; Murrell, M. T.; Goldstein, S. J. *Science* **1997**, *276*, 782-786.
(19) Choi, M. S.; François, R.; Sims, K. W. W.; Bacon, M. P.; Brown-Leger, S.; Fleer, A. P.; Ball, L. A.; Schneider, D.; Pichat, S. *Mar. Chem.* **2001**, *76*, 99-112.
(20) Audi, G.; Bersillon, O.; Blachot, J.; Wapstra, A. H. *Nuclear Physics A* **2003**, *729*, 3-128.
(21) Auro, M. E.; Robinson, L. F.; Burke, A.; Bradtmiller, L. I.; Fleisher, M. Q.; Anderson, R. F. *Limnology and Oceanography-Methods* **2012**, *10*, 464-474.
(22) Negre, C.; Thomas, A. L.; Luis Mas, J.; Garcia-Orellana, J.; Henderson, G. M.; Masque, P.; Zahn, R. *Analytical Chemistry* **2009**, *81*, 1914-1919.
(23) Anderson, R. F.; Fleisher, M. Q.; Robinson, L. F.; Edwards, R. L.; Hoff, J. A.; Moran, S. B.; van der Loeff, M. R.; Thomas, A. L.; Roy-Barman, M.; Francois, R. *Limnology and Oceanography-Methods* **2012**, *10*, 179-213.
(24) Hansen, R. G.; Ring, E. J. **1983**, 12\.
(25) Moran, S. B.; Shen, C. C.; Edwards, R. L.; Edmonds, H. N.; Scholten, J. C.; Smith, J. N.; Ku, T. L. *Earth and Planetary Science Letters* **2005**, *234*, 235-248.
(26) Hayes, C. T.; Anderson, R. F.; Fleisher, M. Q.; Serno, S.; Winckler, G.; Gersonde, R. *Earth and Planetary Science Letters* **2014**, *391*, 307-318.
(27) Vogl, J.; Pritzkow, W. *Mapan-Journal of Metrology Society of India* **2010**, *25*, 135-164.
(28) Guihou, A.; Pichat, S.; Nave, S.; Govin, A.; Labeyrie, L.; Michel, E.; Waelbroeck, C. *Earth and Planetary Science Letters* **2010**, *289*, 520-529.
(29) Sims, K. W. W.; Gill, J. B.; Dosseto, A.; Hoffmann, D. L.; Lundstrom, C. C.; Williams, R. W.; Ball, L.; Tollstrup, D.; Turner, S.; Prytulak, J.; Glessner, J. J. G.; Standish, J. J.; Elliott, T. *Geostandards and Geoanalytical Research* **2008**, *32*, 65-91.

(30) Fischer, L. B. *Analytical Chemistry* **1986**, *58*, 261-263.
(31) Shiraishi, K.; Takaku, Y.; Yoshimizu, K.; Igarashi, Y.; Masuda, K.; McInroy, J. F.; Tanaka, G. *Journal of Analytical Atomic Spectrometry* **1991**, *6*, 335-338.

Figures

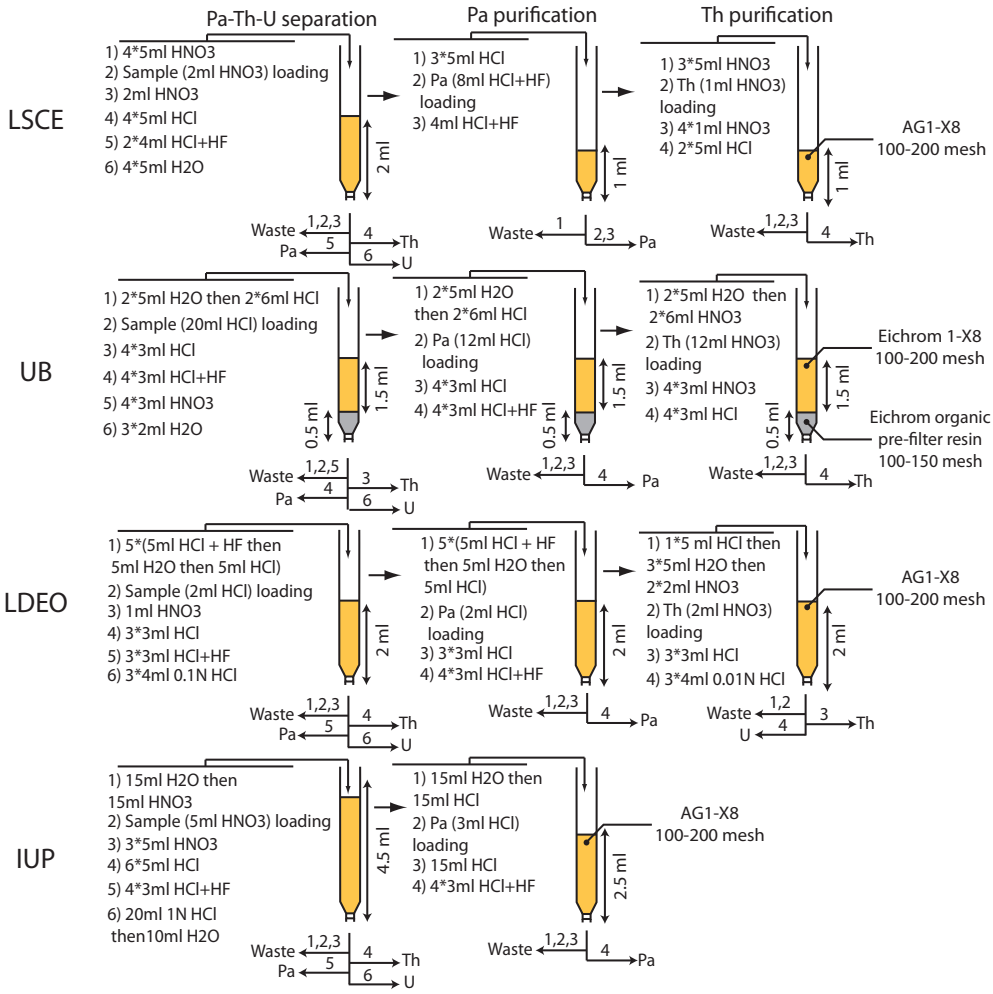

Figure 2.4.**1** : Anion-exchange chromatography separation and purification used by each of the participating laboratories. HCl concentration is 9N, HNO_3 8N and HF 0.13N unless otherwise stated. Resin types indicated for the last chromatography column of each laboratory also stand for the previous columns of the laboratory.

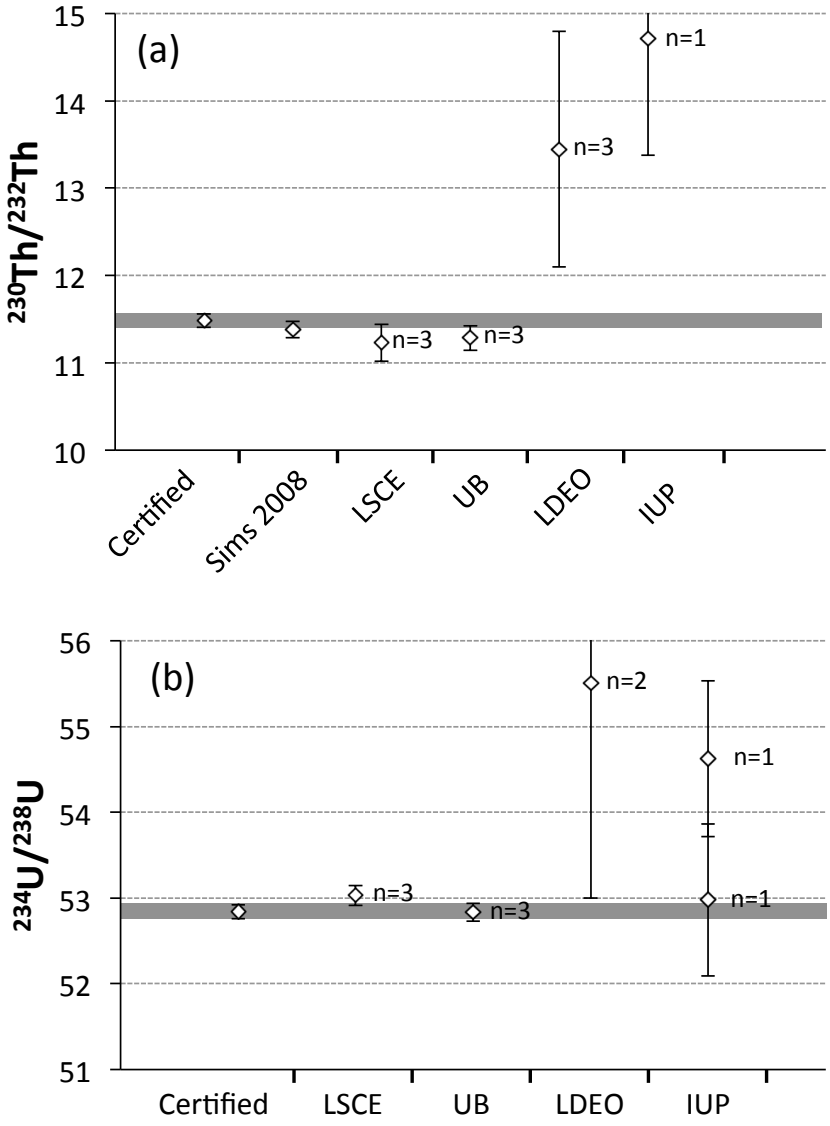

Figure 2.4.**2** : Isotopic ratios measured by each laboratory on thorium and uranium isotopic reference material. (a) $^{230}Th/^{232}Th$ measured on IRMM-035. Certified value is given as reference, as well as inter-laboratory MC-ICP-MS value from Sims et al [29]. (b) $^{234}U/^{238}U$ measured on NBS-SRM-960. Certified value is given as reference. The IUP group measured NBS-SRM-960 twice, on solutions from two different bottles. Error bars are the maximum between 2SE propagated on the mean (error on the sum of replicate measurements divided by the number of measurements) and 2SD on sample replicates (standard deviation of replicate measurements). The number of full chemistry replicates used to calculate the means is written next to each measurement.

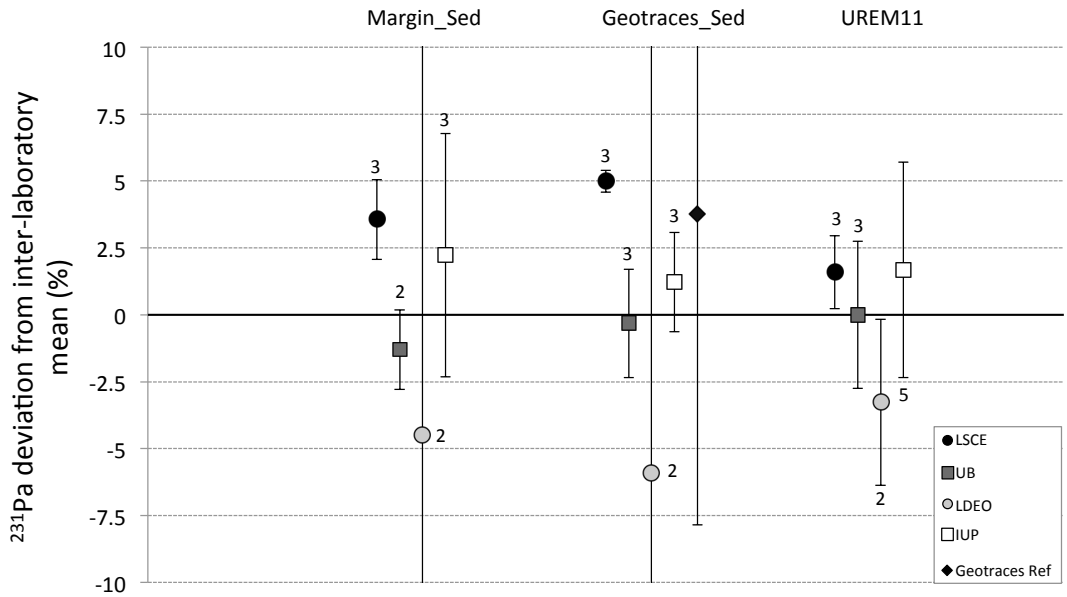

Figure 2.4.**3** : Comparison of the ^{231}Pa concentrations in sediment and UREM11. Results are expressed by the deviation (%)of the concentrations measured by each laboratory from the mean of the 4 laboratories. The deviation of the GEOTRACES intercalibration value from the mean is also given for Geotraces_Sed [23]. Note that the GEOTRACES intercalibration value was not used to compute the mean isotopic concentrations. Error bars are calculated as in Figure 2 and converted in % from the inter-laboratory mean. The number of replicates used to calculate the averages is written next to the error bars.

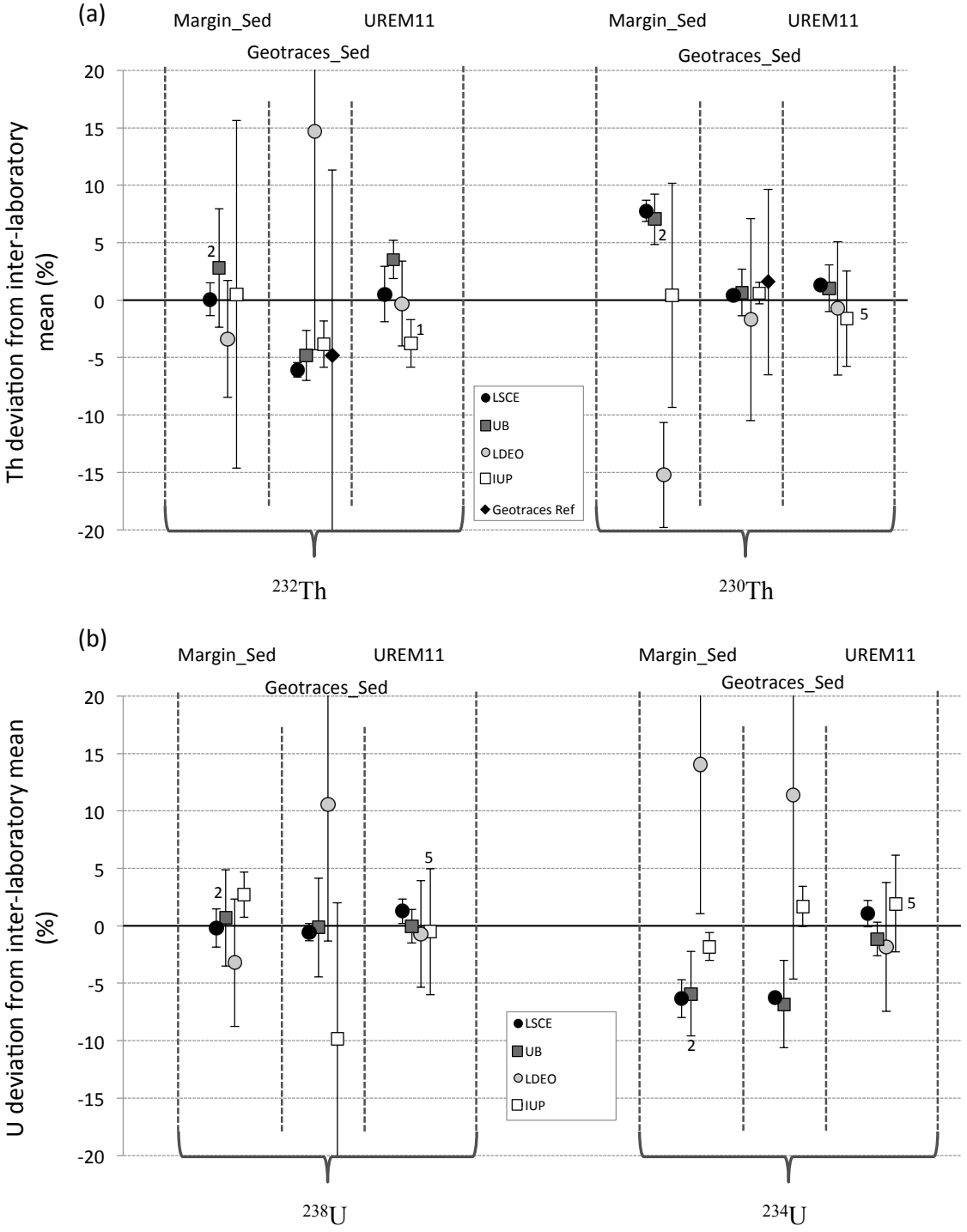

Figure 2.4.**4** : Comparison of the (a) thorium and (b) uranium concentrations in sediment and UREM11. Results are expressed by the deviation (%) of the concentrations measured by each laboratory from the mean of the 4 laboratories. In (a), the deviation of the GEOTRACES intercalibration value from the mean is also given for Geotraces_Sed [23]. Note that the GEOTRACES intercalibration value was not used to compute the mean thorium isotopic concentrations. Error bars are calculated as in Figure 2 and converted in % from the inter-laboratory mean. Mean concentrations for each lab were calculated using three full replicates unless written otherwise on the figure.

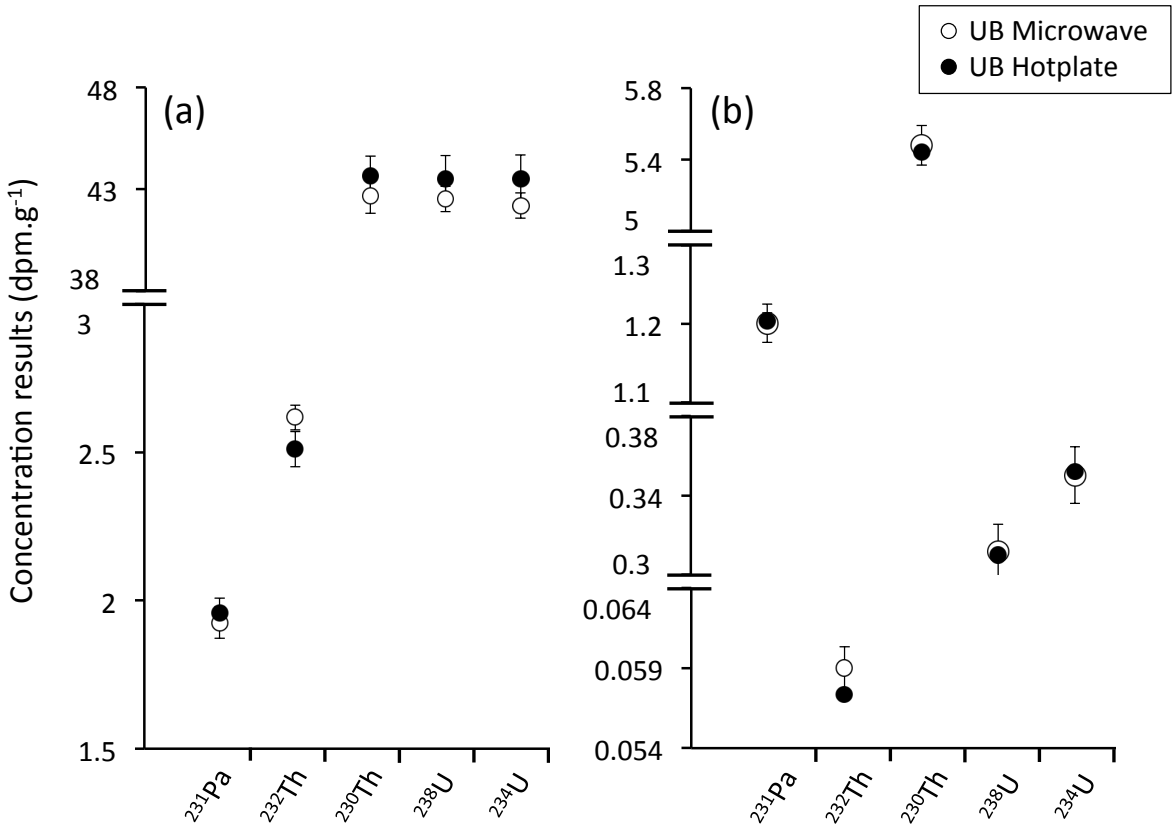

Figure 2.4.**5** : Isotopic concentrations obtained at UB after digestion by microwave (white circles) or hotplate (black circles) on (a) UREM11, (b) Geotraces_Sed. Error bars are calculated as in Figure 2 for microwave measurements. Error bars are 2SE for hotplate measurements (1 replicate only). Error bars on hotplate measurements on the Geotraces_Sed sample are small and cannot be distinguished from the data points.

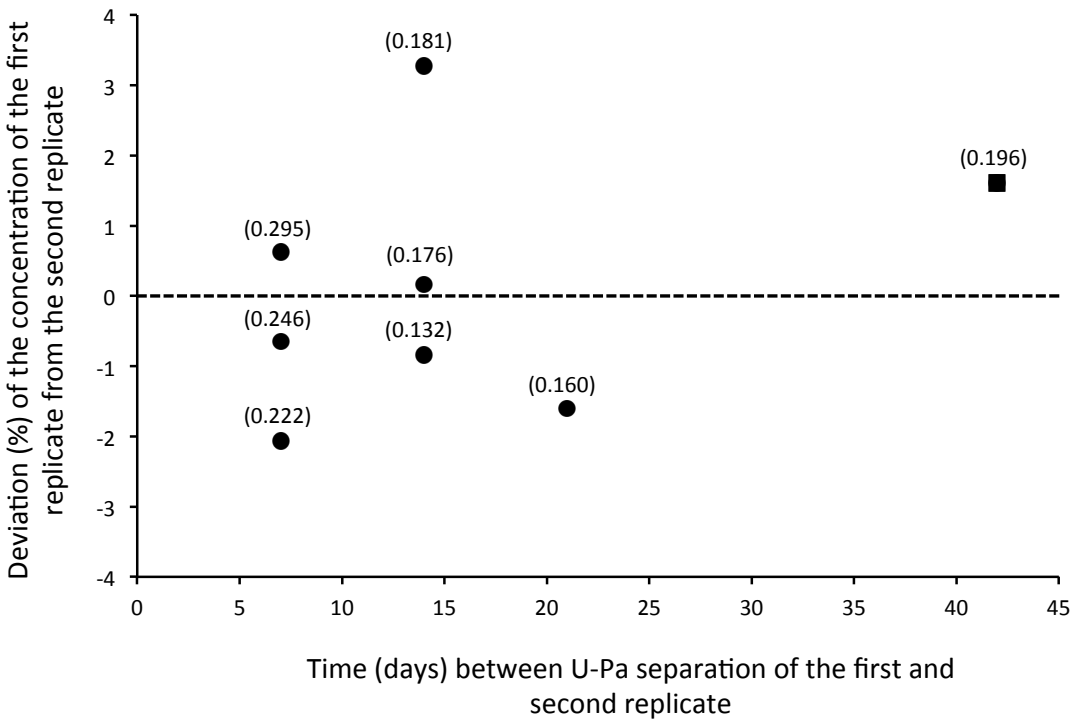

Figure 2.4.**6** : Concentration deviations of one replicate from the other as a function of additional time left for ^{233}Pa to decay in the second replicate (see text). Replicates represented by the square are not full chemistry replicates, but a single Pa fraction that was measured at different times after U-Pa separation (10 and 52 days). Replicates represented by the circles are full chemistry replicates. Numbers indicate the average concentrations of the replicates (dpm.g^{-1}). See table S3 for uncertainties on ^{231}Pa measurements.

Tables

Table 2.4.**1** : Sediment and spike masses, and digestion steps used by each laboratory. * H and MW stand for hotplate and microwave respectively. ** White smoke production indicates that only perchloric acid is left in solution.

Lab	Sediment/Spike addition	Step n°	Acid addition	Temperature /Pressure	Opened/Closed beakers *	Duration
LSCE	Sed. Mass: 0.1-0.2 g Before digestion: 233Pa: 0.3 pg 229Th: 14 pg 236U: 9 pg	1	2ml HNO3 + 5ml HF	140°C	H + closed	12h
		2	None (evaporation)	140°C	H + opened	Until half volume
		3	2ml HClO4 + 1ml HNO3	160°C	H + opened	Until white smoke production **
		4	Several 500µl HNO3 rinces	180°C	H + opened	Until clear solution and clean beaker's sides
UB	Sed. Mass: 0.1 g After digestion: 233Pa: 0.2 pg 229Th: 50 pg 236U: 1500 pg	Hotplate digestion				
		1	7ml HNO3 + 3ml HF + 2ml HClO4	180°C	H + closed	7-10h
		2	None (evaporation)	180°C	H + opened	Until ca 1ml left
		3	2ml HNO3 + 1ml HF	180°C	H + opened	Until complete evaporation
		Microwave digestion				
		1	6ml HNO3 + 2.5ml HCl + 3ml HF	200°C/6MPa	MW + closed	2.5h
		2	None (evaporation)	150°C	H + opened	Until ca 1ml left
		3	1ml HClO4 + 1ml HF	170°C	H + opened	Until complete evaporation
LDEO	Sed. Mass: 0.2-0.3 g Before digestion: 233Pa: ? pg 229Th: ? pg 236U: ? Pg	1	2ml HNO3	180°C	H + opened	2h
		2	3ml HClO4	250°C	H + opened	Until white smoke production **
		3	1ml HF	150°C	H + opened	20h
IUP	Sed. Mass: 0.1-0.2 g Before digestion: 233Pa: 0.8 pg 229Th: 20 pg 236U: 1500 pg	1	3ml HNO3 + 2.5ml HF	120-160°C	MW + closed	Until complete digestion
		2	None	120-160°C	MW + opened	Until complete evaporation
		3	2-3 drop H3BO3, 2-3 drop H2O2, 5*6ml HNO3	215-220°C	H + opened	Until evaporation of each 6ml

Table 2.4.**2** : Total chemistry yields and separation efficiencies for each of the laboratories. Max means that elements (U-Th) separated from the Pa fraction fall below procedural blanks. Separation efficiency of A from Pa fraction equals the A/Pa ratio in the sediment divided by the A/Pa ratio in the Pa fraction (where A is either U or Th). The yield calculated by the LSCE is a rough estimate based on element dilution (acid volume) and signal during mass spectrometry analysis, and on mass-spectrometer sensitivity.

	Chemistry yield			Separation efficiencies	
Lab	Pa	Th	U	U from Pa fraction	Th from Pa fraction
LSCE	40-80 %	70-90 %	50-70 %	1000	500-2500
UB	90-98 %	91-99 %	95-99 %	max	max
LDEO	40-80 %	50-80 %	60-90 %	76	max
IUP	10-50 %	70-90%	70-90 %	8000	2000

Table 2.4.**3** : Mass-spectrometer correction intensities, sensitivity and introduction systems. AS = Abundance sensitivity.

Lab	Th hydrides	U hydrides	AS 1 mass	Sensitivity (10^6 cps/ppb)	Introduction system
LSCE	20 ppm	10 ppm	1-2 ppm	ca 31.25	Apex-HF
UB	4 ppm	negligible	4 ppm	ca 18.75	Aridus I desolvating nebulizer.
LDEO	0.1 ppm	1400 ppm	11 ppm	2.5	Aridus desolvating nebulizer.
IUP	?	?	270 ppm	0.75-5	Apex-HF

Table 2.4.**4** : Comparison of concentration results on Geotraces_Sed with the GEOTRACES intercalibration. Results given in the table are averages of the four laboratories participating in the study, apart from the second values of ^{238}U and ^{234}U concentrations, which are averages of MC-ICP-MS concentrations only.

	231Pa (dpm.g-1)	±2D	230Th (dpm.g-1)	±2D	232Th (dpm.g-1)	±2D	238U (dpm.g-1)	±2D	234U (dpm.g-1)	±2D
This study	1.20	0.12	5.44	0.12	0.062	0.012	0.312	0.052	0.376	0.064
							0.311	0.007	0.351	0.007
GEOTRACES	1.25	0.14	5.53	0.44	0.059	0.010	/		/	

Table 2.4.**5** : Best chemistry methods with respect to efficacy, rapidity, and acid volume used.

Method	Efficacy	Rapidity	Acid volume
Digestion	All	UB/IUP	LDEO
U-Th-Pa separation	UB	IUP	LSCE

2.4.2 Supporting Information

The supporting information provides additional figures and tables, which further illustrate the main text. Details concerning the age of the sediment samples and the mathematical validity of the method for the estimation of ^{231}Pa concentrations are also provided.

Supporting information

Methodological recommendations for the analysis of sedimentary Pa/Th.

P. Burckel, G. Henry, H-C Ng, J. Lippold, S. Pichat, M. Roy Barman, F. Thil, J. Gherardi, C. Waelbroeck, J.F. McManus, L.F. Robinson, B. Antz

1-Sediment age

The age of Geotraces_Sed is unknown. Because excess protactinium and thorium need to be decay corrected back to their concentration at the time of sediment deposition for the calculation of the Pa/Th ratio and because Geotraces_Sed is a near surface sediment, it was ascribed an age of 500 ± 500 y. Although the age is somewhat arbitrary, it allows Pa/Th ratio comparison. Margin_Sed was recovered at 72cm from core MD09-3256Q (03.55°S/35.39°W, 3537 m water depth) on the Brazilian margin. Its age of 25040 ± 124 (1 SD) y is derived from the linear interpolation of ^{14}C ages determined at 70 and 74 cm (26189 ± 119 (1 SD) y and 23890 ± 128 (1 SD) y respectively) and converted to calendar age using the Marine13 calibration curve. Because of the age inversion (deepest level being younger than the shallowest), Margin_Sed might have been deposited by a turbidite.

2-Estimation of the sedimentary ^{231}Pa concentration

To circumvent the problem of the ^{233}Pa decay in the measurement of sedimentary ^{231}Pa concentrations, one ^{233}Pa spiked ^{231}Pa standard must be U-Pa separated and measured at the same time as the protactinium fraction of the sediment samples.
Consider a protactinium sample being measured on mass spectrometer and containing N_{233}Pa, and N_{233}U atoms of ^{233}Pa and ^{233}U respectively as well as N_{231} atoms of ^{231}Pa. This sample can be either a ^{233}Pa spiked ^{231}Pa standard solution (known ^{231}Pa and unknown ^{233}Pa) or dissolved sediment (unknown ^{231}Pa and ^{233}Pa). In both cases, the ^{233}Pa/^{231}Pa ratio R measured on mass spectrometer follows this equation:

$$R = \left(\frac{N_{231}}{N_{233}Pa + N_{233}U}\right)_{mass\ spec} = \frac{N_{231} * S_{Pa}}{N_{233}Pa * S_{Pa} + N_{233}U * S_U}$$

$$= \frac{N_{231} * S_{Pa}}{N_{233} * ((e^{-\lambda * t2}) * S_{Pa} + (1 - e^{-\lambda * t2}) * S_U)}$$

$$= \frac{N_{231}}{N_{233} * ((e^{-\lambda * t2}) + (1 - e^{-\lambda * t2}) * \alpha)}$$

$$= \frac{N_{231}}{N_{233} * A(t2, \alpha)} (1)$$

where N_{233} is the number of atoms of ^{233}(Pa + U), S_U and S_{Pa} are the mass spectrometer counts per atom (so that α is the ratio of ionization efficiencies of U and Pa) of uranium and protactinium respectively, λ the ^{233}Pa decay constant and t2 the time between column chromatography and analysis on mass spectrometer.

Because there should not be any Pa loss during digestion, and because column chemistry does not alter the ^{233}Pa/^{231}Pa ratio, equation (1) can be written:

$$R = \frac{N_{231}i}{N_{233}i * e^{-\lambda * t1} * A(t2, \alpha)}$$
$$= \frac{N_{231}i}{N_{233}i * B(t1, t2, \alpha)} (2)$$

where t1 is the time between spike creation and column chromatography, N_{231}i and N_{233}i the initial number of atoms of ^{231}Pa and ^{233}Pa respectively (i.e. atoms in the mass of sediment or ^{231}Pa standard and in the spike). The term B depends on the timing of the U-Pa separation with respect to spike production and mass spectrometer measurement (t1 and t2), as well as on the ionization efficiency ratio α. Sediments and spiked ^{231}Pa standards are separated and measured at the same time on mass spectrometer and therefore have identical B values.

We can then easily find the sample's ^{231}Pa concentrations. Consider first a standard solution (Std) with known N_{231}i(Std). From equation (2) we have:

$$R(Std) = \frac{N_{231}i(Std)}{N_{233}i(Std) * B(t1, t2, \alpha)}$$

$$= \frac{N_{231}i(Std)}{\mathrm{M_{Spike}(Std)} * [^{233}Pa]_i * \mathrm{B(t1, t2, \alpha)}}$$

$$[^{233}Pa]_i * \mathrm{B(t1, t2, \alpha)} = \frac{N_{231}i(Std)}{\mathrm{M_{Spike}(Std)} * R(Std)} \quad (3)$$

where $[^{233}\mathrm{Pa}]_i$ is the initial concentration of the ^{233}Pa spike (i.e. after spike production) and $\mathrm{M_{spike}(Std)}$ is the mass of ^{233}Pa spike in the standard solution.
Consider now a spiked sediment sample (Smp) with unknown $\mathrm{N_{231}i(Smp)}$ that was Pa purified by column chromatography at the same time as the spiked ^{231}Pa standard. From equation (2) and equation (3) we can eliminate the unknown $[^{233}\mathrm{Pa}]_i$ and B and write:

$$R(Smp) = \frac{N_{231}i(Smp)}{N_{233}i(Smp) * B(t1, t2, \alpha)} = \frac{N_{231}i(Smp)}{\mathrm{M_{Spike}(Smp)} * [^{233}Pa]_i * B(t1, t2, \alpha)}$$

$$= \frac{N_{231}i(Smp)}{\mathrm{M_{Spike}(Smp)}} * R(Std) * \frac{\mathrm{M_{Spike}(Std)}}{N_{231}i(Std)}$$

$$[^{231}Pa]_{sed} = \left(\frac{R(Smp) * \mathrm{M_{Spike}(Smp)} * N_{231}i(Std)}{R(Std) * \mathrm{M_{Spike}(Std)}} \right) \Big/ M_{sed} \quad (4)$$

where $[^{231}\mathrm{Pa}]_{sed}$ is the ^{231}Pa concentration of the sediment and $\mathrm{M_{sed}}$ the sediment's mass. R(Smp) is measured, $\mathrm{M_{Spike}(Smp)}$ and $\mathrm{M_{sed}}$ are known and the rest of the terms are known from the standard solution. We can therefore calculate the sediment's ^{231}Pa concentration.

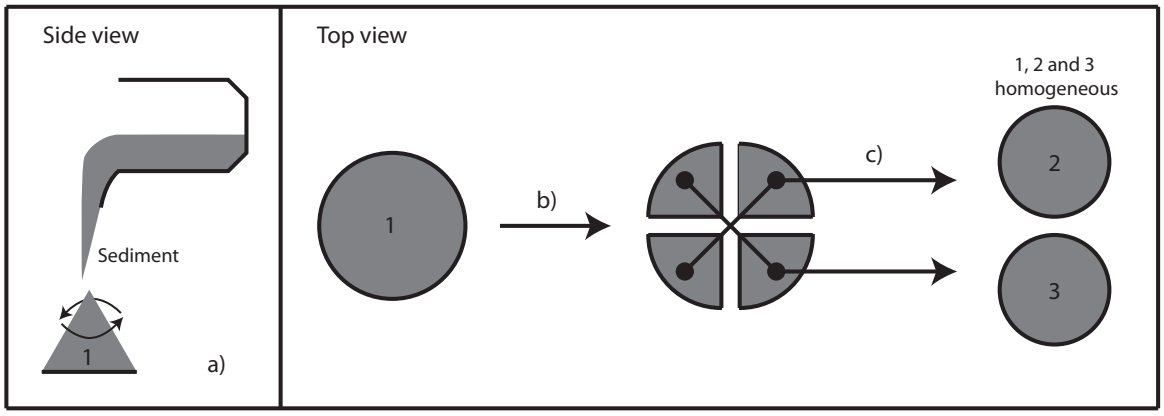

Figure 2.4.**S1** : Illustration of the coning and quartering method. First, a) the sediment is poured on drawing paper by applying a swirling movement to the wrist in order to form a dome then b) the dome is divided in four and c) the opposite quarters are gathered. The resulting sediment piles (2, 3) and the initial sediment (1) are expected to be homogeneous.

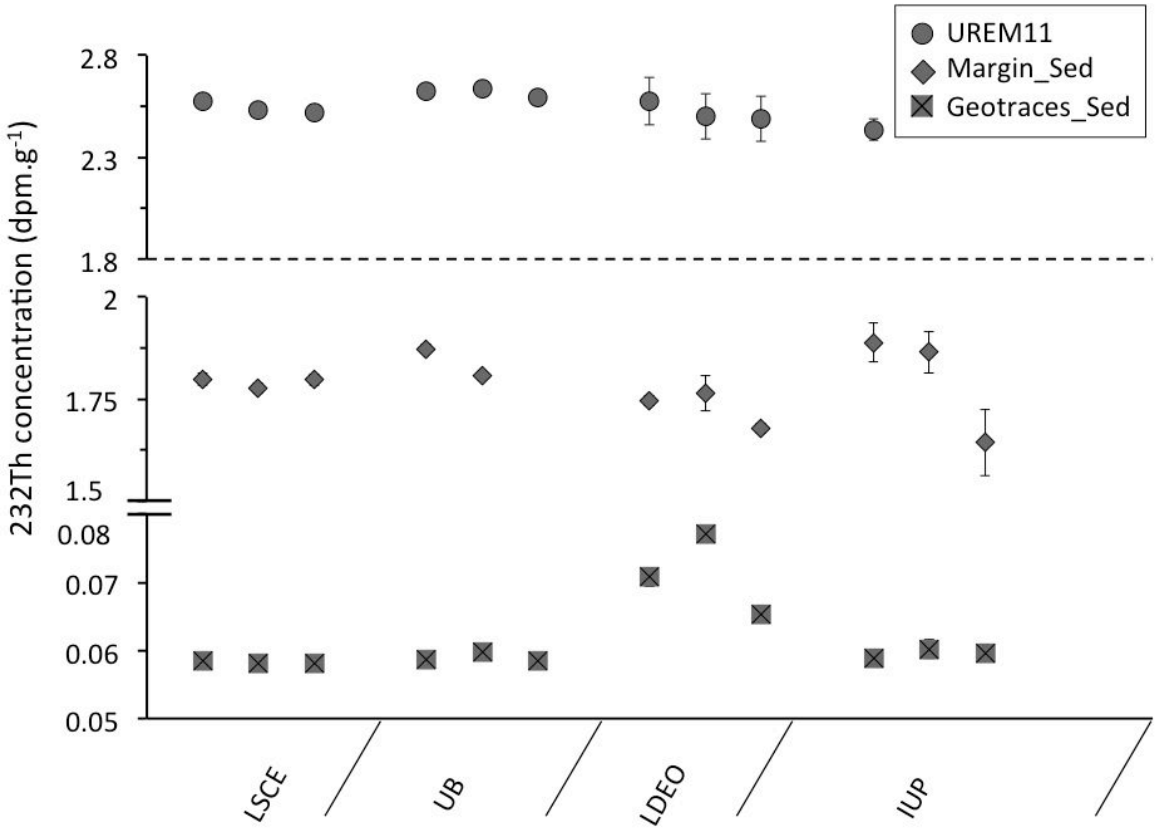

Figure 2.4.**S2** : Sediment and UREM11 ^{232}Th concentration results for each of the participating laboratories. Note that the y axis range for each sample is of around 25% of the sample's mean concentration. This allows to compare the inter and intra-laboratory concentration variability of the samples. Hence care should be taken when comparing absolute concentrations, as the y axis is often split and magnified for some samples. Circles represent the UREM11, squares the Geotraces_Sed and diamonds the Margin_Sed samples. Error bars are 2SE.

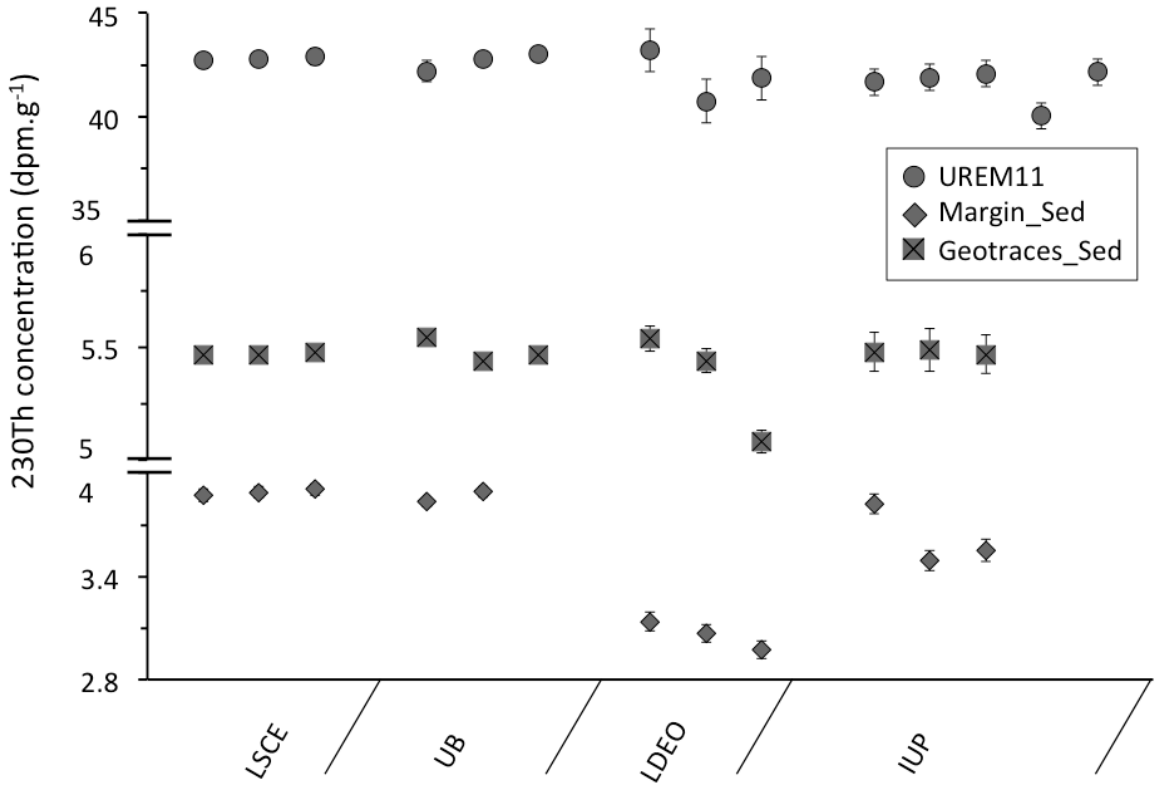

Figure 2.4.**S3** : Sediment and UREM11 ^{230}Th concentration results for each of the participating laboratories. Note that the y axis range for each sample is of around 25% of the sample's mean concentration. This allows to compare the inter and intra-laboratory concentration variability of the samples. Hence care should be taken when comparing absolute concentrations, as the y axis is often split and magnified for some samples. Circles represent the UREM11, squares the Geotraces_Sed and diamonds the Margin_Sed samples. Error bars are 2SE.

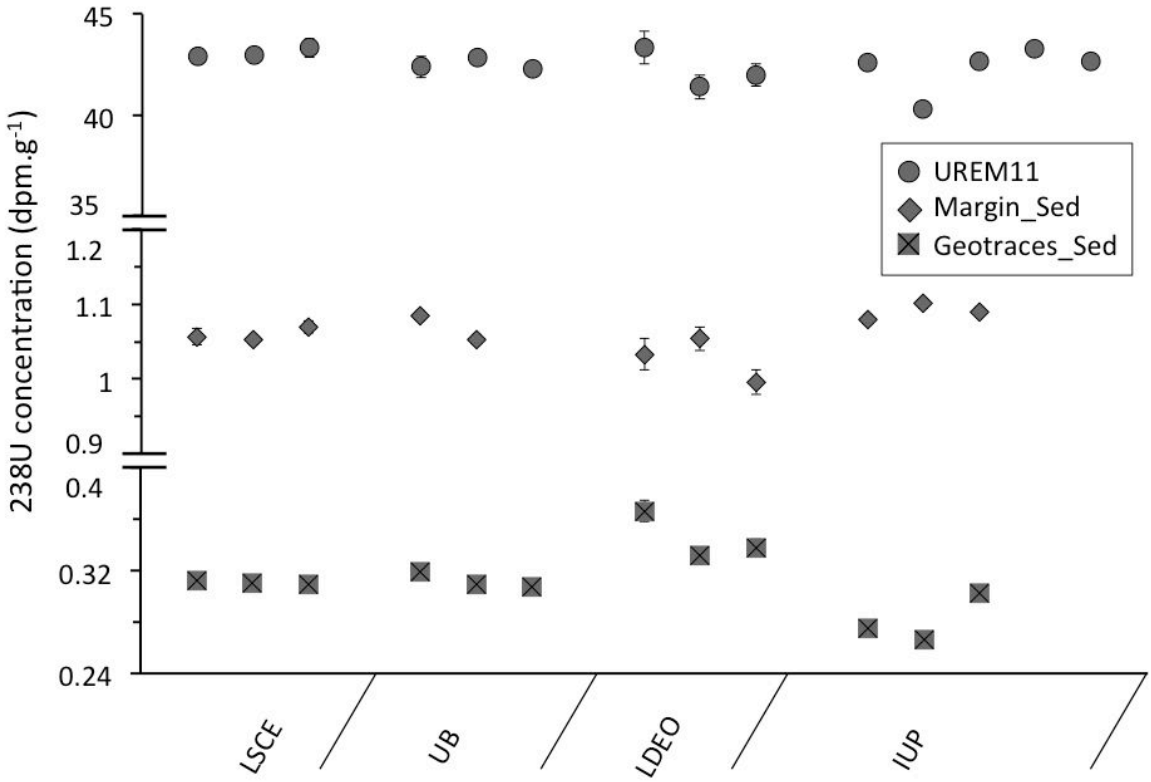

Figure 2.4.**S4** : Sediment and UREM11 ^{238}U concentration results for each of the participating laboratories. Note that the y axis range for each sample is of around 25% of the sample's mean concentration. This allows to compare the inter and intra-laboratory concentration variability of the samples. Hence care should be taken when comparing absolute concentrations, as the y axis is often split and magnified for some samples. Circles represent the UREM11, squares the Geotraces_Sed and diamonds the Margin_Sed samples. Error bars are 2SE.

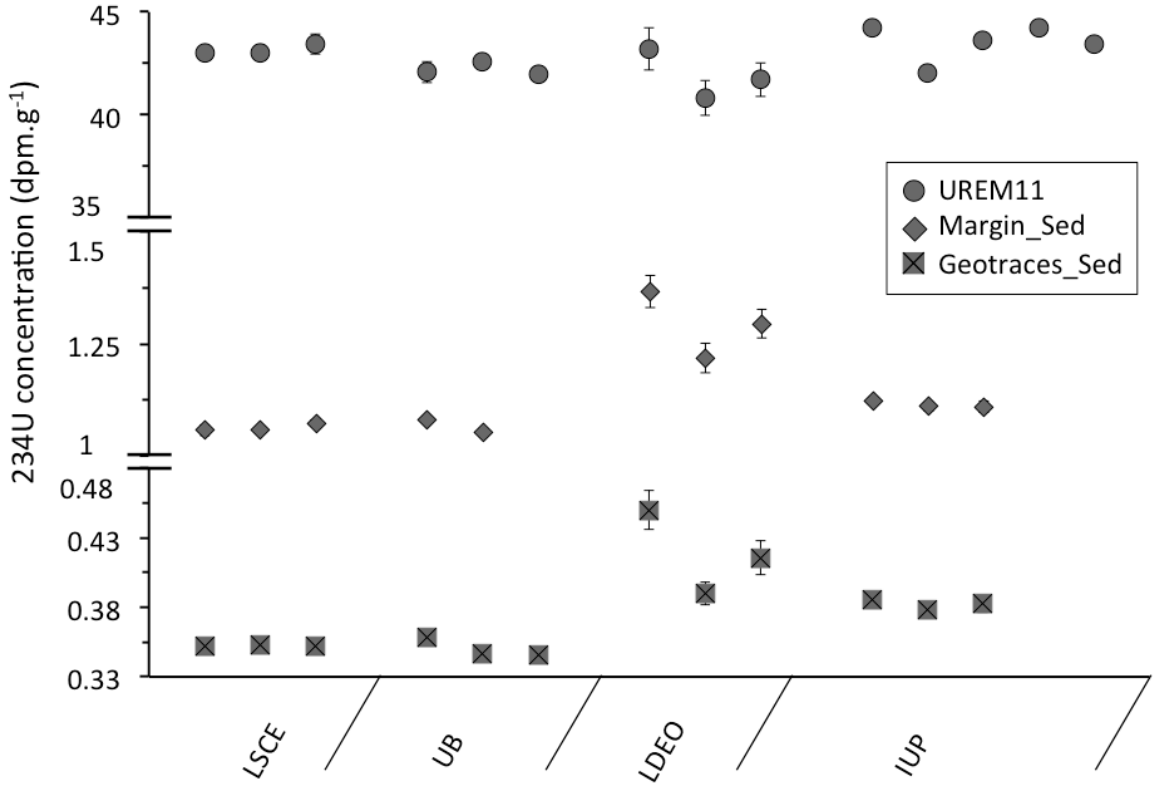

Figure 2.4.**S5** : Sediment and UREM11 ^{234}U concentration results for each of the participating laboratories. Note that the y axis range for each sample is of around 25% of the sample's mean concentration. This allows to compare the inter and intra-laboratory concentration variability of the samples. Hence care should be taken when comparing absolute concentrations, as the y axis is often split and magnified for some samples. Circles represent the UREM11, squares the Geotraces_Sed and diamonds the Margin_Sed samples. Error bars are 2SE.

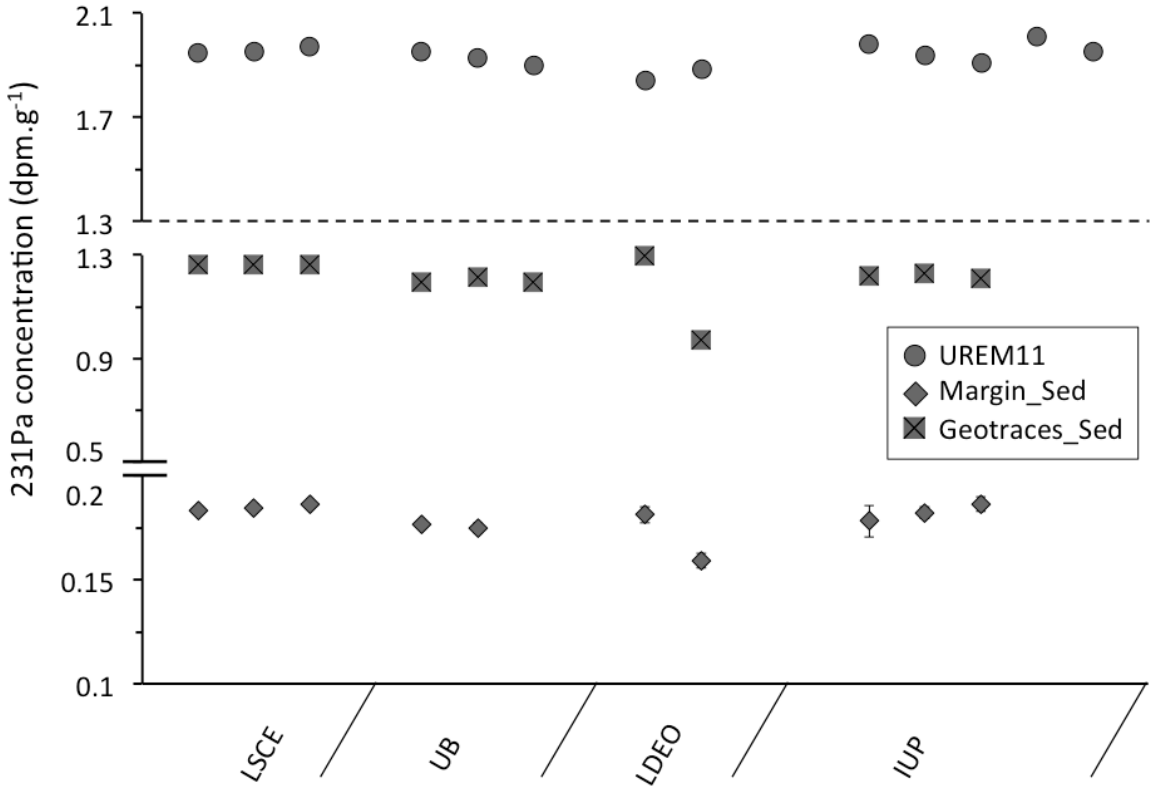

Figure 2.4.**S6** : Sediment and UREM11 ^{231}Pa concentration results for each of the participating laboratories. Note that the y axis range for each sample is of around 25% of the sample's mean concentration. This allows to compare the inter and intra-laboratory concentration variability of the samples. Hence care should be taken when comparing absolute concentrations, as the y axis is often split and magnified for some samples. Circles represent the UREM11, squares the Geotraces_Sed and diamonds the Margin_Sed samples. Error bars are 2SE.

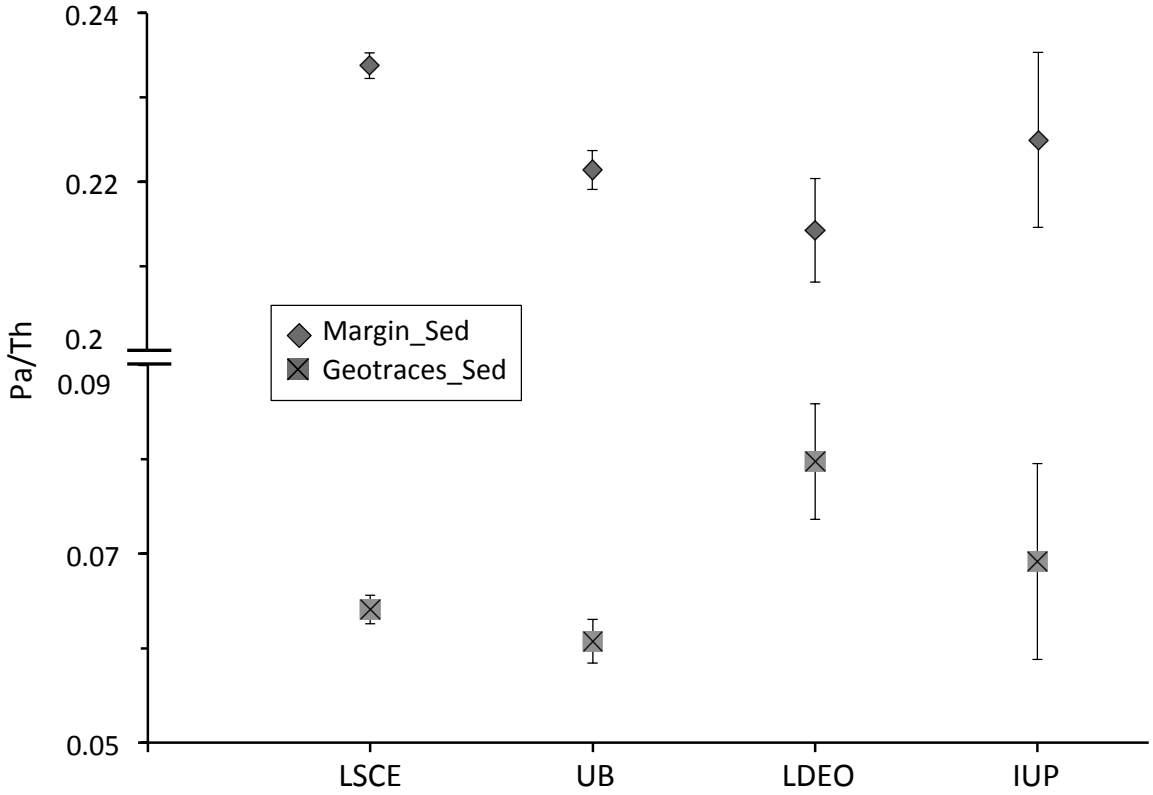

Figure 2.4.**S7** : Mean Pa/Th values obtained by each of the participating labs. Note that the y axis range for both samples is of around 25% of the sample's mean Pa/Th. This allows to compare the inter-laboratory Pa/Th variability of the samples. Hence care should be taken when comparing absolute Pa/Th values, as the y axis is split and magnified. Squares represent the Geotraces_Sed and diamonds the Margin_Sed samples. 2 sigma error is calculated based on the maximum between 2 SE and 2 SD of replicate concentration measurements and does not include the uncertainty on the R value (set to 0.5).

Table 2.4.**S1** : Isotopic ratio measurements ($\times 10^6$) on isotopic reference material NBS-SRM-960 and IRMM-035. 234U/238U measurements by the IUP were done on NBS-SRM-960 from two different bottles. The value given by Sim et al for the $^{230}Th/^{232}Th$ ratio of IRMM-035 is also displayed.

	NBS-SRM-960		IRMM-035	
Lab	234U/238U	± 2SE	230Th/232Th	± 2SE
Certified	52.841	0.082	11.481	0.078
Sims et al., 2008	/	/	11.38	0.096
LSCE	53.003	0.110	11.111	0.098
	53.029	0.101	11.266	0.087
	53.063	0.105	11.313	0.116
UB	52.805	0.142	11.203	0.105
	52.890	0.112	11.315	0.081
	52.797	0.147	11.336	0.063
LDEO	54.620	3.048	13.462	1.842
	56.393	3.159	13.351	2.470
			13.535	2.631
IUP	54.624	0.909	14.710	1.334
	52.977	0.886		

Table 2.4.**S2** : Isotopic concentration results of solid samples Margin_Sed, Geotraces_Sed and UREM11. Lines with a * for UB group measurements indicate that digestion was done using hotplate and not microwave.

		Margin_Sed				Geotraces_Sed				UREM11			
Lab	Isotope	Conc. (dpm/g)	± 2SE	Mean	± 2σ	Conc. (dpm/g)	± 2SE	Mean	± 2σ	Conc. (dpm/g)	± 2SE	Mean	± 2σ
LSCE	231Pa	0.183	0.002	0.185	0.003	1.26	0.01	1.265	0.005	1.95	0.01	1.956	0.026
		0.185	0.002			1.27	0.01			1.95	0.01		
		0.186	0.001			1.27	0.01			1.97	0.01		
	232Th	1.80	0.02	1.791	0.026	0.0584	0.0003	0.058	0.000	2.58	0.02	2.542	0.061
		1.78	0.01			0.0581	0.0003			2.53	0.02		
		1.80	0.01			0.0581	0.0003			2.52	0.02		
	230Th	3.87	0.04	3.889	0.034	5.46	0.03	5.467	0.018	42.7	0.3	42.802	0.195
		3.89	0.03			5.46	0.03			42.8	0.3		
		3.91	0.03			5.47	0.03			42.9	0.4		
	238U	1.056	0.011	1.059	0.018	0.312	0.002	0.311	0.002	42.9	0.3	43.066	0.451
		1.053	0.007			0.311	0.002			42.9	0.3		
		1.069	0.008			0.310	0.002			43.3	0.5		
	234U	1.057	0.012	1.062	0.019	0.352	0.003	0.352	0.002	43.0	0.3	43.150	0.486
		1.057	0.007			0.353	0.003			43.0	0.3		
		1.073	0.008			0.352	0.003			43.4	0.5		
UB	231Pa	0.177	0.002	0.176	0.003	1.19	0.01	1.201	0.024	1.95	0.03	1.925	0.053
		0.175	0.002			1.21	0.01			1.93	0.01		
						1.19	0.02			1.90	0.02		
	*					1.20	0.01	/	/	1.96	0.05	/	/
	232Th	1.87	0.01	1.840	0.092	0.0587	0.0003	0.059	0.001	2.62	0.03	2.618	0.042
		1.81	0.01			0.0598	0.0003			2.64	0.02		
						0.0585	0.0003			2.59	0.01		
	*					0.0573	0.0003	/	/	2.51	0.06	/	/
	230Th	3.83	0.03	3.862	0.080	5.54	0.03	5.480	0.111	42.2	0.5	42.678	0.858
		3.89	0.03			5.44	0.03			42.8	0.3		
						5.46	0.03			43.1	0.3		
	*					5.45	0.03	/	/	43.7	1.0	/	/
	238U	1.084	0.006	1.069	0.044	0.320	0.002	0.312	0.013	42.4	0.5	42.515	0.624
		1.053	0.005			0.309	0.002			42.9	0.3		
						0.307	0.002			42.3	0.3		
	*					0.310	0.002	/	/	43.5	1.1	/	/
	234U	1.082	0.007	1.067	0.042	0.358	0.002	0.350	0.014	42.1	0.5	42.207	0.623
		1.052	0.007			0.347	0.002			42.6	0.3		
						0.345	0.002			42.0	0.3		
	*					0.352	0.003	/	/	43.5	1.2	/	/
LDEO	231Pa	0.181	0.004	0.170	0.031	1.297	0.02	1.134	0.462	1.841	0.02	1.862	0.060
		0.159	0.004			0.970	0.01			1.883	0.01		
	232Th	1.75	0.01	1.730	0.091	0.0708	0.0014	0.071	0.012	2.57	0.12	2.521	0.093
		1.76	0.04			0.0771	0.0006			2.50	0.11		
		1.68	0.01			0.0653	0.0013			2.49	0.11		
	230Th	3.14	0.05	3.059	0.165	5.54	0.05	5.351	0.479	43.2	1.0	41.939	2.451
		3.07	0.05			5.44	0.05			40.8	1.0		
		2.97	0.05			5.08	0.05			41.9	1.0		
	238U	1.03	0.02	1.027	0.059	0.37	0.01	0.345	0.037	43.3	0.8	42.227	1.975
		1.05	0.02			0.33	0.01			41.4	0.6		
		1.00	0.02			0.34	0.01			42.0	0.5		
	234U	1.367	0.035	1.294	0.148	0.450	0.014	0.419	0.060	43.2	1.0	41.913	2.394
		1.219	0.033			0.390	0.008			40.8	0.9		
		1.295	0.032			0.416	0.012			41.7	0.8		

Table 2.4.**S2**: Continued.

		Margin_Sed				Geotraces_Sed				UREM11			
Lab	Isotope	Conc. (dpm/g)	± 2SE	Mean	± 2σ	Conc. (dpm/g)	± 2SE	Mean	± 2σ	Conc. (dpm/g)	± 2SE	Mean	± 2σ
IUP	231Pa	0.178	0.008	0.182	0.008	1.22	0.01	1.219	0.022	1.98	0.02	1.958	0.077
		0.182	0.003			1.23	0.01			1.94	0.02		
		0.186	0.003			1.21	0.01			1.91	0.01		
										2.01	0.01		
										1.95	0.01		
	232Th	1.89	0.048	1.799	0.271	0.0589	0.0012	0.060	0.001	2.43	0.05	/	/
		1.86	0.050			0.0602	0.0014						
		1.64	0.081			0.0597	0.0012						
	230Th	3.82	0.06	3.623	0.352	5.48	0.09	5.478	0.051	41.7	0.7	41.566	1.753
		3.49	0.06			5.49	0.10			41.9	0.6		
		3.55	0.07			5.47	0.08			42.1	0.6		
										40.0	0.6		
										42.2	0.6		
	238U	1.080	0.006	1.090	0.021	0.276	0.002	0.282	0.037	42.6	0.2	42.310	2.334
		1.101	0.006			0.267	0.002			40.3	0.2		
		1.090	0.006			0.302	0.002			42.7	0.2		
										43.3	0.2		
										42.7	0.2		
	234U	1.122	0.008	1.114	0.014	0.385	0.004	0.382	0.007	44.3	0.2	43.529	1.803
		1.110	0.010			0.379	0.003			42.1	0.2		
		1.109	0.012			0.382	0.006			43.6	0.3		
										44.3	0.2		
										43.4	0.3		

Table 2.4.**S3** : ^{231}Pa concentration of replicate samples (e.g. 1 a and 1 b) measured at different times t between U-Pa separation and mass spectrometer analysis. Sample 8 a and 8 b are not full sediment replicates, but a single ^{231}Pa/^{233}(Pa+U) solution measured at different times after U-Pa separation.

Sample n°	231Pa (dpm.g-1)	± 2 sigma	t (days)
1 a	0.296	0.002	6
1 b	0.294	0.003	13
2 a	0.220	0.002	6
2 b	0.225	0.003	13
3 a	0.245	0.002	6
3 b	0.247	0.002	13
4 a	0.184	0.001	6
4 b	0.178	0.002	20
5 a	0.132	0.001	6
5 b	0.133	0.002	20
6 a	0.176	0.002	6
6 b	0.176	0.001	20
7 a	0.159	0.002	6
7 b	0.162	0.002	27
8 a	0.197	0.001	10
8 b	0.194	0.001	52

Table 2.4.**S4** : Mean Pa/Th results for each of the labs. 2 sigma error is calculated based on the maximum between 2 SE and 2 SD of replicate concentration measurements and does not include the uncertainty on the R value (set to 0.5).

	Margin_Sed		Geotraces_Sed	
	Pa/Th	2 sigma	Pa/Th	2 sigma
LSCE	0.064	0.002	0.234	0.003
UB	0.061	0.002	0.221	0.007
LDEO	0.080	0.006	0.214	0.019
IUP	0.069	0.010	0.225	0.005

Table 2.4.**S5** : Acid volumes used by each lab for digestion and elution by column chromatography. Only acids more concentrated than 2N are considered.

	Lab	HNO3 (ml)	HCl (ml)	HF (ml)	HClO4 (ml)	HCl + HF (ml)	Total (ml)
Digestion	LSCE	5	0	5	2	0	12
	UB	6	2.5	4	1	0	13.5
	LDEO	2	0	1	3	0	6
	IUP	33	0	2.5	0	0	35.5
U-Th-Pa separation	LSCE	41	45	0	0	12	98
	UB	36	60	0	0	24	120
	LDEO	5	82	0	0	71	158
	IUP	30	60	0	0	24	114

Chapter 3 : Timing of Oceanic circulation changes in the Atlantic during the last glacial

3.1 Introduction

As discussed in chapter I, climate models are able to simulate a southward shift of the ITCZ, either in response to a slowdown of the AMOC (Kageyama et al., 2009), or through the increased extent of sea ice or ice sheets (Chiang and Bitz, 2005) that generate a cold SST anomaly in the northern tropics, shifting the tropical rain belt to the south. However, it remains unclear which of these processes triggered the southward ITCZ shifts associated with Greenland stadials of the last glacial.

Southward shifts of the ITCZ are associated with increased precipitation in northern South America, and are therefore recorded as Ti/Ca peaks in marine sediments of the Brazilian margin (Jaeschke et al., 2007). As deep western boundary currents also affect our sediment cores, I directly compare oceanic circulation and ventilation proxies to the precipitation signal measured in core MD09-3257 (~2300 m depth), to precisely assess the phase relationship between AMOC variations and ITCZ shifts. A large Pa/Th increase occurs before the onset of the precipitation events associated with Heinrich Stadial 2 and Heinrich Stadial 4. In order to assess the timing of the AMOC slowdown with respect to the ITCZ shift, I build a robust age model based on correlation of the Ti/Ca signal of our core with another nearby ^{14}C dated core, and with a U-Th dated South American speleothem that recorded periods of increased precipitation as decreases in the $\delta^{18}O$ record. As seen in Chapter 2, the Pa/Th data I produced are very precise and can therefore be used to reliably determine the start of the AMOC slowdown, and as sharp Ti/Ca peaks mark periods of increased precipitation, I precisely determine the lead of the AMOC slowdown in terms of core length for HS2 and HS4. Converting the lead expressed as a length in the core into a lead expressed as a time interval, I find that the decreased AMOC intensity preceded the precipitation events by 1420 ± 250 (1σ) y and 690 ± 180 (1σ) y for HS2 and HS4 respectively. Results are presented in the article entitled "Atlantic Ocean circulation changes preceded millennial tropical South America rainfall events during the last glacial".

In the last section of this chapter, I provide another potential explanation for the Pa/Th rise occurring prior to precipitation events, which does not affect the conclusions of the article. I also discuss a recent study (Lynch-Stieglitz et al., 2014) that concluded that the upper circulation cell of the AMOC did not slowdown during Heinrich Stadial 2 and 3, in contradiction with my results.

3.2 Atlantic Ocean circulation changes preceded millennial tropical South America rainfall events during the last glacial

This article has been submitted to Nature Geoscience and Proceedings of the National Academy of Sciences. Unfortunately, with 1/3 and 1/2 positive reviews, the article was not accepted. The format will be changed and the article submitted to Geophysical Research Letters before the defense.

Atlantic Ocean circulation changes preceded millennial tropical South America rainfall events during the last glacial

Pierre Burckel[a*], Claire Waelbroeck[a], Jeanne Marie Gherardi[a], Sylvain Pichat[b], Helge Arz[c], Joerg Lippold[d], Trond Dokken[e], and François Thil[a]

[a]LSCE/IPSL, Laboratoire CNRS-CEA-UVSQ, Bât.12, avenue de la Terrasse, F-91198 Gif sur Yvette, France
[b]Laboratoire de Géologie de Lyon (LGL-TPE), Ecole Normale Supérieure de Lyon, 46 allée d'Italie, 69007 Lyon, France
[c]Leibniz-Institute for Baltic Sea Research, Seestrasse 15, D-18119 Rostock, Germany
[d]Oeschger Centre for Climate Change Research, Institute of Geological Sciences, University of Bern, Zähringerstrasse 25, CH-3012, Bern, Switzerland
[e]Bjerknes Centre for Climate Research, Department of Earth Sciences, University of Bergen, Allégt. 55, N-5007 Bergen

*Corresponding author: pierre.burckel@lsce.ipsl.fr +33 (0)1.69.82.43.47
Keywords : Heinrich, Dansgaard-Oeschger, MIS3, AMOC, ITCZ, Pa/Th

Abstract

During the last glacial period, Greenland's climate experienced millennial-scale shifts between cold (stadial) and warm (interstadial) phases that were accompanied by ocean circulation changes characterized by reduced Atlantic Meridional Overturning Circulation during stadials. Here, we present new $^{231}Pa/^{230}Th$ data from a deep-sea sediment core retrieved off North-East Brazil demonstrating that slowdowns of the Atlantic Meridional Overturning Circulation preceded the large southward shifts of the intertropical convergence zone that took place during last glacial stadial periods. We reliably determine that the Atlantic Meridional Overturning Circulation started to slowdown 1420 ± 250 (1σ) y and 690 ± 180 (1σ) y before the onset of two large precipitation events, associated with Heinrich stadials, recorded in South America. Our results thus bring unprecedented evidence that Atlantic Meridional Overturning Circulation changes could be the origin of the observed precipitation events. In addition, we propose a new mechanism that explains the differences in the extent and timing of Atlantic Meridional Overturning Circulation slowdowns associated with shorter and longer stadial periods.

Introduction

Both paleoproxy records and numerical modeling indicate that the tropical and northern North Atlantic regions are tightly linked on centennial to millennial timescales. Sediment records from the Cariaco Basin show that tropical Atlantic Ocean and atmosphere changes correlate with variations in the North Atlantic region since the last glacial period (1-4). Some modeling studies have suggested that these regions may be connected via a coupled atmosphere-surface ocean mechanism (5, 6), whereas other numerical simulations using fully coupled atmosphere-ocean models have indicated that a reduction in the Atlantic Meridional Overturning Circulation (AMOC) flow rate could induce a southward displacement of the Intertropical Convergence Zone (ITCZ) (7-9).

The western side of the tropical Atlantic is a key region to study the mechanisms behind millennial-scale tropical atmospheric changes. Indeed, during the last glacial, millennial variability in precipitation over tropical South America is recorded in various archives such as marine or lake sediments and speleothems (4, 10-17). Precipitation changes are interpreted as latitudinal shifts of the ITCZ, and appear to covary over South America in the 0-30°S latitude band east of the Andes. Moreover, the western side of the tropical Atlantic is the locus of the western boundary currents and is therefore ideal to monitor changes in the AMOC flow rate (18). Cores MD09-3257 (04°14.69'S, 36°21.18'W, 2344m water depth) and GeoB3910 (04°14.7'S, 36°20.7'W, 2362m water depth) were retrieved from approximately the same location and depth on the North Eastern Brazilian margin (Fig. 1). At present, the cores site is bathed by the upper limb of the North Atlantic Deep Water, originating from the North Atlantic Ocean and circulating between 1200 and 2500m depth, with a maximum circulation intensity of ca. 11 Sv at ~1500m (19). Numerous studies indicate that northern-sourced deep water flowed at shallower depth during the last glacial compared to modern times (20-22). Hence, the location of the sediment cores studied here is ideal to monitor past changes in the AMOC upper circulation cell, as well as their relation to millennial-scale precipitation events that are associated with the shifts in the ITCZ position.

Under modern conditions, the Brazilian northeastern region, called Nordeste (Fig. 1), is a semi-arid region where precipitation is controlled by the position of the ITCZ. Periods of high precipitation (March-April) in the Nordeste occur when the ITCZ is at its southernmost position and the interhemispheric sea surface temperatures (SST) gradient is the weakest (23). During boreal summer, the SST gradient steepens and the ITCZ moves northward, following the position of maximum SST above which convection occurs.

During the last glacial, millennial-scale variability in precipitation led to periods of increased rainfall in the Nordeste. Increased precipitation is marked by a decrease in $\delta^{18}O$ in South American speleothems (10, 11, 14, 24-26) and increased sedimentary Ti/Ca ratios in a marine sediment core off the northeastern Brazilian coast (12) (SI Appendix section A, and Figs. S1-S2).

Precipitation events recorded in South American speleothems can be considered synchronous within age uncertainties (SI Appendix section B, and Figs. S3-S4). These precipitation events were shown to take place during cold stadial periods recorded in Greenland ice cores (10, 11, 14, 25-28). In what follows, we call Heinrich stadials the six stadials characterized by the occurrence of Heinrich events, i.e. thick layers of ice rafted detritus in mid- to high-latitude North Atlantic sediments, indicative of massive iceberg surges. We define PE0 as the precipitation event occurring during the Younger Dryas, and PE1 to PE5, those occurring during Heinrich stadials 1 to 5, respectively (SI Appendix Fig. S3).

Results

Using ^{14}C dating, we could verify that precipitation events in marine cores are synchronous with precipitation events in speleothems for the 10-38 cal. ky BP (ka hereafter) period (Fig. 2 and Methods). This led us to synchronize to speleothems $\delta^{18}O$ records the two high Ti/Ca events, PE4 and 5, which occur during the 38-50 ka period, i.e. beyond the range of precise ^{14}C dating. Doing so, we observe that all the small precipitation events seen in marine sediments between 38 and 50 ka are synchronous with those seen in speleothems, which further confirms the synchronism between precipitation events recorded in marine sediments and speleothems. Importantly, the resulting marine cores age scales are entirely radiometric and based on regional correlations, and hence completely independent from the Greenland ice core chronology.

Comparing the Ti/Ca marine records with Greenland air temperature record on their respective independent calendar age scales, we observe that periods of increased precipitation over our study area take place during cold periods over Greenland (Fig. 3a, d). This is the case for both large precipitation events PE2 to PE5 and smaller ones (Ti/Ca <0.2) associated with the stadials preceding Dansgaard Oeschger (DO) 5, 6, 7, 10 and 11. The only exception is the small precipitation event following PE3 in our sediment core that appears to coincide with the DO4 interstadial. However, the timing of this precipitation event can be reconciled with that of the stadial preceding DO3 within age model uncertainties. Some studies have shown that millennial-scale precipitation events seen in marine sediment cores for the period covered by ^{14}C dating occurred

during Greenland stadials (e.g. ref. (12)). However, these studies then assumed that Greenland stadials and tropical precipitation events were also synchronous beyond 40 ka. Moreover, in some cases, tropical marine records were dated by assuming that the tropical climate and Greenland signals were synchronous over the entire last glacial (4, 29). Such dating methods preclude establishing the sequence of events and determining which component of the climate system has triggered the observed millennial climate variability. In contrast, by building a radiometric age scale for our low latitude marine records that is entirely independent from the Greenland ice core age scale, we are able to assess the respective timing of the different climatic and ocean circulation signals recorded in Greenland and South America 0-30°S latitudinal band.

Sedimentary $^{231}Pa/^{230}Th$ (Pa/Th hereafter) can be used to record changes in AMOC flow rate (22, 30-32) (Methods). In effect, at present, Pa/Th in the western tropical Atlantic is mainly controlled by oceanic circulation (33). While caveats may apply to this proxy in regions of high particle flux, we could verify that during the last glacial, the main drivers of the Pa/Th variability in our core remained the changes in oceanic circulation intensity (Methods). Pa/Th rises from approximately modern day values prior to precipitation events PE2 and PE4, to values close to that of the production ratio (0.093) at their onset (Fig. 3b). This indicates that the overlying water mass flow rate was strongly reduced at the onset of PE2 and PE4. Similarly, decreased flow rate accompanied the smaller precipitation events related to DO stadials, as illustrated by the increase in Pa/Th values during each DO related stadial, namely 6 and 7, for which we have the data. Moreover, increases in Pa/Th are synchronous with decreases in the $\delta^{13}C$ of the benthic foraminifer *Cibicides wuellerstorfi* (Fig. 3c) that can be interpreted as reflecting reduced bottom water ventilation (Methods). The concurrent decrease in benthic $\delta^{13}C$ and increase in Pa/Th ratio in our cores thus indicates longer bottom water residence times and lower ventilation at 2300 m depth on the north-east Brazilian margin during millennial precipitation events. Our marine records thus unambiguously indicate that major decreases in the flow rate of the AMOC upper circulation cell took place before the main and during the small millennial precipitation events.

Sedimentary Pa/Th starts rising before the Ti/Ca increase associated with PE4 and PE2 in core MD09-3257 (Fig. 3b, d, SI Appendix section C, and Fig. S9). Because Ti/Ca and Pa/Th values were measured in the same core, the leads are directly measurable in terms of core length: Pa/Th starts rising nearly 5 cm before the onset of PE4 and more than 9 cm before the onset of PE2. Converting these depths intervals into time intervals, the lead of the Pa/Th signal with respect to the Ti/Ca signal is estimated to be 690 ± 180 (1σ) y and 1,420 ± 250 (1σ) y at the onsets of PE4 and PE2, respectively. The AMOC slowdown therefore starts significantly earlier than the large precipitation events

observed in the 0-30°S latitudinal band in South America. While the sequence of events is straightforward for PE4 and PE2, the phasing between AMOC slowdowns and small precipitation events related to DO stadials is more difficult to assess. Indeed, the Pa/Th signal seems to rise before the start of the Ti/Ca peak for precipitation events associated with stadials preceding DO 7 and 6 (Fig. 3). However, if the AMOC slowdown indeed precedes small precipitation events, then the time lag between the beginning of the AMOC slowdown and of the precipitation event is much smaller than for precipitation events associated with Heinrich stadials (Fig. S9).

Discussion

Our data bring new constraints on the possible trigger mechanisms of the millennial precipitation events observed in the 0-30°S latitudinal band in South America during the last glacial. Our results demonstrate that precipitation events corresponding to Heinrich stadials over our study area occurred 500 to 1,700 y after a slowdown of the AMOC upper circulation cell. Thus, there could be a causal link between the AMOC slowdowns and ITCZ shifts, that is, the observed slowdowns could trigger the precipitation events.

Climate models indeed show that an AMOC slowdown causes a decrease in interhemispheric oceanic heat transport (see ref. (34) for a review), which results in negative SST anomalies in the Northern and positive SST anomalies in the Southern extratropics. The SST anomalies are then propagated equatorwards inducing a southward ITCZ shift (8). This mechanism could thus have led to the southward shift of the convection zone and explain the observed sequence of events (arrow 1a in Fig. 4).

However, other modeling studies produced southward ITCZ shifts in response to extended high-latitudes ice sheets or sea ice cover (5, 6), without any change in the AMOC. In these models, surface cooling in the North Atlantic and Nordic Seas induces the progression of low SST towards the ITCZ latitudes, leading to a southward displacement of the ITCZ after only a few years. Interestingly, the records in Fig. 3 do not support this mechanism as sole cause for the observed precipitation events since PE2 starts after the beginning of Heinrich stadial 2 cold periods above Greenland (arrow 1b in Fig. 4). Extended ice-sheet or sea-ice cover could however be responsible for the small precipitation events. These events indeed occur synchronously with short stadials between DO events and the associated Pa/Th signal, although indicating a strong AMOC slowdown, does not feature the same obvious lead with respect to the Ti/Ca signal as for the main precipitation events. Smaller increases in the Ti/Ca signal may reflect a more northerly final position of the ITCZ and different mechanisms could be at the origin of large and small precipitation events. The latter could reflect a small southward ITCZ shift resulting from northern tropics sea surface cooling in response to an extension of

sea-ice cover in the northern North Atlantic (6). However, as slowdowns of the AMOC upper circulation cell also accompany small precipitation events, the importance of the influence of Atlantic oceanic circulation cannot be ruled out.

The AMOC slowdowns recorded before PE4 and PE2 could result from reduced deep-water convection following freshwater input in the northern North Atlantic (arrow 2 in Fig. 4). Different origins of such a freshwater flux have been suggested: melting of ice sheets during active modes of the AMOC (36), melting of icebergs and ice shelves during Heinrich or precursory events (37, 38), and pulses of fresh water from a Hudson Bay lake (39).

In addition to the main mechanisms described above, an AMOC slowdown could have had an indirect effect on the position of the ITCZ. An AMOC slowdown could indeed impact Greenland climate through a decrease in northward heat transport (arrow 3a in Fig. 4) and thereby induce increased sea-ice cover and/or ice sheet extension which could, in turn, cause a southward shift of the ITCZ (arrow 1b in Fig. 4). However, our records indicate that changes in the AMOC intensity alone do not explain the NGRIP temperature record. Indeed, the D09 interstadial warm event occurred in NGRIP while the AMOC was slackening before PE4, indicating that in this case, Greenland temperatures increased although oceanic interhemispheric heat transport was decreasing. Furthermore, temperature above Greenland did not markedly decrease during the AMOC slowdown preceding PE2 (Fig. 3a, b). These observations indicate that there is no direct linear response of Greenland temperatures to AMOC changes. This is in line with modeling studies showing that feedbacks involving sea-ice extent have a large impact on Greenland temperatures (9, 40).

Finally, we suggest that a positive feedback loop played a key role and lies at the heart of the difference between DO and Heinrich stadials. Recent studies have suggested that an AMOC slowdown and decrease in deep-water formation could lead to warming of North Atlantic subsurface waters, and hence erosion of the ice shelves and destabilization of the Laurentide ice sheet (41, 42). This would result in iceberg surges in the North Atlantic (arrow 3b in Fig. 4) and further decrease deep-water formation and slowdown the AMOC. We suggest that the large lead of the AMOC slowdown with respect to the onset of PE2 and PE4 results from the action of this positive feedback on the AMOC. Hence an initial AMOC slowdown might have been amplified leading to a progressive decrease in overturning circulation. The progressive slowdown of the AMOC would have continued as long as this positive feedback operated, pushing the ITCZ to an increasingly southerly location. Salt accumulation in low latitudes surface waters likely put an end to the progressive AMOC slowdown when the quantity of salt became sufficient to counter the influence of meltwater inputs at higher latitudes and cause the

resumption of the oceanic inter-hemispheric heat transport (36, 43 , 44). The reactivation of the overturning circulation would then cause the ITCZ to move back to its original, more northerly, position. We propose that, in contrast to the progressive amplification of the AMOC slowdown that took place during Heinrich stadials, the AMOC slowdowns that occurred during the stadials preceding DO events did not trigger the afore described positive feedback. As a result, both the decrease in AMOC and latitudinal shift in the ITCZ taking place during DO stadials remained limited. As the feedback is only triggered during Heinrich Stadials, iceberg discharges would be limited during stadials preceding DO events. The proposed mechanism is therefore consistent with the observed higher IRD content of North Atlantic sediments during Heinrich Stadials than during DO stadials.

Moreover, recent data from Antarctic ice cores show that atmospheric CO_2 progressively increased during each Heinrich stadial but remained constant or slightly decreased during DO stadials (45). The fact that the atmospheric CO_2 trend is drastically different during DO stadials than during Heinrich stadials points to the existence of an additional feedback involving the carbon cycle during Heinrich stadials, that does not operate during DO stadials, very likely related to the large changes in ocean circulation demonstrated by our data.

Conclusions

Our results demonstrate that the AMOC upper circulation cell experienced marked slowdowns 500 to 1,700 years before major tropical South American precipitation events that occurred during Heinrich stadials and corresponded to southward shifts of the ITCZ. Our data thereby provide the first unambiguous evidence that changes in Atlantic Ocean circulation indeed preceded changes in other climatic variables during rapid climate changes of the last glacial period. Moreover, our results shed light on major differences in the mechanisms leading to the observed southward ITCZ shifts associated with Heinrich stadials compared to those associated with DO stadials. Our data thus open new prospects for testing causal mechanisms of rapid climate changes using fully coupled earth system models. More specifically, contrary to current climate models that simulate a rapid response of the tropical climate to AMOC changes (34), the present study suggests that coupling these climate models with ice-sheets could yield to the observed large lead of AMOC changes with respect to the tropical climate.

Methods

Marine core age model. A preliminary age model was built for core GeoB3910 based on 20 ^{14}C dates measured on planktic foraminifera *G. ruber* white (12) and converted to calendar age using the Marine13 curve and the Oxcal software with no additional surface reservoir age correction (Fig. 2b) (46, 47). The beginning and end of precipitation events were defined as "boundaries" in Oxcal. The sedimentation rate is allowed to vary abruptly across these limits whereas between two boundaries the variations are smoother.

Precipitation events in marine sediment cores are marked by Ti/Ca peaks. We therefore defined their onset and end based on the inflexion points of the Ti/Ca curve in the same way as for speleothems (SI Appendix Fig. S5). Blue bands in Fig. 3 show precipitation events seen in MD09-3257.

Precipitation events seen in speleothems and in core GeoB3910 are synchronous within dating uncertainty (Fig. 2, and SI Appendix Fig. S5). There are two exceptions: the end of PE0 and the beginning of PE4 (dates in yellow in SI Appendix Fig. S5). For the end of PE0, the non-synchronicity could be due to the absence of a sharp transition in the Ti/Ca record of GeoB3910. For the beginning of PE4, it could be due to the limitation of the ^{14}C method. Indeed, beyond ~35 ka, conversion of ^{14}C dates into calendar ages is less reliable because (i) the calibration curve is based on less data (46) and (ii) the calibration curve is based on less well-defined ^{14}C ages due to the inherent limitation of radiometric dating when reaching large ages with respect to the ^{14}C half-life (5730 y).

Assuming that precipitation signals seen in core GeoB3910 (high Ti/Ca) and in the ELC speleothem (low $\delta^{18}O$) are synchronous within error bars, we correlated PE4 and PE5 in the sedimentary core to PE4 and PE5 $\delta^{18}O$ decreases in ELC speleothem (Fig. 2, dashed lines).

The resulting final age model for GeoB3910 is shown in blue in Fig. 2c. Radiocarbon dates between PE4 and PE5 were not used because the age model for these periods is based on speleothem tuning. The final GeoB3910 age model is therefore based on 17 ^{14}C dates for the 0 to 38 ka period and on four speleothem tie points for the 38 to 50 ka period (SI Table S1).

Core MD09-3257 age model is shown in red in Fig. 2c. As for GeoB3910, the age model for the period 38-50 ka is based on speleothem tuning for PE4 and PE5. The 0-38 ka portion of MD09-3257 was dated using both correlation of its Ti/Ca signal with that of core GeoB3910 core and five ^{14}C dates (SI Table S2). We correlated MD09-3257 to GeoB3910 sediment core because of the existence of 17 ^{14}C dates on core GeoB3910 and because Ti/Ca peaks allow to easily correlate both cores. In order to minimize

correlation uncertainty, we defined the tie points between the two sediment cores where the Ti/Ca increases (onset of precipitation events) and decreases (demise of precipitation events) are the fastest (SI Table S2). Resulting sedimentation rates are shown in SI Appendix Fig. S6. We see that the sedimentation rates during PE4 and PE5 resulting from the correlation of the sediment core to the ELC speleothem are consistent with the ^{14}C-derived sedimentation rates during the other precipitation events. We added a 500 y uncertainty on the U-Th ages of the ELC tie points (SI Table S2). This uncertainty is derived from the maximum age difference between the start/end of a precipitation event seen in core MD09-3257 and in the ELC speleothem over the ^{14}C-dated period. In this assessment, we did not use the difference between the end of PE3 in the ELC speleothem and in core MD09-3257 because the Marine13 calibration curve is highly uncertain over the 29-32 ka time interval and potentially yields calendar ages that are ~1000 y too old (46).

In summary, cores MD09-3257 and GeoB3910 age scales are entirely based on ^{14}C dates over the last 38 ka and tuned to the speleothem $\delta^{18}O$ signal from the ELC speleothem over the period 38-50 ka, because conversion of ^{14}C dates into calendar ages is unreliable over that period. As a result, these marine age scales are radiometric and based on regional correlations, and hence completely independent from the Greenland ice core chronology.

Water mass ventilation and circulation proxies. The $\delta^{13}C$ of epifaunal benthic foraminifer *Cibicides wuellerstorfi* records the carbon isotopic composition of bottom water dissolved inorganic carbon (48). As deep-water $\delta^{13}C$ reflects deep-water nutrient content and largely follows water mass structure and circulation in the modern ocean, *Cibicides* $\delta^{13}C$ has been used to trace water masses, a decrease in *Cibicides* $\delta^{13}C$ being interpreted as a decrease in bottom water ventilation, and conversely (20).

Sedimentary $^{231}Pa/^{230}Th$ (hereafter referred to as Pa/Th), i.e. the activity ratio of ^{231}Pa to ^{230}Th not supported by uranium present in the sediment mineral lattices and decay-corrected to the time of deposition, may be used to record changes in water mass export due to the difference in particle reactivity of ^{231}Pa and ^{230}Th in the water column (30 , 31). Both isotopes are produced in the water column at a constant activity ratio of Pa/Th = 0.093 by the disintegration of uranium which is homogeneously distributed in the oceans. Because of its high particle reactivity, the ^{230}Th is quickly removed from the water column by adsorption on settling particles. This behaviour is reflected by the short residence time of ^{230}Th in the deep ocean: 30-40 y (49). ^{231}Pa is less particle-reactive as exemplified by its longer residence time: 200 y (49). Thus, ^{230}Th will be rapidly removed to underlying sediment while ^{231}Pa can be laterally advected by oceanic currents. In particular, in the Atlantic, the residence time of the NADW is close to that of

the ^{231}Pa (49) allowing the use of Pa/Th as a proxy for the intensity of the AMOC. Slower flow rates thus result in less ^{231}Pa export and higher sedimentary Pa/Th, and conversely. In an ocean basin with no circulation, ^{231}Pa will not be exported and the sedimentary Pa/Th ratio will equal the Pa/Th production ratio in the water column (0.093) (e.g. ref. (50)). Sedimentary Pa/Th is usually interpreted as recording changes in the flow rate of the water mass occupying the first ~1000 m above the sediment (51).

Sedimentary Pa/Th is a relatively recent proxy that has been successfully used to show that major changes in the flow rate of the AMOC occurred during Heinrich event 1 and the last deglaciation (e.g. ref. (22, 31)) or at the onset of the last glacial period (e.g. ref. (52)). However, other factors than the AMOC intensity can influence the Pa/Th variability, and their importance therefore needs to be assessed. In particular, changes in scavenging efficiencies of ^{231}Pa and ^{230}Th can occur because of varying particle mineralogy or vertical fluxes (53). Thus, it is of primary importance to assess the mineralogy and flux of settling particles prior to extract the overturning signal out of the sedimentary record (22, 54). It is particularly necessary to follow the potential biases produced by the most active ^{231}Pa trap such as biogenic silica.

Recent studies have shown that the caveats that may apply to the Pa/Th as a proxy of overturning in some areas do not apply to the western tropical Atlantic region where this study's cores were retrieved. More specifically, a study involving Pa/Th measurements performed on western tropical Atlantic core tops, including core MD09-3257, and using a 2-D model (55) showed that the measured sedimentary Pa/Th vertical profile is consistent with a dominant role of the AMOC, rather than that of particle scavenging, thereby demonstrating that sedimentary Pa/Th can indeed be used to monitor changes in water mass overturning rates in that region (33).

However, because there are variations in terrigenous material deposition on the north-east Brazilian margin during the last glacial (SI Appendix Fig. S1), it is necessary to check whether Pa/Th is affected by this phenomenon. The ^{232}Th flux is indicative of the "true" vertical terrigenous fluxes on the margin (SI Appendix section A). Outside of the main precipitation event PE4, there is no correlation between the Pa/Th ratio and the ^{232}Th flux ($r = 0.18$, p-value= 0.24) (red data points in Fig. S7, left pannel). This indicates that the main driver of the Pa/Th variability is not the change in terrigenous fluxes, including for small precipitation events recorded in MD09-3257. During PE4, the rise of the Pa/Th towards high values could correspond to the increased terrigenous flux (white data points in Fig. S7, left pannel). This observation would need confirmation because it is done on only five points. We however chose to exclude Pa/Th values recorded during PE4 from the discussion of our results, as they might be influenced by

terrigenous influx. Pa/Th could not be measured during PE2 because of the occurrence of two small turbidites during the event (SI Appendix section A).

Variations in the opal flux could as well influence the Pa/Th ratio because of the high affinity of the protactinium for opal particles (56). However, the studied area is known for its low siliceous primary production (17). This is confirmed by ^{230}Th-normalized opal flux measurements which are below 0.05 g cm^{-2} ky^{-1}. Moreover, no correlation can be seen between the Pa/Th ratio and opal flux (Fig. S7, right panel). This result is in agreement with the study of (57) that showed that below an opal flux limit of 0.2 g cm^{-2} ky^{-1}, there seems to be no correlation between the Pa/Th and opal fluxes in the Atlantic Ocean. We thus consider that the potential impact of opal on our Pa/Th record can be neglected.

Two late Holocene samples were measured for sedimentary Pa/Th in this study. Measured Pa/Th values are 0.062±0.003 and 0.067±0.004, respectively at 0.44 and 2.03 ka. We can then define an average late Holocene value of 0.065±0.003 (1 SD), which can be used to compare last glacial and modern circulation. Pa/Th measurements were done following a protocol derived from ref. (52) and Pa/Th values were corrected using a lithogenic (^{238}U/^{232}Th) value (termed R hereafter) of 0.5 (Fig. S8, red curve). Error bars on Pa/Th measurements account for the uncertainty on the Pa, Th and U measurements as well as for the spike calibrations, but not for the uncertainty on the R value. Pa/Th curves computed with various R values (0.4, 0.5, and 0.6) are shown in Fig. S8 (green, red, and blue curves, respectively). The highest difference between the Pa/Th signals computed with different R occurs for samples with high ^{232}Th concentrations, i.e. high lithogenics, for which the R correction is important. While the absolute value of the Pa/Th ratio changes as a function of the R value, the relative variation is preserved and hence the relative changes in the intensity of the AMOC upper circulation cell renewal rate.

Acknowledgments

This work is a contribution to the RETRO project, a joint European Science Foundation (ESF)/EUROMARC, funded by Research Council of Norway (RCN), France (CNRS/INSU), Germany, and the Netherlands. Core MD09-3257 was collected on board R/V Marion Dufresne during RETRO Cruise III, supported by ESF EUROMARC project RETRO, IPEV and ANR project ANR-09-BLAN-0347. We thank the IPEV team, crew members of R/V Marion Dufresne and all scientists who participated in RETRO Cruise III. We are thankful to M. Roy-Barman for expert advices on Pa/Th measurements on LSCE MC-ICP-MS. We

acknowledge C. Moreau, J.-P. Dumoulin, and the UMS ARTEMIS for AMS ^{14}C dates. We are grateful to A. Govin, M. Kageyama, J.-C. Duplessy, E. Michel and J. Jouzel for constructive comments on an earlier version of this article. This is LSCE contribution 5279.

References

1. Hughen KA, Overpeck JT, Peterson LC, & Trumbore S (1996) Rapid climate changes in the tropical Atlantic region during the last deglaciation. *Nature* 380:51-54.
2. Peterson LC, Haug GH, Hughen KA, & Röhl U (2000) Rapid changes in the hydrologic cycle of the tropical Atlantic during the last glacial. *Science* 290:1947-1951.
3. Lea DW, Pak DK, Peterson LC, & Hughen KA (2003) Synchroneity of Tropical and High-Latitude Atlantic Temperatures over the Last Glacial Termination. *Science* 301:1361-1364.
4. Deplazes G, *et al.* (2013) Links between tropical rainfall and North Atlantic climate during the last glacial period. *Nature Geoscience* 6(3):213-217.
5. Chiang JCH, Biasutti M, & Battisti DS (2003) Sensitivity of the Atlantic Intertropical Convergence Zone to Last Glacial Maximum boundary conditions. *Paleoceanography* 18(4):doi:10.1029/2003PA000916.
6. Chiang JCH & Bitz CM (2005) Influence of high latitude ice cover on the marine Intertropical Convergence Zone. *Clim. Dynam.*:DOI 10.1007/s00382-00005-00040-00385.
7. Swingedouw D, *et al.* (2009) Impact of Freshwater Release in the North Atlantic under Different Climate Conditions in an OAGCM. *Journal of Climate* 22:6377-6403.
8. Kageyama M, *et al.* (2009) Glacial climate sensitivity to different states of the Atlantic Meridional Overturning Circulation: results from the IPSL model. *Climate of the Past* 5:551-570.
9. Menviel L, Timmermann A, Friedrich T, & England MH (2014) Hindcasting the continuum of Dansgaard-Oeschger variability: mechanisms, patterns and timing. *Climate of the Past* 10(1):63-77.
10. Cheng H, *et al.* (2013) Climate change patterns in Amazonia and biodiversity. *Nature communications* 4:1411.
11. Cruz FW, *et al.* (2009) Orbitally driven east–west antiphasing of South American precipitation. *Nature Geoscience* 2(3):210-214.
12. Jaeschke A, Rühlemann C, Arz H, Heil G, & Lohmann G (2007) Coupling of millennial-scale changes in sea surface temperature and precipitation off northeastern Brazil with high-latitude climate shifts during the last glacial period. *Paleoceanography* 22:PA4206, doi:4210.1029/2006PA001391.
13. Cheng H, *et al.* (2006) A penultimate glacial monsoon record from Hulu Cave and two-phase glacial terminations. *Geology* 34(3):217-220.
14. Wang X, *et al.* (2004) Wet periods in northeastern Brazil over the past 210 kyr linked to distant climate anomalies. *Nature* 432:740-743.
15. Jennerjahn TC, *et al.* (2004) Asynchronous terrestrial and marine signals of climate change during Heinrich events. *Science* 306(5705):2236-2239.

16. Wang YJ, *et al.* (2001) A High-Resolution Absolute-Dated Late Pleistocene Monsoon Record from Hulu Cave, China. *Science* 294:2345-2348.
17. Arz HW, Pätzold J, & Wefer G (1998) Correlated Millennial-Scale Changes in Surface Hydrography and Terrigenous Sediment Yield Inferred from Last-Glacial Marine Deposits off Northeastern Brazil. *Quaternary Research* 50:157-166.
18. Rhein M, Stramma L, & Send U (1995) The Atlantic Deep Western Boundary Current: Water masses and transports near the equator. *Journal of Geophysical Research* 100(C2):2441.
19. Schott FA (2003) The zonal currents and transports at 35°W in the tropical Atlantic. *Geophysical Research Letters* 30(7).
20. Duplessy J-C, *et al.* (1988) Deepwater source variations during the last climatic cycle and their impact on the global deepwater circulation. *Paleoceanography* 3:343-360.
21. Curry WB & Oppo DW (2005) Glacial water mass geometry and the distribution of d13C of SCO2 in the western Atlantic Ocean. *Paleoceanography* 20:doi:10.1029/2004PA001021.
22. Gherardi J-M, *et al.* (2009) Glacial-interglacial circulation changes inferred from 231Pa/230Th sedimentary record in the North Atlantic region. *Paleoceanography* 24:doi:10.1029/2008PA001696.
23. Hastenrath S (2011) Exploring the climate problems of Brazil's Nordeste: a review. *Climatic Change* 112(2):243-251.
24. Wang X, *et al.* (2007) Millennial-scale precipitation changes in southern Brazil over the past 90,000 years. *Geophysical Research Letters* 34(23):n/a-n/a.
25. Kanner LC, Burns SJ, Cheng H, & Edwards RL (2012) High-latitude forcing of the South American summer monsoon during the Last Glacial. *Science* 335(6068):570-573.
26. Mosblech NAS, *et al.* (2012) North Atlantic forcing of Amazonian precipitation during the last ice age. *Nature Geoscience* 5(11):817-820.
27. Cruz FW, Jr., *et al.* (2005) Insolation-driven changes in atmospheric circulation over the past 116,000 years in subtropical Brazil. *Nature* 434(7029):63-66.
28. Wang X, *et al.* (2006) Interhemispheric anti-phasing of rainfall during the last glacial period. *Quaternary Science Reviews* 25(23-24):3391-3403.
29. Linsley BK (1996) Oxygen-isotope record of sea level and climate variations in the Sulu Sea over the past 150 000 years. *Nature* 380:234-237.
30. Yu E-F, Francois R, & Bacon M (1996) Similar rates of modern and last-glacial ocean thermohaline circulation inferred from radiochemical data. *Nature* 379:689-694.
31. McManus JF, Francois R, Gherardi J-M, Keigwin LD, & Brown-Leger S (2004) Collapse and rapid resumption of Atlantic meridional circulation linked to deglacial climate changes. *Nature* 428:834-837.
32. Guihou A, *et al.* (2010) Late slowdown of the Atlantic Meridional Overturning Circulation during the Last Glacial Inception: new constraints from sedimentary (231Pa/2303 Th). *Earth and Planetary Science Letters* 289:520-529.
33. Lippold J, Gherardi J-M, & Luo Y (2011) Testing the 231Pa/230Th paleocirculation proxy: A data versus 2D model comparison. *Geophys. Res. Lett.* 38(L20603):doi:10.1029/2011GL049282.
34. Kageyama M, Paul A, Roche D, & Van Meerbeeck CJ (2010) Modelling glacial climatic millennial-scale variability related to changes in the Atlantic meridional overturning circulation: a review. *Quat. Sci. Rev.* 29:2931-2956.

35. Broccoli AJ, Dahl KA, & Stouffer RJ (2006) Response of the ITCZ to Northern Hemisphere cooling. *Geophysical Research Letters* 33(1).
36. Broecker WS, Bond G, & Klas M (1990) A salt oscillator in the glacial Atlantic? 1. The concept. *Paleoceanography* 5(4):469-477.
37. Vidal L*, et al.* (1997) Evidence for changes in the North Atlantic Deep Water linked to meltwater surges during the Heinrich events. *Earth and Planetary Science Letters* 146:13-26.
38. Peck VL*, et al.* (2006) High resolution evidence for linkages between NW European ice sheet instability and Atlantic Meridional Overturning Circulation. *Earth and Planetary Science Letters* 243(3-4):476-488.
39. Johnson RG & Lauritzen SE (1995) Hudson Bay-Hudson Strait jökulhlaups and Heinrich events: A hypothesis. *Palaeogeography Palaeoclimatology Palaeoecology* 117(1-2):123-137.
40. Li C, Battisti DS, Schrag DP, & Tziperman E (2005) Abrupt climate shifts in Greenland due to displacements of the sea ice edge. *Geophysical Research Letters* 32(19).
41. Marcott SA*, et al.* (2011) Ice-shelf collapse from subsurface warming as a trigger for Heinrich events. *Proceedings of the National Academy of Sciences of the United States of America* 108(33):13415-13419.
42. Alvarez-Solas J, Robinson A, Montoya M, & Ritz C (2013) Iceberg discharges of the last glacial period driven by oceanic circulation changes. *Proceedings of the National Academy of Sciences of the United States of America* 110(41):16350-16354.
43. Paillard D & Labeyrie L (1994) Role of the thermohaline circulation in the abrupt warming after Heinrich events. *Nature* 372:162-164.
44. Schmidt GA, Spero HJ, & Lea DW (2004) Links between salinity variation in the Caribbean and North Atlantic thermohaline circulation. *Nature* 428:160-163.
45. Ahn J & Brook EJ (2014) Siple Dome ice reveals two modes of millennial CO2 change during the last ice age. *Nature communications* 5.
46. Reimer PJ*, et al.* (2013) IntCal13 and Marine13 Radiocarbon Age Calibration Curves 0–50,000 years Cal BP. *Radiocarbon* 55(4):1869-1887.
47. Ramsey CB (2008) Deposition models for chronological records. *Quaternary Science Reviews* 27(1-2):42-60.
48. Duplessy J-C*, et al.* (1984) 13C record of benthic foraminifera in the last interglacial ocean : implications for the carbon cycle and the global deep water circulation. *Quaternary Research* 21:225-243.
49. Francois R (2007) *Proxies in Late Cenozoic Paleoceanography: Paleoflux and Paleocirculation from Sediment 230Th and 231Pa/230Th* (Elsevier).
50. Marchal O, François R, Stocker TF, & Joos F (2000) Ocean thermohaline circulation and sedimentary $^{231}Pa/^{230}Th$ ratio. *Paleoceanography* 15(6):625-641.
51. Thomas AL, Henderson GM, & Robinson LF (2006) Interpretation of the 231Pa/230Th paleocirculation proxy: New water-column measurements from the southwest Indian Ocean. *Earth and Planetary Science Letters* 241:493-504.
52. Guihou A*, et al.* (2010) Late slowdown of the Atlantic Meridional Overturning Circulation during the Last Glacial Inception: New constraints from sedimentary (Pa-231/Th-230). *Earth and Planetary Science Letters* 289(3-4):520-529.
53. Geibert W & Usbeck R (2004) Adsorption of thorium and protactinium onto different particle types : Experimental findings. *Geochimica and Cosmochimica Acta* 68(7):1489-1501.

54. Gherardi J-M, *et al.* (2005) Evidence from the North Eastern Atlantic Basin for Variability of the Meridional Overturning Circulation through the last Deglaciation. *Earth and Planetary Science Letters* 240:710-723.
55. Luo Y, Francois R, & Allen SE (2010) Sediment 231Pa/230Th as a recorder of the rate of the Atlantic meridional overturning circulation: insights from a 2-D model. *Ocean Science* 6:381-400.
56. Chase Z, Anderson RF, Fleisher MQ, & Kubik PW (2002) The influence of particle composition and particle flux on scavenging of Th, Pa and Be in the ocean. *Earth and Planetary Science Letters* 204(1-2):215-229.
57. Lippold J, *et al.* (2012) Strength and geometry of the glacial Atlantic Meridional Overturning Circulation. *Nature Geoscience* 5(11):813-816.
58. Willmott CJ & Matsuura K (2000) Terrestrial Air Temperature and Precipitation: Monthly and Annual Climatologies.
59. Kindler P, *et al.* (2014) Temperature reconstruction from 10 to 120 kyr b2k from the NGRIP ice core. *Climate of the Past*.

Figures

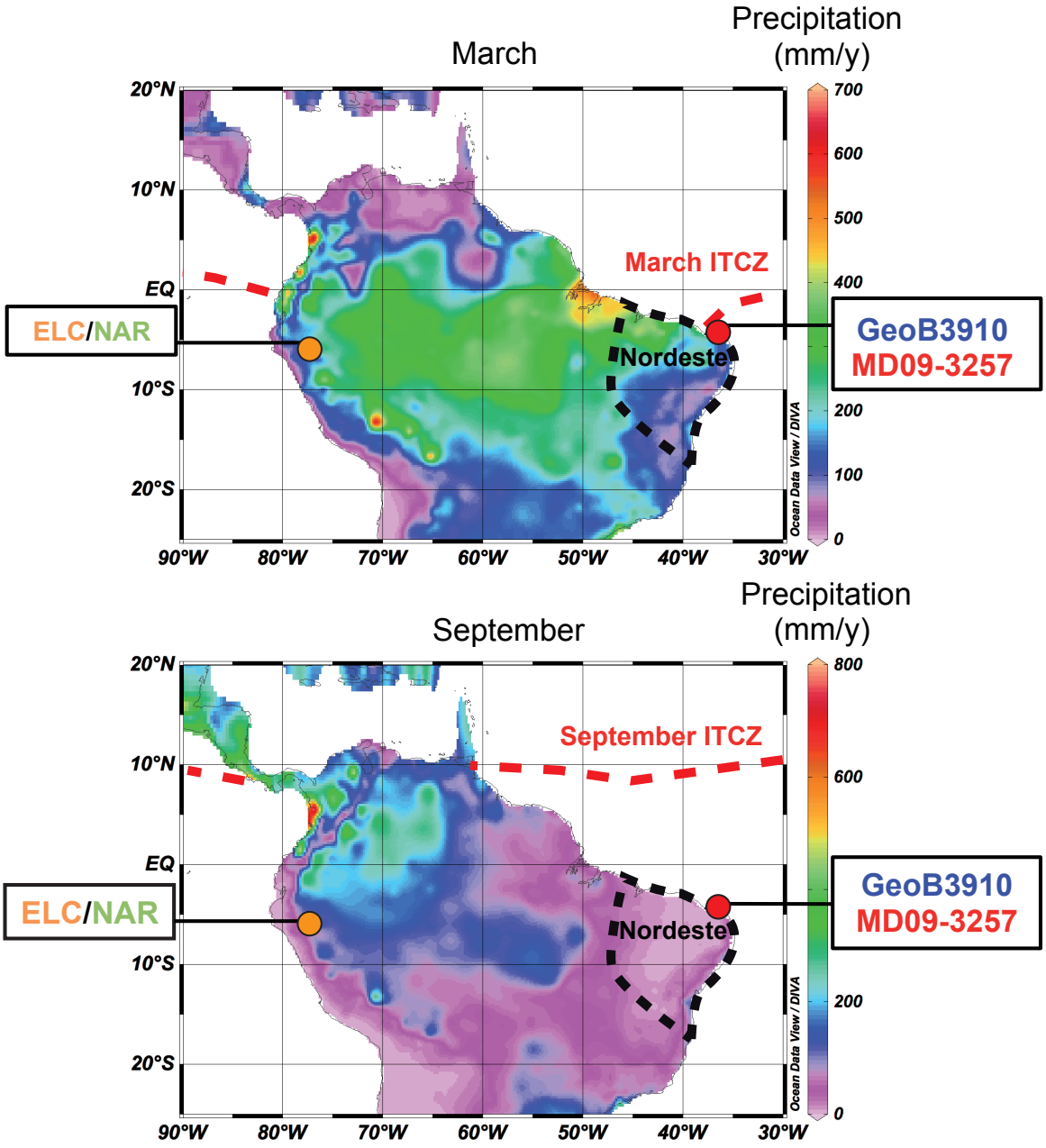

Figure 3.**1** : Map of the study area. The red circle indicates the location of the studied marine sediment cores, the orange circle indicates the position of the El Condor (ELC) and Diamante (NAR) caves (10), the black dashed line delimitates the Nordeste region, and red dashed line shows the position of the present day September and March ITCZ over the Atlantic and Pacific Ocean. The color scale indicates mean precipitation over South America (mm/y) for the months of March and September averaged over the period 1950-1996 AD (58).

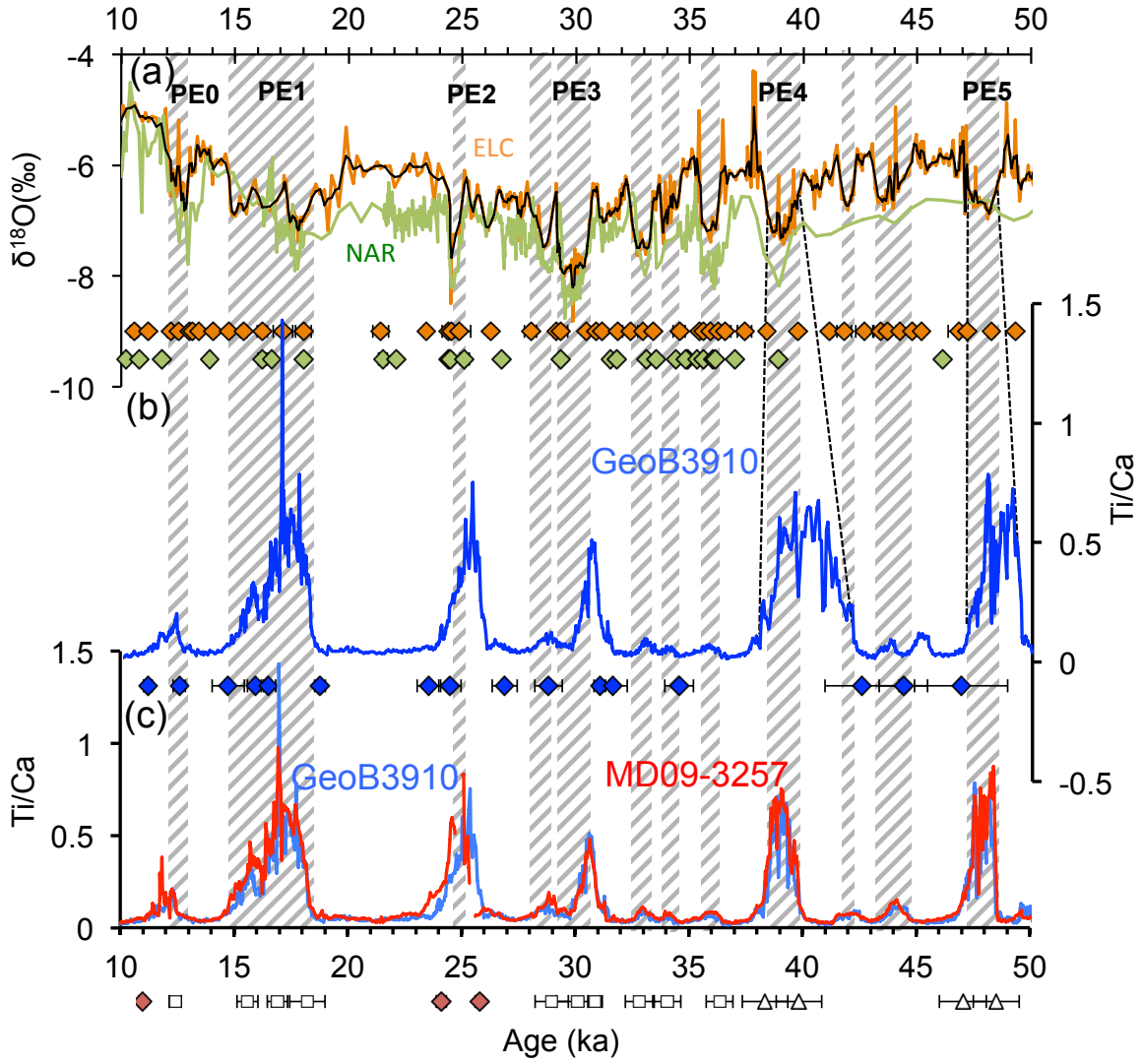

Figure 3.**2** : Comparison between (a) the U-Th dated $\delta^{18}O$ records of ELC/NAR speleothems (10) and (b) the ^{14}C-dated Ti/Ca record of core GeoB3910 (12). (c) Ti/Ca record of marine sediment cores GeoB3910 (12) and MD09-3257 on their final age models. Colored diamonds show the positions of the U-Th dates for speleothems and of the ^{14}C dates for marine sediment cores with their 2 SD error bars. Diamonds below the x-axis depict the ^{14}C dates used to establish the age model of cores MD09-3257 and GeoB3910, diamond colors correspond to that of the cores on which the ^{14}C dates have been measured. Empty squares show the position of GeoB3910-MD09-3257 tie points used to establish the age model of core MD09-3257. Empty triangles are the speleothem tie points used to establish the age model of cores MD09-3257 and GeoB3910 beyond the ^{14}C dating range (see text and SI Table S1, S2).

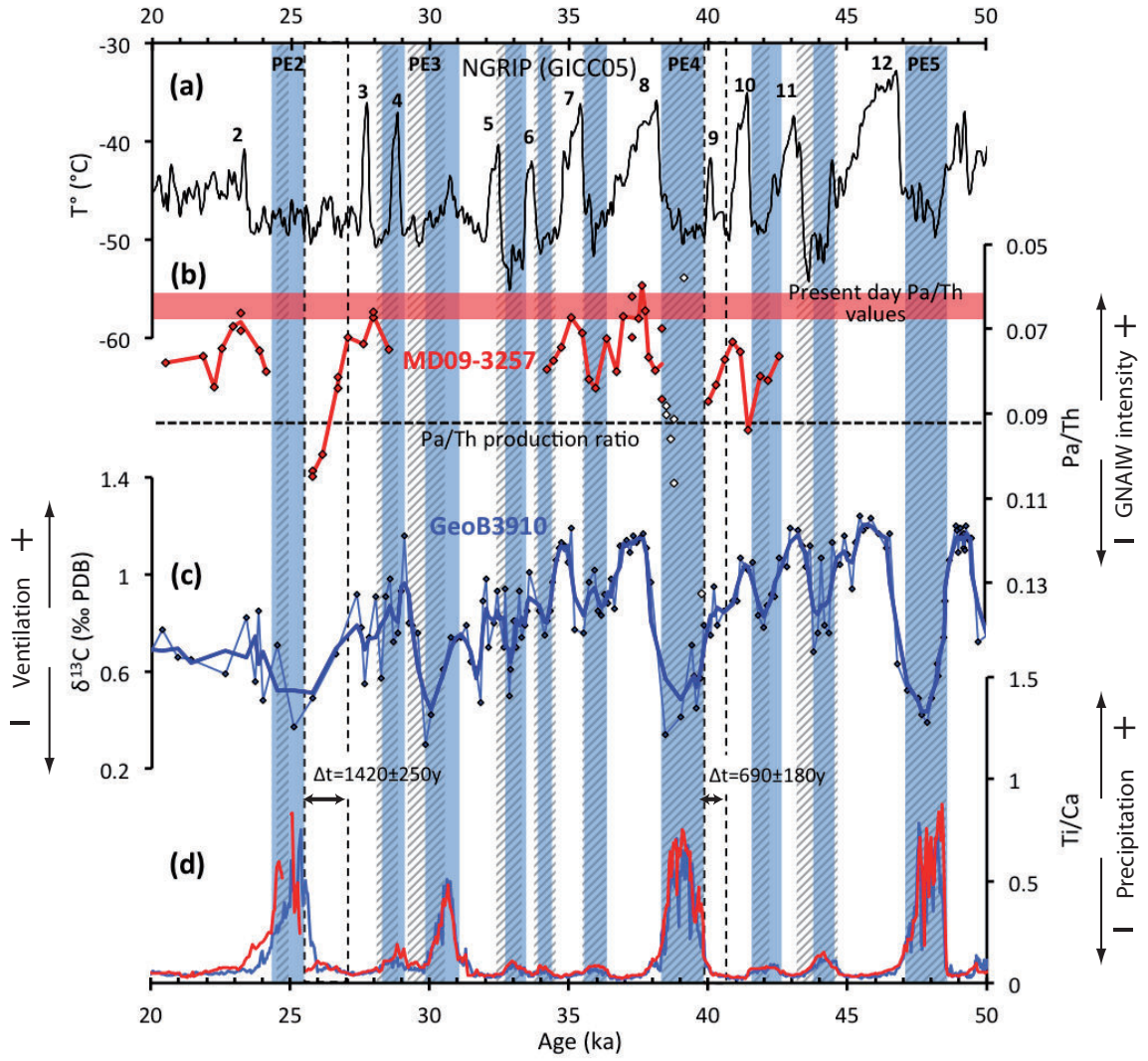

Figure 3.**3** : Comparison between Greenland (a) NGRIP temperature signal on the GICC05 timescale (59) and Brazil (b) MD09-3257 Pa/Th, (c) GeoB3910 *Cibicides wuellerstorfi* $\delta^{13}C$, and (d) GeoB3910 (12) (blue) and MD09-3257 (red) Ti/Ca records. Gray dashed bands delimitate the precipitation events defined on the ELC speleothem $\delta^{18}O$ record (SI Appendix Fig. S3). Blue shaded bands delimitate the precipitation events as seen in the MD09-3257 Ti/Ca record (see text). Vertical black dashed lines indicate the start of the Pa/Th and Ti/Ca rises in core MD09-3257. In (a) numbers indicate the DO events. In (b) the red line passes through average Pa/Th values when there are replicate measurements, the white symbols indicate Pa/Th values are not considered for this study as they might not represent a pure circulation signal (Methods), the red horizontal band indicates the present day Pa/Th value (0.065±0.003, Methods). Error bars on Pa/Th measurements are given in Methods and Fig. S8. No Pa/Th measurements could be made during PE2 because of the occurrence of two small turbidites (SI Appendix section A). In (c) the thick dark blue line is the 3 points running average of the *Cibicides w.* $\delta^{13}C$ record.

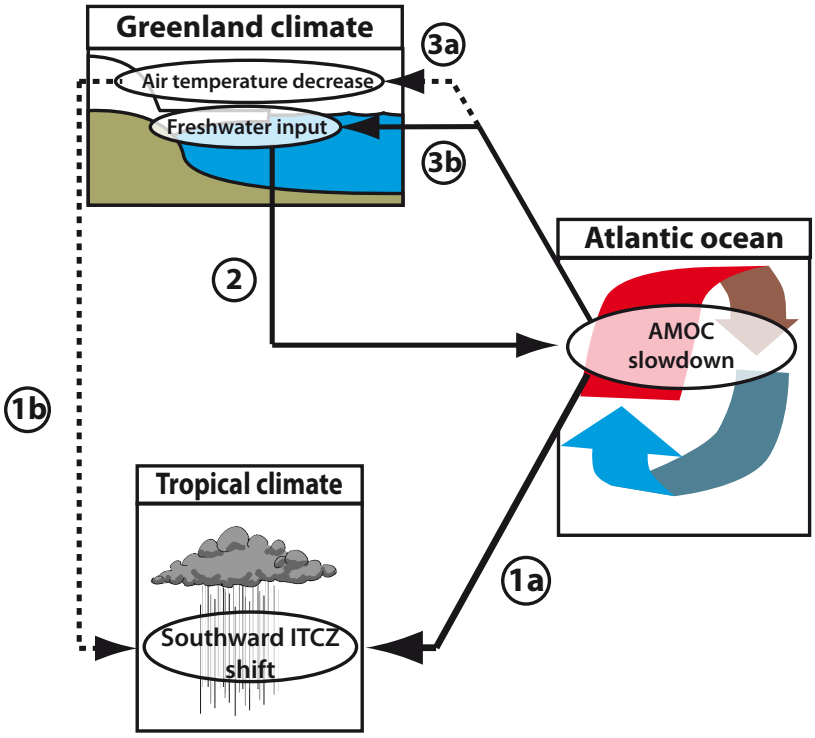

Figure 3.**4** : Illustration of the interactions between Greenland climate, tropical climate and the AMOC. Arrows illustrate causal mechanisms between triggers and climatic response discussed in the text. The thick black arrow illustrates the main mechanism discussed in this study, that is an AMOC slowdown could have triggered millennial-scale ITCZ latitudinal shifts. The dotted arrow 1b indicates an additional potential trigger for ITCZ shifts (see text).

3.3 Supporting Information

The supporting information provides additional information concerning the development of the age scale for cores MD09-3257 and GeoB3910, and details the definition of the start of the AMOC slowdown and precipitation events.

Supporting Information

Atlantic Ocean circulation changes preceded millennial tropical South America rainfall events during the last glacial

P. Burckel, C. Waelbroeck, J.-M Gherardi, S. Pichat, H. Arz, J. Lippold, T. Dokken, and F. Thil

A. Precipitation events recorded in marine cores GeoB3910 and MD09-3257
B. Precipitation recorded by tropical South American speleothems
B.1. Definition of millennial precipitation events PE0 to PE5
B.2. Synchronicity of the millennial precipitation events in South American speleothems
C. Method used to estimate of the lead of the Pa/Th signal with respect to the Ti/Ca signal

Supplementary Figures

Fig. S1. Ti/Ca ratio and ^{232}Th flux versus depth in core MD09-3257
Fig. S2. Map of the Nordeste
Fig. S3. Comparison of U-Th dated South American speleothems δ^{18}O records and definition of the millennial precipitation events PE0 to PE5
Fig. S4. Map showing the position of the South American speleothems and the two marine sedimentary cores MD09-3257 and GeoB3910
Fig. S5. Dates (ka) for the onset and end of the main precipitation events (PE) recorded in South American speleothems and core GeoB3910
Fig. S6. Ti/Ca and sedimentation rate for core MD09-3257.
Fig. S7. Correlation between the Pa/Th ratio and ^{232}Th flux or opal flux.
Fig. S8. Pa/Th in MD09-3257 as a function of time calculated with different values for the lithogenic (^{238}U/^{232}Th) value (R) used to correct for detrital material contribution.
Fig. S9. Comparison between the Pa/Th, Ti/Ca, and ln(Ti/Ca) signals.

Supplementary Tables

Table S1. Age model for core GeoB3910.
Table S2. Age model for core MD09-3257.
Table S3. ^{231}Pa, ^{230}Th, ^{232}Th, and ^{238}U concentrations (dpm.g^{-1}) versus depth in core MD09-3257. Pa/Th values are computed with a R ratio of 0.5.
Table S4. *Cibicides wuellerstorfi* δ^{13}C values versus depth in core GeoB3910.
Table S5. Opal data versus depth in core MD09-3257.

A. Precipitation events recorded in marine cores GeoB3910 and MD09-3257

Marine sediment cores show Ti/Ca peaks during Heinrich Stadials. These peaks could result from (i) a decrease in productivity (particularly carbonate production), (ii) an increase in biogenic sediment dissolution, or (iii) an increase of terrigenous material input. However, the first two hypotheses are unlikely as last glacial changes in both productivity and dissolution on the Brazilian margin were minor between 2000 and 3000m depth (1, 2). Moreover, the covariation of the Ti/Ca ratio and ^{230}Th-normalized ^{232}Th flux, a proxy for the vertical flux of terrigenous material that removes the effect of sediment remobilisation (3), indicates that Ti/Ca peaks are primarily caused by increased terrigenous input (Fig. S1).

The terrigenous flux can rise because of increased precipitation, sea level fluctuations or increased dust inputs. Indeed, increased precipitation enhances continental erosion and global sea level can control sediment discharge through a threshold mechanism (4). Ti/Ca peaks are accompanied by increased concentration and proportion of fern spores in nearby core GeoB3104-1 (5). Since ferns are characteristic of wet environments, the associated increased terrigenous inputs are most likely linked to increased precipitation in the Brazilian hinterland. Precipitation events are therefore the most likely explanation for the increased terrigenous input on the margin.

Terrigenous material input at the study site is mainly delivered from the Nordeste region by local rivers such as Rio Jaguaribe, Rio Apodi, Rio Piranhas and Rio Paraiba (6) (Fig. S2). Extra-Nordeste sediment originating from the larger Sao Francisco river may be delivered to the study site by the northward flowing North Brazilian Current.

Two turbidites marked by sand layers and Ti/Ca drops were observed in core MD09-3257: the first extends from 233.5 to 237cm and the second from 240.5 to 243 cm, i.e. during PE2 (see below). They are indicated by a discontinuity in core MD09-3257 Ti/Ca record in Figs. 2, 3, S1, S6, and S9.

B. Precipitation recorded by tropical South American speleothems

Periods of increased precipitation are marked by a decrease of the δ^{18}O in South American speleothems (7-11). Indeed, the δ^{18}O of speleothems from the Nordeste region, eastern side of the northern Andes and southeastern Brazil has been shown to be directly linked to precipitation intensity and to the source of moisture (8, 10-12).

Over the last 60 ka, South American precipitation variability occurred at orbital and millennial time scales (8-10). The orbital scale variability is controlled by precession through its effect on Austral Summer Insolation (ASI) with a period of about 23 ka (12). During intense ASI, the South American Summer Monsoon (SASM) intensifies. Stronger

trade winds bring more moisture from the Atlantic Ocean towards west Amazonia and enhanced convection induces high precipitation in this region (13). The Andes then deflect the warm and humid air masses southward (forming the Low Level Jets) to feed the southeastern Brazil precipitation (8, 9). While intensified SASM leads to increased precipitation over western Amazonia and southeastern Brazil, the Nordeste region experiences dry conditions (8, 9). This is due to the high convective activity over western Amazonia that enhances the upper tropospheric Nordeste low, increasing subsidence of dry air over the Nordeste (8, 9, 14). ASI related SASM variability thus leads to an antiphased precipitation pattern in the same hemisphere, a precipitation dipole with increased humidity in western Amazonia and southeastern Brazil, increased aridity in the Nordeste region and conversely (8).

In contrast, millennial scale variability in precipitation during the last glacial period produced precipitation events in phase over South America in the 0-30°S latitude band, east of the Andes. These precipitation events are thought to reflect shifts of the ITCZ (9).

B.1. Definition of millennial precipitation events PE0 to PE5

We compared the $\delta^{18}O$ signals in South American speleothems to assess the synchronicity of millennial-scale precipitation events in the 0-30°S latitude band (Figs. S3 and S4). The best dated $\delta^{18}O$ speleothem records, i.e. those with the highest number of dates with the lowest uncertainties, are from the El Condor (ELC) and Diamante (NAR) caves. We thus defined precipitation events as the marked decreases in $\delta^{18}O$ in ELC and NAR records depicted as vertical grey dashed bands in Figs. 2, 3 and S3. Among the marked $\delta^{18}O$ decreases, we defined PE0 as the precipitation event taking place during the Younger Dryas, and PE1 to 5, as those occurring during Heinrich Stadials 1 to 5, respectively. Many studies consider that precipitation events seen in tropical speleothems occur during Heinrich Events. This is mainly based on ref. (15) who suggested that periods of decreased Asian monsoon occurred during periods of increased IRD deposition in three sediment cores of the North Atlantic (16). In the present study, we refer to periods of increased precipitation occurring during the YD or the Heinrich stadials as PE rather than Heinrich Events, as the exact timing of IRD deposition in North Atlantic cores with respect to decreased Asian monsoon in the Hulu cave is not discussed in ref. (15). Moreover, the synchronicity of precipitation events between tropical Asia and South America remains to be fully investigated. We thus chose to use the term PE rather than HE in the present study, as it prevents any potential over-interpretation.

B.2. Synchronicity of the millennial precipitation events in South American speleothems

The comparison of the $\delta^{18}O$ signals of ELC and NAR with those of the other South American speleothems shows that millennial-scale precipitation events are synchronous over the entire 0-30°S latitudinal band within age model uncertainties (Fig. S3).

To assess the synchronicity, we compared the onset and end dates of the main precipitation events (PE) in all speleothems. The onset and end of precipitation events are defined by the inflexion point of the $\delta^{18}O$ curve when it drops towards lower $\delta^{18}O$ values (onset) or rises toward higher $\delta^{18}O$ values (end). There is an overall good synchronism over all the records. Six exceptions can be noticed (Fig. S5, dates in red). Exceptions 1-3: the onset and end of PE1 and the end of PE3 in the Pacupahuain speleothem are not synchronous with the ELC/NAR speleothem. However, these events in all the other speleothems are synchronous within dating uncertainties with the ELC/NAR record and not with that of the Pacupahuain speleothem, which therefore comforts us in the use of ELC/NAR as reference. The fourth exception is the end of PE2 and this might be related to a dating issue on the ELC/NAR speleothem as the end of PE2 in the Santiago speleothem record, although being synchronous with ELC/NAR within error bars, is closer to the end of PE2 seen in the Pacupahuain record. The end of PE2 might therefore be too old in the ELC/NAR speleothem. It is important to note that there is no systematic lead or lag of the Pacupahuain signal with respect to the ELC/NAR signal, showing that asynchronicity probably results from dating errors or local non-systematic effects. Exceptions 5 and 6: the onset and end of PE5 seen in the Santiago speleothem are not synchronous with those of the ELC/NAR record despite the large uncertainty on its U-Th dates. However, the correspondence of PE5 in Pacupahuain and ELC/NAR tends to show that PE5 is too young in the Santiago record.

Five other events (dates in yellow in Fig. S5) appear asynchronous but can be reconciled with the ELC/NAR speleothem if we consider the uncertainty on the definition of the onset and end of precipitation events and error bowing between U-Th dates. In particular, while the onset of PE4 on the Pacupahuain speleothem appears initially difficult to reconcile with ELC/NAR, we argue that there is in fact a very large uncertainty on this date in the Pacupahuain $\delta^{18}O$ record because of the lack of dated levels between ~40 and 44 ka, which precludes the identification of potential changes in growth rate and hence precise dating of the onset of PE4.

Finally, precipitation events seen in the ELC/NAR speleothems also appear to be synchronous with precipitation events seen in speleothems and travertines from the Nordeste region: Toca da Boa Vista (TBV) and Lapa dos Brejoes (LBR) (Fig. S3). Indeed, speleothem and travertine growth intervals from the TBV/LBR caves occur during PE1, 4 and 5 seen in the ELC/NAR speleothems.

In conclusion, the precipitation events seen in ELC/NAR $\delta^{18}O$ records can be considered to be synchronous with those recorded in other South American speleothems within age model uncertainties, since synchronism can be demonstrated in almost all cases (i.e. 22 out of 28).

C. Method used to estimate the lead of the Pa/Th signal with respect to the Ti/Ca signal

The onset of precipitation events seen in marine sediment cores was defined, as discussed in SI Appendix section B, based on the inflexion point in the Ti/Ca signal. As the Pa/Th change is much more gradual, we defined the start of the AMOC upper circulation cell slowdown as the depth where the Pa/Th value rises significantly above the reference Pa/Th value, i.e. reference Pa/Th value + 1 SD, representing the relatively stable circulation conditions prevailing immediately before the AMOC slowdown. We computed the reference values as the average of the last two or three Pa/Th values that are showing a stable or decreasing trend before inversion of the trend toward increasing Pa/Th values (Fig. 3). The start of the Pa/Th rise thus defined takes place at 251.1cm for PE2 and 375.4cm for PE4.

Fig. S9 shows the comparison between the Pa/Th, Ti/Ca and ln(Ti/Ca) records. The lead of the Pa/Th signal over that of the ln(Ti/Ca) signal is similar to that of the Pa/Th over the Ti/Ca. As explained in Methods (Marine core age model), we define the onset of the precipitation events as the timing of the rapid increase in precipitation, that is the inflexion point on the Ti/Ca or ln(Ti/Ca) signals. This choice is supported by the fact that the beginning of the ln(Ti/Ca) rise is different from that of the Ti/Ca rise and, hence, that it is not possible to determine which of the two reflects the onset of the precipitation event. The Ti/Ca signal is however more likely to reflect precipitation as the relative amplitudes of the periods of increased precipitation are very similar to that of the ^{232}Th flux (Fig. S1), which reflects the terrigenous input to the study site. Moreover, the progressive increases in precipitation depicted by the ln(Ti/Ca) signal are difficult to reconcile with our understanding of the latitudinal shifts of the ITCZ and their effect on tropical precipitation.

Additional references

1. Ruhlemann C, *et al.* (1996) Late Quaternary productivity changes in the western equatorial Atlantic: Evidence from Th-230-normalized carbonate and organic carbon accumulation rates. *Marine Geology* 135(1-4):127-152.
2. Jaeschke A, Rühlemann C, Arz H, Heil G, & Lohmann G (2007) Coupling of millennial-scale changes in sea surface temperature and precipitation off northeastern Brazil with high-latitude climate shifts during the last glacial period. *Paleoceanography* 22:PA4206, doi:4210.1029/2006PA001391.
3. Anderson RF, Fleisher MQ, & Lao Y (2006) Glacial-interglacial variability in the delivery of dust to the central equatorial Pacific Ocean. *Earth and Planetary Science Letters* 242(3-4):406-414.
4. Milliman JD, Summerhayes CP, & Barretto HT (1975) Quaternary Sedimentation on the Amazon Continental Margin: A Model *Geological Society of America Bulletin* 86:610-614.
5. Behling H, Arz HW, Patzold J, & Wefer G (2000) Late Quaternary vegetational and climate dynamics in northeastern Brazil, inferences from marine core GeoB 3104-1. *Quaternary Science Reviews* 19(10):981-994.
6. Tintelnot M, Brichta A, & Morais JO (1998) Clay mineralogy of river sediments on the Brazilian coast.
7. Wang X, *et al.* (2007) Millennial-scale precipitation changes in southern Brazil over the past 90,000 years. *Geophysical Research Letters* 34(23):n/a-n/a.
8. Cheng H, *et al.* (2013) Climate change patterns in Amazonia and biodiversity. *Nature communications* 4:1411.
9. Cruz FW, *et al.* (2009) Orbitally driven east–west antiphasing of South American precipitation. *Nature Geoscience* 2(3):210-214.
10. Kanner LC, Burns SJ, Cheng H, & Edwards RL (2012) High-latitude forcing of the South American summer monsoon during the Last Glacial. *Science* 335(6068):570-573.
11. Mosblech NAS, *et al.* (2012) North Atlantic forcing of Amazonian precipitation during the last ice age. *Nature Geoscience* 5(11):817-820.
12. Cruz FW, Jr., *et al.* (2005) Insolation-driven changes in atmospheric circulation over the past 116,000 years in subtropical Brazil. *Nature* 434(7029):63-66.
13. Wang X, *et al.* (2006) Interhemispheric anti-phasing of rainfall during the last glacial period. *Quaternary Science Reviews* 25(23-24):3391-3403.
14. Chen TC, Weng SP, & Schubert S (1999) Maintenance of austral summertime upper-tropospheric circulation over tropical South America: The Bolivian high-Nordeste low system. *Journal of the Atmospheric Sciences* 56(13):2081-2100.
15. Wang YJ, *et al.* (2001) A High-Resolution Absolute-Dated Late Pleistocene Monsoon Record from Hulu Cave, China. *Science* 294:2345-2348.
16. Bond G, *et al.* (1993) Correlations between climate records from North Atlantic sediments and Greenland ice. *Nature* 365:143-147.
17. Wang X, *et al.* (2004) Wet periods in northeastern Brazil over the past 210 kyr linked to distant climate anomalies. *Nature* 432:740-743.
18. Francois R (2007) *Proxies in Late Cenozoic Paleoceanography: Paleoflux and Paleocirculation from Sediment 230Th and 231Pa/230Th* (Elsevier).

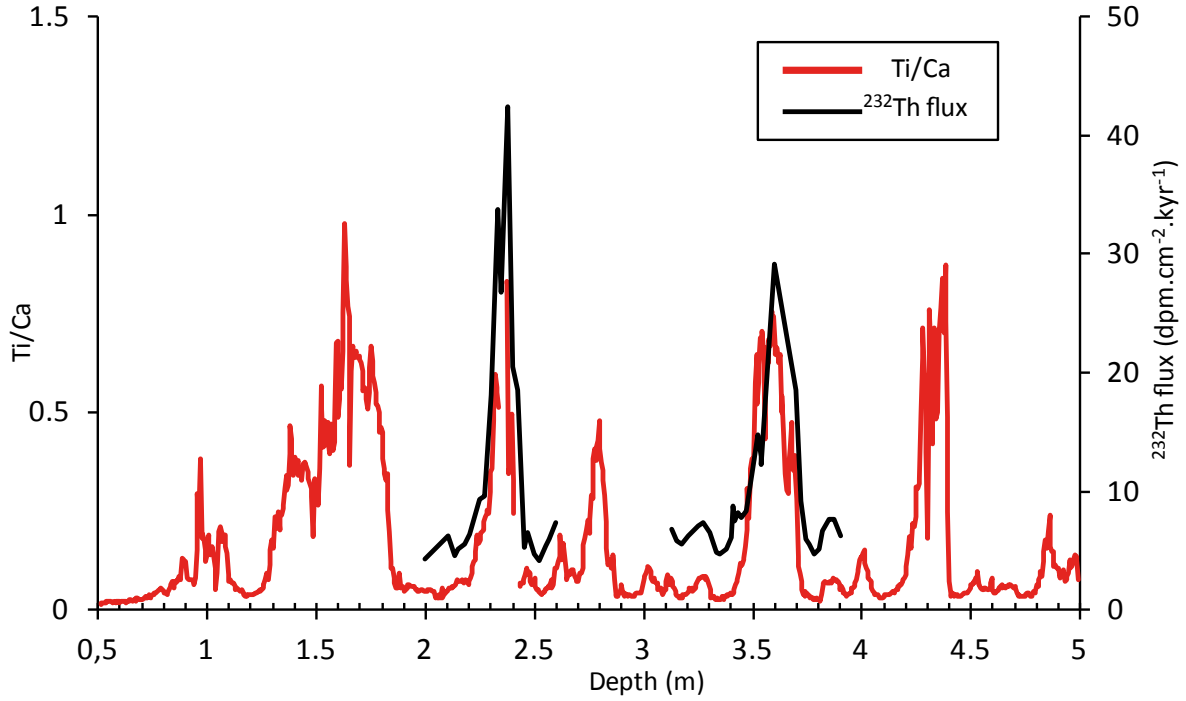

Figure 3.**S1 :** Ti/Ca ratio and ^{232}Th flux versus depth in core MD09-3257.

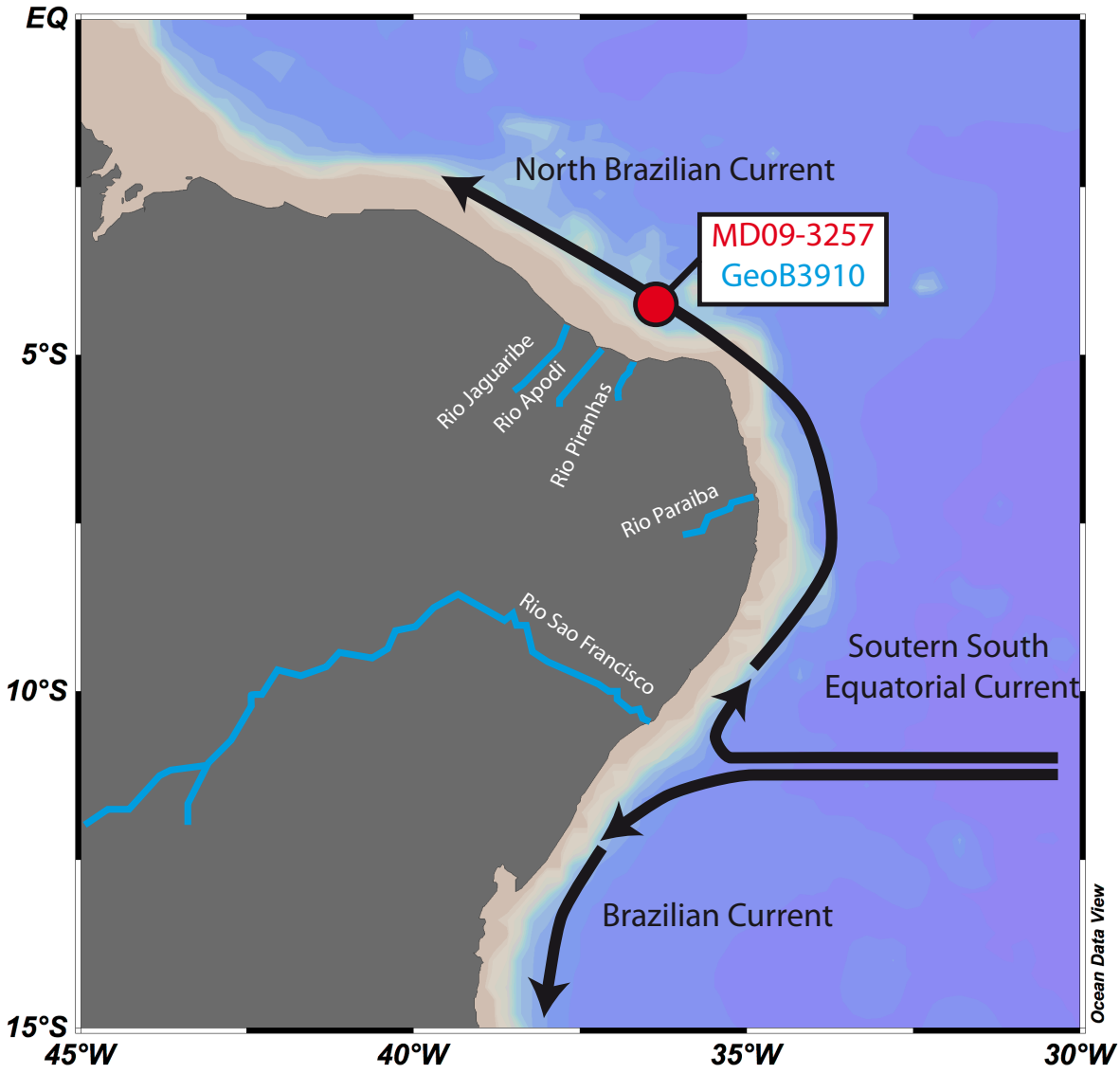

Figure 3.**S2** : Map of the Nordeste showing the position of the main Brazilian rivers and surface currents that could contribute to terrigenous sediment input at the study site indicated by a red circle.

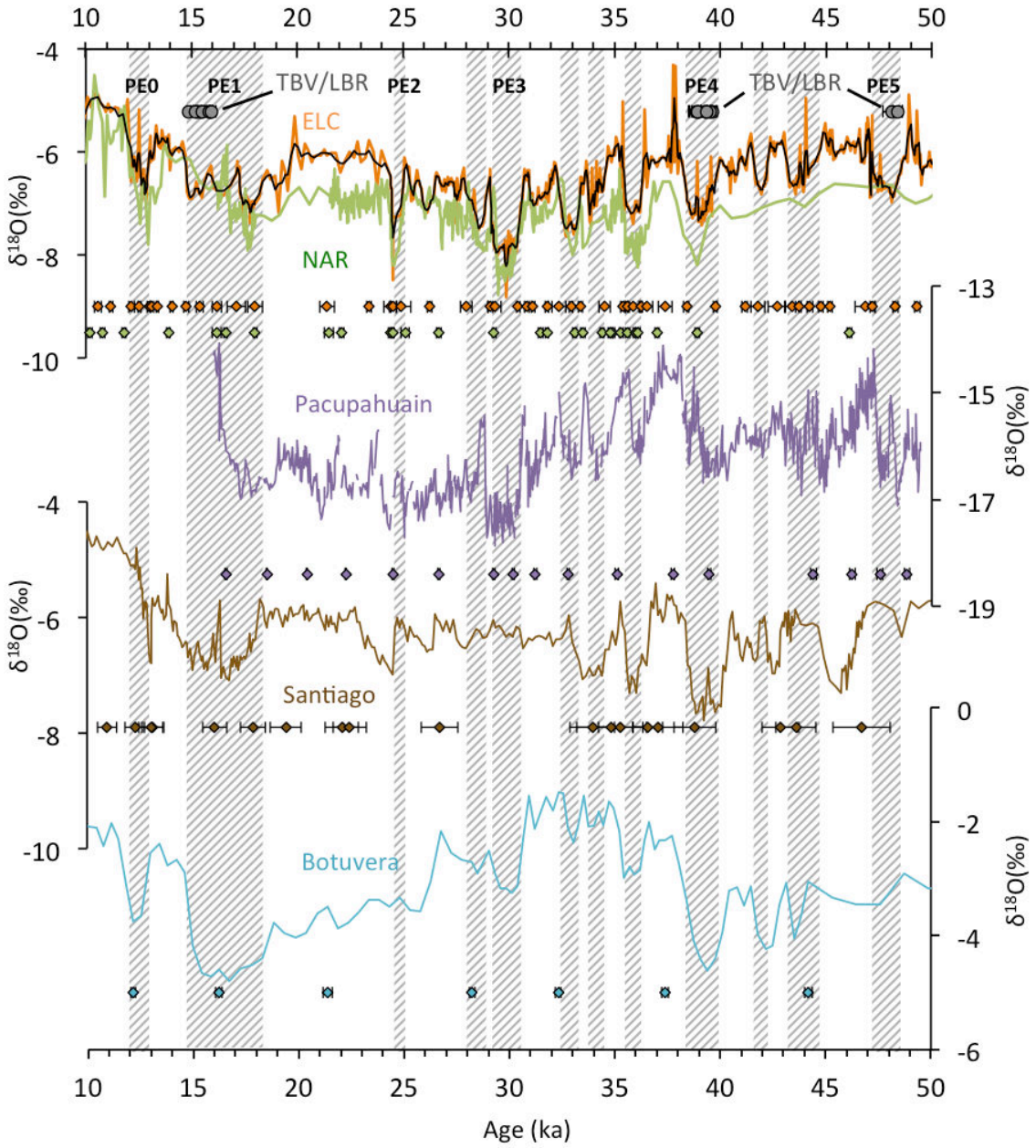

Figure 3.**S3** : Comparison of U-Th dated South American speleothems $\delta^{18}O$ records and definition of the millennial precipitation events PE0 to PE5. Vertical grey dashed bars indicate precipitation events PE0 to PE5 as defined on the ELC/NAR $\delta^{18}O$ records. Coloured diamonds show the position of the U-Th dates for each speleothem and their 2 SD error bars. The colour of the diamonds corresponds to that of their respective curves. Speleothem and travertine growth intervals from the Toca da Boa Vista (TBV)/ Lapa dos Brejoes (LBR) caves (17) are shown as grey circles on the top of the panel as well as their 2 SD error bars. ELC and NAR are the El Condor and Diamante caves, respectively (8). The black line represents the 3 points running average of the ELC $\delta^{18}O$ signal. The Pacupahuain (10), the Santiago (11) and the Botuvera (7) speleothem $\delta^{18}O$ records are shown as well. See Fig. S4 for the location of the speleothems in South America.

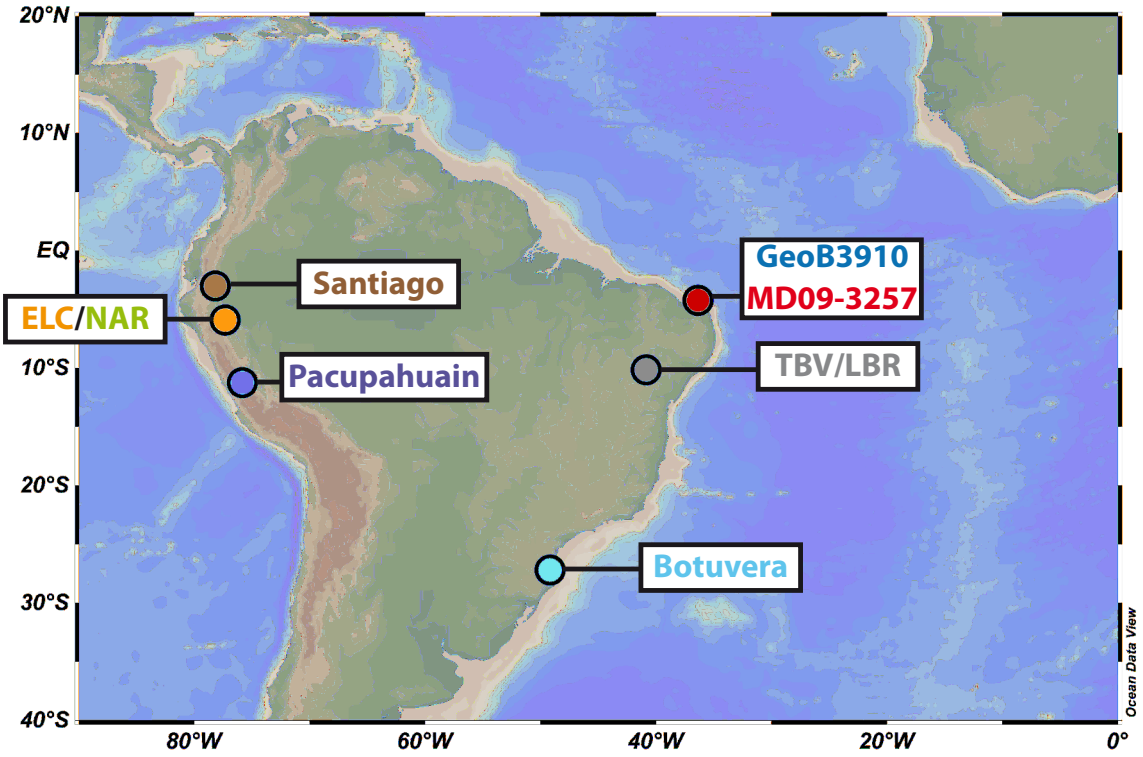

Figure 3.**S4** : Map showing the position of the South American speleothems used in Fig. S3 and the two marine sedimentary cores used in this study, MD09-3257 and GeoB3910. The orange circle includes both El Condor (ELC) and Diamante (NAR) caves.

		PE0				PE1				PE2			
Archive	Name	End	± 2σ	Start	± 2σ	End	± 2σ	Start	± 2σ	End	± 2σ	Start	± 2σ
Speleothem	El Condor	12.05	0.14	12.94	0.08	14.77	0.13	18.38	0.35	24.47	0.29	24.98	0.48
	Pacupahuain	-		-		16.56	0.04	18.92	0.04	24.02	0.05	24.52	0.05
	Santiago	12.66	0.46	13.07	0.57	14.30	0.52	17.90	0.59	23.41	0.79	24.53	0.79
	Botuvera	11.60	0.12	12.70	0.12	14.79	0.15	18.55	0.15	?		?	
Sediment	GeoB3910	11.55	0.21	12.51	0.41	15.14	0.73	18.24	0.78	24.31	0.52	25.93	1.26

		PE3				PE4				PE5			
Archive	Name	End	± 2σ	Start	± 2σ	End	± 2σ	Start	± 2σ	End	± 2σ	Start	± 2σ
Speleothem	El Condor	29.15	0.12	30.54	0.08	38.35	0.11	39.84	0.09	47.06	0.14	48.52	0.13
	Pacupahuain	28.85	0.06	30.54	0.07	38.32	0.09	40.69	0.08	47.39	0.12	48.64	0.12
	Santiago	?		?		38.50	0.99	40.27	0.99	44.92	0.95	46.32	1.36
	Botuvera	29.31	0.14	30.67	0.13	38.39	0.17	40.10	0.17	?		?	
Sediment	GeoB3910	29.86	1.21	31.05	0.48	38.04	2.91	42.15	1.92	47.22	2.34	49.54	4.24

Figure 3.**S5** : Dates (ka) for the onset and end of the main precipitation events (PE) recorded in South American speleothems and core GeoB3910 (see Fig. S4). The age model fore core GeoB3910 is based on ^{14}C dates only. The color code of the speleothem dates indicates the degree of synchronicity of each onset/end of PE with respect to the El Condor (ELC) speleothem signal taken as reference. The reference dates for the PE events in the ELC speleothem are shown in white. Dates in green are synchronous within error bars with the ELC speleothem, dates in yellow are likely to be synchronous and dates in red are asynchronous (see text).

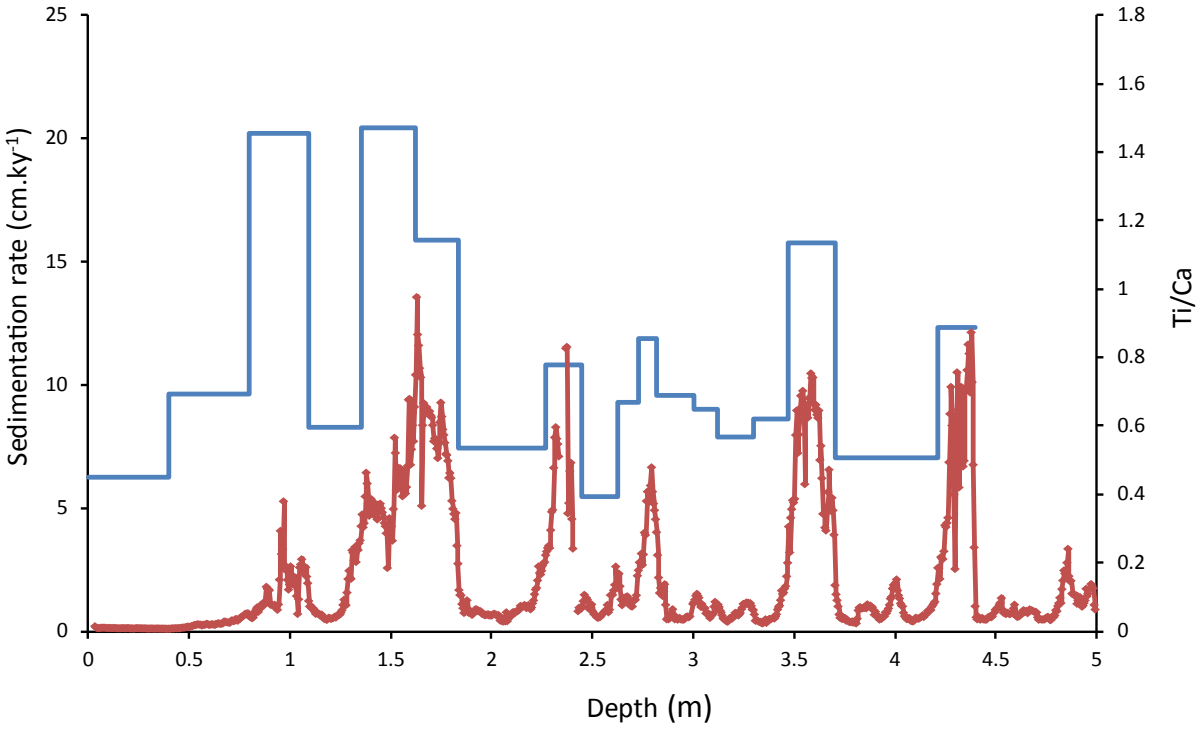

Figure 3.**S6** : Ti/Ca (red) and sedimentation rate (blue) for core MD09-3257.

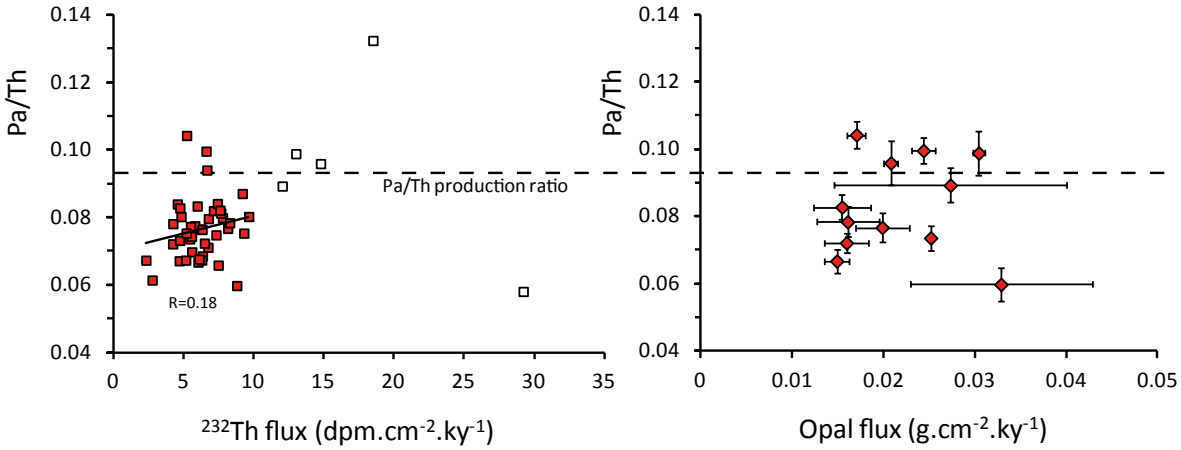

Figure 3.**S7** : Correlation between the Pa/Th ratio and ^{232}Th flux (left panel) or opal flux (right panel). Empty symbols in the left panel are not considered in the computation of the correlation coefficient. Error bars in the right panel are 1 SD.

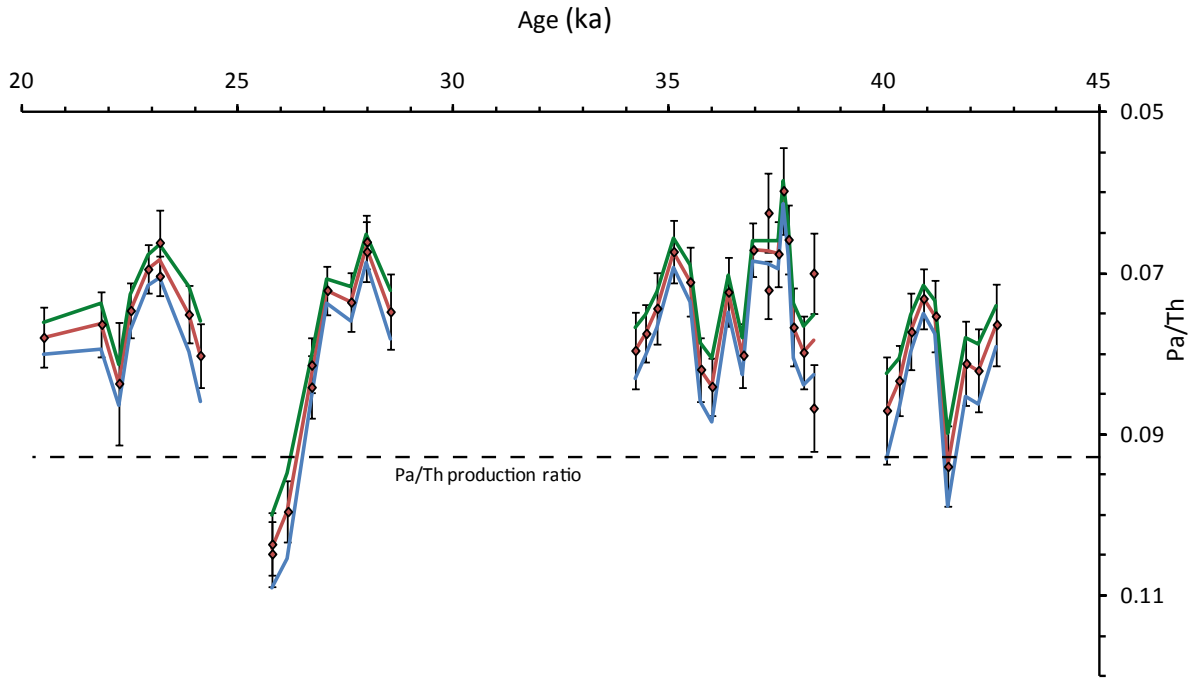

Figure 3.**S8** : Pa/Th in MD09-3257 as a function of time calculated with different values for the lithogenic ($^{238}U/^{232}Th$) value (R) used to correct for detrital material contribution (18). Red curve, R=0.5 (correction used in Fig. 3), green curve R=0.4, and blue curve R=0.6. Error bars are 1 SD.

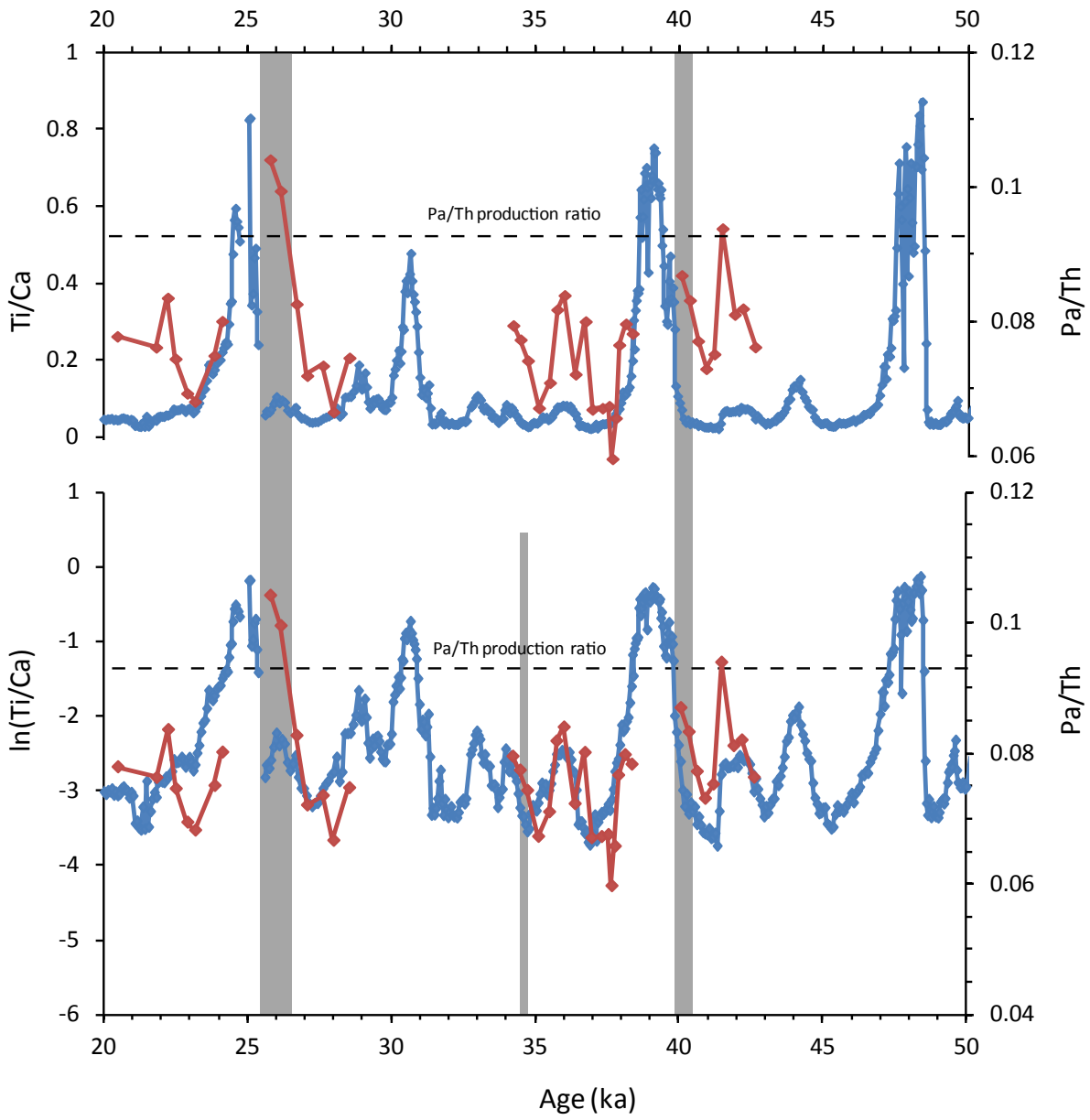

Figure 3.**S9** : Comparison between the Pa/Th (red), Ti/Ca, and ln(Ti/Ca) (blue curves) signals. Grey bands highlight the lead of the Pa/Th signal with respect to the Ti/Ca and ln(Ti/Ca) signals.

Tables

Table 3.**S1** : Age model for core GeoB3910.

	Depth (cm)	14C age (y BP)	± 1σ	Age (Cal y BP)	± 1σ	Modeled Age (Cal y BP)	± 1σ
	0	565	30	202	56	190	74
	13	3930	35	3910	54	3918	80
	23	6160	40	6595	56	6586	72
	38	8430	40	9033	52	9037	76
	58	10090	60	11103	73	11072	94
	73	10940	70	12500	99	12460	131
	88	12840	110	14528	277	14610	352
	103	13550	70	15793	127	15798	177
	113	14000	70	16378	124	16374	164
	148	15780	110	18650	114	18642	119
	173	20000	170	23624	226	23441	256
	183	20580	150	24243	183	24359	246
*	200	22850	130	26764	216	26779	272
	213	25130	260	28763	286	28712	303
	233	27160	310	30921	202	30947	129
	238	28280	430	31742	493	31538	303
	268	30860	430	34419	360	34511	293
***	300	/		38350	713	38316	504
***	324	/		39840	713	39839	504
**	328	38600	1480	42323	1220	/	
**	348	41000	820	44114	707	/	
**	373	44480	1250	47349	1269	/	
***	377	/		47060	721	47060	516
***	400	/		48520	714	48493	506

^{14}C dates are from ref. [2] except one date measured for this study (*)

** ^{14}C dates that were not used and were replaced by speleothem tie points

*** speleothem tie points

^{14}C_age (y BP) is the uncalibrated conventional radiocarbon age, age (Cal y BP) is the calendar age obtained using the Marine13 calibration curve [18] or U-Th dates (***), the modeled age (Cal y BP) is the calendar age model produced by the Oxcal software [19].

Table 3.**S2** : Age model for core MD09-3257.

	Depth GeoB3910 (cm)	Depth MD09-3257 (cm)	14C age (y BP)	± 1σ	Modeled Age (Cal y BP)	± 1σ
*	/	0	795	30	447	31
*	/	40	6355	30	6823	49
*	/	80	9985	35	10984	83
	73	109	/		12425	130
	100	135	/		15594	236
	122	162	/		16914	228
	145	183	/		18234	385
*	/	227	20460	70	24120	115
*	/	245	21870	80	25785	85
	215	262	/		28972	371
	225	273	/		30132	486
	232	282	/		30879	158
	251	301	/		32824	299
	263	312	/		34060	295
	284	330	/		36361	295
**	/	347	/		38350	504
**	/	371	/		39840	504
**	/	422	/		47060	516
**	/	440	/		48520	506

* ^{14}C dates measured on core MD09-3257

** speleothem tie points

Dates are otherwise based on the correlation with core GeoB3910.

Table 3.**S3** : ^{231}Pa, ^{230}Th, ^{232}Th, and ^{238}U concentrations (dpm.g^{-1}) versus depth in core MD09-3257. Pa/Th values are computed with a R ratio of 0.5.

Prof(cm)	Age (y)	1 σ	^{231}Pa	1 σ	^{230}Th	1 σ	^{232}Th	1 σ	^{238}U	1 σ	Pa/Th	1 σ
0	447	31	0.176	0.006	2.98	0.06	1.08	0.02	1.327	0.026	0.062	0.003
10	2041	35	0.219	0.012	3.49	0.06	1.10	0.02	1.390	0.013	0.067	0.004
200	20483	282	0.222	0.007	3.90	0.06	2.24	0.03	1.326	0.009	0.078	0.004
210	21830	220	0.153	0.004	2.79	0.06	2.02	0.04	1.540	0.030	0.076	0.004
213	22234	201	0.223	0.004	3.78	0.22	2.29	0.13	1.470	0.016	0.084	0.008
215	22504	189	0.207	0.004	3.86	0.09	2.58	0.05	1.490	0.013	0.075	0.003
218	22908	170	0.191	0.003	3.76	0.08	2.62	0.03	1.617	0.012	0.069	0.003
220	23177	158	0.178	0.005	3.63	0.09	2.72	0.06	1.683	0.040	0.066	0.004
220	23177	158	0.184	0.003	3.61	0.05	2.76	0.03	1.678	0.045	0.070	0.002
225	23851	127	0.169	0.003	3.28	0.05	3.13	0.04	1.675	0.016	0.075	0.004
227	24120	115	0.190	0.004	3.54	0.05	3.43	0.03	1.906	0.016	0.080	0.004
245	25785	85	0.294	0.006	4.43	0.07	2.92	0.04	2.187	0.033	0.104	0.004
245	25785	85	0.296	0.005	4.43	0.08	2.95	0.04	2.181	0.050	0.105	0.004
247	26151	117	0.252	0.004	4.02	0.07	3.13	0.04	2.061	0.015	0.100	0.004
250	26701	167	0.225	0.006	3.95	0.07	2.51	0.04	1.684	0.031	0.084	0.004
250	26701	167	0.220	0.004	3.96	0.08	2.50	0.04	1.685	0.014	0.081	0.003
252	27067	200	0.187	0.004	3.66	0.07	2.14	0.03	1.482	0.013	0.072	0.003
255	27617	249	0.173	0.004	3.39	0.06	2.38	0.03	1.469	0.013	0.074	0.004
257	27983	282	0.162	0.003	3.38	0.09	2.54	0.05	1.475	0.011	0.067	0.004
257	27983	282	0.159	0.003	3.36	0.07	2.55	0.03	1.467	0.010	0.066	0.003
260	28532	331	0.180	0.003	3.60	0.10	3.11	0.06	1.545	0.010	0.075	0.005
313	34213	295	0.155	0.003	3.06	0.08	2.53	0.05	1.522	0.013	0.080	0.005
315	34467	295	0.153	0.003	3.05	0.06	2.27	0.02	1.533	0.013	0.077	0.004
317	34721	295	0.140	0.003	2.86	0.07	2.08	0.04	1.402	0.014	0.074	0.004
320	35102	295	0.134	0.003	2.91	0.06	2.30	0.04	1.460	0.010	0.067	0.004
323	35484	295	0.137	0.003	2.93	0.07	2.46	0.05	1.375	0.008	0.071	0.004
325	35738	295	0.170	0.002	3.38	0.07	2.96	0.05	1.551	0.012	0.082	0.004
327	35992	295	0.165	0.002	3.24	0.05	2.91	0.03	1.517	0.019	0.084	0.004
330	36373	297	0.138	0.003	2.95	0.07	2.43	0.05	1.367	0.011	0.072	0.004
333	36722	333	0.142	0.003	2.74	0.04	1.77	0.02	1.534	0.012	0.080	0.004
335	36954	358	0.143	0.002	3.02	0.06	1.86	0.03	1.890	0.011	0.067	0.003
338	37303	394	0.130	0.002	2.66	0.05	1.78	0.02	1.634	0.015	0.072	0.003
338	37303	394	0.120	0.004	2.64	0.07	1.75	0.03	1.595	0.012	0.062	0.005
340	37536	419	0.137	0.003	2.94	0.06	2.23	0.03	1.726	0.013	0.068	0.004
341	37652	431	0.143	0.002	2.91	0.07	2.28	0.04	2.994	0.030	0.060	0.005
342	37768	443	0.141	0.002	3.08	0.07	2.63	0.04	1.900	0.011	0.066	0.004
343	37885	455	0.145	0.003	2.98	0.06	2.73	0.04	1.742	0.022	0.077	0.005
345	38117	480	0.155	0.002	3.13	0.06	2.83	0.05	1.737	0.012	0.080	0.004
347	38350	504	0.179	0.003	3.45	0.06	3.18	0.04	2.128	0.034	0.087	0.005
347	38350	504	0.158	0.004	3.39	0.06	3.09	0.04	2.072	0.026	0.070	0.005
350	38540	504	0.176	0.002	3.48	0.07	4.05	0.06	2.019	0.018	0.090	0.006
350	38540	504	0.176	0.003	3.52	0.06	4.03	0.04	2.021	0.011	0.088	0.005
352	38667	504	0.163	0.003	3.16	0.06	3.90	0.06	2.091	0.022	0.096	0.007
354	38794	504	0.189	0.003	3.43	0.06	3.95	0.05	2.317	0.026	0.106	0.007
354	38794	504	0.177	0.004	3.42	0.06	3.84	0.05	2.295	0.017	0.091	0.007
360	39174	504	0.144	0.004	3.01	0.06	4.00	0.06	3.181	0.051	0.058	0.014
370	39808	504	0.169	0.003	2.94	0.05	3.99	0.05	2.009	0.049	0.132	0.011
372	40052	504	0.161	0.002	3.04	0.07	2.75	0.05	2.422	0.046	0.087	0.006
374	40335	505	0.141	0.003	2.82	0.04	2.20	0.02	1.431	0.015	0.083	0.004
376	40619	505	0.138	0.002	2.77	0.06	1.93	0.03	1.763	0.031	0.077	0.004
378	40902	505	0.130	0.002	2.79	0.05	1.87	0.02	1.324	0.008	0.073	0.003
380	41185	506	0.117	0.002	2.48	0.06	1.79	0.04	1.185	0.008	0.075	0.004
382	41468	506	0.137	0.002	2.58	0.05	2.19	0.03	1.305	0.013	0.094	0.005
385	41893	507	0.133	0.003	2.76	0.05	2.56	0.04	1.410	0.009	0.081	0.005
387	42176	508	0.156	0.003	3.24	0.07	3.03	0.05	1.592	0.016	0.082	0.005
390	42601	508	0.148	0.003	3.19	0.09	2.68	0.03	1.474	0.009	0.076	0.005

Table 3.**S4** : *Cibicides wuellerstorfi* $\delta^{13}C$ values versus depth in core GeoB3910.

Depth (cm)	Age (ka)	δ13C (‰)	Depth (cm)	Age (ka)	δ13C (‰)	Depth (cm)	Age (ka)	δ13C (‰)	Depth (cm)	Age (ka)	δ13C (‰)
59.5	11211	-0.13	219.5	29544	0.76	290	37095	1.14	367	45737	1.2
65	11720	0.37	221.5	29800	0.3	291	37212	1.09	368	45875	1.23
69	12090	0.46	223.5	30012	0.42	292	37329	1.16	370	46150	1.17
72	12367	0.44	228	30455	0.61	293	37447	1.13	372	46426	1.11
73	12460	0.4	231	30750	0.74	294	37564	1.15	373	46564	1.17
76	12901	0.27	232.5	30898	0.73	295	37682	1.17	375	46839	0.63
83	13898	0.74	234.5	31134	0.74	296	37799	1.11	379	47208	0.52
90	14875	0.03	236	31307	0.79	297.5	37975	0.97	385	47579	0.49
91.5	15073	0.14	237.5	31480	0.64	302.7	38463	0.34	387	47702	0.42
94	15259	0.08	239.5	31687	0.61	311.5	39026	0.41	390	47888	0.39
96	15379	-0.09	241	31835	0.47	318	39442	0.71	393	48073	0.49
99.5	15588	0.22	242	31934	0.89	319	39506	0.58	396	48258	0.63
105	15913	0.23	243	32033	0.98	320.5	39602	0.45	397	48320	0.58
108	16086	0.07	244	32133	0.7	322.5	39730	0.57	400	48499	0.74
111	16259	0.05	246	32331	0.8	324.5	39880	0.79	401	48529	0.89
114	16431	0.11	247	32430	0.93	326	40087	0.75	402	48560	0.89
118	16660	0.17	248	32529	0.82	327	40225	0.95	407	48712	1.06
127	17177	0.14	249.5	32678	0.7	328	40363	0.79	415	48957	1.2
134.5	17607	0.24	250	32727	0.94	329.5	40569	0.85	416	48987	1.18
138.5	17836	0.29	251.5	32876	0.5	332	40914	0.89	417	49018	1.09
144.5	18181	0.61	252	32925	0.61	333	41052	0.89	419	49079	1.19
146	18310	0.57	253	33024	0.81	334	41189	1.07	421	49140	1.16
148	18642	0.66	254	33123	0.7	335	41327	1.03	423	49201	1.11
150	19026	0.69	255	33223	0.93	336	41465	1.02	424	49231	1.17
153.5	19697	0.62	256	33322	0.74	337	41603	1.05	425	49262	1.1
157	20369	0.77	257	33421	0.79	338.5	41809	0.83	426	49292	1.2
160	20945	0.66	258	33520	0.85	340	42016	0.78	427	49323	1.16
162.5	21425	0.65	258.5	33569	1.01	341	42154	0.87	430	49414	1.14
169	22673	0.59	262	33916	0.85	342	42292	0.92	432	49475	1.15
173	23441	0.82	264	34114	0.75	343	42429	0.91	433	49506	1.15
176	23717	0.56	265	34213	0.81	344	42567	1.07	441	49750	0.72
177.5	23855	0.85	266	34313	0.85	346	42843	1.03	451	50055	0.75
179	23994	0.48	267	34412	0.97	347	42981	1.19	452	50085	0.78
184	24497	0.71	268	34511	1.06	349	43256	1.18	453	50116	0.94
188.5	25117	0.37	269	34628	1.11	350	43394	1.12	454	50146	1
193.5	25805	0.49	270	34746	1.13	351	43532	1.03	456	50207	0.91
199	26628	0.67	271	34863	1.12	352	43669	1.12	458	50268	0.83
204	27374	0.92	272	34981	1.05	353	43807	0.68	459	50299	0.92
205	27523	0.78	273	35098	1.19	354	43945	0.76	460	50329	0.93
206	27672	0.55	274	35215	0.77	355	44083	1.07	461	50360	0.95
207	27820	0.74	276.5	35509	0.76	356	44221	0.79	463	50421	0.84
208.5	28043	0.91	278.5	35744	0.97	357	44359	0.76	464	50451	0.88
210	28266	0.57	280	35920	1.02	358	44496	1.13	466	50512	0.55
211	28415	0.91	281	36038	0.85	359	44634	1.04	468	50573	0.3
212	28564	0.98	282	36155	0.83	360	44772	1.04	471	50664	-0.14
213	28712	0.72	283	36272	0.92	361	44910	1.16	472	50741	0.14
214	28840	0.76	284	36390	0.88	362	45048	1.08	476	51169	-0.11
215	28968	0.93	285	36507	0.98	363	45186	0.94	481	51705	-0.17
216	29096	1.16	286	36625	0.86	364	45323	1.13	482	51812	-0.56
217	29224	0.8	288	36860	1.12	365	45461	1.24	484	52026	-0.2
218	29352	0.79	289	36977	1.12	366	45599	1.18	501	53847	0.02

Table 3.**S5** : Opal data versus depth in core MD09-3257.

Depth (cm)	Opal weight (%)	1SE	Opal flux ($g.cm^{-2}.kyrs^{-1}$)	1SE
245	0.96	0.06	0.017	0.001
247	1.16	0.06	0.024	0.001
250	0.82	0.17	0.015	0.003
252	0.81	0.12	0.016	0.002
255	1.10	0.01	0.025	0.000
257	0.63	0.06	0.015	0.001
341	0.86	0.26	0.033	0.010
343	0.67	0.10	0.020	0.003
347	0.61	0.13	0.016	0.003
350	0.92	0.43	0.027	0.013
352	0.55	0.02	0.021	0.001
354	0.94	0.02	0.030	0.001

3.4 Additional elements of discussion

In this chapter, I interpreted the increase in Pa/Th ratio and decrease in benthic $\delta^{13}C$ preceding southward ITCZ shifts as a reduction in the intensity of the AMOC upper circulation cell. However, one could argue that such a Pa/Th and $\delta^{13}C$ variation could also result from a shoaling of the northern-sourced water mass, giving way to a southern-sourced water mass at 2300 m depth. Because such a circulation scheme would also imply a reduction of the AMOC upper circulation cell intensity my conclusions remain valid. Note that a more complete discussion of the possible structure of the AMOC during Heinrich Stadials is provided in chapter 4.

The data I present in chapter 3 indicates that large slowdowns of the AMOC upper circulation cell took place before the onset of Heinrich Stadials. These results are in contradiction with a recent study of Lynch-Stieglitz et al. (2014), in which the strength of the Florida Current is assessed during HS1-HS3 based on the horizontal density gradient across the Florida Strait, inferred from the benthic $\delta^{18}O$ horizontal gradient at ~550 m depth. This study concluded that the strength of this current, and hence of the AMOC upper circulation cell, did not vary during HS2 and HS3. However, one of the cores used to assess the benthic $\delta^{18}O$ horizontal gradient has a very low sedimentation rate and was measured at low resolution, so that there is only one data point during HS2 and HS3. A slowdown of the AMOC upper circulation cell could thus likely be missed in their record, while our Pa/Th and benthic $\delta^{13}C$ records clearly show that Heinrich Stadial 2 is associated with a substantial AMOC slowdown.

Chapter 4: Changes in the geometry and strength of the AMOC during the last glacial

4.1 Introduction

In chapter 3, I used the sedimentary Pa/Th ratio measured in the equatorial sediment core of intermediate depth to infer changes in the renewal rate of the overlying water mass during the last glacial. I interpreted the sedimentary Pa/Th increase preceding the precipitation events as a decreased renewal rate of the northern-sourced intermediate water mass, and hence likely of the upper circulation cell of the AMOC. Indeed, a slowdown of the intermediate water mass could increase the sedimentary Pa/Th ratio by decreasing the export of dissolved protactinium. However, the replacement of the northern sourced water mass by a southern sourced water mass could cause a similar Pa/Th increase and $\delta^{13}C$ decrease in the intermediate core. Nonetheless, replacing the northern sourced water mass by a southern sourced water mass could also reflect a reduction of the upper circulation cell of the AMOC, so that the conclusions of the study would remain unchanged. Using one sediment core it was possible to assess the timing of the AMOC change with respect to the ITCZ shift but not to infer changes in the strength and geometry of the AMOC.

In order to address this issue, the sedimentary Pa/Th ratio needs to be analyzed in cores recovered from different depths and latitudes. Indeed, sedimentary Pa/Th equilibrates with the water masses occupying the first 1000 m above the seafloor (Thomas et al., 2006). Hence, previous studies used sediment cores recovered from a vertical transect on the northern Brazilian margin or from all over the Atlantic Ocean to reconstruct the strength and geometry of the AMOC at present (Lippold et al., 2011) and during the LGM (Lippold et al., 2012a).

In an ideal ocean affected by a single uniform water mass, the deviation of total protactinium and thorium concentrations from linear increase with depth at a study site is solely dependent on the water mass transfer time from the region of deep-water mass formation to the study site. At present, because the vertical extent of NADW is large (1200–4000 m depth at the equator, (Schott, 2003)), estimating the flow rate of NADW based on total protactinium and thorium concentrations is therefore possible using a simple equation (Moran et al., 2002).

However, reconstructing a more complex vertical layout of water masses of different strengths and origins based on sedimentary Pa/Th measurements is not possible using a

simple equation and requires the use of a Pa/Th model (Luo et al., 2010; Siddall et al., 2005).

To reconstruct the strength and geometry of the AMOC during the last glacial, I measured the sedimentary Pa/Th ratio in the deep equatorial sediment core (MD09-3256Q, 3537 m) over two time intervals encompassing HS2 and HS4. Along with the intermediate equatorial sediment core and with two other cores from the Bermuda Rise (Lippold et al., 2009) and from the Cape Basin (Negre et al., 2010), I study the glacial Pa/Th data of four sediment cores spanning different depths and latitudes. I compare these data to simulated Pa/Th values obtained by forcing a simple 2D Pa/Th box model with various streamfunctions (Luo et al., 2010). Streamfunctions were generated with the iLOVECLIM model under different climatic conditions (Roche et al., 2014, in press). By combining Pa/Th and $\delta^{13}C$ data, I can infer the most likely state of the AMOC during Heinrich Stadials and Dansgaard-Oeschger interstadials.

I use the $\delta^{13}C$ of the deep equatorial core (3537 m depth) in order to evaluate the influence of southern sourced water masses at the core site during the last glacial. However, a decreased $\delta^{13}C$ in the deep core can be interpreted as an increased influence of southern- compared to northern-sourced waters, or as a change in the $\delta^{13}C$ end member of the water mass affecting the core. I therefore investigated published *C. wuellerstorfi* $\delta^{13}C$ records of sediment cores below 4000-4500 m depth close to the study area. Indeed, $\delta^{13}C$ variations of similar amplitude in deep and abyssal cores could be interpreted as variations in the $\delta^{13}C$ end member of the water mass affecting the cores. However, no sediment cores were analyzed for $\delta^{13}C$ below 4000-4500 m in my study area, apart for a few whose age model is not robust enough. Hence, I cannot disentangle changes in $\delta^{13}C$ end members from changes in water masses, and therefore interpret decreases in the $\delta^{13}C$ records as increased influence of southern sourced waters.

Results of the Pa/Th data-model comparison are detailed in section 4.2, within the article entitled “Changes in the geometry and strength of the AMOC during the last glacial”. I find that interstadials of the last glacial were likely characterized by a northern-sourced circulation cell active above ~2500 m depth, and by a southern-sourced circulation cell active below. The strength of the northern sourced water mass was likely lower than present day NADW and the strength of the southern sourced water mass could have been similar to present day AABW. At the onset of Heinrich Stadials, the geometry of the AMOC changed significantly. More specifically, my data suggest that at the onset of HS2, the Atlantic Ocean was dominated by southern sourced waters below 1300 m depth.

4.2 Changes in the geometry and strength of the AMOC during the last glacial

This article has not been sent to all co-authors for an internal review yet, and minor changes are expected before submission.

Changes in the geometry and strength of the AMOC during the last glacial

Pierre Burckel[a], Claire Waelbroeck[a], Yiming Luo[b], Didier Roche[a], Sylvain Pichat[c], Jeanne Gherardi[a], Aline Govin[d], François Thil[a]

[a]LSCE/IPSL, Laboratoire CNRS-CEA-UVSQ, Bât.12, avenue de la Terrasse, F-91198 Gif sur Yvette, France

[b]Dalhousie University, Department of Oceanography, 1355 Oxford Street, PO BOX 15000, Halifax, NS B3H 4J1, Canada

[c]Laboratoire de Géologie de Lyon (LGL-TPE), Ecole Normale Supérieure de Lyon, 46 allée d'Italie, 69007 Lyon, France

[d]MARUM – Center for Marine Environmental Sciences, University of Bremen, Bremen, Germany

*Corresponding author: pierre.burckel@lsce.ipsl.fr +33 (0)1.69.82.43.47

Abstract

We study last glacial sedimentary Pa/Th in sediment cores recovered from various depths and latitude in the Atlantic Ocean. We compare these data to Pa/Th values simulated with a simple 2D box model forced with streamfunctions generated under different climatic conditions. This allows us to reconstruct the geometry and strength of the AMOC during interstadials of the 20-50 ka period. We show that circulation during interstadials was very different from that of the Holocene. Northern sourced waters were likely circulating above 2500 m depth, with a flow rate lower than that of the present day North Atlantic Deep Water (NADW). Southern sourced deep waters flowed northwards below 4000 m depth, and southwards as a return flow between 2500 and 4000 m depth. The flow rate of this southern sourced deep water could have been equivalent to that of the modern Antarctic Botton Water (AABW). At the onset of Heinrich Stadials, the structure of the AMOC significantly changed. The Atlantic Ocean was probably directly affected by a southern sourced water mass below 2500 m depth, while sluggish waters influenced depths between 1300 and 2300 m.

Introduction

Temperature variability recorded in Greenland ice cores shows that the last glacial climate repeatedly shifted between cold (stadial) and warm (interstadial) conditions (Johnsen et al., 1992), the so-called D-O cycles (Dansgaard et al., 1993). Greenland stadials typically lasted several centuries, and were followed by a rapid warming of up to 15°C achieved within a few decades (Kindler et al., 2014). Interstadial conditions then lasted several centuries, with Greenland temperatures slowly decreasing and leading to the onset of a new stadial. During some of the stadials, icebergs were released from the Laurentide ice sheet into the North Atlantic Ocean, depositing ice rafted detritus into marine sediment cores (Heinrich, 1988). We refer to these periods as Heinrich Stadials (HS).

Changes in Atlantic oceanic circulation have long been suggested to impact Greenland temperatures (Broecker et al., 1985) and could be at the origin of the DO variability. Indeed, there are numerous evidences of decreased North Atlantic deep water formation and increased influenced of southern sourced deep waters in the Atlantic Ocean during Heinrich Stadials (Elliot et al., 2002; Robinson and van de Flierdt, 2009; Vidal et al., 1997). Moreover, climate models are able to reproduce the characteristic patterns of the Dansgaard-Oeschger variability through variations of the strength of the Atlantic Meridional Overturning Circulation (AMOC) (Stocker and Johnsen, 2003). However, recent studies show that a shallow circulation cell could have been still active during Heinrich Stadials (Gherardi et al., 2009; Lynch-Stieglitz et al., 2014), meaning that other mechanisms could be required to explain Greenland temperature variability. Further

understanding the vertical layout and flow rate of the water masses constituting the AMOC during the last glacial is therefore required before assessing the relationship between AMOC and DO variability.

Sedimentary $(^{231}Pa/^{230}Th)_{xs,0}$ (activity ratio of ^{231}Pa and ^{230}Th unsupported by lithogenic and authigenic uranium and corrected from decay to the time of sediment deposition, Pa/Th hereafter)(Yu et al., 1996) has been used in the Atlantic to infer changes in oceanic circulation intensity during Heinrich Stadials (Gherardi et al., 2005; Gherardi et al., 2009; McManus et al., 2004; Yu et al., 1996) (Burckel et al., in prep). Although a recent study questions the ability of dissolved Pa/Th to reflect the flow rate of water masses in the south Atlantic (Deng et al., 2014), several studies comparing simulated sedimentary Pa/Th values to core top Pa/Th data have shown that sedimentary Pa/Th reflects circulation intensity in the modern Atlantic Ocean (Lippold et al., 2011; Siddall et al., 2005).

However, interpretation of sedimentary Pa/Th on a single sediment core might be complicated by the non-linear response of Pa/Th to circulation intensity changes (Luo et al., 2010). Reconstructing present and past strength of the AMOC is therefore best achieved by studying sediment cores at different depths and latitudes (Gherardi et al., 2009; Lippold et al., 2011; Lippold et al., 2012).

In this study, we present new sedimentary Pa/Th data from a deep sediment core retrieved off the Brazilian margin. We compare last glacial Pa/Th values of sediment cores from different depths and latitudes to Pa/Th values simulated using a simple 2D box model (Luo et al., 2010) forced by various streamfunctions. The streamfunctions were simulated with the Earth System model iLOVECLIM under different climatic conditions (Roche et al., 2014, in press). Results from this comparison allow us to constrain the geometry and strength of the AMOC during DO interstadials and Heinrich Stadials.

Study area

Sediment cores MD09-3257 (04°14.69'S, 36°21.18'W, 2344m water depth) and MD09-3256Q (03°32.81'S, 35°23.11'W, 3537m water depth) were recovered from the Brazilian margin during R/V Marion Dufresne cruise MD173/RETRO3 (Fig. 1). Core GeoB3910 (04°14.7'S, 36°20.7'W, 2362m water depth) (Jaeschke et al., 2007) was recovered at approximately the same position and depth as core MD09-3257, during Meteor cruise M34/4. We therefore refer to both GeoB3910 and MD09-3257 as intermediate equatorial cores, and to MD09-3256Q as the deep equatorial core. At present, the water mass influencing the Brazilian margin at these depths is the southward flowing North Atlantic Deep Water (NADW), a water mass originating from the Nordic seas and influencing most of the deep Atlantic Ocean (Fig. 1). Because the Brazilian margin is

affected by western boundary currents (Rhein et al., 1995), these sediment cores are ideally located to observe changes in the strength and extent of the intermediate and deep AMOC water masses (Schott, 2003).
We compare our Pa/Th data with published records from other Atlantic cores: ODP Leg 172 site 1063 (33°41'N, 57°37'W, 4584 m) (Lippold et al., 2009) and MD02-2594 (34°43'S, 17°20'E, 2440 m) (Negre et al., 2010) (Fig. 1).

Material and method

Benthic $\delta^{13}C$

$\delta^{13}C$ ($^{13}C/^{12}C$ isotopic ratio) of the epifaunal benthic foraminifer *Cibicides wuellerstorfi* has been shown to record the $\delta^{13}C$ of bottom water dissolved inorganic carbon (DIC) with minor isotopic fractionation (Duplessy et al., 1984; Zahn et al., 1986). Initial DIC carbon isotopic concentration is acquired by a water mass in its formation region by surface productivity, which consumes ^{12}C therefore increasing dissolved $\delta^{13}C$, and temperature dependent air-sea interactions (Lynch-Stieglitz et al., 1995; Rohling and Cooke, 1999). The $\delta^{13}C$ of the DIC then evolves as deep-water ages, because of the constant export of ^{12}C enriched biogenic material remineralized at depth, which decreases the DIC $\delta^{13}C$ along the flow path of the water mass. As DIC $\delta^{13}C$ largely follows water mass structure and circulation in the modern ocean, *Cibicides* $\delta^{13}C$ has been used to trace water masses, a decrease in *Cibicides* $\delta^{13}C$ being interpreted as a decrease in bottom water ventilation, and conversely (Duplessy et al., 1988). However, the information on bottom water ventilation embedded in *Cibicides* $\delta^{13}C$ is complicated by the impact of changes in surface water $\delta^{13}C$ and marine biological productivity.
Holocene and last glacial end member $\delta^{13}C$ values are systematically higher in northern sourced waters (1.1 and 1.5 ‰ respectively) than in southern sourced waters (0.3 and -0.2 ‰ respectively) (Curry et al., 1988; Curry and Oppo, 2005). Because the modern variability of DIC $\delta^{13}C$ largely follows the structure of water masses in the Atlantic Ocean (Kroopnick, 1985), we interpret a decrease in the $\delta^{13}C$ values as an increased influence of nutrient-rich southern sourced deep waters.

Core MD09-3256Q benthic foraminifer *C. wuellerstorfi* were handpicked (>250µm fraction), washed with methanol in an ultrasonic bath then roasted in glass vials at 380°C under vacuum for 45 min. *C. wuellerstorfi* $\delta^{13}C$ (expressed in ‰ VPDB) were measured at LSCE (Gif-sur-Yvette) using an Elementar Isoprime mass spectrometer. VPDB is defined with respect to NBS-19 calcite standard ($\delta^{18}O$ = -2.20 ‰ and $\delta^{13}C$ = +1.95 ‰) (Coplen, 1988). The mean external reproducibility (1σ) of carbonate

standards is ± 0.05 ‰ for $\delta^{18}O$ and ± 0.03 ‰ for $\delta^{13}C$; measured NBS-18 $\delta^{18}O$ is -23.2 ± 0.2 ‰ VPDB and $\delta^{13}C$ is -5.0 ± 0.1 ‰ VPDB. $\delta^{13}C$ measurements were done at the highest possible resolution, depending on the availability of C. *wuellerstorfi* (generally every 1 to 2 cm).

Sedimentary Pa/Th

In contrast to *C. wuellerstorfi* $\delta^{13}C$, which reflects the nutrient content of water masses, sedimentary Pa/Th is a relatively recent proxy that records the renewal rate of water masses occupying the first 1000 m above the seafloor (Thomas et al., 2006). Hence, the proxy has been successfully used as a tracer of oceanic circulation intensity in the Atlantic Ocean (Gherardi et al., 2005; Gherardi et al., 2009; McManus et al., 2004).

^{231}Pa and ^{230}Th are produced at a constant Pa/Th activity ratio of 0.093 by dissolved uranium, which is homogeneously distributed in the oceans. ^{230}Th is however much more particle reactive than ^{231}Pa, as reflected by their respective residence time in the ocean (30-40 y for ^{230}Th, 200 y for ^{231}Pa (Francois, 2007)). ^{230}Th is therefore rapidly removed to the underlying sediment, while ^{231}Pa can be laterally exported by oceanic currents. High flow rates therefore result in high ^{231}Pa export and low sedimentary Pa/Th ratio, and conversely. However, affinities of ^{231}Pa and ^{230}Th for settling particles depend on the particle type (Chase et al., 2002). For instance, ^{231}Pa has a high affinity for opal, so that high opal fluxes can result in a high sedimentary Pa/Th ratio. The origin of sedimentary Pa/Th variability therefore needs to be carefully assessed.

Pa/Th measurements were performed by isotopic dilution mass spectrometry on a Thermo finnigan MC-ICP-MS Neptune, following the method of Guihou et al., 2010. Pa and Th are decay corrected to the time of sediment deposition and from the lithogenic component by using a $^{238}U/^{232}Th$ ratio of 0.5±0.1 (Fig. S1) (Guihou et al., 2010)(Burckel et al., 2014 a, in prep.).

Age model

For the period between 0-27 ka, core MD09-3256Q age model is based on 6 ^{14}C dates measured on planktic foraminifer *G. ruber* white and converted to calendar age using the Marine13 curve (Reimer et al., 2013) (Fig. S2). During the last glacial, Heinrich Stadials were recorded in marine sediment cores from the Brazilian margin as Ti/Ca peaks, related to the increased terrigenous input associated with the southward shifts of the ITCZ (Jaeschke et al., 2007). Ti/Ca peaks are therefore good stratigraphic markers for correlating sediment cores with neighboring well-dated cores. Therefore, from 27 ka to 50 ka, core MD09-3256Q was dated by correlation of its Ti/Ca signal with that of core GeoB3910 using 3 tie points corresponding to the Ti/Ca peaks associated with HS3-5. Resulting sedimentation rates are shown in Fig. S3. The age model is given in Table S1.

Circulation and Pa/Th model

The Pa/Th data of the studied sediment cores were compared to Pa/Th values simulated using a simple 2D box model forced by different streamfunctions, in order to assess the vertical layout and renewal rate of the water masses constituting the AMOC of the last glacial. Streamfunctions were generated using the iLOVECLIM coupled climate model, with atmosphere (ECBilt), ocean (CLIO) and vegetation (VECODE) components (Roche et al., 2014, in press). A Last Glacial Maximum equilibrium state, computed using the PMIP-2 protocol, was used as background climate (see (Roche et al., 2007) for more details). Streamfunctions corresponding to Heinrich Stadial 1 (HS1) and to a complete shutdown of the AMOC (off-mode) were generated by imposing a 0.16 and 0.35 Sv freshwater forcing in the Labrador Sea (Roche et al., 2010) (Roche et al., 2014, in press), respectively. Freshwater forcing was maintained for 300 y, and the streamfunction generated 300 y after the end of the forcing. A freshwater input of 0.16 Sv allows the presence of a shallow circulation cell in the Atlantic Ocean, while at 0.35 Sv the AMOC is almost completely shutdown.

Pa/Th values were simulated along a meridional section in the Atlantic Ocean by forcing a simple 2D box model (Luo et al., 2010) with the aforementioned streamfunctions (Fig. 2). Holocene simulated Pa/Th values and streamfunction are described in Lippold et al., 2012 and Luo et al., 2010.

Dissolved Pa and Th concentrations in the model are controlled by (1) production from U decay in the water column, (2) adsorption and desorption on settling particles and (3) advection by oceanic circulation. Particulate Pa and Th concentrations are controlled by (1) adsorption and desorption from the dissolved pool and (2) by removal of sedimentary particles to the seafloor.

Modeled Pa/Th meridional sections generated with the different streamfunctions are shown in Figure 2. Different water mass configurations can generate sedimentary Pa/Th variations in the model (Luo et al., 2010). Increasing circulation intensity above a specific location will cause Pa/Th to decrease at that depth because of the increased Pa export and conversely. Increasing depth without modifying circulation intensity also causes the sedimentary Pa/Th ratio to decrease in the model because of the increased residence time of Pa with respect to scavenging and conversely. Finally, the sedimentary Pa/Th ratio increases along the flow path of any water mass as the low dissolved Pa concentrations of newly formed water masses increase by desorption of Pa from Pa-concentrated settling particles equilibrating with ambient waters (Francois, 2007). Adsorption and desorption rate constants also impact the simulated Pa/Th ratio. These constants were adjusted to reflect the opal belt in the southern ocean for all Pa/Th

simulations (Luo et al., 2010). For the Holocene, these constants were also changed to reflect opal in the northern North Atlantic (Lippold et al., 2012).

Results

Sedimentary Pa/Th data

Core MD09-3257 and MD09-3256Q Pa/Th measurements were focused on HS2 and HS4 (Fig. 3, a). No Pa/Th values were measured within HS2 in core MD09-3257 because of the presence of turbidite layers (Burckel et al., 2014 b, in prep). During HS4 and before HS2, the sedimentary Pa/Th ratio of core MD09-3257 rises above the production ratio of 0.093, indicating the absence of protactinium export. Pa/Th variability associated with DO stadials and interstadials is also observed, with high Pa/Th values occurring during stadials and low values during interstadials. Pa/Th variations in core MD09-3256Q are more muted, so that the Pa/Th signal of core MD09-3257 drives the Pa/Th difference between the two cores. The main Pa/Th variation in core MD09-3256Q occurs during HS4, when Pa/Th values rise from ~0.06 to ~0.08.

Before interpreting our Pa/Th signals in terms of oceanic circulation, we need to assess if varying lithogenic or opal fluxes impacted the scavenging intensities of Pa and Th. To do so, we use the preserved opal and ^{232}Th fluxes as proxies of past opal and terrigenous fluxes respectively (Anderson et al., 2006; Lippold et al., 2012). Core MD09-3257 Pa/Th data are mainly influenced by oceanic circulation, except during the high lithogenic flux period associated with HS4 (Fig. 3, a, white squares) (Burckel et al., 2014 b, in prep). In core MD09-3256Q, opal fluxes do not covary with the Pa/Th ratio and are very low (0.01-0.025 $g.cm^{-2}.kyr^{-1}$) (Fig. S4). In the Atlantic Ocean, the lower opal flux limit observed to impact the sedimentary Pa/Th ratio is 0.2 $g.cm^{-2}.kyr^{-1}$ (Lippold et al., 2012). Hence, given the much lower opal fluxes recorded in core MD09-3256Q and their lack of correlation with sedimentary Pa/Th, we conclude that biogenic silica had a minor influence if any on the Pa/Th variability. In contrast, ^{232}Th fluxes seem to correlate with the Pa/Th ratio (P value = 0.0003, n = 20) (Fig. S5). This relation appears to be driven by the high Pa/Th values occurring during the period of increased terrigenous fluxes associated with HS4. Not considering these values, the Pa/Th appears to vary independently from the terrigenous fluxes (P value = 0.79, n = 15). As such, we can unfortunately not determine if the Pa/Th increase during HS4 is associated with a flow rate decrease of the water mass above the sediment core. Increased Pa/Th could indeed be due to the higher lithogenic fluxes that would enhance Pa scavenging and increase the sedimentary Pa/Th ratio. Given the uncertainty on the cause of the Pa/Th rise, we present the Pa/Th data within HS4 with different symbols (Fig. 3). Besides the period of high terrigenous fluxes characterizing HS4, we can safely assume that the Pa/Th

variability recorded in our equatorial cores is mainly driven by changes in the flow rate of the water masses occupying the bottom 1000 m at our core sites.

C. *wuellerstorfi* $\delta^{13}C$ *data*

The Holocene $\delta^{13}C$ value of the deep equatorial core was measured at 1.37 ‰, which is assumed to be the modern $\delta^{13}C$ value of NADW at our sites. No *C. wuellerstorfi* could be found during the late Holocene in the intermediate core.

$\delta^{13}C$ values of the last glacial are lower than during the Holocene (Fig. 3), which could indicate a general increased influence of southern sourced water masses on both intermediate and deep sediment cores. It could also reflect the less developed continental biosphere associated with glacial periods (Duplessy et al., 1988).

$\delta^{13}C$ values in the deep core are systematically lower than values in the intermediate core. This could reflect an increased influence of the deep southern sourced water mass with depth. $\delta^{13}C$ of both cores shows millennial scale variability, with low $\delta^{13}C$ values occurring during Heinrich Stadials. DO stadials and interstadials are also recorded in the $\delta^{13}C$ record of the intermediate core by low and high $\delta^{13}C$ values respectively. In the deep core, the low sedimentation rate could have smoothed out the $\delta^{13}C$ decrease associated with the short DO stadials.

Time slice definition

We define 4 time slices to compare the Pa/Th data of the Brazilian margin and Bermuda Rise cores to Pa/Th values simulated with the different streamfunctions (Fig. 3). We do not study core MD02-2594 within the time slices, as Pa/Th during the 20-50 ka period is measured at low resolution in the core (Fig. S6).

Pre-HS2, Post-HS4 and Pre-HS4 time slices are defined as the periods of low equatorial sedimentary Pa/Th values preceding (Pre-) or following (Post-) Heinrich Stadials 2 and 4 (Fig. 3). Pa/Th data are considered low when they equal the minimum Pa/Th value preceding or following the Heinrich Stadial of interest within 1-sigma uncertainties. For Pre-HS2, low Pa/Th values were defined in core MD09-3257, as the Pa/Th signal of core MD09-3256Q presents no variability within 1-sigma uncertainties across the transition towards Heinrich Stadial 2.

We consider that these time slices represent interstadial conditions. Indeed, the Post-HS4 time slice corresponds to DO8, and is characterized by low Pa/Th values, high $\delta^{13}C$ values and high Greenland temperatures (Fig. 3). Pre-HS4 encompasses both DO10 and the short stadial between DO9 and DO10. However, given dating uncertainties as well as the high $\delta^{13}C$ and low Pa/Th at that time in the equatorial core of intermediate depth, we conclude that Pre-HS4 probably recorded interstadial conditions. Pre-HS2 recorded DO3 as well as the two stadials preceeding and following DO3. Given dating uncertainties and

the high $\delta^{13}C$ and low Pa/Th of both equatorial cores at that time, we consider that the Pre-HS2 time slice reflects interstadial conditions.

The HS2 time slice was defined in core MD09-3257 during the period of decreased sedimentary Pa/Th variation with time after the abrupt rise associated with the onset of HS2.

The HS2 time slice probably corresponds to the stadial conditions associated with Heinrich Stadial 2. Indeed, at that time, Pa/Th data of core MD09-3257 are already above the production ratio, Pa/Th data at ODP site 1063 reached their stadial values and Pa/Th data in core MD09-3256Q are similar before and during HS2. Moreover, the $\delta^{13}C$ of both equatorial cores nearly reached their low $\delta^{13}C$ values associated with HS2. Sedimentary Pa/Th values associated to each time slice and cores are given in Table S2.

Discussion

Interstadials

Pa/Th data from the Brazilian margin and Bermuda Rise cores are compared, when available, to the Pa/Th model forced by the different streamfunctions (Fig. 4-6). We often describe the modeled and measured sedimentary Pa/Th of the equatorial cores by referring to the vertical Pa/Th gradient between 2300 and 3500 m (i.e. the depths of the sediment cores). Indeed, vertical Pa/Th gradients are useful indicators of the vertical layout of water masses. A large gradient indicates that the Pa/Th of the deep core is significantly lower than the Pa/Th of the intermediate core. A small gradient indicates that sedimentary Pa/Th values of both cores are similar. In what follows, we will see how each vertical gradient can be interpreted.

A large vertical Pa/Th gradient between the two equatorial core sites is simulated by the model in the presence of a southward flowing northern-sourced deep water mass such as NADW in the Holocene simulation (Fig. 4). This is due to the fact that within a single water mass of uniform flow rate, the sedimentary Pa/Th ratio decreases with depth. This effect is intensified in the case of the Holocene streamfunction, as the flow rate of NADW is not uniform but stronger between 2500-3500 m and weaker between 1300-2300 m (depths of acquisition of sedimentary Pa/Th for the deep and intermediate cores respectively). Hence, Pa export at 3500 m is more intense than at 2300 m, therefore significantly increasing the vertical Pa/Th gradient between the two cores.

Interstadial Pa/Th data in the deep equatorial and Bermuda Rise cores are consistent with simulated Pa/Th values obtained with the Holocene streamfunction (Fig. 4, b-d). However, interstadial sedimentary Pa/Th values in the equatorial core at intermediate depth are lower than predicted by the Pa/Th model forced with the Holocene streamfunction. The vertical Pa/Th gradient between our equatorial cores is therefore small, which is in contradiction with the large vertical Pa/Th gradient generated by the

Holocene streamfunction. Moreover, data from Southern Ocean core MD02-2594 are systematically below 0.06 during the last glacial (Fig. S6), and are in conflict with the high simulated Holocene Pa/Th value (~0.09) at 34°S and ~2400 m depth.
High $\delta^{13}C$ values in the intermediate equatorial core during MIS3 interstadials suggest that northern-sourced deep waters influenced the equatorial Atlantic at 2300 m depth (Fig. 3, b). However, the lower $\delta^{13}C$ values of the deep equatorial core imply that, unlike in the present day Atlantic Ocean, nutrient rich southern sourced deep waters were influent at 3500 m depth.
Therefore, both Pa/Th and $\delta^{13}C$ data indicate that the geometry and strength of the AMOC during interstadials was different from that of the Holocene.

Pa/Th values simulated with the off-mode streamfunction exhibit a small vertical Pa/Th gradient between the two equatorial cores (Fig. 5). However, measured sedimentary Pa/Th during interstadials are much lower than the simulated values at both equatorial sites. Low measured Pa/Th values imply a significant export of Pa by oceanic circulation and therefore exclude the possibility of an almost halted oceanic circulation above 2300 and 3500 m depth (Fig. 5, b-d).
In the off-mode streamfunction, no deep convection occurs in the high latitude North Atlantic. However, the high $\delta^{13}C$ values of the intermediate equatorial core indicate that northern sourced waters were influent at 2300 m.
Hence, it is highly unlikely that the off-mode streamfunction depicts the Atlantic Oceanic circulation during interstadials of the last glacial.

The HS1 streamfunction also generates a small vertical Pa/Th gradient between our equatorial cores (Fig. 6). In contrast to the simulation obtained with the off-mode streamfunction, this small vertical Pa/Th gradient is associated with significant lateral export of Pa at the depth of both the intermediate and deep equatorial cores, as well as at the Bermuda Rise and Southern Ocean cores, consistently with Pa/Th data (Fig. 6, b-d). Such a small vertical Pa/Th gradient is simulated in the case of two water masses overlying each other and flowing in opposite directions (Fig. S7) (Lippold et al., 2012). This circulation scheme results in decreasing or invariant lateral export of Pa with depth, which in turns causes sedimentary Pa/Th to increase or to be constant with depth.
Interstadial benthic $\delta^{13}C$ values indicate a strong northern-sourced water mass influence at the intermediate core site, on the one hand, and a strong southern-sourced water mass influence at deep core sites, on the other hand (Fig. 3, b). Hence, benthic $\delta^{13}C$ data support the existence of two water masses overlying each other and flowing in opposite directions.

Combining the information provided by sedimentary Pa/Th and benthic $\delta^{13}C$ data, we reach the following conclusions concerning the Atlantic circulation below ~1300 m depth during interstadials of the last glacial: southward-flowing northern-sourced deep water likely circulated down to ~2500 m depth, while southern-sourced deep water circulated northwards below ~4000 m depth, and southwards as a return flow between ~2500 and 4000 m depth (Fig. 7, a).

Estimation of the AMOC intensity during interstadial time slices

Our Holocene Pa/Th values agree with previously published data from the Brazilian margin (Lippold et al., 2011) and with Pa/Th values simulated with a 2 and 3 fold increased Holocene streamfunction (Fig. S8). At present, increasing the Holocene streamfunction is indeed necessary for a good correspondence of simulated and measured equatorial Pa/Th values. This increase was proposed to account for the absence of west-east difference in circulation strength in the 2D Pa/Th model, which instead reflects an averaged circulation (Lippold et al., 2011). Moreover, the width of the Atlantic basin is the shortest at the equator, while it is assumed constant in the model. Both these effects could cause the flow speed at the equator to be underestimated, and therefore the simulated Pa/Th ratio to be overestimated.

It is unclear whether the same relationship can apply to the HS1 streamfunction. Sensitivity tests of the Pa/Th model to varying flow rates were performed by multiplying the HS1 streamfunction by a factor 0.5, 1.5, 2 and 3. Results indicate that a factor of 1 (no change in the streamfunction) best reproduces the sedimentary Pa/Th ratio at the equator (Table S3). In the HS1 streamfunction, the strength of both the northern and southern sourced water masses at the equator is of 5-10 Sv. As this streamfunction is the most consistent with our interstadial data, we assume as an extreme that the real flow rate of the water masses was 3 times lower during interstadials, as this is the highest factor applied to the Holocene streamfunction to reconcile simulated and observed Pa/Th data at present. Hence, we obtain a flow rate range of 2-3 Sv for both northern and southern sourced water masses. As another extreme, we assume that the water masses flow rates provided by the HS1 streamfunction (5-10 Sv) depict well the oceanic circulation strength during interstadials of the last glacial. We conclude that the flow rate of the northern and southern sourced water masses affecting the intermediate and deep equatorial cores respectively was probably of 2-10 Sv.

At present, the northern sourced circulation cell is initiated by the formation of NADW in the high latitude North Atlantic, and the southern sourced circulation cell by the formation of the Antarctic Abyssal Bottom Water (AABW) in the southern Ocean. The modern flow rate of NADW and AABW is respectively of 23 ± 3 Sv and ~6 ± 1.3 Sv at the

equator (Ganachaud and Wunsch, 2000). We conclude that during interstadials of the last glacial, the flow rate of the southern sourced deep water was approximately similar to present day AABW, and that the flow rate of the northern sourced deep water was smaller than present day NADW.

Stadials

Pa/Th data from the HS2 time slice display a large vertical Pa/Th gradient between the depths of our equatorial cores (Fig. 6, a). The gradient is initiated by the high Pa/Th value at intermediate depth, which indicates that the core was overlain by sluggish waters. Pa/Th data in the equatorial core are therefore incompatible with the low vertical Pa/Th gradient simulated by the HS1 streamfunction (Fig. 6).

Moreover, the diminution of the $\delta^{13}C$ values of both equatorial cores during HS2 suggests an increased influence of southern sourced deep waters in the Atlantic Ocean at both 3500 and 2300 m depth, which is incompatible with the northern sourced circulation cell active above 2500 m in the HS1 streamfunction (Fig. 3, b).

Hence, circulation and ventilation proxies indicate that there was no northern sourced water mass between 1300 and 2300 m depth at the equator during HS2. The AMOC during Heinrich Stadial 2 is therefore not well depicted by the HS1 streamfunction.

Large vertical Pa/Th gradients are simulated in the model when a single water mass affects both equatorial cores. Pa/Th values simulated with the Holocene streamfunction therefore best fit Pa/Th data during HS2 (Fig. 4, a). However, as discussed before, data from Southern Ocean core MD02-2594 are systematically below 0.06 during the last glacial, in contradiction with the high simulated Holocene Pa/Th values at the site of the core (0.09).

Moreover, the very low $\delta^{13}C$ values measured in both equatorial cores during Heinrich Stadials (Fig. 3, b) exclude the presence of a northern sourced deep-water mass affecting the equatorial Atlantic at that time.

Hence, it is unlikely that the Holocene streamfunction depicts the geometry and strength of the AMOC during Heinrich Stadials.

In contrast, Pa/Th values simulated with the off-mode streamfunction could reconcile the large Pa/Th vertical gradient and the low $\delta^{13}C$ of equatorial cores (Fig. 5, a). However, in the current off-mode simulation by the iLOVECLIM model, the vertical extent of the southern sourced water mass is not large enough to influence the core at 3500 m depth, resulting in an apparent low vertical Pa/Th gradient (Fig. 2, c,d). However, the model was run for a short period of time, preventing a significant response of the southern sourced deep waters to varying climatic and oceanographic conditions

(Roche et al., 2014, in press). With a slightly increased vertical extent, the southern sourced deep water would induce a low sedimentary Pa/Th ratio in the deepest core of the Brazilian margin, resulting in a large vertical Pa/Th gradient between the depths of our equatorial cores in agreement with our Pa/Th data. Pa/Th data from the Bermuda Rise core are also consistent with simulated Pa/Th values from the off-mode streamfuntion.

The very low $\delta^{13}C$ values measured in both equatorial cores during Heinrich Stadials are consistent the off-mode streamfunction, which shows a strong influence of southern sourced water masses at both our equatorial sites.

This is further supported by the increased ε_{Nd} in the Bermuda Rise core (Gutjahr and Lippold, 2011). Indeed, as the isotopic composition of neodymium varies from non-radiogenic (low ε_{Nd}) along the Atlantic Ocean, to radiogenic (high ε_{Nd}) along the Pacific Ocean, ε_{Nd} indicates the origin of the water masses affecting sediment cores (Jeandel et al., 2007; Lacan and Jeandel, 2005; Lacan et al., 2012). High ε_{Nd} at ODP site 1063 therefore indicates an increased influence of southern sourced water masses at 4500 m in the North Atlantic Ocean.

Considering that both Pa/Th and water mass proxies suggest an increased influence of southern sourced water at the equatorial and Bermuda Rise sites, the off-mode streamfunction likely depicts the geometry of the AMOC during HS2, i.e. southern sourced deep waters likely dominated the Atlantic Ocean below 1300 m (Fig. 7, b). However, the direct influence of the southern sourced water mass probably extended vertically above 3500 m depth, as indicated by the low Pa/Th value of the deep equatorial core. The absence of Pa export on the intermediate depth core indicates that a sluggish water mass of unknown origin likely influenced the equatorial Atlantic between 1300 and 2300 m depth.

We do not calculate the flow rate of the southern sourced water mass during Heinrich Stadial 2. Indeed, the streamfunction does not yet reproduce the large Pa/Th gradient we observe. We therefore cannot test the sensitivity of the simulated Pa/Th to varying flow rates, which is necessary to assess the flow rate of the southern sourced water mass.

Conclusion

During interstadials of the last glacial, the geometry and strength of the AMOC was markedly different from that of the modern AMOC. A northern sourced water mass circulated above 2500 m depth at a flow rate of 2-10 Sv, which is significantly lower than the intensity of present day NADW. Below 4000 m depth, a southern sourced deep water mass flowed northward, with an intensity of 2-10 Sv, which encompasses the strength of modern AABW. Between 2500 and 4000 m depth, the southern sourced deep

water likely circulated southwards as a return flow. At the onset of Heinrich Stadials, the geometry of the AMOC changed and below 1300 m depth, the Atlantic Ocean was probably dominated by a single southern sourced water mass that can be traced up to 35°N at 4500 m depth. This water mass probably directly affected the equatorial Atlantic between 2500 and 3500 m depth. A sluggish and poorly ventilated water mass circulated between 1300 and 2300 m at the equator, but is origin is difficult to assess

Acknowledgments
Pa/Th measurements were funded by the CNRS/INSU LEFE project ACCENT. This work is a contribution to the RETRO project, a joint European Science Foundation (ESF)/EUROMARC, funded by Research Council of Norway (RCN), France (CNRS/INSU), Germany, and the Netherlands. Cores MD09-3256Q and MD09-3257 were collected on board R/V Marion Dufresne during RETRO Cruise III, supported by ESF EUROMARC project RETRO, IPEV and ANR project ANR-09-BLAN-0347. We thank the IPEV team, crew members of R/V Marion Dufresne and all scientists who participated in RETRO Cruise III. We are thankful to M. Roy-Barman for expert advices on Pa/Th measurements on LSCE MC-ICP-MS. We acknowledge C. Moreau, J.-P. Dumoulin, and the UMS ARTEMIS for AMS ^{14}C dates. This is LSCE contribution xxxx.

References

Anderson, R. F., Fleisher, M. Q., and Lao, Y.: Glacial-interglacial variability in the delivery of dust to the central equatorial Pacific Ocean, Earth and Planetary Science Letters, 242, 406-414, 2006.
Broecker, W. S., Peteet, D. M., and Rind, D.: Does the ocean-atmosphere system have more than one stable mode of operation?, Nature, 315, 21-26, 1985.
Burckel, P., Henry, G., Ng, H. C., Lippold, J., Pichat, S., Roy Barman, M., Thil, F., Antz, B., Gherardi, J. M., Waelbroeck, C., McManus, J. F., Robinson L. F. : Methodological recommendations for the analysis of sedimentary Pa/Th, in prep., 2014 a.
Burckel, P., Waelbroeck, C., Gherardi, J. M., Pichat, S., Arz, H., Lippold, J., Dokken, T., Thil, F. : Atlantic Ocean circulation changes preceded millennial tropical South America rainfall events during the last glacial, in prep., 2014 b.
Chase, Z., Anderson, R. F., Fleisher, M. Q., and Kubik, P. W.: The influence of particle composition and particle flux on scavenging of Th, Pa and Be in the ocean, Earth and Planetary Science Letters, 204, 215-229, 2002.
Coplen, T. B.: Normalization of oxygen and hydrogen isotope data, Chem. Geol., 72, 293-297, 1988.
Curry, W. B., Duplessy, J. C., Labeyrie, L. D., and Shackleton, N. J.: Changes in the distribution of partial derivative c-13 of deep water sigma co2 between the last glaciation and the holocene, Paleoceanography, 3, 317-341, 1988.
Curry, W. B. and Oppo, D. W.: Glacial water mass geometry and the distribution of d13C of SCO2 in the western Atlantic Ocean, Paleoceanography, 20, doi:10.1029/2004PA001021, 2005.

Dansgaard, W., Johnsen, S. J., Clausen, H. B., Dahl-Jensen, D., Gundestrup, N. S., Hammer, C. U., Hvidberg, C. S., Steffensen, J. P., Sveinbjörnsdottir, A. E., Jouzel, J., and Bond, G.: Evidence for general instability of past climate from a 250-kyr ice-core record, Nature, 364, 218-220, 1993.
Deng, F., Thomas, A. L., Rijkenberg, M. J. A., and Henderson, G. M.: Controls on seawater Pa-231, Th-230 and Th-232 concentrations along the flow paths of deep waters in the Southwest Atlantic, Earth and Planetary Science Letters, 390, 93-102, 2014.
Duplessy, J.-C., Shackleton, N. J., Fairbanks, R. G., Labeyrie, L., Oppo, D., and Kallel, N.: Deepwater source variations during the last climatic cycle and their impact on the global deepwater circulation, Paleoceanography, 3, 343-360, 1988.
Duplessy, J.-C., Shackleton, N. J., Matthews, R. K., Prell, W., Ruddiman, W. F., Caralp, M., and Hendy, C. H.: 13C record of benthic foraminifera in the last interglacial ocean : implications for the carbon cycle and the global deep water circulation, Quaternary Research, 21, 225-243, 1984.
Elliot, M., Labeyrie, L., and Duplessy, J. C.: Changes in North-Atlantic deep-water formation associated with the Dansgaard-Oeschger temperature oscillations (60-10 ka), Quaternary Science Reviews, 21, 1153-1165, 2002.
Francois, R.: Proxies in Late Cenozoic Paleoceanography: Paleoflux and Paleocirculation from Sediment 230Th and 231Pa/230Th, Elsevier, 2007.
Ganachaud, A. and Wunsch, C.: Improved estimates of global ocean circulation, heat transport and mixing from hydrographic data, Nature, 408, 453-457, 2000.
Gherardi, J.-M., Labeyrie, L., McManus, J., Francois, R., Skinner, L., and Cortijo, E.: Evidence from the North Eastern Atlantic Basin for Variability of the Meridional Overturning Circulation through the last Deglaciation, Earth and Planetary Science Letters, 240, 710-723, 2005.
Gherardi, J.-M., Labeyrie, L., Nave, S., Francois, R., McManus, J. F., and Cortijo, E.: Glacial-interglacial circulation changes inferred from 231Pa/230Th sedimentary record in the North Atlantic region, Paleoceanography, 24, doi:10.1029/2008PA001696, 2009.
Guihou, A., Pichat, S., Nave, S., Govin, A., Labeyrie, L., Michel, E., and Waelbroeck, C.: Late slowdown of the Atlantic Meridional Overturning Circulation during the Last Glacial Inception: new constraints from sedimentary (231Pa/2303 Th), Earth and Planetary Science Letters, 289, 520-529, 2010.
Gutjahr, M. and Lippold, J.: Early arrival of Southern Source Water in the deep North Atlantic prior to Heinrich event 2, Paleoceanography, 26, 2011.
Heinrich, H.: Origin and consequences of cyclic ice-rafting in the Northeast Atlantic ocean during the past 130000 years, Quaternary Research, 29, 142-152, 1988.
Jaeschke, A., Rühlemann, C., Arz, H., Heil, G., and Lohmann, G.: Coupling of millennial-scale changes in sea surface temperature and precipitation off northeastern Brazil with high-latitude climate shifts during the last glacial period, Paleoceanography, 22, PA4206, doi:4210.1029/2006PA001391, 2007.
Jeandel, C., Arsouze, T., Lacan, F., Techine, P., and Dutay, J. C.: Isotopic Nd compositions and concentrations of the lithogenic inputs into the ocean: A compilation, with an emphasis on the margins, Chemical Geology, 239, 156-164, 2007.
Johnsen, S. J., Clausen, H. B., Dansgaard, W., Fuhrer, K., Gundestrup, N., Hammer, C. U., Iversen, P., Jouzel, J., Stauffer, B., and Steffensen, J. P.: Irregular glacial interstadials recorded in a new Greenland ice core, Nature, 359, 311-313, 1992.
Kindler, P., Guillevic, M., Baumgartner, M., Schwander, J., Landais, A., and Leuenberger, M.: Temperature reconstruction from 10 to 120 kyr b2k from the NGRIP ice core, Climate of the Past, 2014. 2014.

Kroopnick, P. M.: The distribution of 13C of SCO2 in the world oceans, Deep-Sea Research, Part A, 32, 57-84, 1985.
Lacan, F. and Jeandel, C.: Acquisition of the neodymium isotopic composition of the North Atlantic Deep Water. , Geochemistry Geophysics Geosystems, 6, Q12008, doi:12010.11029/12005GC000956
, 2005.
Lacan, F., Tachikawa, K., and Jeandel, C.: Neodymium isotopic composition of the oceans: A compilation of seawater data, Chemical Geology, 300, 177-184, 2012.
Lippold, J., Gherardi, J.-M., and Luo, Y.: Testing the 231Pa/230Th paleocirculation proxy: A data versus 2D model comparison, Geophys. Res. Lett., 38, doi:10.1029/2011GL049282, 2011.
Lippold, J., Gruetzner, J., Winter, D., Lahaye, Y., Mangini, A., and Christl, M.: Does sedimentary Pa-231/Th-230 from the Bermuda Rise monitor past Atlantic Meridional Overturning Circulation?, Geophysical Research Letters, 36, 2009.
Lippold, J., Luo, Y., Francois, R., Allen, S. E., Gherardi, J., Pichat, S., Hickey, B., and Schulz, H.: Strength and geometry of the glacial Atlantic Meridional Overturning Circulation, Nature Geoscience, 5, 813-816, 2012.
Luo, Y., Francois, R., and Allen, S. E.: Sediment 231Pa/230Th as a recorder of the rate of the Atlantic meridional overturning circulation: insights from a 2-D model, Ocean Science, 6, 381-400, 2010.
Lynch-Stieglitz, J., Schmidt, M. W., Henry, L. G., Curry, W. B., Skinner, L. C., Mulitza, S., Zhang, R., and Chang, P.: Muted change in Atlantic overturning circulation over some glacial-aged Heinrich events, Nature Geoscience, 7, 144-150, 2014.
Lynch-Stieglitz, J., Stocker, T., Broecker, W. S., and Fairbanks, R. G.: The influence of air-sea exchange on the isotopic composition of oceanic carbon: Observations and modeling, Global Biogeochemical Cycles, 9, 653-665, 1995.
McManus, J. F., Francois, R., Gherardi, J.-M., Keigwin, L. D., and Brown-Leger, S.: Collapse and rapid resumption of Atlantic meridional circulation linked to deglacial climate changes, Nature, 428, 834-837, 2004.
Negre, C., Zahn, R., Thomas, A. L., Masque, P., Henderson, G. M., Martinez-Mendez, G., Hall, I. R., and Mas, J. L.: Reversed flow of Atlantic deep water during the Last Glacial Maximum, Nature, 468, 84-+, 2010.
Reimer, P. J., Bard, E., Bayliss, A., Beck, J. W., Blackwell, P. G., Bronk Ramsey, C., Buck, C. E., Cheng, H., Edwards, R. L., Friedrich, M., Grootes, P. M., Guilderson, T. P., Haflidason, H., Hajdas, I., Hatté, C., Heaton, T. J., Hoffman, D. L., Hogg, A. G., Hughen, K. A., Kaiser, K. F., Kromer, B., Manning, S. W., Niu, M., Reimer, R. W., Richards, D. A., Scott, E. M., Southon, J. R., Staff, R. A., Turney, C. S. M., and van der Plicht, J.: IntCal13 and Marine13 Radiocarbon Age Calibration Curves 0–50,000 years Cal BP, Radiocarbon, 55, 1869-1887, 2013.
Rhein, M., Stramma, L., and Send, U.: The Atlantic Deep Western Boundary Current: Water masses and transports near the equator, Journal of Geophysical Research, 100, 2441, 1995.
Robinson, L. F. and van de Flierdt, T.: Southern Ocean evidence for reduced export of North Atlantic Deep Water during Heinrich event 1, Geology, 37, 195-198, 2009.
Roche, D., Dokken, T. M., Goosse, H., Renssen, H., and Weber, S. L.: Climate of the Last Glacial Maximum: sensitivity studies and model-data comparison with the LOVECLIM coupled model, Clim. Past, 3, 205–224, 2007.
Roche, D. M., Wiersma, A. P., and Renssen, H.: A systematic study of the impact of freshwater pulses with respect to different geographical locations, Clim. Dyn., 34, 997–1013, 2010.

Roche, D. M., Paillard, D., Caley, T., Waelbroeck, C. : LGM hosing approach to Heinrich Event 1: results and perspectives, Quaternary Science Reviews, in press, 2014.
from dataemodel integration using water isotopes
Rohling, E. J. and Cooke, S.: Stable oxygen and carbon isotope ratios in foraminiferal carbonate in Gupta. In: Modern foraminifera, Kluwer Academic, Dordrecht, The Netherlands, 1999.
Schott, F. A.: The zonal currents and transports at 35°W in the tropical Atlantic, Geophysical Research Letters, 30, 2003.
Siddall, M., Henderson, G. M., Edwards, N. R., Frank, M., Müller, S. A., Stocker, T. F., and Joos, F.: 231Pa/ 230Th fractionation by ocean transport, biogenic particle flux and particle type, Earth and Planetary Science Letters, 237, 135– 155, 2005.
Stocker, T. F. and Johnsen, S. J.: A minimum thermodynamic model for the bipolar seesaw, Paleoceanography, 18, doi:10.1029/2003PA000920, 2003.
Talley, L. D., Reid, J. L., and Robbins, P. E.: Data-based meridional overturning streamfunctions for the global ocean, Journal of Climate, 16, 3213-3226, 2003.
Thomas, A. L., Henderson, G. M., and Robinson, L. F.: Interpretation of the 231Pa/230Th paleocirculation proxy: New water-column measurements from the southwest Indian Ocean, Earth and Planetary Science Letters, 241, 493-504, 2006.
Vidal, L., Labeyrie, L., Cortijo, E., Arnold, M., Duplessy, J. C., Michel, E., Becqué, S., and van Weering, T. C. E.: Evidence for changes in the North Atlantic Deep Water linked to meltwater surges during the Heinrich events, Earth and Planetary Science Letters, 146, 13-26, 1997.
Yu, E.-F., Francois, R., and Bacon, M.: Similar rates of modern and last-glacial ocean thermohaline circulation inferred from radiochemical data, Nature, 379, 689-694, 1996.
Zahn, R., Winn, K., and Samthein, M.: Benthic foraminiferal delta 13C and accumulation rates of organic carbon: uvigerina peregrina group and cibicidoides wuellerstorfi, Paleoceanography, 1, 27-42, 1986.

Figures

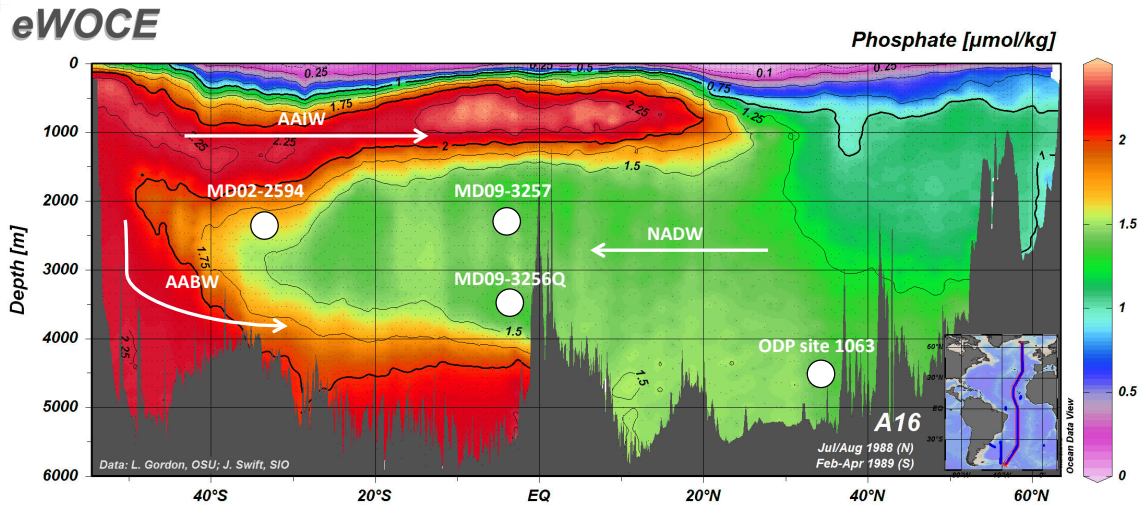

Figure 4.**1** : Phosphate section of the Atlantic Ocean showing the sites of cores MD09-3257 (04°14.69'S, 36°21.18'W, 2344 m), MD09-3256Q (03°32.81'S, 35°23.11'W, 3537 m), ODP Leg 172, site 1063 (33°41'N, 57°37'W, 4584 m) (Lippold et al., 2009) and MD02-2594 (34°43'S, 17°20'E, 2440 m) (Negre et al., 2010). Phosphate content follows the structure of the present day AMOC. White arrows indicate the approximate flow directions of the Antarctic Intermediate Water (AAIW), Antarctic Bottom Water (AABW) and North Atlantic Deep Water (NADW).

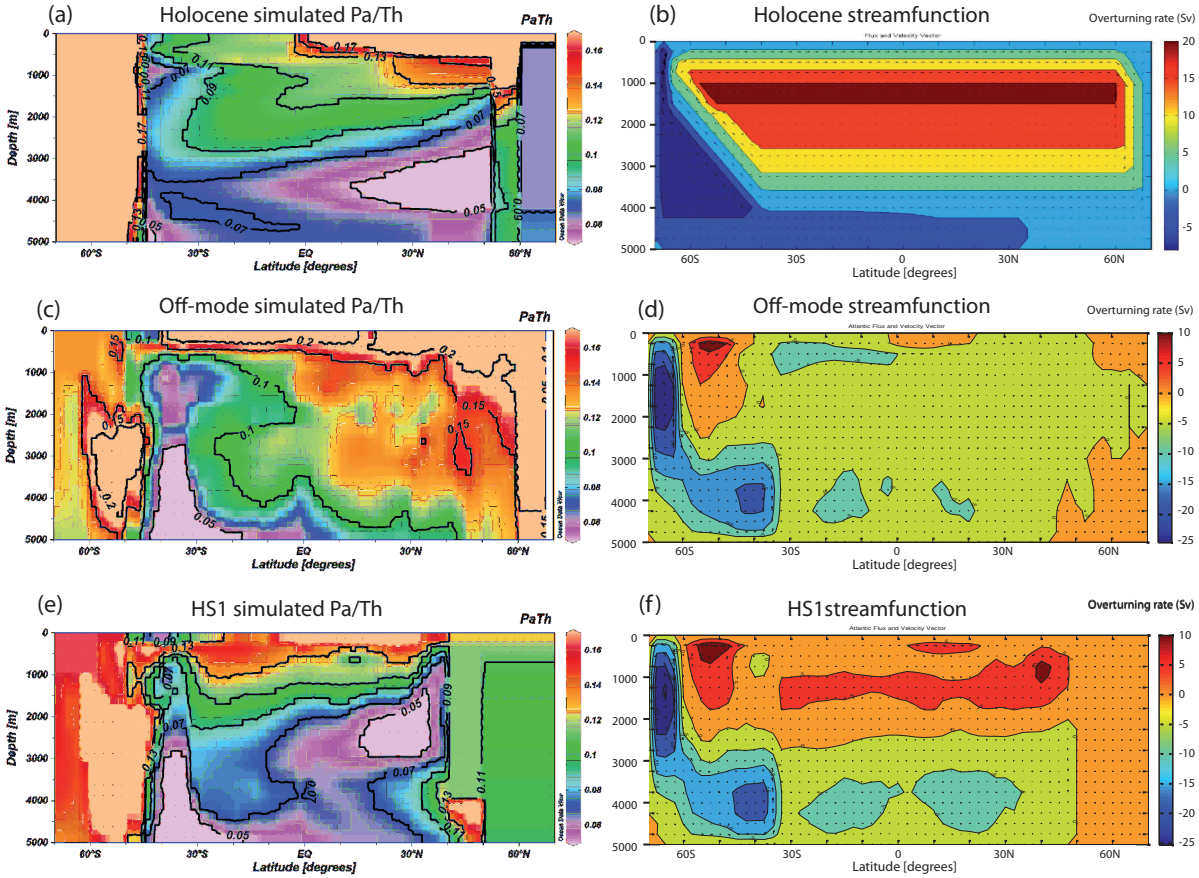

Figure 4.**2** : Simulated sedimentary Pa/Th values and associated streamfunctions: (a, b) Holocene, (c, d) Off-mode, (e, f) HS1.

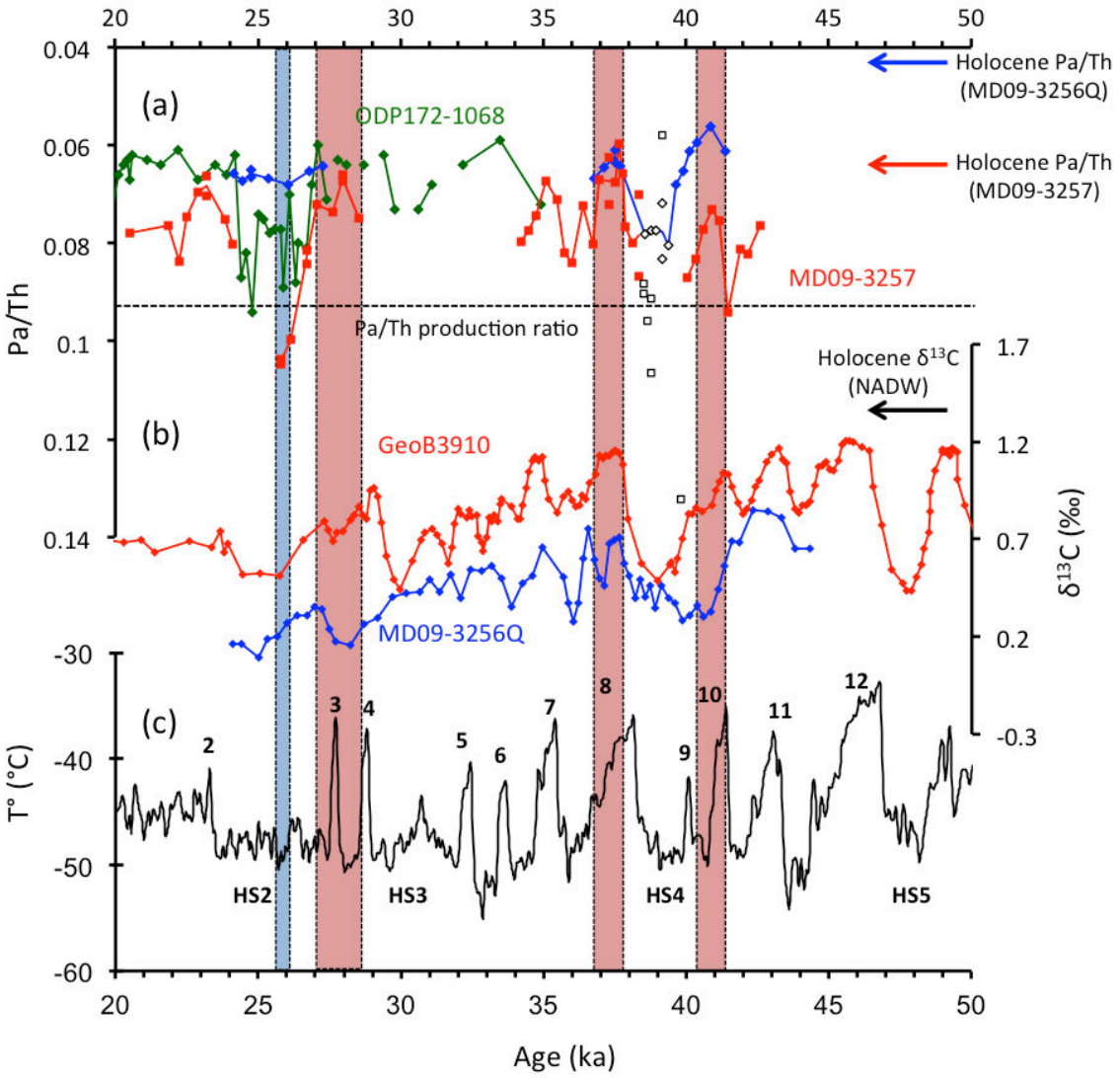

Figure 4.**3** : Comparison between oceanic circulation and water mass proxies on the Brazilian margin and Bermuda Rise, and Greenland temperatures. (a) MD09-3256Q, MD09-3257 (Burckel et al., submitted) and ODP172-1063 (Lippold et al., 2009) Pa/Th (b) MD09-3256Q and GeoB3910 (Burckel et al., submitted) *Cibicides wuellerstorfi* $\delta^{13}C$ and (c) NGRIP temperature signal on the GICC05 timescale (Kindler et al., 2014). In (a) the average Pa/Th for each core is represented by the lines and individual measurements by diamonds (MD09-3256Q, ODP site 1063) and squares (MD09-3257). The white squares indicate Pa/Th values not considered in core MD09-3257 (Burckel et al., submitted), the white diamonds indicate the Pa/Th values that may not represent a pure circulation signal in core MD09-3256Q (see results). The red arrow indicates the late Holocene Pa/Th value on core MD09-3257 (0.065±0.003, Burckel et al., 2014 b, submitted) and the blue arrow the late Holocene Pa/Th value on core MD09-3256Q (0.043±0.001). Error bars on Pa/Th measurements are given in Fig. S1, Table S4. In (b) the signal is the 3 points running average of the *Cibicides w.* $\delta^{13}C$ record, the black arrow indicates present day NADW $\delta^{13}C$ value (~1.37 ‰). $\delta^{13}C$ values are given in Table S5. In (c) numbers indicate the DO events. MD09-3257 and GeoB3910 data are presented in red, MD09-3256Q data in blue and ODP172-1063 in green. Red vertical bands represent the Pre-HS2, Post-HS4 and Pre-HS4 time slices and the blue vertical band the HS2 time slice.

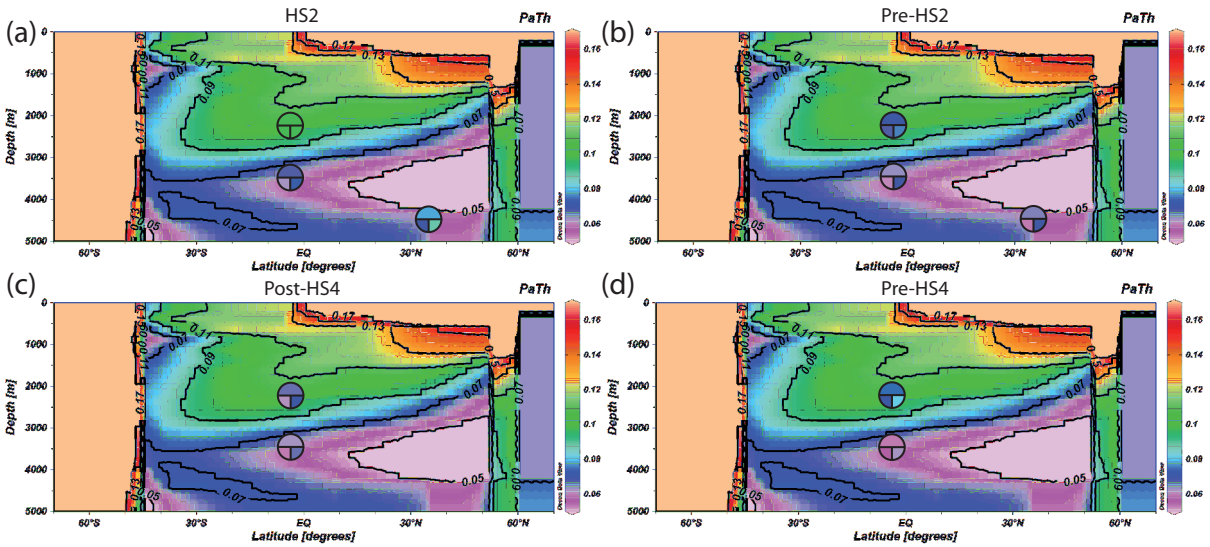

Figure 4.**4** : Comparison of the Pa/Th data (circles) for each of the time slices to the simulated Pa/Th values using the Holocene streamfunction. Time slices are (a) HS2, (b) Pre-HS2, (c) Post-HS4 and (d) Pre-HS4 Pa/Th data. The upper half of the circles represent the Pa/Th data, the lower left quarter Pa/Th – 1 sigma and the lower right quarter Pa/Th + 1 sigma.

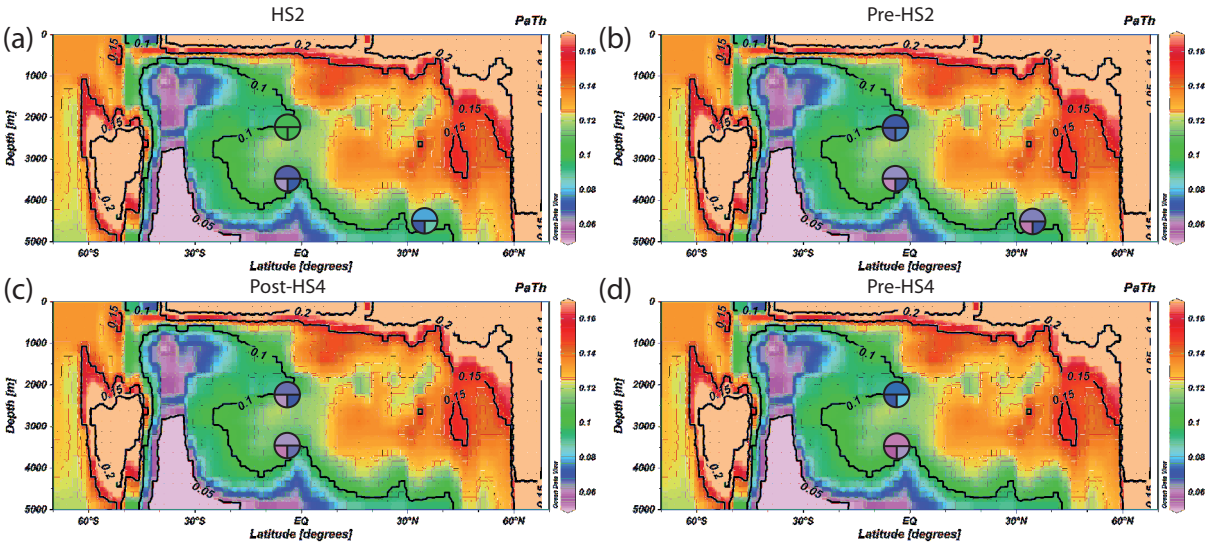

Figure 4.**5** : Comparison of the Pa/Th data for each of the time slices to the simulated Pa/Th values using the off-mode streamfunction. Time slices are (a) HS2, (b) Pre-HS2, (c) Post-HS4 and (d) Pre-HS4 Pa/Th data. The upper half of the circles represent the Pa/Th data, the lower left quarter Pa/Th – 1 sigma and the lower right quarter Pa/Th + 1 sigma.

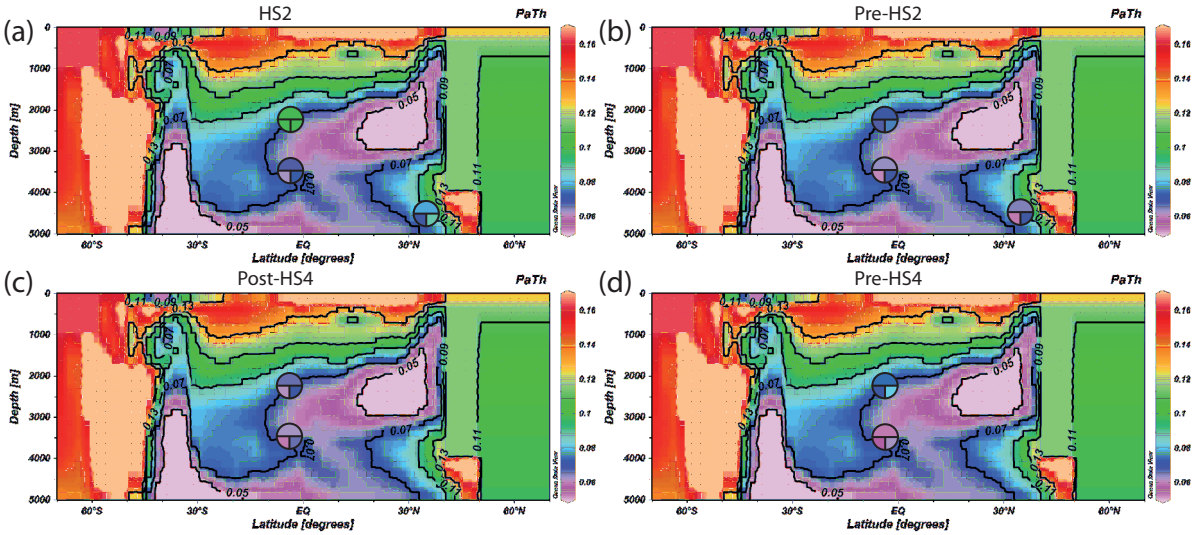

Figure 4.**6** : Comparison of the Pa/Th data for each of the time slices to the simulated Pa/Th values using the HS1 streamfunction. Time slices are (a) HS2, (b) Pre-HS2, (c) Post-HS4 and (d) Pre-HS4 Pa/Th data. The upper half of the circles represent the Pa/Th data, the lower left quarter Pa/Th – 1 sigma and the lower right quarter Pa/Th + 1 sigma.

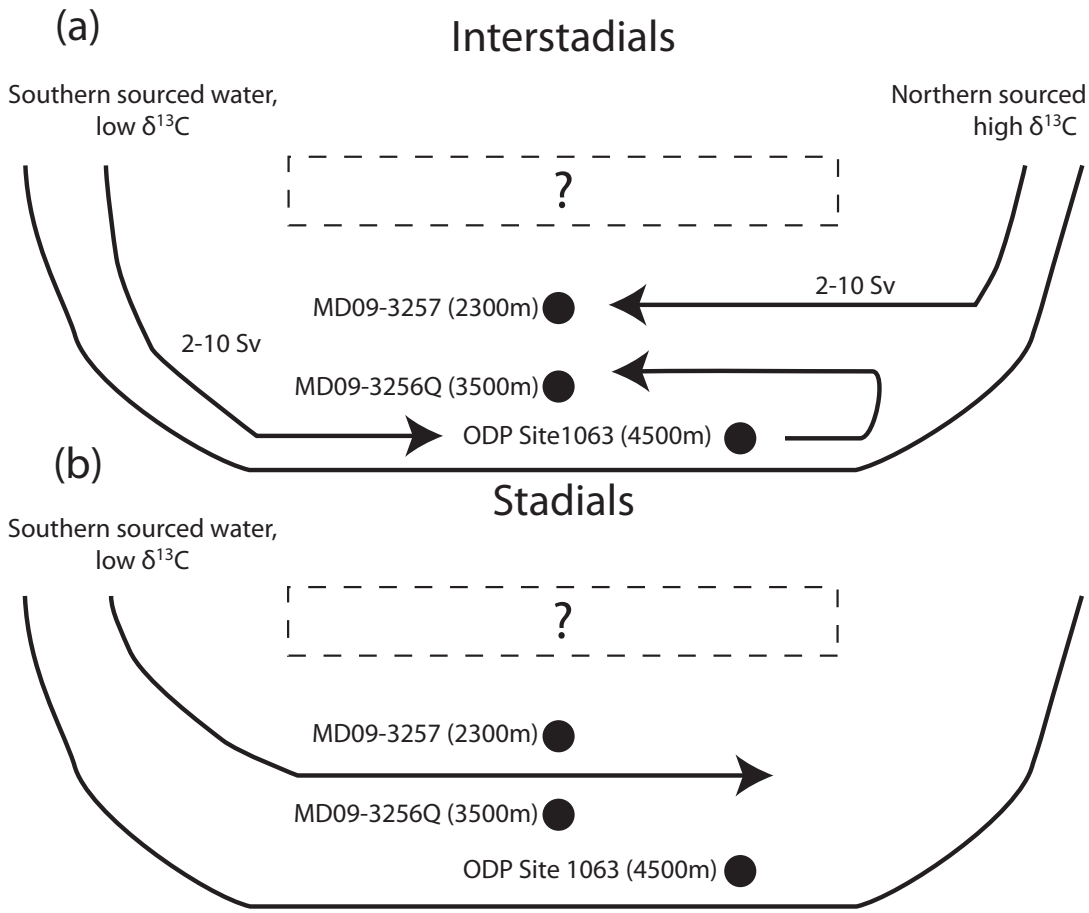

Figure 4.**7** : Sketch of the possible states of the AMOC during (a) DO interstadials and (b) Heinrich Stadials. See text for explanation.

4.3 Supporting Information

The supporting information provides additional figures, which further illustrate the main text.

Supporting Information

Changes in the geometry and strength of the AMOC during the last glacial

P. Burckel, C. Waelbroeck, Y. Luo , D. Roche, S. Pichat, J. Gherardi, A. Govin, F. Thil

Figures

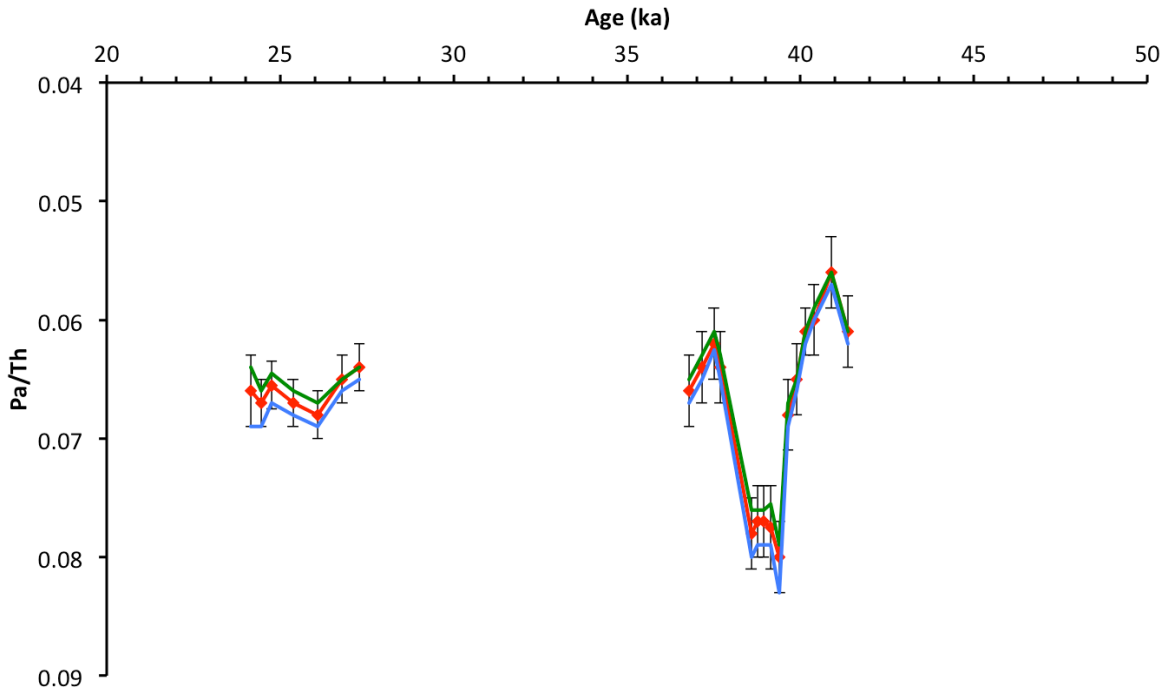

Figure 4.**S1** : Pa/Th in MD09-3256Q as a function of time calculated with different lithogenic ($^{238}U/^{232}Th$) (R) values used to correct for detrital material contribution (Francois, 2007). Red curve, R=0.5 (correction used in Fig. 3), green curve R=0.4, and blue curve R=0.6. Error bars are 1 SD and do not account for the error on R.

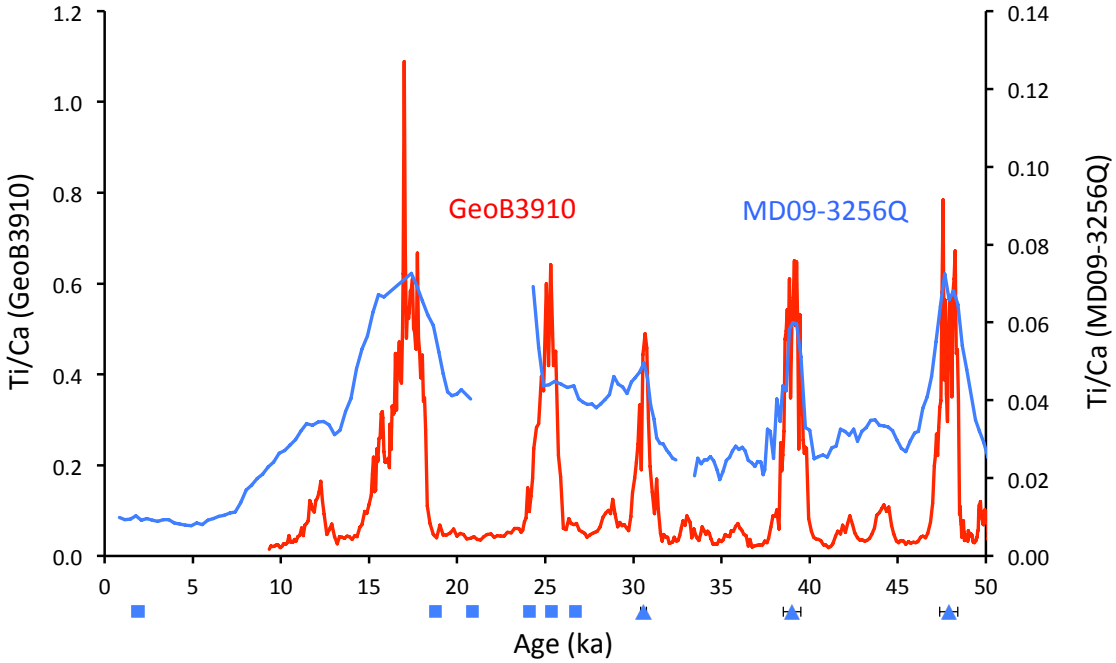

Figure 4.**S2** : Core MD09-3256Q age model. Blue squares indicate the position of the ^{14}C dates in the core, blue triangles indicate tie points between core GeoB3910 and MD09-3256Q. Discontinuities in the Ti/Ca record correspond to the position of turbidite layers. Error bars are 1 sigma and do not include the uncertainty on correlation for the tie points.

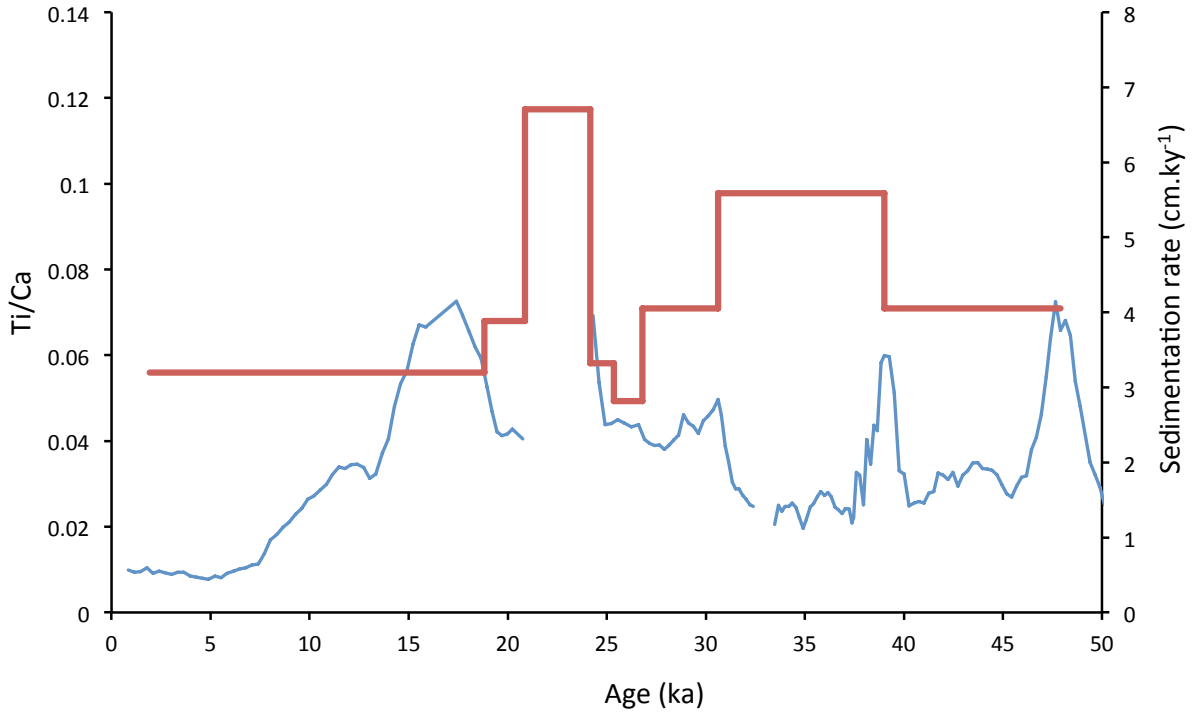

Figure 4.**S3** : Core MD09-3256Q Ti/Ca (blue curve) and sedimentation rate (red curve).

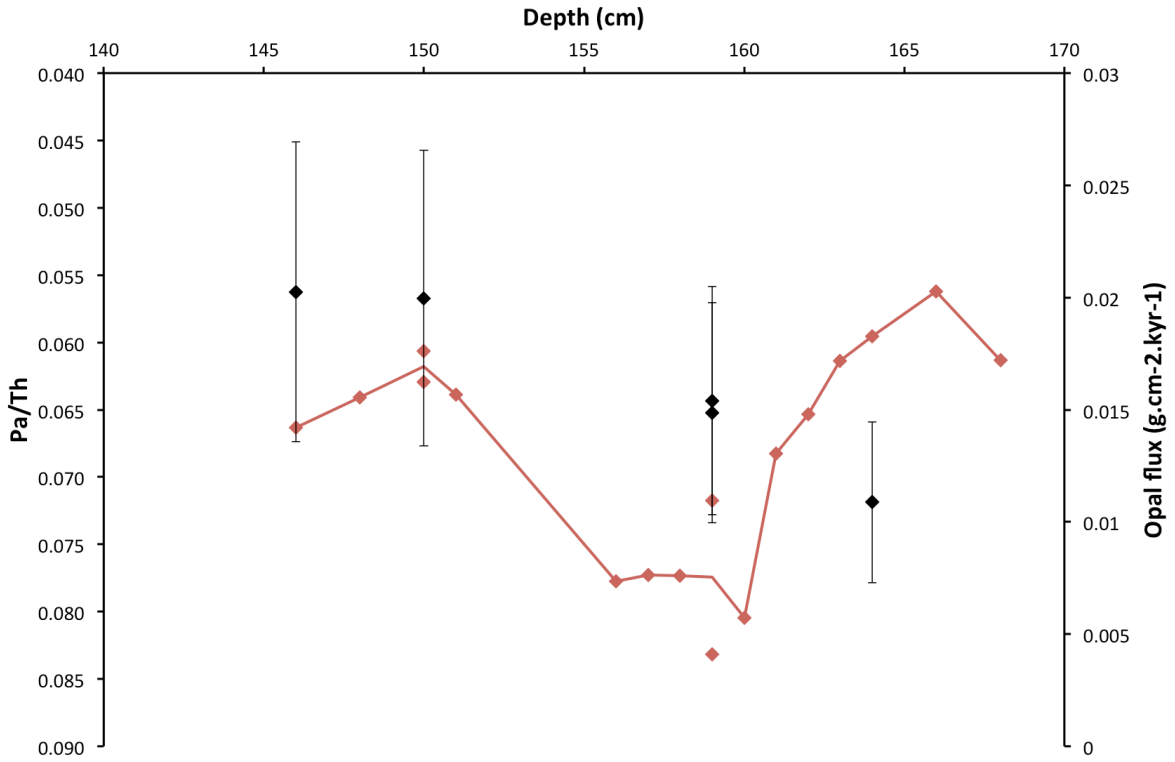

Figure 4.**S4** : Sedimentary Pa/Th (red) and opal flux (black) as a function of depth in core MD09-3256Q. Error bars are 1 SE.

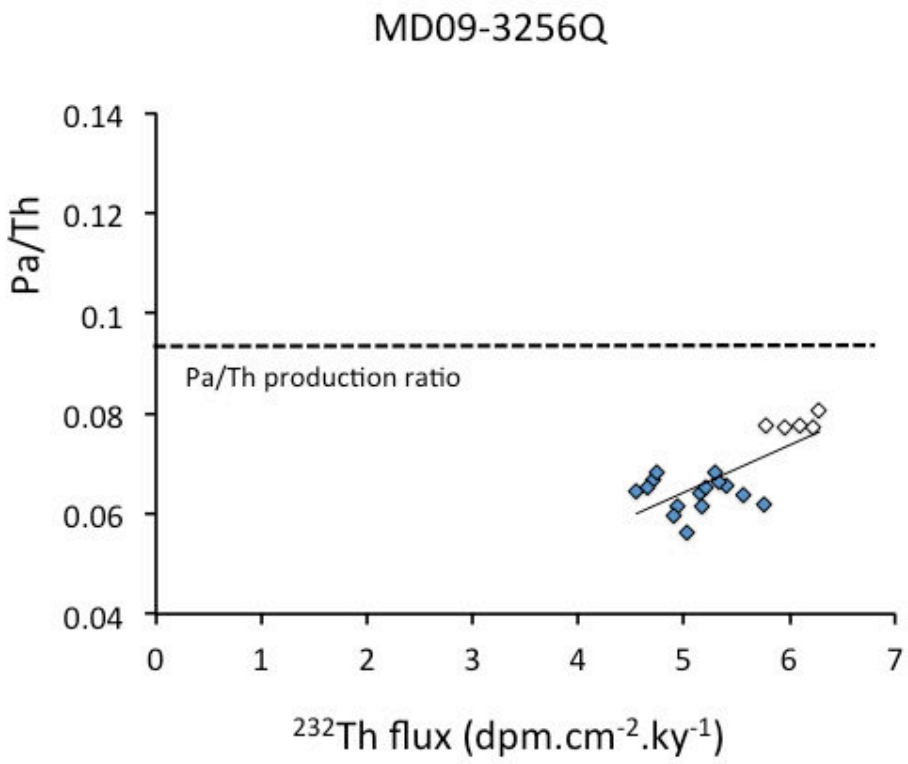

Figure 4.**S5** : Correlation between the 232Th flux and sedimentary Pa/Th ratio on core MD09-3256Q. White diamonds represent Pa/Th data that may not represent a pure circulation signal.

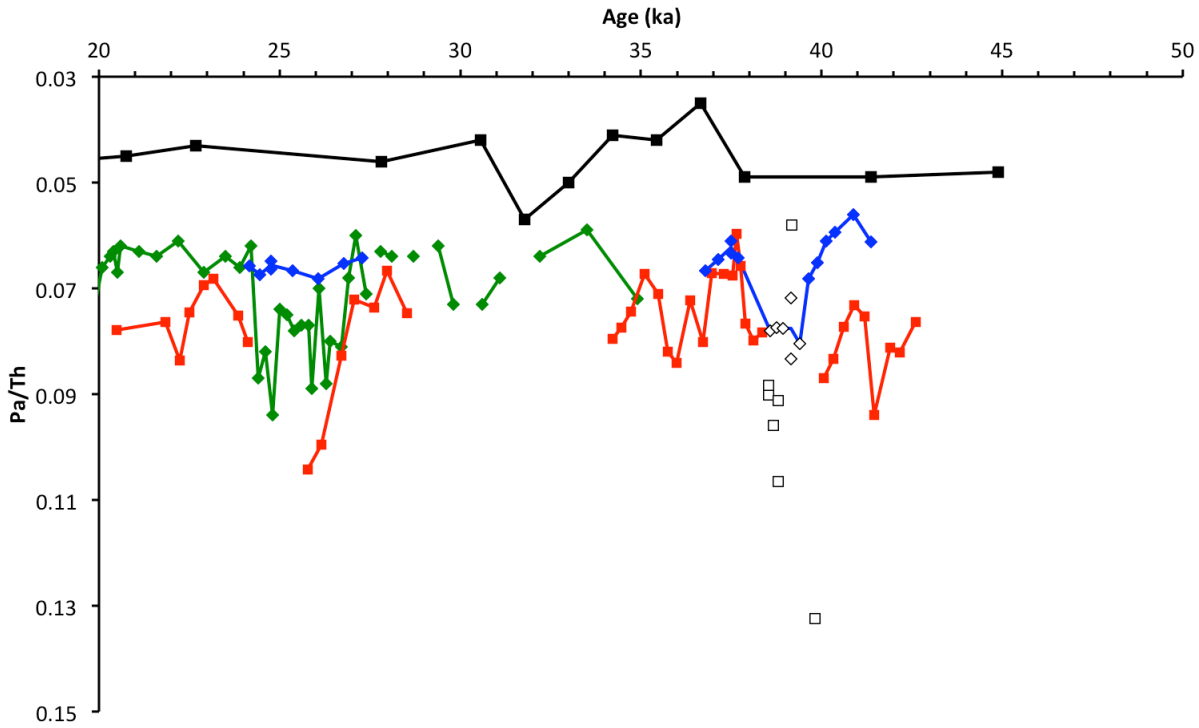

Figure 4.**S6** : Pa/Th of core MD09-3257 (red), MD09-3256Q (blue), ODP site 172 (Lippold et al., 2009)(green) and MD02-2594 (Negre et al., 2010)(black). White symbols represent Pa/Th data that may not reflect a pure circulation signal.

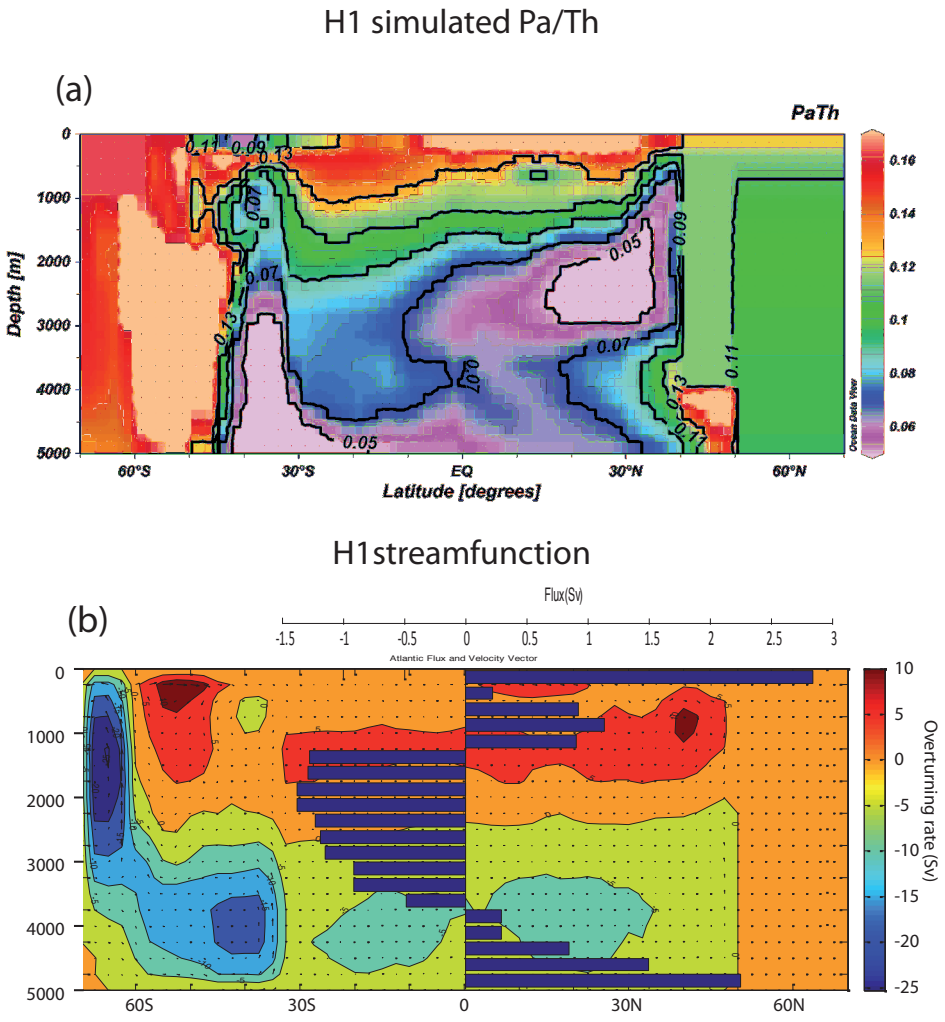

Figure 4.**S7** : H1 simulated (a) Pa/Th and (b) streamfunction and flux (Sv, blue bars, scale on top) at the equator. Note the large flow rate decrease at the equator from ~2500 m to ~3500 m.

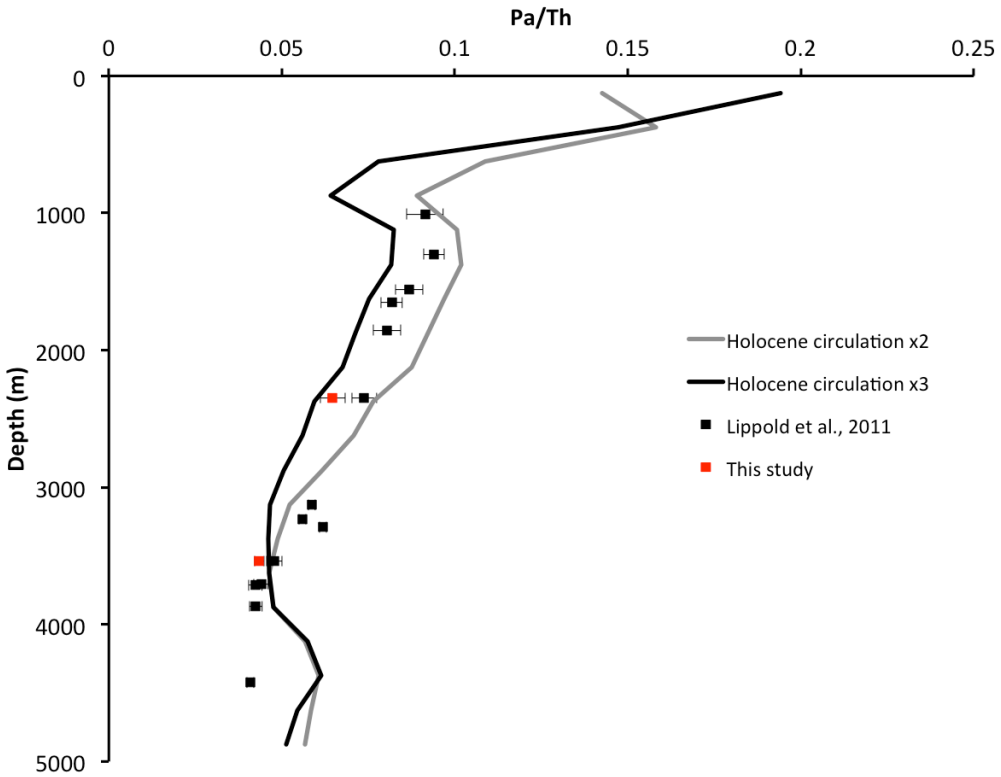

Figure 4.**S8** : Pa/Th on the Brazilian margin. Red squares, data obtained from Holocene sediments in this study. Black squares, data obtained from Holocene sediments in (Lippold et al., 2011). Grey and black lines, simulated Pa/Th values with the 2 and 3x increased Holocene streamfunction respectively.

Tables

Table 4.**S1** : Core MD09-3256Q age model. ^{14}C age is converted to calendar age using the Marine13 curve (Reimer et al., 2013) with no additional reservoir age correction. * GeoB3910 tie points.

	Depth (m)	Age ^{14}C (kyr)	1σ	Age (Cal kyr)	1σ
	0.040	2.32	0.03	1.93	0.04
	0.580	15.97	0.06	18.82	0.06
	0.660	17.72	0.06	20.88	0.11
	0.880	20.5	0.08	24.16	0.12
	0.920	21.41	0.08	25.36	0.12
	0.960	22.87	0.08	26.79	0.18
*	1.115	/		30.61	0.16
*	1.585	/		39.03	0.50
*	1.945	/		47.91	0.51

Table 4.**S2** : Pa/Th for each of the time slices at the different cores. Error bars are the maximum between standard deviation on Pa/Th values within the time slice and the propagation of individual measurement errors on the averaged Pa/Th value defining the time slice.

Core	Depth (m)	HS2 Pa/Th	1σ	Pre-HS2 Pa/Th	1σ	Post-HS4 Pa/Th	1σ	Pre-HS4 Pa/Th	1σ
MD09-3257	2344	0.103	0.003	0.071	0.004	0.066	0.004	0.075	0.005
MD09-3256Q	3537	0.068	0.005	0.064	0.005	0.063	0.003	0.059	0.003
ODP site 1063	4584	0.079	0.010	0.065	0.004	/		/	

Table 4.**S3** : Square root of the sum of squared difference between Pa/Th data and simulated value using the HS1 streamfunction intensified by various factors for the two equatorial cores. The minimum values indicate the best agreement of the simulated Pa/Th with the measured Pa/Th.

Factor	Pre-H2	Post-H4	Pre-H4
x0.5	2.9E-02	3.5E-02	3.5E-02
x1	8.0E-03	8.1E-03	1.6E-02
x1.5	1.8E-02	1.0E-02	2.0E-02
x2	2.6E-02	1.9E-02	2.7E-02
x3	3.5E-02	2.8E-02	3.4E-02

Table 4.**S4** : Pa/Th and isotopic concentrations (dpm.g^{-1}) in core MD09-3256Q

Depth (m)	Age(Cal kyr BP)	1 σ	231Pa	1 σ	230Th	1 σ	232Th	1 σ	238U	1 σ	Pa/Th	1 σ
0	0.50	0.50	0.240	0.003	5.51	0.11	1.19	0.02	1.085	0.007	0.043	0.001
0	0.50	0.50	0.240	0.004	5.52	0.08	1.20	0.02	1.082	0.006	0.043	0.001
0.88	24.16	0.12	0.181	0.003	3.76	0.07	3.46	0.05	1.906	0.011	0.066	0.003
0.89	24.46	0.12	0.241	0.004	4.92	0.08	3.40	0.05	1.804	0.018	0.067	0.002
0.9	24.76	0.12	0.247	0.004	5.09	0.11	2.76	0.04	1.346	0.007	0.066	0.002
0.9	24.76	0.12	0.245	0.004	5.14	0.11	2.64	0.04	1.333	0.007	0.065	0.002
0.92	25.37	0.12	0.259	0.004	5.36	0.12	2.57	0.04	1.255	0.010	0.067	0.002
0.94	26.08	0.15	0.267	0.004	5.45	0.12	2.63	0.05	1.381	0.008	0.068	0.002
0.96	26.79	0.18	0.254	0.004	5.38	0.11	2.56	0.05	1.432	0.007	0.065	0.002
0.98	27.28	0.17	0.242	0.004	5.20	0.09	2.45	0.03	1.314	0.012	0.064	0.002
1.46	36.79	0.41	0.151	0.003	3.41	0.06	1.90	0.03	1.129	0.024	0.066	0.003
1.48	37.15	0.43	0.153	0.003	3.55	0.08	1.94	0.04	1.121	0.015	0.064	0.003
1.5	37.50	0.44	0.151	0.004	3.59	0.07	2.14	0.03	1.392	0.010	0.061	0.003
1.5	37.50	0.44	0.152	0.004	3.53	0.06	2.00	0.03	1.365	0.019	0.063	0.003
1.51	37.68	0.45	0.160	0.003	3.64	0.07	2.02	0.03	1.600	0.031	0.064	0.003
1.56	38.58	0.49	0.226	0.004	4.55	0.07	2.59	0.04	2.115	0.018	0.078	0.003
1.57	38.76	0.49	0.233	0.004	4.81	0.07	2.91	0.03	1.822	0.013	0.077	0.003
1.58	38.94	0.50	0.232	0.003	4.82	0.09	3.04	0.05	1.748	0.014	0.077	0.003
1.59	39.15	0.50	0.235	0.004	4.66	0.11	2.94	0.06	1.643	0.015	0.083	0.004
1.59	39.15	0.50	0.213	0.005	4.67	0.08	2.88	0.04	1.635	0.012	0.072	0.003
1.6	39.40	0.50	0.230	0.004	4.71	0.09	3.05	0.03	1.493	0.012	0.080	0.003
1.61	39.64	0.50	0.186	0.003	4.27	0.09	2.45	0.04	1.267	0.008	0.068	0.003
1.62	39.89	0.50	0.176	0.003	4.14	0.07	2.33	0.03	1.291	0.011	0.065	0.003
1.63	40.14	0.50	0.156	0.003	3.80	0.06	2.04	0.03	1.270	0.009	0.061	0.002
1.64	40.38	0.50	0.150	0.004	3.74	0.06	2.00	0.02	1.245	0.022	0.060	0.003
1.66	40.88	0.51	0.146	0.004	3.76	0.09	2.04	0.04	1.350	0.008	0.056	0.003
1.68	41.37	0.51	0.148	0.004	3.66	0.07	2.05	0.03	1.209	0.009	0.061	0.003

Table 4.**S5** : Core MD09-3256Q $\delta^{13}C$ (*C. wuellerstorfi*)

Age (Cal kyr BP)	Depth (m)	∂13C (‰)	Age (Cal kyr BP)	Depth (m)	∂13C (‰)	Age (Cal kyr BP)	Depth (m)	∂13C (‰)
1.93	0.04	1.29	35.00	1.36	0.32	38.58	1.56	0.39
1.93	0.04	1.33	35.00	1.36	0.89	38.58	1.56	0.97
1.93	0.04	1.32	35.71	1.4	0.65	38.76	1.57	0.40
1.93	0.04	1.38	35.71	1.4	0.53	38.76	1.57	0.02
1.93	0.04	1.38	35.89	1.41	0.77	38.94	1.58	0.38
24.16	0.88	0.30	35.89	1.41	-0.11	38.94	1.58	0.19
24.46	0.89	-0.16	36.07	1.42	0.56	38.94	1.58	0.93
25.06	0.91	0.34	36.07	1.42	-0.35	39.15	1.59	0.34
25.37	0.92	0.10	36.07	1.42	0.40	39.40	1.6	0.55
25.72	0.93	0.12	36.25	1.43	-0.16	39.64	1.61	0.31
26.08	0.94	0.39	36.25	1.43	0.40	39.89	1.62	0.21
26.43	0.95	0.31	36.25	1.43	0.66	39.89	1.62	0.29
26.79	0.96	0.23	36.43	1.44	0.61	40.14	1.63	0.30
27.03	0.97	0.39	36.43	1.44	0.62	40.38	1.64	0.38
27.28	0.98	0.44	36.61	1.45	0.85	40.63	1.65	0.27
27.53	0.99	0.20	36.61	1.45	0.92	40.63	1.65	0.52
27.77	1	0.07	36.79	1.46	0.66	40.88	1.66	0.13
28.27	1.02	0.25	36.79	1.46	0.86	41.12	1.67	0.33
28.76	1.04	0.15	36.97	1.47	0.24	41.12	1.67	0.57
29.25	1.06	0.40	36.97	1.47	0.03	41.37	1.68	0.71
29.75	1.08	0.34	37.15	1.48	0.39	41.37	1.68	0.80
30.24	1.1	0.48	37.15	1.48	0.83	41.62	1.69	0.55
30.70	1.12	0.45	37.33	1.49	0.80	41.62	1.69	0.41
31.06	1.14	0.35	37.33	1.49	0.48	41.86	1.7	0.77
31.42	1.16	0.68	37.50	1.5	0.86	41.86	1.7	0.88
31.78	1.18	0.25	37.50	1.5	0.70	42.36	1.72	1.20
32.13	1.2	0.62	37.68	1.51	1.01	42.36	1.72	0.28
32.49	1.22	0.33	37.68	1.51	0.33	42.85	1.74	0.98
32.85	1.24	0.68	37.86	1.52	0.67	43.35	1.76	0.80
33.21	1.26	0.70	38.04	1.53	0.26	43.84	1.78	0.73
33.21	1.26	0.50	38.04	1.53	0.51	43.84	1.78	0.56
33.57	1.28	0.41	38.22	1.54	0.87	44.33	1.8	0.33
33.92	1.3	0.48	38.22	1.54	0.09	44.33	1.8	0.70
34.28	1.32	0.17	38.40	1.55	0.23			
34.64	1.34	0.77	38.40	1.55	0.41			

Additional references

Francois, R.: Proxies in Late Cenozoic Paleoceanography: Paleoflux and Paleocirculation from Sediment 230Th and 231Pa/230Th, Elsevier, 2007.

Lippold, J., Gherardi, J.-M., and Luo, Y.: Testing the 231Pa/230Th paleocirculation proxy: A data versus 2D model comparison, Geophys. Res. Lett., 38, doi:10.1029/2011GL049282, 2011.

Lippold, J., Gruetzner, J., Winter, D., Lahaye, Y., Mangini, A., and Christl, M.: Does sedimentary Pa-231/Th-230 from the Bermuda Rise monitor past Atlantic Meridional Overturning Circulation?, Geophysical Research Letters, 36, 2009.

Negre, C., Zahn, R., Thomas, A. L., Masque, P., Henderson, G. M., Martinez-Mendez, G., Hall, I. R., and Mas, J. L.: Reversed flow of Atlantic deep water during the Last Glacial Maximum, Nature, 468, 84-+, 2010.

Reimer, P. J., Bard, E., Bayliss, A., Beck, J. W., Blackwell, P. G., Bronk Ramsey, C., Buck, C. E., Cheng, H., Edwards, R. L., Friedrich, M., Grootes, P. M., Guilderson, T. P., Haflidason, H., Hajdas, I., Hatté, C., Heaton, T. J., Hoffman, D. L., Hogg, A. G., Hughen, K. A., Kaiser, K. F., Kromer, B., Manning, S. W., Niu, M., Reimer, R. W., Richards, D. A., Scott, E. M., Southon, J. R., Staff, R. A., Turney, C. S. M., and van der Plicht, J.: IntCal13 and Marine13 Radiocarbon Age Calibration Curves 0–50,000 years Cal BP, Radiocarbon, 55, 1869-1887, 2013.

Chapter 5: Conclusion and perspectives

5.1 Conclusion

The first objective of this thesis was to reconstruct the dynamics of the Atlantic Meridional Overturning Circulation during the last glacial. In order to do that, I measured the sedimentary Pa/Th ratio, a proxy of water mass renewal rate, in two sediment cores of the equatorial Atlantic. I also measured the benthic $\delta^{13}C$, which provides information about the nutrient content of water masses, in one of the two cores. The Pa/Th and benthic $\delta^{13}C$ are complementary and provide information about the flow rate and ventilation of water masses respectively.

The second objective of this thesis was to investigate the relationship between AMOC variations and climate. In order to do that, I first built an age model for both equatorial sediment cores that is entirely radiometric and independent of the GICC05 age scale. I then compared the flow rate and ventilation of the water masses influencing my sediment cores during the last glacial to Greenland temperature and tropical precipitation.

My results show that the vertical layout and strength of the water masses constituting the AMOC changed over the course of the last glacial. In this conclusion, I summarize each of the results presented in this thesis and classify them based on their associated climatic period.

5.1.1 Dansgaard-Oeschger interstadials

During Dansgaard-Oeschger interstadials, two circulation cells were likely active in the Atlantic Ocean (Chapter 4.2). A first circulation cell was initiated by deep convection in the northern North Atlantic, and consisted of a deep-water mass circulating southwards above ~2500 m depth. This northern-sourced water mass was likely characterized by flow rates of 2-10 Sv at the equator, which is lower than the flow rate of present day NADW (i.e. 23 ± 3 Sv (Ganachaud and Wunsch, 2000)). A second circulation cell was initiated in the Southern Ocean by the formation of a deep-water mass, which flowed northwards below 4000 m depth, and reached at least 35°N at 4500 m depth. The flow rate of this southern sourced water mass was likely of 2-10 Sv, which encompasses the strength of modern AABW (i.e. 6 ± 1.3 Sv, (Ganachaud and Wunsch, 2000)). Between 2500 and 4000 m depth at the equator, the southern-sourced water mass circulated southwards as a return flow.

5.1.2 Heinrich Stadials

As detailed in Chapter 3, a southward shift of the Inter Tropical Convergence Zone is simulated in climate models either through a slowdown of the AMOC upper circulation cell, or through the development of sea ice and ice sheets in the high latitudes of the northern Hemisphere. My results show that the Pa/Th signal at 2300 m on the Brazilian margin rises 1420 ± 250 (1σ) and 690 ± 180 (1σ) y before the onset of the precipitation events associated with HS2 and HS4 respectively (Chapter 3). I interpret the Pa/Th rise as a decrease in the flow rate of the upper overturning cell of the AMOC. Hence, I confirm that a reduction of the oceanic inter-hemispheric heat transport could be at the origin of the ITCZ shifts occurring during Heinrich Stadials.

These large leads contrast with model results, which show that 50% of the final tropical precipitation anomaly occurs only 200 y after the start of an AMOC slowdown in response to freshwater input in the high latitude North Atlantic (Kageyama et al., 2009). Such a rapid response of the tropical atmosphere in the model could be related to the fast simulated AMOC slowdown, as minimum overturning rate is achieved only 400 y after the start of the slowdown. A more gradual decrease of the flow rate could lead to a delayed establishment of the SST anomaly required for the ITCZ to shift above the Brazilian margin, in agreement with our data.

We now consider the structure of the AMOC during the Heinrich Stadials following the gradual slowdown of the AMOC upper circulation cell that likely caused the southward ITCZ shifts. My data at the onset of HS2 show that the layout of the equatorial water masses at that time was significantly different from that of preceding DO interstadials (Chapter 4). Below 1300 m depth, the Atlantic Ocean was likely dominated by a southern sourced water mass that reached at least 35°N at 4500 m depth. The southern sourced water mass probably directly affected the equator between 2500-3500 m depth. Sluggish and poorly ventilated waters of unknown origin likely influenced the equatorial Atlantic between 1300 and 2300 m depth.

My results do not show major differences between HS2 and HS4, despite the large difference in Northern hemisphere ice sheet extent between these two periods. In both cases, the slowdown of the upper AMOC circulation cell precedes the southward ITCZ shift (Chapter 3). However, I was not able to assess the strength and geometry of the AMOC during HS4 because, at that time, Pa/Th data in both equatorial cores could not reflect a pure circulation signal (Chapter 4). Hence, I cannot conclude that both Heinrich Events are similar in terms of AMOC configuration. The only difference between the two periods is that the benthic $\delta^{13}C$ of the preceding and following interstadials is higher for HS4 than for HS2 (Chapter 4), which might be related to the more developed continental biosphere occurring during early MIS3 (Duplessy et al., 1988).

5.1.3 Dansgaard Oeschger Stadials

During Dansgaard-Oeschger stadials, the flow rate of the AMOC upper circulation cell likely decreased, but less than during HS2. At the same time, increased precipitation is observed on the Brazilian margin, although the associated terrigenous input was smaller than during Heinrich Stadials. These periods of increased precipitation also correspond to clear decreases in South American speleothem $\delta^{18}O$ attributed to southward ITCZ shifts (Kanner et al., 2012). However, there is no significant lead of the oceanic circulation signal with respect to the ITCZ shifts. Both the AMOC and Greenland temperature changes appear to be in phase with increased precipitation. A short time lag of increased tropical precipitation with respect to decreased Greenland temperature would be consistent with atmospheric processes driving the ITCZ shifts associated with DO-stadials. However, slowdowns of the AMOC upper circulation cell also occur during DO-stadials. Based on these evidences, it is difficult to infer what processes were at the origin of the small ITCZ shifts associated to DO-stadials.

5.1.4 Mechanisms of climate variability

5.1.4 a) Difference between Dansgaard Oeschger and Heinrich Stadials

Based on the large lead of the upper AMOC circulation cell slowdown with respect to the ITCZ shifts associated with Heinrich Stadials, we proposed a mechanism to explain the difference between Heinrich and DO stadials. During Heinrich Stadials, an initial decrease in the overturning rate of the upper overturning cell of the AMOC could have led to a warming of subsurface waters in the North Atlantic Ocean (Mignot et al., 2007). This could have resulted in the destabilization of high latitude North Atlantic ice shelves, leading to the calving of the Laurentide ice sheet (Alvarez-Solas et al., 2013). This input of freshwater would have further reduced the intensity of the upper circulation cell of the AMOC, leading to further subsurface warming and ice calving. This positive feedback would have progressively reduced the flow rate of the AMOC upper circulation cell and heat transport towards the high latitude North Atlantic, thereby pushing the ITCZ to an increasingly southerly position. In contrast, the circulation slowdown occurring during DO stadials would have been unable to trigger the aforementioned feedback. Thus, both the decreased intensity of the upper circulation cell of the AMOC and the southward shift of the ITCZ remained limited. Hence, during Heinrich Stadials, the large iceberg discharges associated with the positive feedback described above could have resulted in the deposition of large quantities of IRD in the high latitude North Atlantic. This mechanism could explain the thick and thin IRD layers observed during Heinrich and DO Stadials respectively.

5.1.4 b) Effect of the AMOC on Greenland temperatures

My results also show that, although the AMOC is an important source of heat for the high latitude North Atlantic, the temperature response of Greenland to a slowdown of the AMOC upper circulation cell is largely modulated by other processes.

Indeed, no major Greenland air temperature variations occur during the decreased AMOC flow rate associated with HS2. It suggests the importance of other processes in regulating Greenland temperatures. Sea ice for instance, during periods of cold Greenland temperatures preceding HS2, could have acted on Greenland as an insulator, preventing further temperature decrease with decreasing heat transport (Li et al., 2010).

Moreover, heat transport by atmospheric processes could be increased during periods of decreased oceanic heat transport (Kageyama et al., 2009; Shaffrey and Sutton, 2006). Indeed, decreased oceanic heat transport could result in decreased SST in the high latitude North Atlantic, hence increasing the meridional temperature gradient. This would increase baroclinicity of the atmosphere, leading to higher atmospheric heat transport to the high latitude North Atlantic (van der Swaluw et al., 2007). Increased atmospheric heat transport could therefore partly compensate for the decreased oceanic heat transport.

5.2 Perspectives

The results of this thesis provide new insights into the deep Atlantic circulation during the last glacial. Unfortunately, we could not analyze the Pa/Th signal of shallow sedimentary cores (Chapter 1). Pa/Th measurements in shallow sediment cores (~1000 m depth) would be extremely valuable to improve our understanding of the changes in the AMOC upper overturning cell flow rate during the last glacial. More specifically, it could serve to verify if a decreased southward flow rate at 2300 m depth is also accompanied by a decreased northward flow rate and heat export in surface waters.

Analyses of the Pa/Th ratio of new sediment cores along latitudinal sections or depth transects in the Atlantic Ocean during the last glacial would help better constraining the geometry and flow rate of the water masses constituting the AMOC. It would probably allow a more accurate quantification of overturning rates during Dansgaard-Oeschger interstadials, and provide information on the southern-sourced water mass flow rate during Heinrich Stadials.

In order to better understand the evolution of the ITCZ during Heinrich and DO stadials, a careful estimation of the lead of decreased precipitation in the northern tropics with

respect to increased precipitation in the southern tropics would be required. Indeed, the mechanisms of ITCZ variability could likely be discriminated based on the rapidity of the ITCZ shifts The slowly decreasing oceanic meridional heat transport that we propose would for instance be reflected by a gradual southward ITCZ shift, unless SST anomalies need to reach a certain threshold for the tropical convection zone to shift. Such a study would require a precise chronological framework, and would likely be possible using varved sediments or speleothems, which can be dated with a precision of a few decades even during the last glacial.

Finally, correlation of high latitude North Atlantic SST signals to Greenland temperatures would allow placing the periods of IRD deposition on the GICC05 timescale. Because the age model of our sediment cores is completely independent from the GICC05 timescale, we could directly compare the timing of iceberg releases related to Heinrich and precursory events (Peck et al., 2006) to periods of decreased strength of the upper AMOC circulation cell. Hence, it could be possible to determine whether the circulation slowdown observed in the Atlantic Ocean are the cause or the consequence of iceberg releases.

LIST OF FIGURES AND TABLES

Figures

FIGURE 1 : GREENLAND AIR TEMPERATURES OF THE LAST 20-50 KA (KINDLER ET AL., 2014). NUMBERS INDICATE DANSGAARD-OESCHGER INTERSTADIALS AND HS INDICATES HEINRICH STADIALS. 15
FIGURE 2 : SKETCH OF THE ATLANTIC MERIDIONAL OVERTURNING CIRCULATION (AMOC) FROM (KUHLBRODT ET AL., 2007). BLUE ARROWS INDICATE THE APPROXIMATE FLOW DIRECTION OF NADW (NORTH ATLANTIC DEEP WATER) AND AABW (ANTARCTIC BOTTOM WATER), THE NORTHERN AND SOUTHERN SOURCED DEEP WATER MASSES INITIATING THE UPPER AND LOWER OVERTURNING CELLS OF THE AMOC RESPECTIVELY. 16
FIGURE 1.1 : DISSOLVED ^{231}PA AND ^{230}TH PROFILES IN THE EQUATORIAL ATLANTIC FROM (CHOI ET AL., 2001). NOTE THAT THE ^{230}TH PROFILE INCREASES LINEARLY WITH DEPTH AS PREDICTED BY REVERSIBLE SCAVENGING, WHILE PROTACTINIUM IS EXPORTED AT DEPTH, RESULTING IN AN ALMOST CONSTANT CONCENTRATION WITH DEPTH BELOW 1000 M. 26
FIGURE 1.2 : STUDY AREA AND POSITION OF THE MAIN SURFACE CURRENTS (MODIFIED FROM (FRATANTONI AND GLICKSON, 2002)) 29
FIGURE 1.3 : SURFACE CURRENTS DURING APRIL (TOP) AND NOVEMBER (BOTTOM). DURING TIMES OF MINIMUM NECC INTENSITY (APRIL), AMAZON WATERS ARE DEVIATED NORTHWARDS. DURING TIMES OF MAXIMUM NECC (NOVEMBER), AMAZON WATERS ARE DEVIATED EASTWARDS BUT DO NOT REACH OUR STUDY AREA (LUMPKIN AND GARZOLI, 2005). 30
FIGURE 1.4 : MAP OF THE NORTH EASTERN BRAZILIAN MARGIN. NAMES OF RETRO3 CORES ARE WRITTEN IN RED AND NAMES OF M34/4 CORES IN GREEN. 32
FIGURE 1.5 : PHOSPHATE SECTION OF THE ATLANTIC OCEAN SHOWING THE SITES OF THE CORES LISTED IN TABLE 1. WHITE ARROWS INDICATE THE APPROXIMATE FLOW DIRECTIONS OF THE ANTARCTIC INTERMEDIATE WATER (AAIW), ANTARCTIC BOTTOM WATER (AABW) AND NORTH ATLANTIC DEEP WATER (NADW). 33
FIGURE 1.6 : TI/CA RECORD OF CORE GEOB3910. EACH TI/CA PEAK IS ASSOCIATED WITH ONE HEINRICH STADIAL (HS1-5). 34
FIGURE 1.7 : (A) Δ^{18}O AND (B) TI/CA SIGNALS OF INTERMEDIATE DEPTH CORES ON THE GEOB3910 DEPTH SCALE. 35
FIGURE 1.8 : (A) TI/CA AND (B) ^{14}C DATES (MARINE13, (REIMER ET AL., 2013)) IN CORE MD09-3257 35
FIGURE 1.**9** : (A) Δ^{18}O AND (B) TI/CA SIGNALS OF INTERMEDIATE (GEOB3910) AND DEEP (MD09-3256Q) CORES ON THE GEOB3910 DEPTH SCALE. NOTE THAT CORRELATION OF HS2 BETWEEN CORE MD09-3256Q AND CORE GEOB3910 REVEALED TO BE INCORRECT, AS INFERRED FROM ^{14}C DATING. 37
FIGURE 1.10 : PRESENT DAY TEMPERATURE AND SALINITY AT 30 M DEPTH ON THE BRAZILIAN MARGIN (WOA09). 37
FIGURE 1.11 : (A) TI/CA AND (B) ^{14}C DATES (MARINE13, (REIMER ET AL., 2013)) IN CORE MD09-3256Q 38
FIGURE 1.12 : (A) Δ^{18}O AND (B) TI/CA SIGNALS IN SHALLOW SEDIMENT CORES. 39
FIGURE 2.1 : SI (MG) AS A FUNCTION OF ABSORBANCE. SI CONTENT OF A SAMPLE SOLUTION IS ESTIMATED BASED ON ITS MEASURED ABSORBANCE AND ON THE RELATION ABSORBANCE-WEIGHT(SI) OF THE STANDARDS. 44
FIGURE 2.**2** : EXTRACTION OF SI AS A FUNCTION OF TIME IN A SEDIMENT SAMPLE CONTAINING BIOGENIC SILICA AND ALUMINO-SILICATE. AFTER 1-2H, ALL BIOGENIC SILICA IS DISSOLVED (DEMASTER, 2013). SI LEACHING CONTINUES AT A CONSTANT RATE, WHICH ALLOWS FINDING THE INITIAL %SI BIOGENIC IN THE SAMPLE FROM THE INTERCEPT. 44
FIGURE 2.3 : %OPAL IN TWO SAMPLES MEASURED BOTH AT THE IUP (BLUE DIAMONDS) AND LSCE (RED SQUARES). 45
FIGURE 2.4.1 : ANION-EXCHANGE CHROMATOGRAPHY SEPARATION AND PURIFICATION USED BY EACH OF THE PARTICIPATING LABORATORIES. HCL CONCENTRATION IS 9N, HNO_3 8N AND HF 0.13N UNLESS OTHERWISE STATED. RESIN TYPES INDICATED FOR THE LAST CHROMATOGRAPHY COLUMN OF EACH LABORATORY ALSO STAND FOR THE PREVIOUS COLUMNS OF THE LABORATORY. 68

FIGURE 2.4.2 : ISOTOPIC RATIOS MEASURED BY EACH LABORATORY ON THORIUM AND URANIUM ISOTOPIC REFERENCE MATERIAL. (A) $^{230}TH/^{232}TH$ MEASURED ON IRMM-035. CERTIFIED VALUE IS GIVEN AS REFERENCE, AS WELL AS INTER-LABORATORY MC-ICP-MS VALUE FROM SIMS ET AL [29]. (B) $^{234}U/^{238}U$ MEASURED ON NBS-SRM-960. CERTIFIED VALUE IS GIVEN AS REFERENCE. THE IUP GROUP MEASURED NBS-SRM-960 TWICE, ON SOLUTIONS FROM TWO DIFFERENT BOTTLES. ERROR BARS ARE THE MAXIMUM BETWEEN 2SE PROPAGATED ON THE MEAN (ERROR ON THE SUM OF REPLICATE MEASUREMENTS DIVIDED BY THE NUMBER OF MEASUREMENTS) AND 2SD ON SAMPLE REPLICATES (STANDARD DEVIATION OF REPLICATE MEASUREMENTS). THE NUMBER OF FULL CHEMISTRY REPLICATES USED TO CALCULATE THE MEANS IS WRITTEN NEXT TO EACH MEASUREMENT. 69

FIGURE 2.4.3 : COMPARISON OF THE ^{231}PA CONCENTRATIONS IN SEDIMENT AND UREM11. RESULTS ARE EXPRESSED BY THE DEVIATION (%)OF THE CONCENTRATIONS MEASURED BY EACH LABORATORY FROM THE MEAN OF THE 4 LABORATORIES. THE DEVIATION OF THE GEOTRACES INTERCALIBRATION VALUE FROM THE MEAN IS ALSO GIVEN FOR GEOTRACES_SED [23]. NOTE THAT THE GEOTRACES INTERCALIBRATION VALUE WAS NOT USED TO COMPUTE THE MEAN ISOTOPIC CONCENTRATIONS. ERROR BARS ARE CALCULATED AS IN FIGURE 2 AND CONVERTED IN % FROM THE INTER-LABORATORY MEAN. THE NUMBER OF REPLICATES USED TO CALCULATE THE AVERAGES IS WRITTEN NEXT TO THE ERROR BARS. 70

FIGURE 2.4.4 : COMPARISON OF THE (A) THORIUM AND (B) URANIUM CONCENTRATIONS IN SEDIMENT AND UREM11. RESULTS ARE EXPRESSED BY THE DEVIATION (%) OF THE CONCENTRATIONS MEASURED BY EACH LABORATORY FROM THE MEAN OF THE 4 LABORATORIES. IN (A), THE DEVIATION OF THE GEOTRACES INTERCALIBRATION VALUE FROM THE MEAN IS ALSO GIVEN FOR GEOTRACES_SED [23]. NOTE THAT THE GEOTRACES INTERCALIBRATION VALUE WAS NOT USED TO COMPUTE THE MEAN THORIUM ISOTOPIC CONCENTRATIONS. ERROR BARS ARE CALCULATED AS IN FIGURE 2 AND CONVERTED IN % FROM THE INTER-LABORATORY MEAN. MEAN CONCENTRATIONS FOR EACH LAB WERE CALCULATED USING THREE FULL REPLICATES UNLESS WRITTEN OTHERWISE ON THE FIGURE. 71

FIGURE 2.4.5 : ISOTOPIC CONCENTRATIONS OBTAINED AT UB AFTER DIGESTION BY MICROWAVE (WHITE CIRCLES) OR HOTPLATE (BLACK CIRCLES) ON (A) UREM11, (B) GEOTRACES_SED. ERROR BARS ARE CALCULATED AS IN FIGURE 2 FOR MICROWAVE MEASUREMENTS. ERROR BARS ARE 2SE FOR HOTPLATE MEASUREMENTS (1 REPLICATE ONLY). ERROR BARS ON HOTPLATE MEASUREMENTS ON THE GEOTRACES_SED SAMPLE ARE SMALL AND CANNOT BE DISTINGUISHED FROM THE DATA POINTS. 72

FIGURE 2.4.6 : CONCENTRATION DEVIATIONS OF ONE REPLICATE FROM THE OTHER AS A FUNCTION OF ADDITIONAL TIME LEFT FOR ^{233}PA TO DECAY IN THE SECOND REPLICATE (SEE TEXT). REPLICATES REPRESENTED BY THE SQUARE ARE NOT FULL CHEMISTRY REPLICATES, BUT A SINGLE PA FRACTION THAT WAS MEASURED AT DIFFERENT TIMES AFTER U-PA SEPARATION (10 AND 52 DAYS). REPLICATES REPRESENTED BY THE CIRCLES ARE FULL CHEMISTRY REPLICATES. NUMBERS INDICATE THE AVERAGE CONCENTRATIONS OF THE REPLICATES ($DPM.G^{-1}$). SEE TABLE S3 FOR UNCERTAINTIES ON ^{231}PA MEASUREMENTS. 73

FIGURE 2.4.S1 : ILLUSTRATION OF THE CONING AND QUARTERING METHOD. FIRST, A) THE SEDIMENT IS POURED ON DRAWING PAPER BY APPLYING A SWIRLING MOVEMENT TO THE WRIST IN ORDER TO FORM A DOME THEN B) THE DOME IS DIVIDED IN FOUR AND C) THE OPPOSITE QUARTERS ARE GATHERED. THE RESULTING SEDIMENT PILES (2, 3) AND THE INITIAL SEDIMENT (1) ARE EXPECTED TO BE HOMOGENEOUS. 79

FIGURE 2.4.S2 : SEDIMENT AND UREM11 ^{232}TH CONCENTRATION RESULTS FOR EACH OF THE PARTICIPATING LABORATORIES. NOTE THAT THE Y AXIS RANGE FOR EACH SAMPLE IS OF AROUND 25% OF THE SAMPLE'S MEAN CONCENTRATION. THIS ALLOWS TO COMPARE THE INTER AND INTRA-LABORATORY CONCENTRATION VARIABILITY OF THE SAMPLES. HENCE CARE SHOULD BE TAKEN WHEN COMPARING ABSOLUTE CONCENTRATIONS, AS THE Y AXIS IS OFTEN SPLIT AND MAGNIFIED FOR SOME SAMPLES. CIRCLES REPRESENT THE UREM11, SQUARES THE GEOTRACES_SED AND DIAMONDS THE MARGIN_SED SAMPLES. ERROR BARS ARE 2SE. 80

FIGURE 2.4.S3 : SEDIMENT AND UREM11 ^{230}TH CONCENTRATION RESULTS FOR EACH OF THE PARTICIPATING LABORATORIES. NOTE THAT THE Y AXIS RANGE FOR EACH SAMPLE IS OF AROUND 25% OF THE SAMPLE'S MEAN CONCENTRATION. THIS ALLOWS TO COMPARE THE INTER AND INTRA-LABORATORY CONCENTRATION VARIABILITY OF THE SAMPLES. HENCE CARE SHOULD BE TAKEN WHEN COMPARING ABSOLUTE CONCENTRATIONS, AS THE Y AXIS IS OFTEN SPLIT AND MAGNIFIED FOR SOME SAMPLES. CIRCLES REPRESENT THE UREM11, SQUARES THE GEOTRACES_SED AND DIAMONDS THE MARGIN_SED SAMPLES. ERROR BARS ARE 2SE. 81

FIGURE 2.4.S4 : SEDIMENT AND UREM11 ^{238}U CONCENTRATION RESULTS FOR EACH OF THE PARTICIPATING LABORATORIES. NOTE THAT THE Y AXIS RANGE FOR EACH SAMPLE IS OF AROUND 25% OF THE SAMPLE'S MEAN CONCENTRATION. THIS ALLOWS TO COMPARE THE INTER AND INTRA-LABORATORY CONCENTRATION VARIABILITY OF THE SAMPLES. HENCE CARE SHOULD BE TAKEN WHEN COMPARING ABSOLUTE CONCENTRATIONS, AS THE Y AXIS IS OFTEN SPLIT AND MAGNIFIED FOR SOME SAMPLES. CIRCLES REPRESENT THE UREM11, SQUARES THE GEOTRACES_SED AND DIAMONDS THE MARGIN_SED SAMPLES. ERROR BARS ARE 2SE. 82
FIGURE 2.4.S5 : SEDIMENT AND UREM11 ^{234}U CONCENTRATION RESULTS FOR EACH OF THE PARTICIPATING LABORATORIES. NOTE THAT THE Y AXIS RANGE FOR EACH SAMPLE IS OF AROUND 25% OF THE SAMPLE'S MEAN CONCENTRATION. THIS ALLOWS TO COMPARE THE INTER AND INTRA-LABORATORY CONCENTRATION VARIABILITY OF THE SAMPLES. HENCE CARE SHOULD BE TAKEN WHEN COMPARING ABSOLUTE CONCENTRATIONS, AS THE Y AXIS IS OFTEN SPLIT AND MAGNIFIED FOR SOME SAMPLES. CIRCLES REPRESENT THE UREM11, SQUARES THE GEOTRACES_SED AND DIAMONDS THE MARGIN_SED SAMPLES. ERROR BARS ARE 2SE. 83
FIGURE 2.4.S6 : SEDIMENT AND UREM11 ^{231}PA CONCENTRATION RESULTS FOR EACH OF THE PARTICIPATING LABORATORIES. NOTE THAT THE Y AXIS RANGE FOR EACH SAMPLE IS OF AROUND 25% OF THE SAMPLE'S MEAN CONCENTRATION. THIS ALLOWS TO COMPARE THE INTER AND INTRA-LABORATORY CONCENTRATION VARIABILITY OF THE SAMPLES. HENCE CARE SHOULD BE TAKEN WHEN COMPARING ABSOLUTE CONCENTRATIONS, AS THE Y AXIS IS OFTEN SPLIT AND MAGNIFIED FOR SOME SAMPLES. CIRCLES REPRESENT THE UREM11, SQUARES THE GEOTRACES_SED AND DIAMONDS THE MARGIN_SED SAMPLES. ERROR BARS ARE 2SE. 84
FIGURE 2.4.S7 : MEAN PA/TH VALUES OBTAINED BY EACH OF THE PARTICIPATING LABS. NOTE THAT THE Y AXIS RANGE FOR BOTH SAMPLES IS OF AROUND 25% OF THE SAMPLE'S MEAN PA/TH. THIS ALLOWS TO COMPARE THE INTER-LABORATORY PA/TH VARIABILITY OF THE SAMPLES. HENCE CARE SHOULD BE TAKEN WHEN COMPARING ABSOLUTE PA/TH VALUES, AS THE Y AXIS IS SPLIT AND MAGNIFIED. SQUARES REPRESENT THE GEOTRACES_SED AND DIAMONDS THE MARGIN_SED SAMPLES. 2 SIGMA ERROR IS CALCULATED BASED ON THE MAXIMUM BETWEEN 2 SE AND 2 SD OF REPLICATE CONCENTRATION MEASUREMENTS AND DOES NOT INCLUDE THE UNCERTAINTY ON THE R VALUE (SET TO 0.5). 85
FIGURE 3.1 : MAP OF THE STUDY AREA. THE RED CIRCLE INDICATES THE LOCATION OF THE STUDIED MARINE SEDIMENT CORES, THE ORANGE CIRCLE INDICATES THE POSITION OF THE EL CONDOR (ELC) AND DIAMANTE (NAR) CAVES (10), THE BLACK DASHED LINE DELIMITATES THE NORDESTE REGION, AND RED DASHED LINE SHOWS THE POSITION OF THE PRESENT DAY SEPTEMBER AND MARCH ITCZ OVER THE ATLANTIC AND PACIFIC OCEAN. THE COLOR SCALE INDICATES MEAN PRECIPITATION OVER SOUTH AMERICA (MM/Y) FOR THE MONTHS OF MARCH AND SEPTEMBER AVERAGED OVER THE PERIOD 1950-1996 AD (58). 111
FIGURE 3.2 : COMPARISON BETWEEN (A) THE U-TH DATED $\delta^{18}O$ RECORDS OF ELC/NAR SPELEOTHEMS (10) AND (B) THE ^{14}C-DATED TI/CA RECORD OF CORE GEOB3910 (12). (C) TI/CA RECORD OF MARINE SEDIMENT CORES GEOB3910 (12) AND MD09-3257 ON THEIR FINAL AGE MODELS. COLORED DIAMONDS SHOW THE POSITIONS OF THE U-TH DATES FOR SPELEOTHEMS AND OF THE ^{14}C DATES FOR MARINE SEDIMENT CORES WITH THEIR 2 SD ERROR BARS. DIAMONDS BELOW THE X-AXIS DEPICT THE ^{14}C DATES USED TO ESTABLISH THE AGE MODEL OF CORES MD09-3257 AND GEOB3910, DIAMOND COLORS CORRESPOND TO THAT OF THE CORES ON WHICH THE ^{14}C DATES HAVE BEEN MEASURED. EMPTY SQUARES SHOW THE POSITION OF GEOB3910-MD09-3257 TIE POINTS USED TO ESTABLISH THE AGE MODEL OF CORE MD09-3257. EMPTY TRIANGLES ARE THE SPELEOTHEM TIE POINTS USED TO ESTABLISH THE AGE MODEL OF CORES MD09-3257 AND GEOB3910 BEYOND THE ^{14}C DATING RANGE (SEE TEXT AND SI TABLE S1, S2). 112
FIGURE 3.3 : COMPARISON BETWEEN GREENLAND (A) NGRIP TEMPERATURE SIGNAL ON THE GICC05 TIMESCALE (59) AND BRAZIL (B) MD09-3257 PA/TH, (C) GEOB3910 *CIBICIDES WUELLERSTORFI* $\delta^{13}C$, AND (D) GEOB3910 (12) (BLUE) AND MD09-3257 (RED) TI/CA RECORDS. GRAY DASHED BANDS DELIMITATE THE PRECIPITATION EVENTS DEFINED ON THE ELC SPELEOTHEM $\delta^{18}O$ RECORD (SI APPENDIX FIG. S3). BLUE SHADED BANDS DELIMITATE THE PRECIPITATION EVENTS AS SEEN IN THE MD09-3257 TI/CA RECORD (SEE TEXT). VERTICAL BLACK DASHED LINES INDICATE THE START OF THE PA/TH AND TI/CA RISES IN CORE MD09-3257. IN (A) NUMBERS INDICATE THE DO EVENTS. IN (B) THE RED LINE PASSES THROUGH AVERAGE PA/TH VALUES WHEN THERE ARE REPLICATE MEASUREMENTS, THE WHITE SYMBOLS INDICATE PA/TH VALUES ARE NOT CONSIDERED FOR THIS STUDY AS THEY MIGHT NOT REPRESENT A PURE CIRCULATION SIGNAL (METHODS), THE RED HORIZONTAL BAND INDICATES THE PRESENT DAY PA/TH VALUE

(0.065±0.003, METHODS). ERROR BARS ON PA/TH MEASUREMENTS ARE GIVEN IN METHODS AND FIG. S8. NO PA/TH MEASUREMENTS COULD BE MADE DURING PE2 BECAUSE OF THE OCCURRENCE OF TWO SMALL TURBIDITES (SI APPENDIX SECTION A). IN (C) THE THICK DARK BLUE LINE IS THE 3 POINTS RUNNING AVERAGE OF THE *CIBICIDES W.* $\delta^{13}C$ RECORD. 113
FIGURE 3.4 : ILLUSTRATION OF THE INTERACTIONS BETWEEN GREENLAND CLIMATE, TROPICAL CLIMATE AND THE AMOC. ARROWS ILLUSTRATE CAUSAL MECHANISMS BETWEEN TRIGGERS AND CLIMATIC RESPONSE DISCUSSED IN THE TEXT. THE THICK BLACK ARROW ILLUSTRATES THE MAIN MECHANISM DISCUSSED IN THIS STUDY, THAT IS AN AMOC SLOWDOWN COULD HAVE TRIGGERED MILLENNIAL-SCALE ITCZ LATITUDINAL SHIFTS. THE DOTTED ARROW 1B INDICATES AN ADDITIONAL POTENTIAL TRIGGER FOR ITCZ SHIFTS (SEE TEXT). 114
FIGURE 3.**S1 :** TI/CA RATIO AND ^{232}TH FLUX VERSUS DEPTH IN CORE MD09-3257. 121
FIGURE 3.S2 : MAP OF THE NORDESTE SHOWING THE POSITION OF THE MAIN BRAZILIAN RIVERS AND SURFACE CURRENTS THAT COULD CONTRIBUTE TO TERRIGENOUS SEDIMENT INPUT AT THE STUDY SITE INDICATED BY A RED CIRCLE. 122
FIGURE 3.S3 : COMPARISON OF U-TH DATED SOUTH AMERICAN SPELEOTHEMS $\Delta^{18}O$ RECORDS AND DEFINITION OF THE MILLENNIAL PRECIPITATION EVENTS PE0 TO PE5. VERTICAL GREY DASHED BARS INDICATE PRECIPITATION EVENTS PE0 TO PE5 AS DEFINED ON THE ELC/NAR $\Delta^{18}O$ RECORDS. COLOURED DIAMONDS SHOW THE POSITION OF THE U-TH DATES FOR EACH SPELEOTHEM AND THEIR 2 SD ERROR BARS. THE COLOUR OF THE DIAMONDS CORRESPONDS TO THAT OF THEIR RESPECTIVE CURVES. SPELEOTHEM AND TRAVERTINE GROWTH INTERVALS FROM THE TOCA DA BOA VISTA (TBV)/ LAPA DOS BREJOES (LBR) CAVES (17) ARE SHOWN AS GREY CIRCLES ON THE TOP OF THE PANEL AS WELL AS THEIR 2 SD ERROR BARS. ELC AND NAR ARE THE EL CONDOR AND DIAMANTE CAVES, RESPECTIVELY (8). THE BLACK LINE REPRESENTS THE 3 POINTS RUNNING AVERAGE OF THE ELC $\Delta^{18}O$ SIGNAL. THE PACUPAHUAIN (10), THE SANTIAGO (11) AND THE BOTUVERA (7) SPELEOTHEM $\Delta^{18}O$ RECORDS ARE SHOWN AS WELL. SEE FIG. S4 FOR THE LOCATION OF THE SPELEOTHEMS IN SOUTH AMERICA. 123
FIGURE 3.S4 : MAP SHOWING THE POSITION OF THE SOUTH AMERICAN SPELEOTHEMS USED IN FIG. S3 AND THE TWO MARINE SEDIMENTARY CORES USED IN THIS STUDY, MD09-3257 AND GEOB3910. THE ORANGE CIRCLE INCLUDES BOTH EL CONDOR (ELC) AND DIAMANTE (NAR) CAVES. 124
FIGURE 3.S5 : DATES (KA) FOR THE ONSET AND END OF THE MAIN PRECIPITATION EVENTS (PE) RECORDED IN SOUTH AMERICAN SPELEOTHEMS AND CORE GEOB3910 (SEE FIG. S4). THE AGE MODEL FORE CORE GEOB3910 IS BASED ON ^{14}C DATES ONLY. THE COLOR CODE OF THE SPELEOTHEM DATES INDICATES THE DEGREE OF SYNCHRONICITY OF EACH ONSET/END OF PE WITH RESPECT TO THE EL CONDOR (ELC) SPELEOTHEM SIGNAL TAKEN AS REFERENCE. THE REFERENCE DATES FOR THE PE EVENTS IN THE ELC SPELEOTHEM ARE SHOWN IN WHITE. DATES IN GREEN ARE SYNCHRONOUS WITHIN ERROR BARS WITH THE ELC SPELEOTHEM, DATES IN YELLOW ARE LIKELY TO BE SYNCHRONOUS AND DATES IN RED ARE ASYNCHRONOUS (SEE TEXT). 125
FIGURE 3.S6 : TI/CA (RED) AND SEDIMENTATION RATE (BLUE) FOR CORE MD09-3257. 126
FIGURE 3.S7 : CORRELATION BETWEEN THE PA/TH RATIO AND ^{232}TH FLUX (LEFT PANEL) OR OPAL FLUX (RIGHT PANEL). EMPTY SYMBOLS IN THE LEFT PANEL ARE NOT CONSIDERED IN THE COMPUTATION OF THE CORRELATION COEFFICIENT. ERROR BARS IN THE RIGHT PANEL ARE 1 SD. 127
FIGURE 3.S8 : PA/TH IN MD09-3257 AS A FUNCTION OF TIME CALCULATED WITH DIFFERENT VALUES FOR THE LITHOGENIC ($^{238}U/^{232}TH$) VALUE (R) USED TO CORRECT FOR DETRITAL MATERIAL CONTRIBUTION (18). RED CURVE, R=0.5 (CORRECTION USED IN FIG. 3), GREEN CURVE R=0.4, AND BLUE CURVE R=0.6. ERROR BARS ARE 1 SD. 128
FIGURE 3.S9 : COMPARISON BETWEEN THE PA/TH (RED), TI/CA, AND LN(TI/CA) (BLUE CURVES) SIGNALS. GREY BANDS HIGHLIGHT THE LEAD OF THE PA/TH SIGNAL WITH RESPECT TO THE TI/CA AND LN(TI/CA) SIGNALS. 129
FIGURE 4.1 : PHOSPHATE SECTION OF THE ATLANTIC OCEAN SHOWING THE SITES OF CORES MD09-3257 (04°14.69'S, 36°21.18'W, 2344 M), MD09-3256Q (03°32.81'S, 35°23.11'W, 3537 M), ODP LEG 172, SITE 1063 (33°41'N, 57°37'W, 4584 M) (LIPPOLD ET AL., 2009) AND MD02-2594 (34°43'S, 17°20'E, 2440 M) (NEGRE ET AL., 2010). PHOSPHATE CONTENT FOLLOWS THE STRUCTURE OF THE PRESENT DAY AMOC. WHITE ARROWS INDICATE THE APPROXIMATE FLOW DIRECTIONS OF THE ANTARCTIC INTERMEDIATE WATER (AAIW), ANTARCTIC BOTTOM WATER (AABW) AND NORTH ATLANTIC DEEP WATER (NADW). 157
FIGURE 4.2 : SIMULATED SEDIMENTARY PA/TH VALUES AND ASSOCIATED STREAMFUNCTIONS: (A, B) HOLOCENE, (C, D) OFF-MODE, (E, F) HS1. 158

FIGURE 4.**3** : COMPARISON BETWEEN OCEANIC CIRCULATION AND WATER MASS PROXIES ON THE BRAZILIAN MARGIN AND BERMUDA RISE, AND GREENLAND TEMPERATURES. (A) MD09-3256Q, MD09-3257 (BURCKEL ET AL., SUBMITTED) AND ODP172-1063 (LIPPOLD ET AL., 2009) PA/TH (B) MD09-3256Q AND GEOB3910 (BURCKEL ET AL., SUBMITTED) *CIBICIDES WUELLERSTORFI* $\delta^{13}C$ AND (C) NGRIP TEMPERATURE SIGNAL ON THE GICC05 TIMESCALE (KINDLER ET AL., 2014). IN (A) THE AVERAGE PA/TH FOR EACH CORE IS REPRESENTED BY THE LINES AND INDIVIDUAL MEASUREMENTS BY DIAMONDS (MD09-3256Q, ODP SITE 1063) AND SQUARES (MD09-3257). THE WHITE SQUARES INDICATE PA/TH VALUES NOT CONSIDERED IN CORE MD09-3257 (BURCKEL ET AL., SUBMITTED), THE WHITE DIAMONDS INDICATE THE PA/TH VALUES THAT MAY NOT REPRESENT A PURE CIRCULATION SIGNAL IN CORE MD09-3256Q (SEE RESULTS). THE RED ARROW INDICATES THE LATE HOLOCENE PA/TH VALUE ON CORE MD09-3257 (0.065±0.003, BURCKEL ET AL., 2014 B, SUBMITTED) AND THE BLUE ARROW THE LATE HOLOCENE PA/TH VALUE ON CORE MD09-3256Q (0.043±0.001). ERROR BARS ON PA/TH MEASUREMENTS ARE GIVEN IN FIG. S1, TABLE S4. IN (B) THE SIGNAL IS THE 3 POINTS RUNNING AVERAGE OF THE *CIBICIDES W.* $\delta^{13}C$ RECORD, THE BLACK ARROW INDICATES PRESENT DAY NADW $\delta^{13}C$ VALUE (~1.37 ‰). $\delta^{13}C$ VALUES ARE GIVEN IN TABLE S5. IN (C) NUMBERS INDICATE THE DO EVENTS. MD09-3257 AND GEOB3910 DATA ARE PRESENTED IN RED, MD09-3256Q DATA IN BLUE AND ODP172-1063 IN GREEN. RED VERTICAL BANDS REPRESENT THE PRE-HS2, POST-HS4 AND PRE-HS4 TIME SLICES AND THE BLUE VERTICAL BAND THE HS2 TIME SLICE. 159

FIGURE 4.4 : COMPARISON OF THE PA/TH DATA (CIRCLES) FOR EACH OF THE TIME SLICES TO THE SIMULATED PA/TH VALUES USING THE HOLOCENE STREAMFUNCTION. TIME SLICES ARE (A) HS2, (B) PRE-HS2, (C) POST-HS4 AND (D) PRE-HS4 PA/TH DATA. THE UPPER HALF OF THE CIRCLES REPRESENT THE PA/TH DATA, THE LOWER LEFT QUARTER PA/TH – 1 SIGMA AND THE LOWER RIGHT QUARTER PA/TH + 1 SIGMA. 160

FIGURE 4.5 : COMPARISON OF THE PA/TH DATA FOR EACH OF THE TIME SLICES TO THE SIMULATED PA/TH VALUES USING THE OFF-MODE STREAMFUNCTION. TIME SLICES ARE (A) HS2, (B) PRE-HS2, (C) POST-HS4 AND (D) PRE-HS4 PA/TH DATA. THE UPPER HALF OF THE CIRCLES REPRESENT THE PA/TH DATA, THE LOWER LEFT QUARTER PA/TH – 1 SIGMA AND THE LOWER RIGHT QUARTER PA/TH + 1 SIGMA. 161

FIGURE 4.6 : COMPARISON OF THE PA/TH DATA FOR EACH OF THE TIME SLICES TO THE SIMULATED PA/TH VALUES USING THE HS1 STREAMFUNCTION. TIME SLICES ARE (A) HS2, (B) PRE-HS2, (C) POST-HS4 AND (D) PRE-HS4 PA/TH DATA. THE UPPER HALF OF THE CIRCLES REPRESENT THE PA/TH DATA, THE LOWER LEFT QUARTER PA/TH – 1 SIGMA AND THE LOWER RIGHT QUARTER PA/TH + 1 SIGMA. 162

FIGURE 4.7 : SKETCH OF THE POSSIBLE STATES OF THE AMOC DURING (A) DO INTERSTADIALS AND (B) HEINRICH STADIALS. SEE TEXT FOR EXPLANATION. 163

FIGURE 4.S1 : PA/TH IN MD09-3256Q AS A FUNCTION OF TIME CALCULATED WITH DIFFERENT LITHOGENIC ($^{238}U/^{232}TH$) (R) VALUES USED TO CORRECT FOR DETRITAL MATERIAL CONTRIBUTION (FRANCOIS, 2007). RED CURVE, R=0.5 (CORRECTION USED IN FIG. 3), GREEN CURVE R=0.4, AND BLUE CURVE R=0.6. ERROR BARS ARE 1 SD AND DO NOT ACCOUNT FOR THE ERROR ON R. 164

FIGURE 4.S2 : CORE MD09-3256Q AGE MODEL. BLUE SQUARES INDICATE THE POSITION OF THE ^{14}C DATES IN THE CORE, BLUE TRIANGLES INDICATE TIE POINTS BETWEEN CORE GEOB3910 AND MD09-3256Q. DISCONTINUITIES IN THE TI/CA RECORD CORRESPOND TO THE POSITION OF TURBIDITE LAYERS. ERROR BARS ARE 1 SIGMA AND DO NOT INCLUDE THE UNCERTAINTY ON CORRELATION FOR THE TIE POINTS. 165

FIGURE 4.S3 : CORE MD09-3256Q TI/CA (BLUE CURVE) AND SEDIMENTATION RATE (RED CURVE). 166

FIGURE 4.S4 : SEDIMENTARY PA/TH (RED) AND OPAL FLUX (BLACK) AS A FUNCTION OF DEPTH IN CORE MD09-3256Q. ERROR BARS ARE 1 SE. 167

FIGURE 4.S5 : CORRELATION BETWEEN THE 232TH FLUX AND SEDIMENTARY PA/TH RATIO ON CORE MD09-3256Q. WHITE DIAMONDS REPRESENT PA/TH DATA THAT MAY NOT REPRESENT A PURE CIRCULATION SIGNAL. 168

FIGURE 4.S6 : PA/TH OF CORE MD09-3257 (RED), MD09-3256Q (BLUE), ODP SITE 172 (LIPPOLD ET AL., 2009)(GREEN) AND MD02-2594 (NEGRE ET AL., 2010)(BLACK). WHITE SYMBOLS REPRESENT PA/TH DATA THAT MAY NOT REFLECT A PURE CIRCULATION SIGNAL. 169

FIGURE 4.S7 : H1 SIMULATED (A) PA/TH AND (B) STREAMFUNCTION AND FLUX (SV, BLUE BARS, SCALE ON TOP) AT THE EQUATOR. NOTE THE LARGE FLOW RATE DECREASE AT THE EQUATOR FROM ~2500 M TO ~3500 M. 170

FIGURE 4.S8 : PA/TH ON THE BRAZILIAN MARGIN. RED SQUARES, DATA OBTAINED FROM HOLOCENE SEDIMENTS IN THIS STUDY. BLACK SQUARES, DATA OBTAINED FROM HOLOCENE SEDIMENTS IN (LIPPOLD ET AL., 2011). GREY AND BLACK LINES, SIMULATED PA/TH VALUES WITH THE 2 AND 3X INCREASED HOLOCENE STREAMFUNCTION RESPECTIVELY. 171

Tables

TABLE 1.**1** : NAME, POSITION AND DEPTH OF THE CORES DISPLAYED IN FIGURE 1 AND DISCUSSED IN THE TEXT. GRAVITY CORES ARE INDICATED IN RETRO3 CORES BY THE LETTER "Q". RETRO3 CORES ARE OTHERWISE PISTON CORES. 32

TABLE 2.1 : SI MASS AND RELATED ABSORBANCE FOR STANDARDS USED TO FORM THE LINEAR REGRESSION IN FIG. 1. SI CALCULATED IS THE ESTIMATE OF THE CONCENTRATION IN THE STANDARDS BASED ON THE LINEAR REGRESSION. 44

TABLE 2.2 : MC-ICP-MS CUP CONFIGURATION FOR THE ANALYSIS OF U AND PA ISOTOPIC RATIOS. "SOLUTION" COLUMN: THE TYPE OF SOLUTION ANALYZED, "IC4"-"H3" COLUMNS: ION COUNTERS AND FARADAY CUPS USED FOR ISOTOPIC ANALYSES, "RATIO" COLUMN: THE RATIOS OF INTEREST, "USE" COLUMN: HOW ARE THE ISOTOPIC RATIOS USED, "FOR" COLUMN: ELEMENTS FOR WHICH THE MEASURED ISOTOPIC RATIOS ARE USEFUL. AS STANDS FOR ABUNDANCE SENSITIVITY. SHADED CELLS IN COLUMN C(C)/IC1 INDICATE WHICH DETECTOR WAS USED (ION COUNTER VERSUS FARADAY CUP). SHADED=C(C), NOT SHADED = IC1. CUP DISTANCES IN ATOMIC MASS UNITS (U) ARE SHOWN ON TOP. LX, HX AND C(C) ARE FARADAY CUPS, ICX ARE ION COUNTERS. 49

TABLE 2.3 : MC-ICP-MS CUP CONFIGURATION FOR THE ANALYSIS TH ISOTOPIC RATIOS. "SOLUTION" COLUMN: THE TYPE OF SOLUTION ANALYZED, "IC4"-"H3" COLUMNS: ION COUNTERS AND FARADAY CUPS USED FOR ISOTOPIC ANALYSES, "RATIO" COLUMN: THE RATIOS OF INTEREST, "USE" COLUMN: HOW ARE THE ISOTOPIC RATIOS USED, "FOR" COLUMN: ELEMENTS FOR WHICH THE MEASURED ISOTOPIC RATIOS ARE USEFUL. AS STANDS FOR ABUNDANCE SENSITIVITY. SHADED CELLS IN COLUMN C(C)/IC1 INDICATE WHICH DETECTOR WAS USED (ION COUNTER VERSUS FARADAY CUP). SHADED=C(C), NOT SHADED = IC1. CUP DISTANCES IN ATOMIC MASS UNITS (U) ARE SHOWN ON TOP. LX, HX AND C(C) ARE FARADAY CUPS, ICX ARE ION COUNTERS. 50

TABLE 2.4 : CALCULATION AND APPLICATION OF CORRECTIONS TO ISOTOPIC SIGNALS AND RATIOS. "CORRECTION" COLUMN: TYPE OF CORRECTION, "CALCULATION" COLUMN: CALCULATION OF THE CORRECTION, "APPLICATION" COLUMN: APPLICATION OF THE CORRECTION ON ISOTOPIC RATIOS OR SIGNALS, "NOTE" COLUMN: NOTES FOR CLARIFICATION OF THE EQUATIONS. X AND Y ARE ELEMENTS. X CAN BE THE SAME ELEMENT AS Y. COR. STANDS FOR CORRECTED. "U" STANDS FOR ATOMIC MASS UNIT. 50

TABLE 2.4.1 : SEDIMENT AND SPIKE MASSES, AND DIGESTION STEPS USED BY EACH LABORATORY. * H AND MW STAND FOR HOTPLATE AND MICROWAVE RESPECTIVELY. ** WHITE SMOKE PRODUCTION INDICATES THAT ONLY PERCHLORIC ACID IS LEFT IN SOLUTION. 74

TABLE 2.4.2 : TOTAL CHEMISTRY YIELDS AND SEPARATION EFFICIENCIES FOR EACH OF THE LABORATORIES. MAX MEANS THAT ELEMENTS (U-TH) SEPARATED FROM THE PA FRACTION FALL BELOW PROCEDURAL BLANKS. SEPARATION EFFICIENCY OF A FROM PA FRACTION EQUALS THE A/PA RATIO IN THE SEDIMENT DIVIDED BY THE A/PA RATIO IN THE PA FRACTION (WHERE A IS EITHER U OR TH). THE YIELD CALCULATED BY THE LSCE IS A ROUGH ESTIMATE BASED ON ELEMENT DILUTION (ACID VOLUME) AND SIGNAL DURING MASS SPECTROMETRY ANALYSIS, AND ON MASS-SPECTROMETER SENSITIVITY. 75

TABLE 2.4.**3** : MASS-SPECTROMETER CORRECTION INTENSITIES, SENSITIVITY AND INTRODUCTION SYSTEMS. AS = ABUNDANCE SENSITIVITY. 75

TABLE 2.4.**4** : COMPARISON OF CONCENTRATION RESULTS ON GEOTRACES_SED WITH THE GEOTRACES INTERCALIBRATION. RESULTS GIVEN IN THE TABLE ARE AVERAGES OF THE FOUR LABORATORIES PARTICIPATING IN THE STUDY, APART FROM THE SECOND VALUES OF ^{238}U AND ^{234}U CONCENTRATIONS, WHICH ARE AVERAGES OF MC-ICP-MS CONCENTRATIONS ONLY. 75

TABLE 2.4.5 : BEST CHEMISTRY METHODS WITH RESPECT TO EFFICACY, RAPIDITY, AND ACID VOLUME USED. 75

TABLE 2.4.S1 : ISOTOPIC RATIO MEASUREMENTS ($\times 10^6$) ON ISOTOPIC REFERENCE MATERIAL NBS-SRM-960 AND IRMM-035. 234U/238U MEASUREMENTS BY THE IUP WERE DONE ON NBS-SRM-960 FROM TWO DIFFERENT BOTTLES. THE VALUE GIVEN BY SIM ET AL FOR THE ^{230}TH/^{232}TH RATIO OF IRMM-035 IS ALSO DISPLAYED. 86

TABLE 2.4.S2 : ISOTOPIC CONCENTRATION RESULTS OF SOLID SAMPLES MARGIN_SED, GEOTRACES_SED AND UREM11. LINES WITH A * FOR UB GROUP MEASUREMENTS INDICATE THAT DIGESTION WAS DONE USING HOTPLATE AND NOT MICROWAVE. 87
TABLE 2.4.S3 : ^{231}PA CONCENTRATION OF REPLICATE SAMPLES (E.G. 1 A AND 1 B) MEASURED AT DIFFERENT TIMES T BETWEEN U-PA SEPARATION AND MASS SPECTROMETER ANALYSIS. SAMPLE 8 A AND 8 B ARE NOT FULL SEDIMENT REPLICATES, BUT A SINGLE ^{231}PA/^{233}(PA+U) SOLUTION MEASURED AT DIFFERENT TIMES AFTER U-PA SEPARATION. 89
TABLE 2.4.S4 : MEAN PA/TH RESULTS FOR EACH OF THE LABS. 2 SIGMA ERROR IS CALCULATED BASED ON THE MAXIMUM BETWEEN 2 SE AND 2 SD OF REPLICATE CONCENTRATION MEASUREMENTS AND DOES NOT INCLUDE THE UNCERTAINTY ON THE R VALUE (SET TO 0.5). 90
TABLE 2.4.**S5** : ACID VOLUMES USED BY EACH LAB FOR DIGESTION AND ELUTION BY COLUMN CHROMATOGRAPHY. ONLY ACIDS MORE CONCENTRATED THAN 2N ARE CONSIDERED. 91
TABLE 3.S1 : AGE MODEL FOR CORE GEOB3910. 130
TABLE 3.S2 : AGE MODEL FOR CORE MD09-3257. 131
TABLE 3.S3 : ^{231}PA, ^{230}TH, ^{232}TH, AND ^{238}U CONCENTRATIONS (DPM.G^{-1}) VERSUS DEPTH IN CORE MD09-3257. PA/TH VALUES ARE COMPUTED WITH A R RATIO OF 0.5. 132
TABLE 3.S4 : *CIBICIDES WUELLERSTORFI* Δ^{13}C VALUES VERSUS DEPTH IN CORE GEOB3910. 133
TABLE 3.S5 : OPAL DATA VERSUS DEPTH IN CORE MD09-3257. 134
TABLE 4.S1 : CORE MD09-3256Q AGE MODEL. ^{14}C AGE IS CONVERTED TO CALENDAR AGE USING THE MARINE13 CURVE (REIMER ET AL., 2013) WITH NO ADDITIONAL RESERVOIR AGE CORRECTION. * GEOB3910 TIE POINTS. 172
TABLE 4.S2 : PA/TH FOR EACH OF THE TIME SLICES AT THE DIFFERENT CORES. ERROR BARS ARE THE MAXIMUM BETWEEN STANDARD DEVIATION ON PA/TH VALUES WITHIN THE TIME SLICE AND THE PROPAGATION OF INDIVIDUAL MEASUREMENT ERRORS ON THE AVERAGED PA/TH VALUE DEFINING THE TIME SLICE. 172
TABLE 4.S3 : SQUARE ROOT OF THE SUM OF SQUARED DIFFERENCE BETWEEN PA/TH DATA AND SIMULATED VALUE USING THE HS1 STREAMFUNCTION INTENSIFIED BY VARIOUS FACTORS FOR THE TWO EQUATORIAL CORES. THE MINIMUM VALUES INDICATE THE BEST AGREEMENT OF THE SIMULATED PA/TH WITH THE MEASURED PA/TH. 172
TABLE 4.S4 : PA/TH AND ISOTOPIC CONCENTRATIONS (DPM.G^{-1}) IN CORE MD09-3256Q 173
TABLE 4.S5 : CORE MD09-3256Q Δ^{13}C (C. *WUELLERSTORFI*) 174

REFERENCES

Alley, R. B. and Clark, P. U.: The deglaciation of the northern hemisphere: A global perspective, Annual Review of Earth and Planetary Sciences, 27, 149-182, 1999.

Alvarez-Solas, J., Robinson, A., Montoya, M., and Ritz, C.: Iceberg discharges of the last glacial period driven by oceanic circulation changes, Proceedings of the National Academy of Sciences of the United States of America, 110, 16350-16354, 2013.

Anderson, R. F., Ali, S., Bradtmiller, L. I., Nielsen, S. H. H., Fleisher, M. Q., Anderson, B. E., and Burckle, L. H.: Wind-Driven Upwelling in the Southern Ocean and the Deglacial Rise in Atmospheric CO2, Science, 323, 1443-1448, 2009.

Anderson, R. F. and Fleer, A. P.: Determination of natural actinides and plutonium in marine particulate material, Analytical Chemistry, 54, 1142-1147, 1982.

Anderson, R. F., Lao, Y., Broecker, W. S., Trumbore, S. E., Hofmann, H. J., and Wolfli, W.: Boundary scavenging in the pacific-ocean - a comparison of Be-10 and Pa-231, Earth and Planetary Science Letters, 96, 287-304, 1990.

Arz, H. W., Pätzold, J., and Wefer, G.: Climatic changes during the last deglaciation recorded in sediment cores from the northeastern Brazilian Continental Margin, Geo-Marine Letters, 19, 209-218, 1999.

Arz, H. W., Pätzold, J., and Wefer, G.: Correlated Millennial-Scale Changes in Surface Hydrography and Terrigenous Sediment Yield Inferred from Last-Glacial Marine Deposits off Northeastern Brazil, Quaternary Research, 50, 157-166, 1998.

Audi, G., Bersillon, O., Blachot, J., and Wapstra, A. H.: The NUBASE evaluation of nuclear and decay properties, Nuclear Physics A, 729, 3-128, 2003.

Auro, M. E., Robinson, L. F., Burke, A., Bradtmiller, L. I., Fleisher, M. Q., and Anderson, R. F.: Improvements to 232-thorium, 230-thorium, and 231-protactinium analysis in seawater arising from GEOTRACES intercalibration, Limnology and Oceanography-Methods, 10, 464-474, 2012.

Bard, E., Rostek, F., Turon, J. L., and Gendreau, S.: Hydrological impact of Heinrich events in the subtropical Northeast Atlantic, Science, 289, 1321-1324, 2000.

Blunier, T. and Brook, E. J.: Timing of millennial-scale climate change in Antarctica and Greenland during the last glacial period, Science, 291, 109-112, 2001.

Bond, G., Broecker, W., Johnsen, S., McManus, J., Labeyrie, L., Jouzel, J., and Bonani, G.: Correlations between climate records from North Atlantic sediments and Greenland ice, Nature, 365, 143-147, 1993.

Bond, G., Heinrich, H., Broecker, W. S., Labeyrie, L., MacManus, J., Andrews, J., Huon, S., Jantschik, R., Clasen, S., Simet, C., Tedesco, K., Klas, M., Bonani, G., and Ivy, S.: Evidence for massive discharges of icebergs into the North Atlantic ocean during the last glacial period., Nature, 360, 245-251, 1992.

Boyle, E. A. and Keigwin, L. D.: North Atlantic thermohaline circulation during the past 20,000 years linked to high-latitude surface temperature, Nature, 330, 35-40, 1987.

Bradtmiller, L. I., Anderson, R. F., Fleisher, M. Q., and Burckle, L. H.: Comparing glacial and Holocene opal fluxes in the Pacific sector of the Southern Ocean, Paleoceanography, 24, 2009.

Bradtmiller, L. I., Anderson, R. F., Fleisher, M. Q., and Burckle, L. H.: Opal burial in the equatorial Atlantic Ocean over the last 30 ka: Implications for glacial-interglacial changes in the ocean silicon cycle, Paleoceanography, 22, 2007.

Braun, H., Christl, M., Rahmstorf, S., Ganopolski, A., Mangini, A., Kubatzki, C., Roth, K., and Kromer, B.: Possible solar origin of the 1,470-year glacial climate cycle demonstrated in a coupled model, Nature, 438, 208-211, 2005.

Broecker, W. S., Bond, G., Klas, M., Bonani, G., and Wolfli, W.: A salt oscillator in the glacial atlantic? 1. THE CONCEPT, Paleoceanography, 5, 469-477, 1990.

Broecker, W. S. and Peng, T. H.: Tracers in the sea, Eldigio Press, Palisades, NY, 1982. 1982.

Broecker, W. S., Peteet, D. M., and Rind, D.: Does the ocean-atmosphere system have more than one stable mode of operation?, Nature, 315, 21-26, 1985.

Carton, J. A. and Katz, E. J.: Estimates of the zonal slope and seasonal transport of the atlantic north equatorial countercurrent, Journal of Geophysical Research-Oceans, 95, 3091-3100, 1990.

Burckel, P., Waelbroeck, C., Gherardi, J. M., Pichat, S., Arz, H., Lippold, J., Dokken, T., Thil, F. : Atlantic Ocean circulation changes preceded millennial tropical South America rainfall events during the last glacial, in prep., 2014 a.

Burckel, P., Waelbroeck, C., Luo, Y., Roche, D. M., Pichat, S., Gherardi, J. M., Govin, A., Thil, F. : Changes in the geometry and strength of the AMOC during the last glacial, in prep., 2014 b.

Burckel, P., Henry, G., Ng, H. C., Lippold, J., Pichat, S., Roy Barman, M., Thil, F., Antz, B., Gherardi, J. M., Waelbroeck, C., McManus, J. F., Robinson L. F. : Methodological recommendations for the analysis of sedimentary Pa/Th, in prep., 2014 c.

Charles, C. D., Lynch-Stieglitz, J., Ninnemann, U. S., and Fairbanks, R. G.: Climate connections between the hemisphere revealed by deep sea sediment core/ice core correlations, Earth and Planetary Science Letters, 142, 19-27, 1996.

Chase, Z., Anderson, R. F., Fleisher, M. Q., and Kubik, P. W.: The influence of particle composition and particle flux on scavenging of Th, Pa and Be in the ocean, Earth and Planetary Science Letters, 204, 215-229, 2002.

Chase, Z., Anderson, R. F., Fleisher, M. Q., and Kubik, P. W.: Scavenging of Th-230 Pa-231 and Be-10 in the Southern Ocean (SW Pacific sector): the importance of particle flux, particle composition and advection, Deep-Sea Research Part Ii-Topical Studies in Oceanography, 50, 739-768, 2003.

Cheng, H., Sinha, A., Cruz, F. W., Wang, X., Edwards, R. L., d'Horta, F. M., Ribas, C. C., Vuille, M., Stott, L. D., and Auler, A. S.: Climate change patterns in Amazonia and biodiversity, Nature communications, 4, 1411, 2013.

Chiang, J. C. H. and Bitz, C. M.: Influence of high latitude ice cover on the marine Intertropical Convergence Zone, Clim. Dynam., 2005. DOI 10.1007/s00382-00005-00040-00385, 2005.

Choi, M. S., François, R., Sims, K. W. W., Bacon, M. P., Brown-Leger, S., Fleer, A. P., Ball, L. A., Schneider, D., and Pichat, S.: Rapid determination of 230Th and 231Pa in seawater by desolvated micro-nebulization Inductively Coupled Plasma magnetic sector mass spectrometry, Mar. Chem., 76, 99-112, 2001.

Condon, D. J., McLean, N., Noble, S. R., and Bowring, S. A.: Isotopic composition (U-238/U-235) of some commonly used uranium reference materials, Geochimica Et Cosmochimica Acta, 74, 7127-7143, 2010.

Cortijo, E., Labeyrie, L., Vidal, L., Vautravers, M., Chapman, M., Duplessy, J. C., Elliot, M., Arnold, M., Turon, J. L., and Auffret, G.: Changes in sea surface hydrology associated with Heinrich event 4 in the North Atlantic Ocean between 40°N and 60°N., Earth and Planetary Science Letters, 146, 29-45, 1997.

Curry, W. B. and Oppo, D. W.: Glacial water mass geometry and the distribution of d13C of SCO2 in the western Atlantic Ocean, Paleoceanography, 20, doi:10.1029/2004PA001021, 2005.

Dansgaard, W., Johnsen, S. J., Clausen, H. B., Dahl-Jensen, D., Gundestrup, N. S., Hammer, C. U., Hvidberg, C. S., Steffensen, J. P., Sveinbjörnsdottir, A. E., Jouzel, J., and Bond, G.: Evidence for general instability of past climate from a 250-kyr ice-core record, Nature, 364, 218-220, 1993.

Demaster, D. J.: - Measuring Biogenic Silica in Marine Sediments and Suspended Matter, 2013. - 367, 2013.

Deng, F., Thomas, A. L., Rijkenberg, M. J. A., and Henderson, G. M.: Controls on seawater Pa-231, Th-230 and Th-232 concentrations along the flow paths of deep waters in the Southwest Atlantic, Earth and Planetary Science Letters, 390, 93-102, 2014.

Deplazes, G., Lückge, A., Peterson, L. C., Timmermann, A., Hamann, Y., Hughen, K. A., Röhl, U., Laj, C., Cane, M. A., Sigman, D. M., and Haug, G. H.: Links between tropical rainfall and

North Atlantic climate during the last glacial period, Nature Geoscience, 6, 213-217, 2013.

Dickson, R. R. and Brown, J.: The production of north-atlantic deep-water - sources, rates, and pathways, Journal of Geophysical Research-Oceans, 99, 12319-12341, 1994.

Ditlevsen, P. D., Andersen, K. K., and Svensson, A.: The DO-climate events are probably noise induced: statistical investigation of the claimed 1470 years cycle, Climate of the Past, 3, 129-134, 2007.

Dunk, R. M., Mills, R. A., and Jenkins, W. J.: A reevaluation of the oceanic uranium budget for the Holocene, Chemical Geology, 190, 45-67, 2002.

Duplessy, J.-C., Shackleton, N. J., Fairbanks, R. G., Labeyrie, L., Oppo, D., and Kallel, N.: Deepwater source variations during the last climatic cycle and their impact on the global deepwater circulation, Paleoceanography, 3, 343-360, 1988.

Elliot, M., Labeyrie, L., and Duplessy, J. C.: Changes in North-Atlantic deep-water formation associated with the Dansgaard-Oeschger temperature oscillations (60-10 ka), Quaternary Science Reviews, 21, 1153-1165, 2002.

Emery, W. J.: Water types and water masses. In: Encyclopedia of Ocean Sciences, Press, A. (Ed.), San Diego, 2001.

EPICA, C. M.: One-to-one coupling of glacial climate variability in Greenland and Antarctica, Nature, 444, 195-198, 2006.

Flood, R. D., Piper, D. J. W., and Party, S. S.: Introduction. In: Proceedings of the Ocean Drilling Program, scientific results, 1995.

Francois, R.: Proxies in Late Cenozoic Paleoceanography: Paleoflux and Paleocirculation from Sediment 230Th and 231Pa/230Th, Elsevier, 2007.

Fratantoni, D. M. and Glickson, D. A.: North Brazil current ring generation and evolution observed with SeaWiFS, Journal of Physical Oceanography, 32, 1058-1074, 2002.

Galhardo, C. X. and Masini, J. C.: Spectrophotometric determination of phosphate and silicate by sequential injection using molybdenum blue chemistry, Analytica Chimica Acta, 417, 191-200, 2000.

Ganachaud, A. and Wunsch, C.: Improved estimates of global ocean circulation, heat transport and mixing from hydrographic data, Nature, 408, 453-457, 2000.

Geibert, W. and Usbeck, R.: Adsorption of thorium and protactinium onto different particle types : Experimental findings, Geochimica and Cosmochimica Acta, 68, 1489-1501, 2004.

Gherardi, J.-M., Labeyrie, L., McManus, J., Francois, R., Skinner, L., and Cortijo, E.: Evidence from the North Eastern Atlantic Basin for Variability of the Meridional

Overturning Circulation through the last Deglaciation, Earth and Planetary Science Letters, 240, 710-723, 2005.

Gherardi, J.-M., Labeyrie, L., Nave, S., Francois, R., McManus, J. F., and Cortijo, E.: Glacial-interglacial circulation changes inferred from 231Pa/230Th sedimentary record in the North Atlantic region, Paleoceanography, 24, doi:10.1029/2008PA001696, 2009.

Guihou, A., Pichat, S., Nave, S., Govin, A., Labeyrie, L., Michel, E., and Waelbroeck, C.: Late slowdown of the Atlantic Meridional Overturning Circulation during the Last Glacial Inception: new constraints from sedimentary (231Pa/2303 Th), Earth and Planetary Science Letters, 289, 520-529, 2010a.

Guihou, A., Pichat, S., Nave, S., Govin, A., Labeyrie, L., Michel, E., and Waelbroeck, C.: Late slowdown of the Atlantic Meridional Overturning Circulation during the Last Glacial Inception: New constraints from sedimentary (Pa-231/Th-230), Earth and Planetary Science Letters, 289, 520-529, 2010b.

Gutjahr, M. and Lippold, J.: Early arrival of Southern Source Water in the deep North Atlantic prior to Heinrich event 2, Paleoceanography, 26, 2011.

Hastenrath, S.: Exploring the climate problems of Brazil's Nordeste: a review, Climatic Change, 112, 243-251, 2011.

Heinrich, H.: Origin and consequences of cyclic ice-rafting in the Northeast Atlantic ocean during the past 130000 years, Quaternary Research, 29, 142-152, 1988.

Hemming, S. R.: Heinrich events: massive Late Pleistocene detritus layers of the North Atlantic and their global climate imprint, Reviews of Geophysics, 42, 1-43, 2004.

Henderson, G. M. and Anderson, R. F.: The U-series toolbox for paleoceanography, Uranium-Series Geochemistry, 52, 493-531, 2003.

Huang, K.-F., Oppo, D. W., and Curry, W. B.: Decreased influence of Antarctic intermediate water in the tropical Atlantic during North Atlantic cold events, Earth and Planetary Science Letters, 389, 200-208, 2014.

Jaeschke, A., Rühlemann, C., Arz, H., Heil, G., and Lohmann, G.: Coupling of millennial-scale changes in sea surface temperature and precipitation off northeastern Brazil with high-latitude climate shifts during the last glacial period, Paleoceanography, 22, PA4206, doi:4210.1029/2006PA001391, 2007.

Johns, W. E., Lee, T. N., Beardsley, R. C., Candela, J., Limeburner, R., and Castro, B.: Annual cycle and variability of the North Brazil Current, Journal of Physical Oceanography, 28, 103-128, 1998.

Johnsen, S. J., Clausen, H. B., Dansgaard, W., Fuhrer, K., Gundestrup, N., Hammer, C. U., Iversen, P., Jouzel, J., Stauffer, B., and Steffensen, J. P.: Irregular glacial interstadials recorded in a new Greenland ice core, Nature, 359, 311-313, 1992.

Kageyama, M., Mignot, J., Swingedouw, D., Marzin, C., Alkama, R., and Marti, O.: Glacial climate sensitivity to different states of the Atlantic Meridional Overturning Circulation: results from the IPSL model, Climate of the Past, 5, 551-570, 2009.

Kageyama, M., Paul, A., Roche, D., and Van Meerbeeck, C. J.: Modelling glacial climatic millennial-scale variability related to changes in the Atlantic meridional overturning circulation: a review, Quat. Sci. Rev., 29, 2931-2956, 2010.

Kanner, L. C., Burns, S. J., Cheng, H., and Edwards, R. L.: High-latitude forcing of the South American summer monsoon during the Last Glacial, Science, 335, 570-573, 2012.

Kaspi, Y., Sayag, R., and Tziperman, E.: A ''triple sea-ice state'' mechanism for the abrupt warming and synchronous ice sheet collapses during Heinrich events, Paleoceanography, 19, 2004.

Kindler, P., Guillevic, M., Baumgartner, M., Schwander, J., Landais, A., and Leuenberger, M.: Temperature reconstruction from 10 to 120 kyr b2k from the NGRIP ice core, Climate of the Past, 2014. 2014.

Kissel, C., Laj, C., Labeyrie, L., Dokken, T., Voelker, A., and Blamart, D.: Rapid climatic variations during marine isotopic stage 3: magnetic analysis of sediments from Nordic Seas and North Atlantic, Earth and Planetary Science Letters, 171, 489-502, 1999.

Kretschmer, S., Geibert, W., van der Loeff, M. M. R., Schnabel, C., Xu, S., and Mollenhauer, G.: Fractionation of Th-230, Pa-231, and Be-10 induced by particle size and composition within an opal-rich sediment of the Atlantic Southern Ocean, Geochimica Et Cosmochimica Acta, 75, 6971-6987, 2011.

Kroopnick, P. M.: The distribution of 13C of SCO2 in the world oceans, Deep-Sea Research, Part A, 32, 57-84, 1985.

Kuhlbrodt, T., Griesel, A., Montoya, M., Levermann, A., Hofmann, M., and Rahmstorf, S.: On the driving processes of the Atlantic meridional overturning circulation, Reviews of Geophysics, 45, 2007.

Labeyrie, L., Vidal, L., Cortijo, E., Paterne, M., Arnold, M., Duplessy, J. C., Vautravers, M., Labracherie, M., Duprat, J., Turon, J. L., Grousset, F., and van Weering, T.: Surface and deep hydrology of the northern Atlantic Ocean during the last 150,000 years, Philophical Transaction of Royal Society of London, 348, 255-264, 1995.

Lambeck, K. and Chappell, J.: Sea level change through the last glacial cycle, Science, 292, 679-686, 2001.

Lankhorst, M., Fratantoni, D., Ollitrault, M., Richardson, P., Send, U., and Zenk, W.: The mid-depth circulation of the northwestern tropical Atlantic observed by floats, Deep-Sea Research Part I-Oceanographic Research Papers, 56, 1615-1632, 2009.

Lea, D. W., Pak, D. K., Peterson, L. C., and Hughen, K. A.: Synchroneity of Tropical and High-Latitude Atlantic Temperatures over the Last Glacial Termination, Science, 301, 1361-1364, 2003.

Li, C., Battisti, D. S., and Bitz, C. M.: Can North Atlantic Sea Ice Anomalies Account for Dansgaard-Oeschger Climate Signals?, Journal of Climate, 23, 5457-5475, 2010.

Lippold, J., Gherardi, J.-M., and Luo, Y.: Testing the 231Pa/230Th paleocirculation proxy: A data versus 2D model comparison, Geophys. Res. Lett., 38, doi:10.1029/2011GL049282, 2011.

Lippold, J., Gruetzner, J., Winter, D., Lahaye, Y., Mangini, A., and Christl, M.: Does sedimentary Pa-231/Th-230 from the Bermuda Rise monitor past Atlantic Meridional Overturning Circulation?, Geophysical Research Letters, 36, 2009.

Lippold, J., Luo, Y., Francois, R., Allen, S. E., Gherardi, J., Pichat, S., Hickey, B., and Schulz, H.: Strength and geometry of the glacial Atlantic Meridional Overturning Circulation, Nature Geoscience, 5, 813-816, 2012a.

Lippold, J., Mulitza, S., Mollenhauer, G., Weyer, S., Heslop, D., and Christl, M.: Boundary scavenging at the East Atlantic margin does not negate use of Pa-231/Th-230 to trace Atlantic overturning, Earth and Planetary Science Letters, 333, 317-331, 2012b.

Lumpkin, R. and Garzoli, S. L.: Near-surface circulation in the tropical Atlantic Ocean, Deep-Sea Research Part I-Oceanographic Research Papers, 52, 495-518, 2005.

Luo, S. D. and Ku, T. L.: On the importance of opal, carbonate, and lithogenic clays in scavenging and fractionating Th-230, Pa-231 and Be-10 in the ocean, Earth and Planetary Science Letters, 220, 201-211, 2004.

Luo, Y., Francois, R., and Allen, S. E.: Sediment 231Pa/230Th as a recorder of the rate of the Atlantic meridional overturning circulation: insights from a 2-D model, Ocean Science, 6, 381-400, 2010.

Lynch-Stieglitz, J., Fairbanks, R. G., and Charles, C. D.: Glacial-interglacial history of Antarctic Intermediate Water : relative strengths of Antarctic versus Indian Ocean sources, Paleoceanography, 9, 7-29, 1994.

Lynch-Stieglitz, J., Schmidt, M. W., Henry, L. G., Curry, W. B., Skinner, L. C., Mulitza, S., Zhang, R., and Chang, P.: Muted change in Atlantic overturning circulation over some glacial-aged Heinrich events, Nature Geoscience, 7, 144-150, 2014.

Mangini, A., Godoy, J. M., Godoy, M. L., Kowsmann, R., Santos, G. M., Ruckelshausen, M., Schroeder-Ritzrau, A., and Wacker, L.: Deep sea corals off Brazil verify a poorly ventilated Southern Pacific Ocean during H2, H1 and the Younger Dryas, Earth and Planetary Science Letters, 293, 269-276, 2010.

Marcott, S. A., Clark, P. U., Padman, L., Klinkhammer, G. P., Springer, S. R., Liu, Z., Otto-Bliesner, B. L., Carlson, A. E., Ungerer, A., Padman, J., He, F., Cheng, J., and Schmittner, A.:

Ice-shelf collapse from subsurface warming as a trigger for Heinrich events, Proceedings of the National Academy of Sciences of the United States of America, 108, 13415-13419, 2011.

Maslin, M. A., Shackleton, N. J., and Pflaumann, U.: Surface water temperature, salinity and density changes in the northeast Atlantic during the last 45000 years: Heinrich events, deep water formation and climaic rebounds, Paleoceanography, 10, 527-544, 1995.

McManus, J. F., Francois, R., Gherardi, J.-M., Keigwin, L. D., and Brown-Leger, S.: Collapse and rapid resumption of Atlantic meridional circulation linked to deglacial climate changes, Nature, 428, 834-837, 2004.

McManus, J. F., Oppo, D. W., and Cullen, J. L.: A 0.5-million-year record of millenial-scale climate variability in the North Atlantic, Science, 283, 971-975, 1999.

Mignot, J., Ganopolski, A., and Levermann, A.: Atlantic subsurface temperatures: Response to a shutdown of the overturning circulation and consequences for its recovery, Journal of Climate, 20, 4884-4898, 2007.

Moran, S. B., Shen, C. C., Edmonds, H. N., Weinstein, S. E., Smith, J. N., and Edwards, R. L.: Dissolved and particulate Pa-231 and Th-230 in the Atlantic Ocean: constraints on intermediate/deep water age, boundary scavenging, and Pa-231/Th-230 fractionation, Earth and Planetary Science Letters, 203, 999-1014, 2002.

Mortlock, R. A. and Froelich, P. N.: A simple method for the rapid-determination of biogenic opal in pelagic marine-sediments, Deep-Sea Research Part a-Oceanographic Research Papers, 36, 1415-1426, 1989.

Muller, P. J. and Schneider, R.: An automated leaching method for the determination of opal in sediments and particulate matter, Deep-Sea Research Part I-Oceanographic Research Papers, 40, 425-444, 1993.

Murray, K. K., Boyd, R. K., Eberlin, M. N., Langley, G. J., Li, L., and Naito, Y.: Definitions of terms relating to mass spectrometry (IUPAC Recommendations 2013), Pure and Applied Chemistry, 85, 1515-1609, 2013.

Negre, C., Thomas, A. L., Luis Mas, J., Garcia-Orellana, J., Henderson, G. M., Masque, P., and Zahn, R.: Separation and Measurement of Pa, Th, and U Isotopes in Marine Sediments by Microwave-Assisted Digestion and Multiple Collector Inductively Coupled Plasma Mass Spectrometry, Analytical Chemistry, 81, 1914-1919, 2009.

Negre, C., Zahn, R., Thomas, A. L., Masque, P., Henderson, G. M., Martinez-Mendez, G., Hall, I. R., and Mas, J. L.: Reversed flow of Atlantic deep water during the Last Glacial Maximum, Nature, 468, 84-+, 2010.

Oppo, D. W. and Lehman, S. J.: Mid-depth circulation of the subpolar north ATlantic during the last glacial maximum, Science, 259, 1148-1151, 1993.

Oppo, D. W. and Lehman, S. J.: Suborbital timescale variability of North Atlantic deep water during the past 200,000 years, Paleoceanography, 10, 901-910, 1995.

Pahnke, K., Goldstein, S. L., and Hemming, S. R.: Abrupt changes in Antarctic Intermediate Water circulation over the past 25,000 years, Nature Geoscience, 1, 870-874, 2008.

Peck, V. L., Hall, I. R., Zahn, R., Elderfield, H., Grousset, F., Hemming, S. R., and Scourse, J. D.: High resolution evidence for linkages between NW European ice sheet instability and Atlantic Meridional Overturning Circulation, Earth and Planetary Science Letters, 243, 476-488, 2006.

Pena, L. D., Goldstein, S. L., Hemming, S. R., Jones, K. M., Calvo, E., Pelejero, C., and Cacho, I.: Rapid changes in meridional advection of Southern Ocean intermediate waters to the tropical Pacific during the last 30 kyr, Earth and Planetary Science Letters, 368, 20-32, 2013.

Rahmstorf, S.: Ocean circulation and climate during the past 120,000 years, Nature, 419, 207-214, 2002.

Rasmussen, T. L. and Thomsen, E.: The role of the North Atlantic Drift in the millennial timescale glacial climate fluctuations, Palaeogeography Palaeoclimatology Palaeoecology, 210, 101-116, 2004.

Rasmussen, T. L., Thomsen, E., van Weering, T. C. E., and Labeyrie, L.: Rapid changes in surface and deep water conditions at the Faeroe Margin during the last 58,000 years, Paleoceanography, 11, 757-771, 1996.

Regelous, M., Turner, S. P., Elliot, T. R., Rostami, K., and Hawkesworth, C. J.: Measurement of femtogram quantities of protactinium in silicate rock Samples by multicollector inductively coupled plasma mass spectrometry, Anal. Chem., 76, 3584-3589, 2004.

Reid, J. L.: On the total geostrophic circulation of the north-atlantic ocean - flow patterns, tracers, and transports, Progress in Oceanography, 33, 1-92, 1994.

Reimer, P. J., Bard, E., Bayliss, A., Beck, J. W., Blackwell, P. G., Bronk Ramsey, C., Buck, C. E., Cheng, H., Edwards, R. L., Friedrich, M., Grootes, P. M., Guilderson, T. P., Haflidason, H., Hajdas, I., Hatté, C., Heaton, T. J., Hoffman, D. L., Hogg, A. G., Hughen, K. A., Kaiser, K. F., Kromer, B., Manning, S. W., Niu, M., Reimer, R. W., Richards, D. A., Scott, E. M., Southon, J. R., Staff, R. A., Turney, C. S. M., and van der Plicht, J.: IntCal13 and Marine13 Radiocarbon Age Calibration Curves 0–50,000 years Cal BP, Radiocarbon, 55, 1869-1887, 2013.

Robinson, L. F., Belshaw, N. S., and Henderson, G.: U and Th concentrations and isotope ratios in modern carbonates and waters from the bahamas, Geochimica and Cosmochimica Acta, 68, 1777-1789, 2004a.

Robinson, L. F., Henderson, G. M., Hall, L., and Matthews, I.: Climatic control of riverine and Seawater uranium-isotope ratios, Science, 305, 851-854, 2004b.

Roche, D., Paillard, D., and Cortijo, E.: Constraints on the duration and freshwater release of Heinrich event 4 through isotope modelling, Nature, 432, 379-382, 2004.

Roche, D. M., Paillard, D., Caley, T., Waelbroeck, C. : LGM hosing approach to Heinrich Event 1: results and perspectives, Quaternary Science Reviews, in press, 2014.

Ruhlemann, C., Diekmann, B., Mulitza, S., and Frank, M.: Late Quaternary changes of western equatorial Atlantic surface circulation and Amazon lowland climate recorded in Ceara Rise deep-sea sediments, Paleoceanography, 16, 293-305, 2001.

Sachs, J. P. and Lehman, S. J.: Subtropical North Atlantic temperatures 60,000 to 30,000 years ago, Science, 286, 756-759, 1999.

Scholten, J. C., Fietzke, J., Mangini, A., Garbe-Schbnberg, C. D., Eisenhauer, A., Schneider, R., and Stoffers, P.: Advection and scavenging: Effects on (230)Th and (231)Pa distribution off Southwest Africa, Earth and Planetary Science Letters, 271, 159-169, 2008.

Scholten, J. C., Fietzke, J., Mangini, A., Stoffers, P., Rixen, T., Gaye-Haake, B., Blanz, T., Ramaswamy, V., Sirocko, F., Schulz, H., and Ittekkot, V.: Radionuclide fluxes in the Arabian Sea: the role of particle composition, Earth and Planetary Science Letters, 230, 319-337, 2005.

Schott, F. A.: The zonal currents and transports at 35°W in the tropical Atlantic, Geophysical Research Letters, 30, 2003.

Schulz, M.: On the 1470-year pacing of Dansgaard-Oeschger warm events, Paleoceanography, 17, 2002.

Shaffrey, L. and Sutton, R.: Bjerknes compensation and the decadal variability of the energy transports in a coupled climate model, Journal of Climate, 19, 1167-1181, 2006.

Siddall, M., Henderson, G. M., Edwards, N. R., Frank, M., Müller, S. A., Stocker, T. F., and Joos, F.: 231Pa/ 230Th fractionation by ocean transport, biogenic particle flux and particle type, Earth and Planetary Science Letters, 237, 135– 155, 2005.

Siddall, M., Stocker, T. F., Henderson, G. M., Joos, F., Frank, M., Edwards, N. R., Ritz, S. P., and Müller, S. A.: Modeling the relationship between 231Pa/230Th distribution in North Atlantic sediment and Atlantic meridional overturning circulation, Paleoceanography, 22, doi:10.1029/2006PA001358, 2007.

Stocker, T. F.: The seesaw effect, Science, 282, 61-62, 1998.

Stocker, T. F. and Johnsen, S. J.: A minimum thermodynamic model for the bipolar seesaw, Paleoceanography, 18, doi:10.1029/2003PA000920, 2003.

Straub, M., Sigman, D. M., Ren, H., Martinez-Garcia, A., Meckler, A. N., Hain, M. P., and Haug, G. H.: Changes in North Atlantic nitrogen fixation controlled by ocean circulation, Nature, 501, 200-+, 2013.

Talley, L. D., Reid, J. L., and Robbins, P. E.: Data-based meridional overturning streamfunctions for the global ocean, Journal of Climate, 16, 3213-3226, 2003.

Thomas, A. L., Henderson, G. M., and Robinson, L. F.: Interpretation of the 231Pa/230Th paleocirculation proxy: New water-column measurements from the southwest Indian Ocean, Earth and Planetary Science Letters, 241, 493-504, 2006.

van der Swaluw, E., Drijfhout, S. S., and Hazeleger, W.: Bjerknes compensation at high northern latitudes: The ocean forcing the atmosphere, Journal of Climate, 20, 6023-6032, 2007.

Vautravers, M. J., Shackleton, N. J., Lopez-Martinez, C., and Grimalt, J. O.: Gulf Stream variability during marine isotope stage 3, Paleoceanography, 19, 2004.

Viana, A. R., Faugeres, J. C., Kowsmann, R. O., Lima, J. A. M., Caddah, L. F. G., and Rizzo, J. G.: Hydrology, morphology and sedimentology of the Campos continental margin, offshore Brazil, Sedimentary Geology, 115, 133-157, 1998.

Vidal, L., Labeyrie, L., Cortijo, E., Arnold, M., Duplessy, J. C., Michel, E., Becqué, S., and van Weering, T. C. E.: Evidence for changes in the North Atlantic Deep Water linked to meltwater surges during the Heinrich events, Earth and Planetary Science Letters, 146, 13-26, 1997.

Voelker, A. H. L.: Global distribution of centennial-scale records for Marine Isotope Stage (MIS) 3: a database, Quaternary Science Reviews, 21, 1185-1212, 2002.

Vogl, J. and Pritzkow, W.: Isotope Dilution Mass Spectrometry - A Primary Method of Measurement and Its Role for RM Certification, Mapan-Journal of Metrology Society of India, 25, 135-164, 2010.

Wang, Y. J., Cheng, H., Edwards, R. L., An, Z. S., Wu, J. Y., Shen, C.-C., and Dorale, J. A.: A High-Resolution Absolute-Dated Late Pleistocene Monsoon Record from Hulu Cave, China, Science, 294, 2345-2348, 2001.

Weyer, S., Anbar, A. D., Gerdes, A., Gordon, G. W., Algeo, T. J., and Boyle, E. A.: Natural fractionation of U-238/U-235, Geochimica Et Cosmochimica Acta, 72, 345-359, 2008.

Wilson, K. E., Maslin, M. A., and Burns, S. J.: Evidence for a prolonged retroflection of the North Brazil Current during glacial stages, Palaeogeography Palaeoclimatology Palaeoecology, 301, 86-96, 2011.

Yu, E.-F., Francois, R., and Bacon, M.: Similar rates of modern and last-glacial ocean thermohaline circulation inferred from radiochemical data, Nature, 379, 689-694, 1996.